# 3. Final Report

## «Multiscale Computational Electromagnetics Modeling and Validation of Current and Energy Flows in the Skin Tissue Microstructure at mm-Wave Frequencies (MicroBioEM)»

**Summary**

The final report addresses the research carried out in the last period of this project. This includes a numerical multiscale human tissue analysis aiming at (i) a precise *macroscopic* multi-layer model of the human skin, which is based on the specific tissue layer's cellular microstructure (*bottom-up approach*), yielding corresponding effective material parameters (i.e. dielectric functions); and (ii) the entanglement of a *virtual microdosimetry* to the corresponding *macrosopic skin exposure scenarios* (*scale-back projection*). In this study, we initiated the analysis of the impact of electromagnetic (EM) exposure on the detailed microstructure of tissue cells. Here we specifically focused on differentiated keratinocytes within the epidermis (preferably in the basal layer) based on a unique *histochemically parametrized* cell model, which allows for corresponding cell shapes and textures. The study examines diverse field quantities (E-field, current density, power density, EM energy uptake for *micro-SAR* determination) in different cell compartments at various frequencies. Using a Monte-Carlo-like stochastic analysis of the cell's microstructure, it deduces statistical field quantities such as mean values (i.e. expectation values) and variances (i.e. coefficients of variations, CVs, as its corresponding relative figures). Specifically, the power absorption within the microscopic model volume of a keratinocyte serves as a crucial link between the exposure of the *macroscopic* skin model and the subsequent quasi-static analysis on the cellular level, allowing for the intended *virtual microdosimetry* within the skin's and cellular microstructure. We aim to methodically explore variations of the *micro-SAR* originating from the cellular microstructure of the skin and assess how they potentially influence the *SAR* exposure limits set by ICNIRP for 5G frequencies. As an exemplary finding, the CV of the *micro-SAR* within the basal layer turned out to amount to 58 % at 3.5 GHz, which is in the 5G NR/FR1 band. The experimental studies encompass precise transmission/reflection measurements with the MCK test kit in the $K_a$- and D-band using tissue samples like Lyonnais sausage slices, salami slices, artificial skin and pig skin. The inherent leakage issues of the MCK setup, which are potentially impacting mainly the imaginary part of the retrieved dielectric function, are investigated in detail using precise azimuthal nearfield scans around the gap region where the tissue sample is usually from-fitted into. In addition our just installed robotized near-field scanner *DASY8 MP8B TX2-60L* bearing the *EUmmWVx* field probe from SPEAG is described together with the further developments of our home-made coaxial near-field probe setups (and their inherent resolution issues). As a final contribution we report on a numerical study based on a Turkish dermatological data set to reveal a gender-specific electromagnetic power absorption in human skin tissue apparent in the distinct frequency band between 3-25 GHz.

Kevin Jerbic, Jan-Taro Svejda, and Daniel Erni

General and Theoretical Electrical Engineering (ATE)
Department of Electrical Engineering and Information Technology
Faculty of Engineering
University of Duisburg Essen
D-47048 Duisburg

## 3. Final report

Final annual status report regarding the period 01.01.2022-31.12.2023 of the research project

«Multiscale Computational Electromagnetics Modeling and Validation of Current and Energy Flows in the Skin Tissue Microstructure at mm-Wave Frequencies (MicroBioEM)»

FSM-Project No. A2019-01.

### Project management

General and Theoretical Electrical Engineering (ATE)
Department of Electrical Engineering and Information Technology
Faculty of Engineering
University of Duisburg Essen

Bismarckstraße 81
D-47057 Duisburg

phone: +49-(0)-203-379-4212
fax: +49-(0)-203-379-3499
e-mail: daniel.erni@uni-due.de
web: https://www.ate.uni-due.de

December 31, 2023

M.Sc. Kevin Jerbic (reporter)

Prof. Dr. sc. techn. Daniel Erni (coordination)

### Project collaborators

| | |
|---|---|
| Dr.-Ing. Jan Taro Svejda | exposure experiments, 3D printing, tissue measurements (ATE, University of Duisburg-Essen) |
| Dr. Mandana Jalali | skin modeling, head of the ATE Bioelectromagnetics Center (ATE, University of Duisburg-Essen) |
| M.Sc. Marvin Degen | exposure experiments, data retrieval algorithms (ATE, University of Duisburg-Essen) |
| M.Sc. Sinan Doğusan | exposure model, gender- & ethnicity related exposure campaign (ATE, University of Duisburg-Essen) |
| M.Sc. Benedikt Sievert | coaxial near-field probes, near-field scanner fabrication (ATE, University of Duisburg-Essen) |
| Dr.-Ing. Andreas Rennings | theory and modeling (ATE, University of Duisburg-Essen) |
| Dr. sc. techn. Jürg Fröhlich | EM microdosimetry, bioelectromagnetics (Fields at Work GmbH) |
| Dr. sc. techn. Sonja Huclova | EM microdosimetry (Zürcher Kantonalbank) |

## Table of contents

# 1 Recap on electromagnetic field restrictions in human tissue exposure

As an introduction into the topic of electromagnetic exposure of human skin we briefly recap the essentials of the field restrictions already provided in the prior research report [A18] (readers who are familiar with the following sections are welcome to skip them). This includes a concise summary of the guidelines on electromagnetic field exposure (100 kHz to 300 GHz) provided by the *International Commission on Non-Ionizing Radiation Protection (ICNIRP)* [3, 4]. Following the recap, the document specifies the current exposure scenario, introducing developed skin and underlying cell models.

## 1.1 Electromagnetic exposure of skin tissue

The guidelines aim to restrict electromagnetic field (EMF) exposure below thresholds for adverse health effects while addressing the health impacts of thermal exposure, based on absolute temperature rises above the body part's normothermic level. Limiting absolute temperatures is impractical due to factors like clothing and environmental conditions. Hence, the guidelines aim to regulate any temperature increase looking at physical measures to quantify EMF restrictions preventing temperature elevation. An important quantity to restrict temperature increases due to EM energy uptake is the specific absorption rate (*SAR*) defined as

$$SAR(\vec{r}) = \frac{\sigma(\vec{r})\left|\underline{\vec{E}}(\vec{r})\right|^2}{\rho(\vec{r})} = \frac{p(\vec{r})}{\rho(\vec{r})}. \tag{1.1}$$

where $\sigma$, $\left|\underline{\vec{E}}\right|$, $\rho$ and $p$ denote the electric conductivity, the rms-magnitude of the electric field strength, the mass density and the power density respectively, all as a function of $\vec{r}$ which denotes the position within the tissue. In this context, the SAR is treated as a function of location measured in W/kg. In practical terms, it is more relevant to view SAR as an average over a specific volume, which is associated to the involved mass [3]

$$SAR_i = \frac{\iiint_{v_i} p(\vec{r})dv}{\iiint_{v_i} \rho(\vec{r})dv} = \frac{P_i}{m_i}. \tag{1.2}$$

In the $SAR_i$, definition, the index $i \in \{\mathrm{wb}, 10\mathrm{g}\}$ represents two volume types: (a) the entire body and (b) a standardized cubic volume (side length 2.15 cm) at an arbitrary position, representing 10 g of mass with tissue density assumed to be that of water ($\rho_{\mathrm{water}} = 1000\ \mathrm{kg/m^3}$). This generic volume effectively captures thermal heat diffusion processes arising from diverse electromagnetic field-induced energy inputs into realistic tissue microstructures during exposure scenarios. Actually, the *SAR* is derived from a more practical definition, specifically involving the temperature increase within this volume over time.

$$SAR_i = C\frac{\Delta T_i}{\Delta t}, \tag{1.3}$$

where $\Delta T_i$, $\Delta t$ and $C$ respectively denote the spatial average of the temperature increase within the investigated volume, a time interval in which this occurs and the specific heat capacity of the tissue under investigation. These two definitions together provide a physical foundation to determine the approximate relationship between the power absorbed by the tissue and its subsequent increase in temperature:

$$SAR_i = \frac{P_i}{m_i} = C\frac{\Delta T_i}{\Delta t}, \tag{1.4}$$

## 1.2 Exposure limits

The relationship is labeled as approximate due to the non-linear nature of the specific heat capacity, $C$, influenced by various factors. ICNIRP establishes health effect thresholds conservatively, setting

a 1 °C core body temperature increase within a 30-minute interval as the threshold (whole body $SAR_{wb}$ of 4 W/kg). Reduction factors of 10 and 50 are applied for occupational and general exposure, yielding basic restrictions of 0.4 W/kg and 0.08 W/kg for $SAR_{wb}$ over 30 min. To prevent local temperature increase, a nuanced approach considers different normothermic temperatures in type 1 and type 2 tissues. Thresholds for adverse health effects are set at 5 °C for type 1 tissues and 2 °C for type 2 tissues within a 6-minute interval, corresponding to $SAR_{10g}$ values of 40 W/kg and 20 W/kg. Reduction factors result in basic restrictions of 20 W/kg and 4 W/kg for type 1 tissues, and 10 W/kg and 2 W/kg for type 2 tissues in occupational and general exposure.

Determining *adverse health effect thresholds* and *basic restrictions* is complex due to the wide frequency range covered by the guidelines. At higher frequencies, EM fields penetrate less, resulting in increased absorption by surface tissues like skin and cornea. To address this, additional measures are required for local exposure restrictions beyond 6 GHz, including the absorbed power density $S_{ab}$.

$$S_{\mathrm{ab}} = \frac{\iint_A \mathrm{Re}\{\vec{S}\}\,\vec{n}\,dA}{A} \tag{1.5}$$

$\mathrm{Re}\{\vec{S}\}$ denotes the real part of the Poynting vector and $\vec{n}$ denotes the normal vector to the surface area $A$ over which the power density is integrated. At high frequencies, with low penetration depths, the threshold for *adverse health effects* is conceptualized according to a 5 °C temperature increase in type 1 tissue. Referring to [1, 2], the absorbed power density of 200 W/m$^2$ is set as the operational threshold over a 6-minute interval and a 4 cm$^2$ area. Beyond 30 GHz, the threshold is 400 W/m$^2$ over the same interval but for a 1 cm$^2$ area. Occupational and general exposure reduction factors of 2 and 10 are applied, resulting in basic restrictions for $S_{ab}$ of 100 W/m$^2$ and 40 W/m$^2$ over 6 minutes. A comprehensive overview summarizing the basic restrictions limiting exposure from 100 kHz to 300 GHz is given in Tab. 1.1.

*Tab.1.1: Basic restrictions limiting exposure from 100 kHz to 300 GHz, for averaging intervals ≥ 6 min (adapted from [3].*

| Exposure Scenario | Frequency Range | $SAR_{\mathrm{wb}}$ (W/kg) | Type 2 Tissue $SAR_{10g}$ (W/kg) | Type 1 Tissue $SAR_{10g}$ (W/kg) | $S_{\mathrm{ab}}$ (W/kg) |
|---|---|---|---|---|---|
| **Occupational** | 100 kHz to 6 GHz | 0.4 | 20 | 10 | NA |
| | >6 GHz to 30 GHz | 0.4 | NA | NA | 100 |
| | >30 GHz to 300 GHz | 0.4 | NA | NA | 200 |
| **General Public** | 100 kHz to 6 GHz | 0.08 | 4 | 2 | NA |
| | >6 GHz to 30 GHz | 0.08 | NA | NA | 20 |
| | >30 GHz to 300 GHz | 0.08 | NA | NA | 40 |

*Tab. 1.2: Reference levels corresponding to the basic restrictions summarized in Tab. 4.1 adopted form [3].*

| Exposure Scenario | Frequency Range | Whole Body $S_{\mathrm{inc}}$ (W/kg) | Local $S_{\mathrm{inc}}$ (W/kg) |
|---|---|---|---|
| **Occupational** | >2 GHz to 6 GHz | 50 | 200 |
| | >6 GHz to 30 GHz | 50 | $275/f_{\mathrm{G}}^{0.177}$ |
| | >30 GHz to 300 GHz | 50 | $550/f_{\mathrm{G}}^{0.177}$ |
| **General Public** | >2 GHz to 6 GHz | 10 | 40 |
| | >6 GHz to 30 GHz | 10 | $55/f_{\mathrm{G}}^{0.177}$ |
| | >30 GHz to 300 GHz | 10 | $110/f_{\mathrm{G}}^{0.177}$ |

Basic restrictions are challenging to implement, so *reference levels* are derived for practical applicability, aiming to offer similar protection. Within the 2 GHz to 100 GHz frequency range considered, the incident power density $S_{inc}$ is the restricted measure. $S_{inc}$ values vary based on exposure scenarios (occupational or general public) and the extent of exposure (whole body or local). Refer to Tab. 1.2 for an overview of reference levels in the investigated frequency range, applicable under far-field conditions.

# 2 Introduction

## 2.1 Short recap of the project proposal

The overall task of this project [A30] encompasses the setup of a multiscale EM simulation engine (i.e. the *simulation workbench*) for the efficient modeling of EM field exposure within the whole scale hierarchy of the tissue morphology and to link the numerically retrieved exposure data to corresponding exposure experiments. This includes field quantities such as the EM fields, the electric current density and the associated unaveraged specific absorption rate *SAR* respective energy flux/power density. This multiscale modeling task is divided into the following steps and displayed in Fig.2.1:

The first step includes (i) the setup of the *hierarchical multiscale EM full-wave model* of the skin. This encompasses (ii) an additional *quasi-static EM model* for the homogenization of the tissue layer's *randomized* microstructure (starting from the proper cells and their relevant compartments including the membrane, the cytosol, nucleus, organelles, the endoplasmic reticulum (ER) and the subsequent cell arrangements) yielding the associated frequency-dependent effective permittivity tensors. The model keeps track on the retrieved field quantities mentioned above and in particular on their *mean values* [from (i)] and *variances* [from (ii)] [A17].

The second step comprise the overall *simulation workbench* acting as a simultaneous *transmission, reflectometry* and *exposure setup* supporting plane-wave and *beam illumination* (preferably with parametrizable complex origin beams) for operating frequencies around 1-300 GHz. This overall model serves as the *backbone* for the mentioned *«scale back-projection» approach* linking e.g. power densities of the illuminating mm-wave beam to «internal» field quantities (including e.g. the unaveraged *SAR* and temperatures) in any representative microstructure respective microvolume within the skin tissue. The simulation workbench may thus act as *calibration* and *projection* engine to calibrate simulated power densities to the measured ones within an exposure experiment and project them numerically into the microstructure of the tissue and subsequently into the cell. The main question to be answered here is where exactly in the overall multiscale tissue morphology do the electrical currents flow and the resulting energy intake really takes place and in particular, how do these findings relate to the ICNIRP basic restrictions?

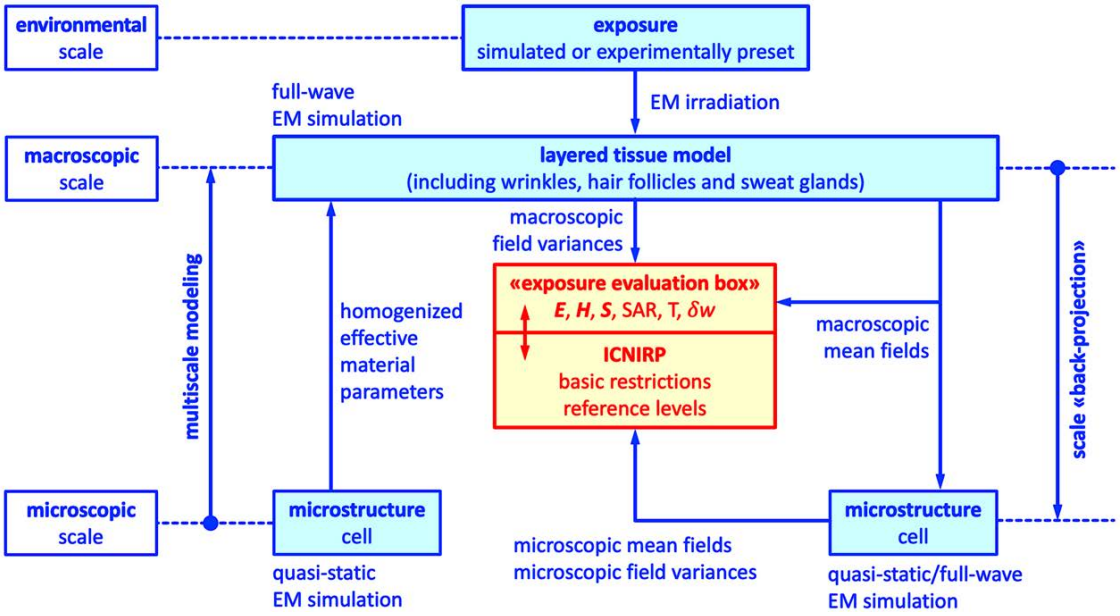


*Fig.2.1: Schematic of the hierarchically organized multiscale simulation workbench. The simulation procedure involves the multiscale tissue model (bottom up: from the cellular microstructure model to the layered skin model via homogenization), and the «scale back-projection» scheme (top down: using mean fields as boundary conditions in the microstructure). The EM irradiation encompassing simulated or experimentally preset values is introduced on the macroscopic level, namely on the surface of the layered tissue model and then «back-projected» into the microscopic scale of the cellular microstructure. Macroscopic and microscopic field quantities (i.e. mean values and variances) are evaluated respective compared in the «exposure validation box» with respect to ICNIRP exposure levels for 5G/mm-wave frequencies [A30].*

## 2.2 Outline of the report

This final report is divided into 3 content-related parts, which defines the different angles to the analysis of the electromagnetic interaction with human skin tissue.

■ Part I is the most comprehensive one and is dedicated to our developed computational multiscale models for microdosimetric investigations of skin tissues under electromagnetic exposure. In the framework of 5 sections two main ventures were investigated and completed: namely (i) the *bottom-up multiscale modeling* of the human skin, starting at the cellular level up to the effective dielectric function of the associated skin layer; and (ii) the *scale-back projection*, where the numerically retrieved electromagnetic field quantities within such *macroscopic* skin layer model are projected into the cellular scale of a chosen skin layer (here the vital basal layer in the epidermis) operating as an excitation quantity for a subsequent virtual microdosimetry in the cellular microstructure [A17]. One of the main outcomes is the quantitative assessment potential statistical variations of the *micro-SAR* given the strongly inhomogeneous cellular microstructure and its discussion in the framework of the exposure limits provided by ICNIRP [3].

■ Part II consists of 5 sections describing our experimental studies, which include the transmission and reflection measurements of tissue samples. The latter consist of sausage slices, artificial skin and pig skin. A detailed analysis is also carried out with respect to the power leakage issue in the transmission and reflection measurement kit MCK from SWISSto12. The various coaxial and vectorial near-field probes and associated scanner systems are described in the outlook.

■ Part III describes a numerical study based on a Turkish dermatological data set to reveal the gender-specific electromagnetic power absorption in human skin tissue.

# Part I: Computational multiscale models for microdosimetric investigations of skin tissues under electromagnetic exposure

## 3 Executive summary

### 3.1 Objectives

■ Objective and Methodology: The primary objective of this investigation is to develop a computational approach for the microdosimetric analysis of the effects of EM exposure on skin tissues. This approach will take into account the precise spatial positioning of discrete cells within the targeted tissue. To accomplish this complex objective, it was necessary to develop hierarchical bottom-up tissue models that are capable of capturing physiological variations in the anatomical structure of discrete, tissue-specific cells.

■ Development of an Epidermis Model: A hierarchical, bottom-up model of the epidermis has been developed. This model simulates the formation, maturation, and eventual death of epidermal cells and translates these life-cycle stages into effective material properties. The model integrates both macroscopic and microscopic scales into a single, unified computational framework, by capturing the differentiation of keratinocytes in terms of cell geometry, internal structure and histochemical composition using parametric computational cell models.

■ Dosimetric Studies & Significance: The developed model facilitates detailed dosimetric investigations of the skin, focusing on the epidermis as the outermost layer. This is critical for understanding potential impedance matching effects as recently discussed in [34]. In addition, the model allows for targeted dosimetric assessments of the basal and sub-basal layers. These layers are of particular importance for two main reasons: they function as the proliferative pool essential for skin resurfacing, and they are located above the basement membrane. The latter has been identified by ICNIRP as heat sensitive under EM radiation exposure due to its significant role in skin thermoregulation and metabolic transport [3].

■ Scale-Back Projection & Results: The application of scale-back projection to the bottom-up model of the epidermis allowed a detailed analysis of EM exposure affecting individual epidermal cells and allowed the complex interplay between morphology, histochemical composition and EM absorption to be considered at the cellular level, taking into account the specific spatial location of each epidermal cell. Microdosimetric studies revealed a high degree of variability of EM fields within these cellular microstructures – up to 71% – and exposure levels up to 45% higher than those predicted by conventional dosimetric studies focusing only on macroscopic scales. As a result, scale-back projection not only provides a detailed exposure map, but also proves to be a valuable complement to existing multiphysics simulation techniques currently used for EM dosimetry.

### 3.1 Outline

■ Section 4 introduces the concept of scale-back projection, which is designed to integrate both bottom-up and top-down multiscale approaches in EM dosimetry. In this section, the alignment of scale-back projection with existing multiphysics simulation techniques is elaborated and its compatibility with the ICNIRP guidelines is discussed.

■ Section 5 details the development of a high-resolution bottom-up model of the epidermis. This model is stratified into 24 anatomical layers, each represented by parametric cell models for keratinocytes and corneocytes. These models encapsulate critical histochemical and morphological variations, providing a comprehensive representation of the epidermis.

■ In Section 6, the bottom-up model of the epidermis is integrated into a comprehensive skin model and validated against existing literature. Extensive dosimetric studies are conducted to examine physiological variations across the epidermis, focusing on their impact on both EM energy transmission

into the body surface and its distribution within the epidermis. Special attention is given to the proliferative pool, particularly the basal and sub-basal rows, due to their relevance in skin resurfacing.

■ Section 7 applies the concept of scale-back projection to microdosimetric investigations of the epidermis. Using this approach, macroscopically determined EM field distributions are accurately projected onto the microstructure of individual epidermal cells. This section introduces a novel parameter, termed «*micro-SAR*», developed to quantify EM absorption at the microscopic level using statistical measures.

■ Finally, Section 8 serves as a synthesis, summarizing the methods, key findings, and lessons learned from Section 4 through 7. It also evaluates the potential for integrating scale-back projection into established multiphysics simulation frameworks for focused microdosimetric studies.

# 4 The conceptualization of scale-back projection

The following section outlines how scale-back projection can be used to extend the established methodological framework of multiphysics simulations applied to dosimetric investigations of the skin.

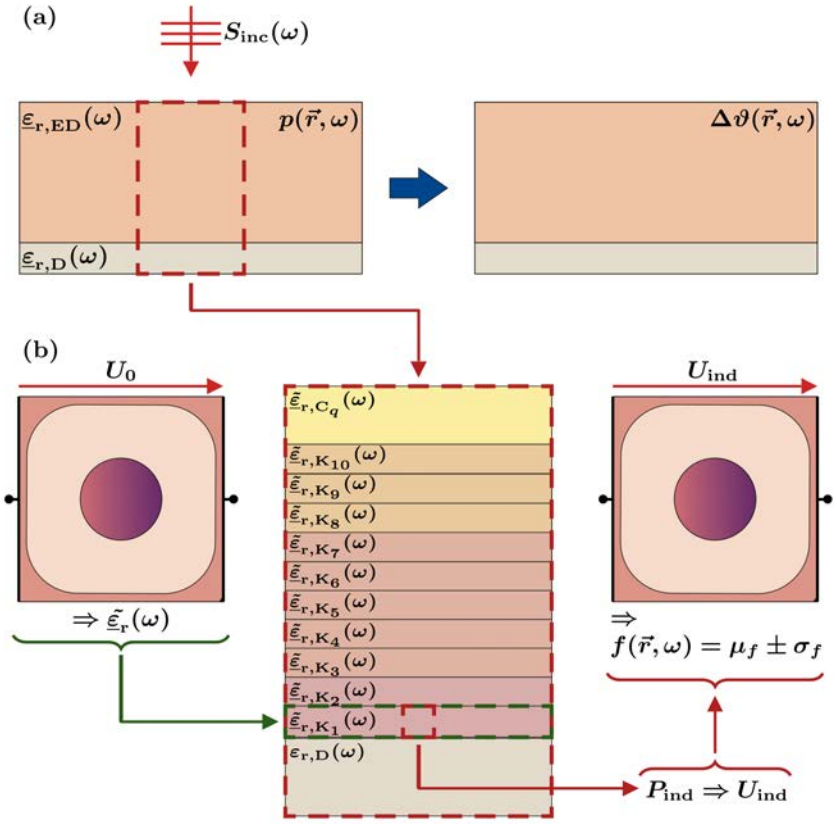


*Fig. 4.1: Overview of scale-back projection as an extension of multiphysics simulations established in dosimetric studies of the skin: (a) Multiphysics simulation approach applied to dosimetric studies on the skin. This establishes a causal relationship between the incident power $S_{inc}(\vec{r},\omega)$, representing the anthropogenic EM exposure, and the volumetric loss density $p(\vec{r},\omega)$, representing the absorbed EM energy. Temperature increases, $\Delta\vartheta(\vec{r},\omega)$, are then determined based on these data. (b) The proposed scale-back projection, described as a top-down multiscale approach that requires bottom-up multiscale modeling based on appropriate cell models to ensure coherence between the macroscopic and microscopic scales. For the epidermis, this procedure can be implemented as a three-step simulation cycle: (1) Impedance spectroscopy on cell models of the epidermis using quasi-static EM simulations to determine the dispersive effective macroscopic permittivity, $\underline{\tilde{\varepsilon}}_r$. (2) Derivation of a macroscopic tissue model of the epidermis, representing the life cycle of keratinocytes across several homogeneous cell layers illustrated in this figure by color gradation. (3) Determination of losses ($P_{ind}$) across epidermal cell layers within microvolumes corresponding in size to those of the underlying cells being simulated. This allows back projection of microexposure at the cellular level ($U_{ind}$) and performance of microdosimetric studies based on the variability of the fields projected into the microstructure ($f(\vec{r},\omega) = \mu_f \pm \sigma_f$).*

As illustrated in Fig. 4.1(a), this multiphysics approach can be considered as a nested procedure in which both thermal and EM simulations are performed. The scale-back projection, as proposed and discussed in this work, is designed to extend only the EM simulations of this multiphysics approach, as shown on the left in Fig. 4.1(a). This allows the consideration of EM absorption by investigating the effects of induced EM fields at the cellular level, as shown in Fig. 4.1(b). The scale-back projection is essentially a top-down multiscale approach, which must assume coherence between the length scales under consideration and requires bottom-up modeling of the tissue under investigation based on appropriate cell models. Applied to the epidermis, the procedure shown in Fig. 4.1(b) can be interpreted as a simulation cycle that can be divided into three steps. In the first

step, virtual impedance spectroscopy is performed on the cell models of the epidermis using quasi-static EM simulations, which allows the dispersive effective macroscopic permittivity, $\underline{\tilde{\varepsilon}}_{\mathrm{r}}$, to be determined. The exact methodology for this numerical homogenization approach, which can be interpreted phenomenologically as a virtual capacitor experiment in which the cell models are subjected to an arbitrary voltage $U_0$, was first described in the first annual report and is repeated in Appendix A for completeness. This procedure is based on parametric cell models that account for changes in overall cell size and shape, internal organization, and histochemical composition during the keratinization process in the epidermis. Therefore, it can be used to derive a macroscopic model of the epidermis that represents the life cycle of keratinocytes, with each stage represented by a homogeneous cell layer. As shown in the middle of Fig. 4.1(b), the epidermis in this model is represented by 10 such cell layers within the viable epidermis ($\underline{\tilde{\varepsilon}}_{\mathrm{r,K_1}}$ to $\underline{\tilde{\varepsilon}}_{\mathrm{r,K_{10}}}$), where the color gradation between cell layers indicates association with the stratum basale, stratum spinosum, and stratum granulosum, as well as $q$ cell layers within the stratum corneum ($\underline{\tilde{\varepsilon}}_{\mathrm{r,C}_q}$). In the context of an overall skin model, it is now possible to determine losses, $P_{\mathrm{ind}}$, across the epidermal cell layers within microvolumes similar in size to those of the underlying cell models. Based on these losses, it is possible to determine voltages, $U_{\mathrm{ind}}$, that allow the definition of a microexposure at the cellular level of an equivalent power for use in parametric cell models of the underlying keratinocytes. Using this procedure, it is now possible to perform microdosimetric investigations based on the variability of the fields projected into the microstructure in terms of spatial means and standard deviations (i.e., $f(\vec{r},\omega) = \mu_f \pm \sigma_f$).

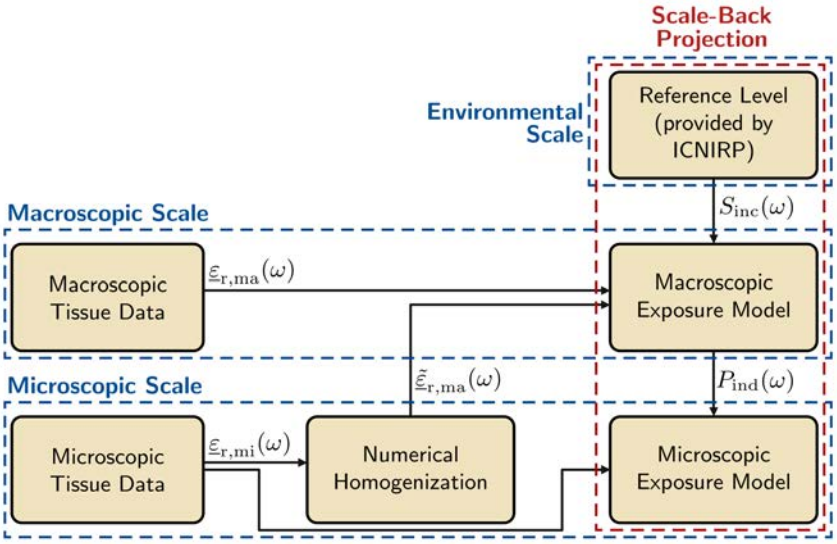


*Fig. 4.2: Conceptual block diagram illustrating the hierarchical organization of the simulation environment implemented to perform scale-back projection in epidermal tissue. The simulation environment encompasses three hierarchical scales: An environmental scale defining the exposure scenario, a macroscopic scale representing the stratified structure of the skin consisting of the epidermis, dermis, hypodermis, and underlying muscle tissue, and a microscopic scale consisting of parametric cell models representing the microstructure of individual epidermal cell layers.*

In the course of this report, the methodological framework described above will be implemented in a simulation environment that allows modeling of the epidermis and efficient simulation of EM field exposure of the skin in order to predict the effects of this on the epidermal microstructure. This simulation environment is divided into three hierarchical scales: An environmental scale at which the exposure set up is defined; A macroscopic scale at which the skin is considered as a stratified material structure comprising the epidermis, dermis, hypodermis and underlying muscle tissue; A microscopic scale which comprises parametric cell models representing the microstructure of the individual epidermal cell layers. To show the high level of interaction between these functional blocks across all hierarchical levels, a conceptual block diagram is presented in Fig. 4.2.

The flow of information in the block diagram is from the left to the right and starts with the identification of appropriate material parameters that describe the tissue at the microscopic and macroscopic levels. The macroscopic tissue data, $\underline{\tilde{\varepsilon}}_{\mathrm{r,ma}}(\omega)$, include the dispersive permittivities of the individual skin layers measured by Sasaki et al. [1, 2]. The adaptation of this data allows the development of a modular skin model and also serves as a metrological reference to validate the bottom-up model of the epidermis. The microscopic tissue data, $\underline{\tilde{\varepsilon}}_{\mathrm{r,mi}}(\omega)$, provides essential information about the dispersive material properties of subcellular structures and fundamental biochemical components, enabling the accurate modeling of the histochemical composition of the parametric cell models for the epidermal cell layers. Using these parametric cell models, numerical homogenization is employed to calculate the effective macroscopic material properties, $\underline{\tilde{\varepsilon}}_{\mathrm{r,ma}}(\omega)$, of the individual skin layers at the macroscopic scale. This is achieved by utilizing $\underline{\tilde{\varepsilon}}_{\mathrm{r,mi}}(\omega)$ as input for bottom-up multiscale simulations, wherein the size, shape, and internal organization of the modeled keratinocytes are resolved in great detail. In the scale-back projection, environmental exposure is simulated using a plane EM wave, adhering to ICNIRP regulations [3] briefly summarized Section 1, which limit the incident power density, $S_{\mathrm{inc}}(\omega)$, to the latest reference levels. The skin is modeled as a layered material, incorporating the bottom-up model of the epidermis, while other sublayers (dermis, hypodermis, and underlying muscle tissue) adopt measured dispersive permittivities from Sasaki. By implementing this exposure scenario in an FEM-based simulation environment, the macroscopic exposure model enables the determination of induced losses, $P_{\mathrm{inc}}(\omega)$, in microvolumes corresponding to the size of epidermal cell models. Using $P_{\mathrm{inc}}(\vec{r},\omega)$, local tissue exposure is finally back-projected onto the high-resolution models of the keratinocytes.

## 5 Bottom-up multiscale model of the epidermis

In the following section, a hierarchical multiscale model of the epidermis is developed that allows to account for physiological changes across individual epidermal cell layers in terms of cell shape, structure, and histochemical composition. This model is then used to perform microdosimetric studies of the epidermis using scale-back projection in later sections of this report.

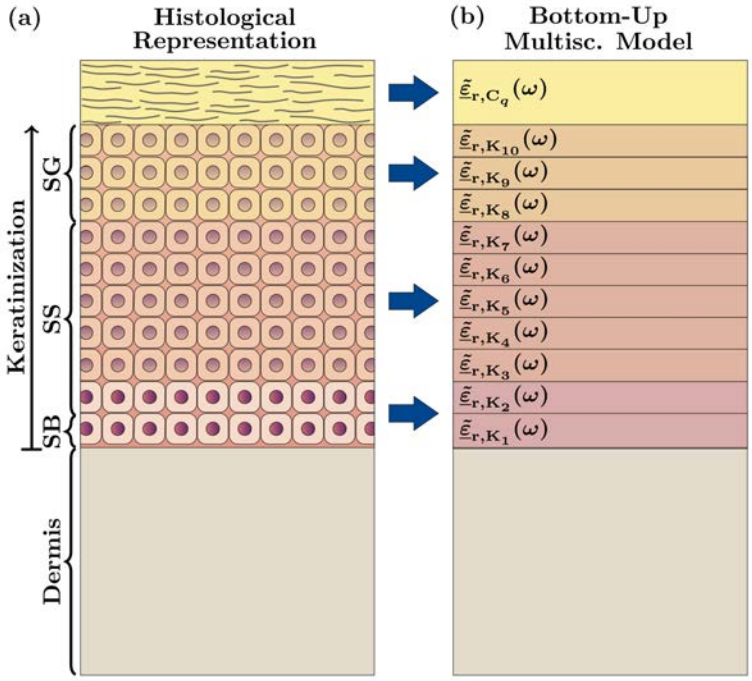


*Fig. 5.1: Bottom-up multiscale model of the epidermis: (a) Simplified histological representation of the epidermis. The epidermis is considered to be a stratified material structure consisting of 10 cell layers forming the viable epidermis and 14 cell layers forming the stratum corneum (SC). The viable epidermis comprises the stratum basale (SB), the stratum spinosum (SS) and the stratum granulosum (SG). The keratinocytes within the viable epidermis show different stages of keratinization and the corneocytes within the SC show different stages of hydration. The epidermis is contiguous with the dermis (D), which is considered homogeneous. (b) Bottom-up multiscale model of the epidermis in which the individual cell layers are represented as homogeneous material layers. The dispersive material properties of these layers, $\underline{\tilde{\varepsilon}}_{r,K_p}(\omega)$ and $\underline{\tilde{\varepsilon}}_{r,C_q}(\omega)$, are obtained using numerical homogenization. The indices $p$ and $q$, with $p \in \{1; 2; \dots; 10\}$ and $q \in \{1; 2; \dots; 14\}$, correspond to the individual cell layers from the inside outwards.*

To conceptualize a comprehensive bottom-up multiscale model of the epidermis (see Fig. 5.1(a)), the system must be considered on both a macroscopic and microscopic scale. On the macroscopic scale, the epidermis is considered to be a stratified material structure consisting of 10 cell layers comprising the viable epidermis (i.e. the SB, the SS and the SG) [5] and 14 cell layers comprising the SC [6]. At the microscopic scale, the layers of the viable epidermis are represented by 10 individual keratinocyte models showing all stages of keratinization, and the layers of the stratum corneum are represented by 14 individual corneocyte models showing different stages of hydration. In order to convert this purely conceptual, histological representation of the epidermis into a bottom-up model (see Fig. 5.1(b)), parametric CAD models of the two cell types must first be created and adapted to the physiological conditions of the individual cell layers. These adapted cell models can then be used in numerical quasi-static EM simulations to determine the effective material parameters of each cell layer. This allows the microstructure of the cells to be represented on a macroscopic scale by frequency-dependent effective permittivities, $\underline{\tilde{\varepsilon}}_{\mathrm{r},K_p}(\omega)$ and $\underline{\tilde{\varepsilon}}_{\mathrm{r},C_q}(\omega)$, where the indices $p$ and $q$, with $p \in \{1; 2; \dots; 10\}$ and $q \in \{1; 2; \dots; 14\}$, correspond to the individual cell layers from the inside outwards.

In order to derive the parameters of the CAD models used to represent the physiological conditions in each of the cell layers mentioned above, the stages of keratinization in the viable epidermis and hydration in the stratum corneum will be discussed in terms of two aspects: (1) geometrical changes of the cell and its organelles, and (2) histochemical changes within the cell compartments and the extracellular space. Following this discussion, the effective material properties of the epidermis at both the microscopic and the macroscopic scale will be derived yielding a dielectric representation of the epidermis that allows microdosimetric investigations.

## 5.1 Geometric parametrization of the bottom-up model of the epidermis derived from the scientific literature

The following section is divided into three subsections. The first subsection presents the geometric parameters of the keratinocytes and the second subsection presents those of the corneocytes. Both of these subsections follow the same structure: First, the CAD model of the corresponding cell type and its geometric parameters are presented in general, and then the design rules for each cell layer are derived based on skin anatomy. In the third subsection, the geometric dimensions of the epidermal sublayers are summarized and the macroscopic model of the epidermis is derived.

### 5.1.1 Parametric model of the keratinocytes

The parametric CAD model of keratinocytes is introduced using Fig. 5.2, which shows a basal keratinocyte as an illustrative example.

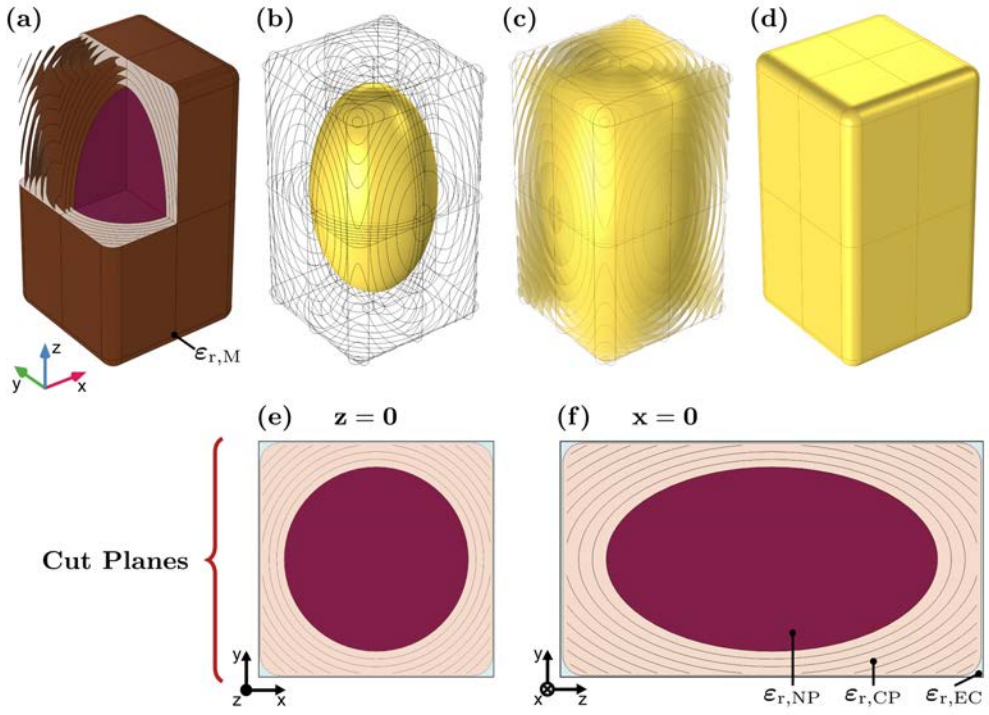


*Fig. 5.2: Parametric CAD model of a keratinocyte in the viable epidermis showing a basal keratinocyte as an illustrative example: (a) Keratinocyte modeled as a square cuboid containing an ellipsoidal nucleus concentrically surrounded by shells emulating organelle membranes. The plasma membrane, the nuclear envelope and the organelle membranes are considered as phospholipid bilayers and are depicted in brown. The keratinocyte can be further subdivided into the cytoplasm colored beige and the nucleoplasm colored purple. The cytoplasm is separated from the cell exterior by the plasma membrane and the nucleoplasm is separated from the cytoplasm by the nuclear envelope. (b)-(d) Transparent wire frames of the cell models highlighting the nucleus, the organelle membranes and the cytoplasm respectively. (e)-(f) Cross-sectional planes through the cell showing the xy plane and the yz plane respectively. The extracellular space is colored light blue. The material properties of the extracellular medium (EC), the cytoplasm (CP), the nucleoplasm (NP) and the membranes (M) are denoted by $\underline{\tilde{\varepsilon}}_{r,EC}$, $\underline{\tilde{\varepsilon}}_{r,CP}$, $\underline{\tilde{\varepsilon}}_{r,NP}$ and $\underline{\tilde{\varepsilon}}_{r,M}$ respectively.*

The plasma membrane, the nuclear envelope and the organelle membranes are considered as phospholipid bilayers depicted in brown in Fig. 5.2(a). The cell interior can be subdivided into two compartments: (1) the cytoplasm (CP) depicted in beige, and (2) the nucleoplasm (NP) depicted in purple. The CAD model of the keratinocytes is embedded in a cuboidal computational unit cell (UC) with a volume approximately 2 % larger than the cell body. The cytoplasm is separated from the cell exterior by the plasma membrane (PM) and the nucleoplasm is separated from the cytoplasm by the nuclear envelope (NE). The organelle membranes (OM) are contained in the cytoplasm. Figs. 5.2(b)-(d) show the nucleus, organelle membranes and cell body as wireframe representations. Cross-sectional planes through the cell showing the xy plane and the yz plane are illustrated in Fig. 5.2(e)-(f), with the extracellular space (EC) colored light blue

The cell bodies of the keratinocytes are modeled as square cuboids with rounded edges and corners. The cell is characterized by its dimensions with axes aligned to the spatial dimensions x, y and z. The nucleus is modeled as a spheroid with major and minor axes aligned with those of the cell. The length of the axes of the cell body are expressed by the parameters $l_{\mathrm{Cell,xy}}$ and $l_{\mathrm{Cell,z}}$ and those of the nucleus by $d_{\mathrm{N,xy}}$ and $d_{\mathrm{N,z}}$. Another key parameter here is the ratio between the long and short dimensions of the cell as well as the major and minor axes of the nucleus, $c_{\mathrm{Cell,l/s}}$ and $c_{\mathrm{N,l/s}}$. The organelles contained in the cytoplasm are modeled as shells arranged concentrically around the nucleus. The decision to approximate these organelles by only their membranes is based on results published in [A6]. In this reference, it was shown that although high volumetric loss densities occur within organelle membranes at frequencies above 1 GHz and must therefore be accounted for in microdosimetric studies, the membranes no longer represent rigid barriers. The current flow within the organelle is, therefore, no longer significantly impeded by its membrane, so that a volumetric representation of the organelle bodies can be dispensed with, at least for the estimation of total cell losses. In order to create a generalized representation of organelle structures within the cytoplasm while maintaining a high degree of realism, the surface areas of the organelle membranes, $S_{\mathrm{OM}}$, and that of the nuclear envelope, $S_{\mathrm{NE}}$, are derived from the scientific literature [7]. These parameters are related to each other and included in the model as a single geometrical design parameter, $c_{\mathrm{s,OM/NE}}$, where $c_{\mathrm{s,OM/NE}} = S_{\mathrm{OM}}/S_{\mathrm{NE}}$. All design parameters listed in this paragraph are summarized in Tab. 5.1. In addition to all of the parameters above, the compartmentalization of the cell results in the volume ratios of each compartment to the total volume of the UC, expressed as

$$c_{\mathrm{v},i} = \frac{V_i}{V_{\mathrm{UC}}} \tag{5.1}$$

where $i \in \{\mathrm{EC};\ \mathrm{CP};\ \mathrm{NP};\ \mathrm{Cell}\}$. The index «Cell» denotes the volume of the cell body and includes both the volume of the cytoplasm and the volume of the nucleoplasm. These volume ratios, $c_{\mathrm{v},i}$, are important for the description and derivation of chemical changes between the cell layers during keratinization, which is described in detail in Section 5.2.

*Tab. 5.1: Geometry parameter of the parametric CAD model of the keratinocytes.*

| Parameter | Description |
|---|---|
| $l_{\mathrm{Cell,xy}}$ | Axes of the cell oriented in the x-direction and the y-direction |
| $l_{\mathrm{Cell,z}}$ | Axis of the cell oriented in the z-direction |
| $c_{\mathrm{Cell,l/s}}$ | Ratio between the longer and shorter axis of the cell |
| $d_{\mathrm{N,xy}}$ | Axes of the nucleus oriented in the x-direction and the y-direction |
| $d_{\mathrm{N,z}}$ | Minor axis of the nucleus oriented in the z-direction |
| $c_{\mathrm{N,l/s}}$ | Ratio between the longer and shorter axis of the nucleus |
| $c_{\mathrm{s,OM/NE}}$ | Ratio between the surface area of organelles within a cell and the nucleus |

Having introduced the parametric CAD model, the geometric parameters of the keratinocytes within each cell layer are now derived from published data, allowing physiological conditions to be considered

specifically for each of these layers within the viable epidermis. First, the geometric parameters of the cells of the SB and the cells of the sub-basal row (i.e. the first cell layer of the SS) are determined. The decision to design these two cell layers according to the same rule is based on the fact that the cells of both layers are very similar in shape, size and function and together form the proliferative pool of the epidermis containing about 97 % of the miotic activity [8, 9, 10]. The longitudinal axes of the cell body and nucleus are perpendicular to the skin surface [11, 12], with axis lengths of $l_{\mathrm{Cell,z}} = 10\ \mu\mathrm{m}$ [10] and $d_{\mathrm{N,z}} = 8\ \mu\mathrm{m}$ [12]. The length ratio of the longitudinal axis to the other two axes, $c_{\mathrm{l/s}}$, is 1.8 for both the cell body and the nucleus [11]. According to [7], the ratio of the surface area of organelle membranes to the surface area of the nuclear envelope, $c_{\mathrm{s,OM/NE}}$, is about 10 and the volume ratio of extracellular space to the UC, $c_{\mathrm{v,EC}}$, approximately 0.26 %. However, the latter ratio has been increased to approximately 2 % to avoid small mesh lengths and their associated numerical instabilities in simulation. In higher cell layers, keratinocytes lose their proliferative abilities and instead grow by metabolizing substances for cornification. The cells in the SS therefore have larger cell bodies and nuclei which are still perpendicular to the skin surface. The longitudinal axes, $l_{\mathrm{Cell,z}}$ and $d_{\mathrm{N,z}}$, are documented in the scientific literature as 16 µm and 12 µm, with $c_{\mathrm{l/s}}$ now 1.4. Keratinocytes in the SG show signs of programmed cell death, known as apoptosis, which is primarily manifested by karyopyknosis, a process in which the nucleus shrinks and the chromatin it contains condenses into a homogeneous mass [13]. Shrinkage of the nucleus causes the cell body to flatten, changing its orientation from perpendicular to parallel to the skin surface. The longitudinal axes of the cell body, $l_{\mathrm{Cell,xy}}$,and the nucleus, $d_{\mathrm{N,xy}}$, are now 16 µm and 15 µm respectively, with $c_{\mathrm{l/s}}$ increasing again to 1.8. The geometric changes described above take place over a growth process of 30-50 days [5] and must therefore be accounted for in the geometric setups of the CAD cell models by gradual changes from one cell layer to the next. This is implemented mathematically by geometric compressing and stretching operations applied to the cell body and nucleus.

*Tab. 5.2: Geometrical parameters of the keratinocyte models of the individual cell layers, p.*

| $p$ | Layer | Phase | $c_{\mathrm{Cell,l/s}}$ | $l_{\mathrm{Cell,xy}}$ | $l_{\mathrm{Cell,z}}$ | $c_{\mathrm{N,l/s}}$ | $d_{\mathrm{N,xy}}$ | $d_{\mathrm{N,z}}$ | $c_{\mathrm{s,OM/N}}$ |
|---|---|---|---|---|---|---|---|---|---|
| **1** | SB | - | **1.8** | 5.56µm | **10 µm** | **1.8** | 4.44µm | **8 µm** | **9.78** |
| **2** | SS | - | **1.8** | 5.56µm | **10 µm** | **1.8** | 4.44µm | **8 µm** | **9.78** |
| 3 | SS | $P_1$ | 1.67 | 7.2µm | 12µm | 1.67 | 5.6µm | 9.33µm | 11.09 |
| 4 | SS | $P_1$ | 1.53 | 9.13µm | 14µm | 1.53 | 6.95µm | 10.67µm | 12.11 |
| **5** | SS | $P_1$ | **1.4** | 11.43µm | **16 µm** | **1.4** | 8.57µm | **12 µm** | 12.91 |
| 6 | SS | $P_2$ | 1.53 | 12.95µm | 13.63µm | 1.53 | 10.71µm | 10.78µm | 9.13 |
| 7 | SS | $P_2$ | 1.67 | 14.48µm | 11.26µm | 1.67 | 12.86µm | 9.56µm | 6.56 |
| **8** | SG | $P_2$ | **1.8** | **16 µm** | 8.89µm | **1.8** | **15 µm** | 8.33µm | 4.46 |
| 9 | SG | $P_3$ | 2.11 | 16.75µm | 7.94µm | 2.34 | 15µm | 6.42µm | 8.19 |
| 10 | SG | $P_3$ | 2.51 | 17.57µm | 7µm | 3.33 | 15µm | 4.5µm | 7.4627 |

The geometric parameters of each cell layer, $p$, are summarized in Tab. 5.2. The numerical values in bold type are taken directly from the literature and serve as "boundary values" from which the transition values between the layers, due to compression or stretching, are linearly interpolated. In this way, three transition phases, $P_1$ to $P_3$, can be distinguished, occurring between the source data layers highlighted in gray in the table. In phase $P_1$, the keratinocytes start to grow and metabolizes material for cornification, while the orientation of the cell and nucleus relative to the skin surface remains vertical (compare the values of $l_{\mathrm{Cell,xy}}$ and $l_{\mathrm{Cell,z}}$ in the table). In phase $P_2$, the cell shows the first signs of karyopyknosis resulting in the flattening of the cell body and the nucleus without significant variation in cell size. This process coincides with a change in the orientation of the cell from perpendicular to parallel to the skin surface. In phase $P_3$, apoptosis is modeled by further

flattening of the nucleus and thus of the cell body, but here also represents the fragmentation of the nucleus and corresponding loss of cell size. The cell dimensions are such that the cell volumes in layers 9 and 10 decrease by 2 % and 5 %, respectively, compared to layer 8, so that a smooth transition from viable epidermis to SC also occurs at the microscopic level.

### 5.1.2 Parametric model of the corneocytes

The basic structure of the parametric model of the corneocytes is derived from that of the keratinocytes, in which the cell body is still a square cuboid with rounded corners embedded in a cuboidal UC. However, the keratinocytes of the SG (see cell model $K_{10}$) undergo profound biochemical changes during the transition to the SC, which have a massive impact on the interior of the cell. As mentioned above, apoptosis is terminated in the uppermost layer of the SG, leading to exocytosis of the remaining metabolites of the cell (i.e. keratinosomes), which compacts the extracellular space into a lipid-containing binding mass that ensures the mechanical integrity of the SC [14, 15, 16]. In addition, the nucleus fragments and the intracellular space hardens into an undifferentiated protein mass with a high keratin content. For this reason, the interior of the cell is no longer divided into individual compartments with organelles, but is represented as a homogeneous cell body. However, the shape of the cell body is still considered to be a square cuboid with rounded corners, embedded in a cuboidal UC. For the CAD model, the only directly accessible geometric design parameter is the axis length of the unit cell in the z direction, $l_{\mathrm{UC,z}}$. The other geometric dimensions of the cell model, i.e. the axis lengths of the UC in the x-direction and the y-direction, $l_{\mathrm{UC,xy}}$, as well as the axis lengths of the cell body, $l_{\mathrm{Cell,xy}}$and $l_{\mathrm{Cell,z}}$, result from the histochemical composition of the SC. The reason for this is that the hydration of the individual cell layers of the SC must be taken into account in the cell models of the corneocytes. To account for hydration within these layers, $l_{\mathrm{Cell,xy}}$ and $l_{\mathrm{Cell,z}}$ are determined to match the reduction of cell volume due to water loss from one cell layer to the next. The volume of the UC of the $\mathrm{K}_{10}$ keratinocytes is the reference volume from which the volume of the UC of the corneocytes, $\mathrm{C}_q$, is deduced as a function of the water content within each layer. The histochemical composition of the SC and the exact calculation of $l_{\mathrm{UC,xy}}$, $l_{\mathrm{Cell,xy}}$ and $l_{\mathrm{Cell,z}}$ are discussed in more detail in Section 5.2. However, the parameterisation of $l_{\mathrm{UC,z}}$ can be obtained from the scientific literature [6, 17]. Based on these references, the thickness of the top layer $l_{\mathrm{Cell,z,C_{14}}}$ is set to 1 µm and, to allow for the gradual water loss of the cell bodies from one layer to the next, the thickness of the bottom layer $l_{\mathrm{UC,z,C_1}}$ is set to 2 µm. The thickness of all intermediate layers is determined by linear interpolation between these values. The values for all of these geometric parameters are summarized in Tab. 5.3.

*Tab. 5.3: Geometric parameters of the corneocyte models of the individual cell layers, q.*

| $q$ | 1 | 2 | 3 | 4 | 5 | 6 | 7 | 8 | 9 | 10 | 11 | 12 | 13 | 14 |
|---|---|---|---|---|---|---|---|---|---|---|---|---|---|---|
| $l_{\mathrm{UC,xy}}$ (µm) | 28.45 | 26.81 | 26.34 | 26.11 | 26.01 | 26.05 | 26.2 | 26.46 | 26.82 | 27.29 | 27.86 | 28.54 | 29.36 | 30.31 |
| $l_{\mathrm{UC,z}}$ (µm) | 2 | 1.92 | 1.84 | 1.77 | 1.69 | 1.62 | 1.54 | 1.46 | 1.38 | 1.31 | 1.23 | 1.15 | 1.08 | 1 |
| $l_{\mathrm{Cell,xy}}$ (µm) | 28.32 | 26.67 | 26.2 | 25.96 | 25.87 | 25.91 | 26.06 | 26.32 | 26.68 | 27.15 | 27.73 | 28.42 | 29.24 | 30.2 |
| $l_{\mathrm{Cell,z}}$ (µm) | 1.88 | 1.78 | 1.70 | 1.62 | 1.55 | 1.47 | 1.39 | 1.32 | 1.25 | 1.17 | 1.1 | 1.03 | 0.96 | 0.89 |

To give an overview of the spatial dimensions of the cell models introduced above, cross-sections through the yz plane of the cell models $K_{1\&2}$, $K_5$, $K_8$, $C_1$ and $C_{14}$ are illustrated in Appendix B.

### 5.1.3 The macroscopic model of the epidermis related to the microscopic cell models

The configuration of the different stages of keratinization and hydration in the parametric cell models is summarized in Fig. 5.3. The upper diagram shows the volumes of the cell compartments, $V_{\mathrm{i}}$, illustrated by stacked bars categorized according to the models of the keratinocytes, $K_p$, and the corneocytes, $C_q$, in the different sublayers of the epidermis, along with the transition phases $P_1$ to $P_3$.

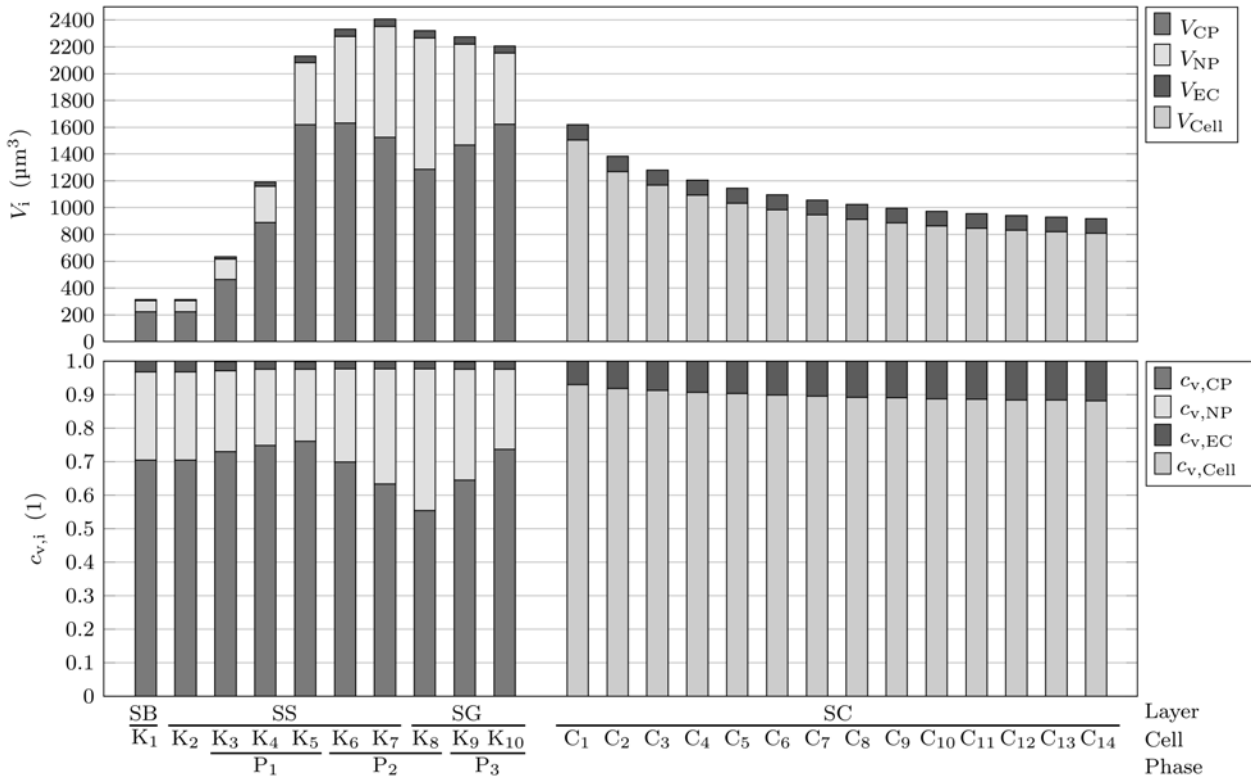


*Fig. 5.3: Geometrical configurations of the cell models under investigation: (top) Volumes of the cell compartments, $V_i$, illustrated by stacked bars categorized according to the models of the keratinocytes, $K_p$, and the corneocytes, $C_q$, in the different sublayers of the epidermis, along with the transition phases $P_1$ to $P_3$. (bottom) Ratios of the volume of the cell compartments to that of computational domain, $c_{v,i}$, using the same categories. The index $i \in \{CP; NP; EC; Cell\}$ denotes the cytoplasm, the nucleoplasm, the extracellular medium and the cell body respectively.*

The bottom diagram shows the ratios of the volume of these compartments to that of the UC, $c_{v,i}$, using the same categories. In order to describe the bottom-up model of the epidermis on a macroscopic scale, the axial lengths of the UC must be added together in the z-direction. The resulting thicknesses of the epidermal sublayers are summarized in Tab. 5.4.

*Tab. 5.4: Overview of the thickness and number of cell layers corresponding to all of the epidermal sublayers.*

| | SB | SS | SG | SC |
|---|---|---|---|---|
| **Thickness** | 10.04µm | 77.31µm | 24.08µm | 21µm |
| **# of Layers** | 1 | 6 | 3 | 14 |

## 5.2 Histochemical parameterization of the bottom-up model of the epidermis derived from the scientific literature

Following the introduction of the parametric CAD models of keratinocytes and corneocytes in Section 5.3, the histochemical changes within the epidermis are now described. The problem with describing these changes is that there is no histochemical model of the epidermis available in the scientific literature that provides a coherent summary of the biochemical composition of the skin in the form of a concentration profile across all layers. As such a model is necessary for realistic modelling of the skin, it is derived below on the basis of available scientific data on both (1) a macroscopic scale and (2) a microscopic scale.

### 5.2.1 Histochemical parameterization of the epidermis on a *macroscopic* scale

A coherent concentration profile describing the biochemical composition [18, 25] of the human epidermis at a microscopic scale is derived in this subsection and illustrated in Fig.5.4.

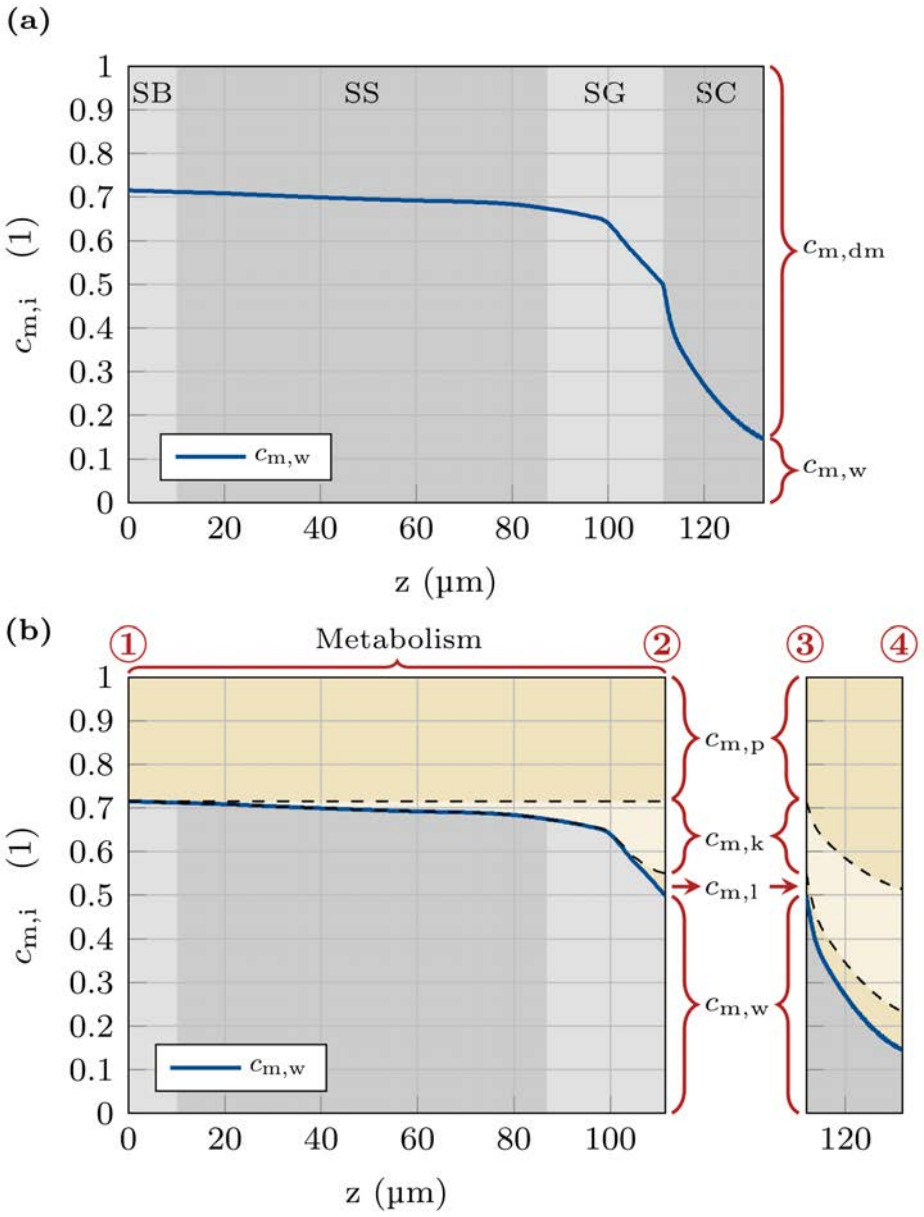


*Fig. 5.4: Overview of the histochemical composition of the human epidermis considered in the bottom-up model on a macroscopic scale: (a) Water concentration profile [25] across the human epidermis, considering its biochemical composition as a two-phase material represented by the mass fractions of water, $c_{m,w}$, and dry biological material, $c_{m,dm}$, where $c_{m,j} = m_j/m_{tot}$, with $m_{tot}$ denoting the total mass of any given sample. Such a water concentration profile was originally published by [18], and here, the thickness of the stratum basale (SB), the stratum spinosum (SS), the stratum granulosum (SG) and the stratum corneum (SC) are adapted to those derived form the parametric CAD models of the keratinocytes and corneocytes summarized in Tab. 5.4. (b) Derivation of a refined concentration profile which further subdivides $c_{m,dm}$ into a lipid, a keratin and a general protein concentration denoted by $c_{m,l}$, $c_{m,k}$ and $c_{m,p}$ respectively. The epidermis is divided into the viable epidermis having an active metabolism and the SC comprising only dead cells showing different stages of hydration. The boundary layers between the dermis and the SC, ①, the SG and the SC, ② and ③, and the skin surface, ④, form intervals in which this metabolization (①-②) and dehydration (③-④) can be determined.*

The starting point for this derivation is the water concentration profile across the human epidermis shown in Fig. 5.4(a). Originally published in [18], this concentration profile has been adapted to the thicknesses of the epidermal sublayers summarized in Tab. 5.4 which are illustrated using a gray-shaded background. At this stage, the epidermis is considered to be a two-phase material represented by the mass fractions of water, $c_{\mathrm{m,w}}$, and dry biological material, $c_{\mathrm{m,dm}}$. The mass fractions, $c_{\mathrm{m},j}$, are defined as

$$c_{\mathrm{m},j} = \frac{m_j}{m_{\mathrm{tot}}} \tag{5.2}$$

where $m_j$ and $m_{\mathrm{tot}}$ are the mass of each material and the total mass of any given sample. However, to create a more refined material model of the epidermis, $c_{\mathrm{m,dm}}$ is further subdivided into $c_{\mathrm{m,l}}$, $c_{\mathrm{m,k}}$ and $c_{\mathrm{m,p}}$, denoting lipid, keratin and general protein concentrations respectively. For this purpose, Fig. 5.4 (b) divides the epidermis into the viable epidermis, which has an active metabolism, and the SC, which consists only of dead cells in various stages of hydration. In a first step, the metabolism of keratin and lipids within the viable epidermis is derived by considering keratinization as a developmental process during the life cycle of the cells, starting from the basement membrane (i.e. $z = 0\ \mu\mathrm{m}$), denoted by ①. At this location, basal keratinocytes are considered to be cells that have the potential to migrate through higher cell layers and differentiate, but have not yet started this process. Therefore, $c_{\mathrm{m,dm}}$ is assumed to consist only of a general protein content, $c_{\mathrm{m,p}}$, which accounts for all macromolecules that form organelles. Considering this as a basic assumption, the concentration of $c_{\mathrm{m,p}}$ remains constant during the migration to higher layers. The diminishing concentration of water illustrated by the blue line, $c_{\mathrm{m,w}}$, is not considered as a loss of water but rather a shift in concentration ratios due to the deposition of keratohyalin granules in the cell. Thus, the difference between the constant concentration of protein, $c_{\mathrm{m,p}}$, and the decreasing concentration of water, $c_{\mathrm{m,w}}$, represents the concentration of keratin in the cells, $c_{\mathrm{m,k}}$. According to [19], lipid formation in the SG is accounted for by an exponential function approaching a maximum value of 10.3 % normalized to the total ammount of dry biological material at the end of the viable epidermis (i.e., $z = 111.43\ \mu\mathrm{m}$), denoted by ②.

The SG/SC interface marks the point at which the epidermis can no longer be considered a living system. It is therefore necessary to make a conceptual distinction in the following derivation of the epidermal material composition, and this is illustrated by the graphical separation of the viable epidermis and the SC in the figure. In analogy to the continuity at an interface within a boundary value problem, the metabolized material composition within the viable epidermis is taken from ② as the starting point for the dehydration process across the SC in ③ (i.e. $z = 111.43\ \mu\mathrm{m}$). Starting from the given initial mass $m_{\mathrm{tot}} = m_{\mathrm{dm}} + m_{\mathrm{w}}$, the material composition within the SC is no longer dominated by the formation of new substances, but by the loss of water, which results in a change in the concentrations towards the skin surface (i.e. $z = 132.43\ \mu\mathrm{m}$), denoted by ④.

However, the above mass fractions must be converted into volume fractions. This is done in order to be able to use the concentration profile across the epidermis to derive the dielectric material properties of the cells and their compartments at the molecular level using mixing formulae, which will be presented in detail in Section 5.3. The volume fractions of the biochemical compounds under investigation are defined as

$$c_{\mathrm{v},j} = \frac{V_j}{V_{\mathrm{tot}}} \tag{5.3}$$

with $V_j = (c_{\mathrm{m},j} \cdot m_{\mathrm{tot}})/\rho_j$ and $V_{\mathrm{tot}} = \sum_j V_j$. The volumetric mass densities of the individual compounds are represented by $\rho_j$. The densities of water, $\rho_{\mathrm{w}}$, protein, $\rho_{\mathrm{p}}$, keratin, $\rho_{\mathrm{k}}$, and lipids, $\rho_{\mathrm{l}}$, considered in this conversion are summarized in Tab. 5.5. Based on the above, Fig. 5.5 shows the histochemical concentration profile across the human epidermis illustrating its composition using the volume fractions of water, $c_{\mathrm{v,w}}$, lipids, $c_{\mathrm{v,l}}$, keratin, $c_{\mathrm{v,k}}$, and protein, $c_{\mathrm{v,p}}$. The vertical red dashed lines in the viable epidermis correspond to the midpoints of the cell layers in the z-direction denoted by $K_1$ to $K_{10}$.

*Tab. 5.5: Volumetric mass densities, $\rho_j$, of the biochemical compounds of the epidermis. The indices w, p, k and l denote water, protein, keratin and lipids. The densities of the latter three compounds have been adopted from [20, 21, 22] and [23], respectively.*

| | w | p | k | l |
|---|---|---|---|---|
| $\rho_j \left(\frac{\text{kg}}{\text{m}^3}\right)$ | 1000 | 1410 | 1410 | 950 |

The concentrations at these midpoints will be used in Section 5.2.2 to derive the chemical composition of the individual cell compartments within each cell layer. Although the midpoints of the cell layers in the SC are not shown for clarity, the same procedure is applied to the corneocytes.

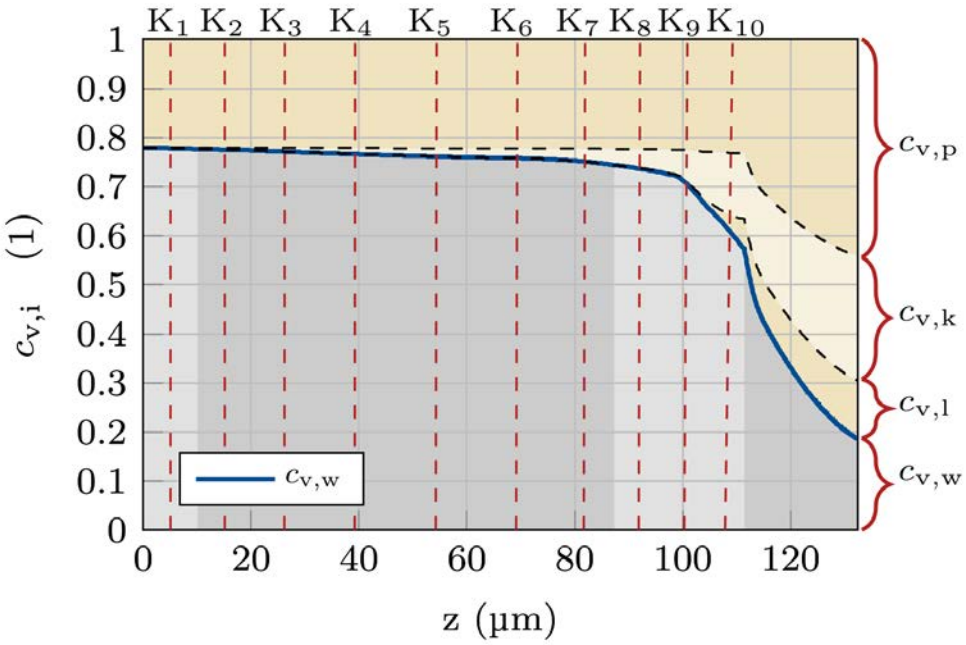


*Fig. 5.5: Histochemical concentration profile across the human epidermis illustrating its composition using the volume fractions of water, $c_{v,w}$, lipids, $c_{v,l}$, keratin, $c_{v,k}$, and protein, $c_{v,p}$. The vertical red dashed lines correspond to the midpoints of the cell layers (i.e. keratinocytes) denoted by $K_1$ to $K_{10}$.*

The Tab. 5.6 below summarizes the concentrations at $z = 0\ \mu\text{m}$ (i.e. ①), $z = 111.43\ \mu\text{m}$ (i.e. ② & ③) and $z = 132.43\ \mu\text{m}$ (i.e. ④) in terms of both mass and volume fractions.

*Tab. 5.6: Material composition of the epidermis at $z = 0\ \mu m$ (i.e. ①), $z = 111.43\ \mu m$ (i.e. ② & ③) and $z = 132.43\ \mu m$(i.e. ④) expressed as mass fractions. The concentration of the water, protein, keratin and lipid content is denoted by $c_{m,w}$,$c_{m,p}$, $c_{m,k}$ and $c_{m,l}$ respectively. The corresponding volume fractions,$c_{v,j}$, are given on the right-hand side.*

| | $c_{m,w}$ | $c_{m,p}$ | $c_{m,k}$ | $c_{m,l}$ | $c_{v,w}$ | $c_{v,p}$ | $c_{v,k}$ | $c_{v,l}$ |
|---|---|---|---|---|---|---|---|---|
| ① | 0.715 | 0.285 | 0 | 0 | 0.78 | 0.22 | 0 | 0 |
| ② & ③ | 0.499 | 0.285 | 0.164 | 0.052 | 0.573 | 0.231 | 0.133 | 0.063 |
| ④ | 0.146 | 0.285 | 0.280 | 0.088 | 0.187 | 0.441 | 0.254 | 0.118 |

### 5.2.2 Histochemical parameterization of the epidermis on a *microscopic* scale

The biochemical concentrations of the individual cell compartments of each cell layer will be derived below, starting with the keratinocytes. In a first step, the geometrical composition of the CAD models of each cell layer must be considered in terms of the volumes of the individual compartments, $V_{i,\mathrm{K}_p}$:

$$c_{\mathrm{v},i,\mathrm{K}_p} = \frac{V_{i,\mathrm{K}_p}}{V_{\mathrm{UC},\mathrm{K}_p}} \tag{5.4}$$

$$c_{\mathrm{v},i,\mathrm{Cell}} = \frac{V_{i,\mathrm{K}_p}}{V_{\mathrm{Cell},\mathrm{K}_p}} \tag{5.5}$$

with $V_{\mathrm{UC},\mathrm{K}_p} = V_{\mathrm{EC},\mathrm{K}_p} + V_{\mathrm{CP},\mathrm{K}_p} + V_{\mathrm{NP},\mathrm{K}_p}$, $V_{\mathrm{Cell},\mathrm{K}_p} = +V_{\mathrm{CP},\mathrm{K}_p} + V_{\mathrm{NP},\mathrm{K}_p}$ and $i \in \{\mathrm{EC};\ \mathrm{CP};\ \mathrm{NP}\}$. In a second step, the volume of each biochemical component is determined by multiplying the unit cell volume of each CAD model by the biochemical concentrations at the midpoints of each cell layer (see Fig. 5.5):

$$V_{j,\mathrm{K}_p} = V_{\mathrm{UC},\mathrm{K}_p} \cdot c_{\mathrm{v},j,\mathrm{K}_p} \tag{5.6}$$

with $j \in \{\mathrm{w};\ \mathrm{l};\ \mathrm{k};\ \mathrm{p}\}$. In a third step, these volumes are each distributed across the individual cell compartments, beginning with the EC space. This is done by assuming the extracellular medium to be filled with water only

$$V_{\mathrm{w},\mathrm{EC},\mathrm{K}_p} = V_{\mathrm{EC},\mathrm{K}_p}. \tag{5.7}$$

The residual cell water, $V_{\mathrm{w},\mathrm{Cell},\mathrm{K}_p} = V_{\mathrm{w},\mathrm{K}_p} - V_{\mathrm{w},\mathrm{EC},\mathrm{K}_p}$, and the volumes of each remaining substance now needs to be distributed to the CP and the NP. In the cell layers $K_1$ to $K_8$, the NP is considered to be a two-phase mixture containing protein and water to an extent proportional to the total amount of water in the cell:

$$V_{\mathrm{w},\mathrm{NP},\mathrm{K}_p} = V_{\mathrm{w},\mathrm{Cell},\mathrm{K}_p} \cdot c_{\mathrm{NP},\mathrm{Cell}} \tag{5.8}$$

$$V_{\mathrm{p},\mathrm{NP},\mathrm{K}_p} = \left(V_{\mathrm{Cell},\mathrm{K}_p} - V_{\mathrm{w},\mathrm{Cell},\mathrm{K}_p}\right) \cdot c_{\mathrm{NP},\mathrm{Cell}} \tag{5.9}$$

In cell layers $K_9$ and $K_{10}$ the amount of protein remains constant compared to cell layer $K_8$. However, the water content decreases according to the shrinkage of the nucleus due to karyopyknosis (see Section 5.1.1, Fig. 5.3):

$$V_{\mathrm{w},\mathrm{NP},\mathrm{K}_9} = V_{\mathrm{w},\mathrm{NP},\mathrm{K}_8} - (V_{\mathrm{NP},\mathrm{K}_8} - V_{\mathrm{NP},\mathrm{K}_9}) \tag{5.10}$$

$$V_{\mathrm{p},\mathrm{NP},\mathrm{K}_9} = V_{\mathrm{p},\mathrm{NP},\mathrm{K}_8} \tag{5.11}$$

$$V_{\mathrm{w},\mathrm{NP},\mathrm{K}_{10}} = V_{\mathrm{w},\mathrm{NP},\mathrm{K}_8} - (V_{\mathrm{NP},\mathrm{K}_8} - V_{\mathrm{NP},\mathrm{K}_{10}}) \tag{5.12}$$

$$V_{\mathrm{p},\mathrm{NP},\mathrm{K}_9} = V_{\mathrm{p},\mathrm{NP},\mathrm{K}_8} \tag{5.13}$$

The remaining cell water and protein are distributed to the CP. The metabolized keratin and lipids are also deposited there:

$$V_{\mathrm{w},\mathrm{CP},\mathrm{K}_p} = V_{\mathrm{w},\mathrm{Cell},\mathrm{K}_p} - V_{\mathrm{w},\mathrm{NP},\mathrm{K}_p} \tag{5.14}$$

$$V_{\mathrm{p},\mathrm{CP},\mathrm{K}_p} = V_{\mathrm{p},\mathrm{K}_p} - V_{\mathrm{p},\mathrm{NP},\mathrm{K}_p} \tag{5.15}$$

$$V_{\mathrm{k,CP,K}_p} = V_{\mathrm{k,K}_p} \tag{5.16}$$

$$V_{\mathrm{l,CP,K}_p} = V_{\mathrm{l,K}_p} \tag{5.17}$$

In a final step, the volume fractions of the biochemical compounds in each compartment in any given cell layer, $c_{\mathrm{v},j,i,\mathrm{K}_p}$, can be defined as

$$c_{\mathrm{v},j,i,\mathrm{K}_p} = \frac{V_{j,i,\mathrm{K}_p}}{V_{i,\mathrm{K}_p}} \tag{5.18}$$

Based on $c_{\mathrm{v},j,i,\mathrm{K}_p}$, the volumetric mass density within the cell compartments, $\rho_{i,\mathrm{K}_p}$, can now also be determined qualitatively. These are calculated by

$$\rho_{i,\mathrm{K}_p} = \sum_j \rho_j \cdot c_{\mathrm{v},j,i,\mathrm{K}_p} \tag{5.19}$$

The relationship is only labeled qualitatively, as the simple summation of the products of the individual densities and their volume fractions can only be assumed if the individual substances do not react chemically with each other. Fig. 5.6 provides an overview of the histochemical configurations of the keratinocytes in each cell layer of the viable epidermis. The top diagram illustrates the volumetric mass densities, $\rho_{i,\mathrm{K}_p}$, by black bars for each different keratinocyte model,

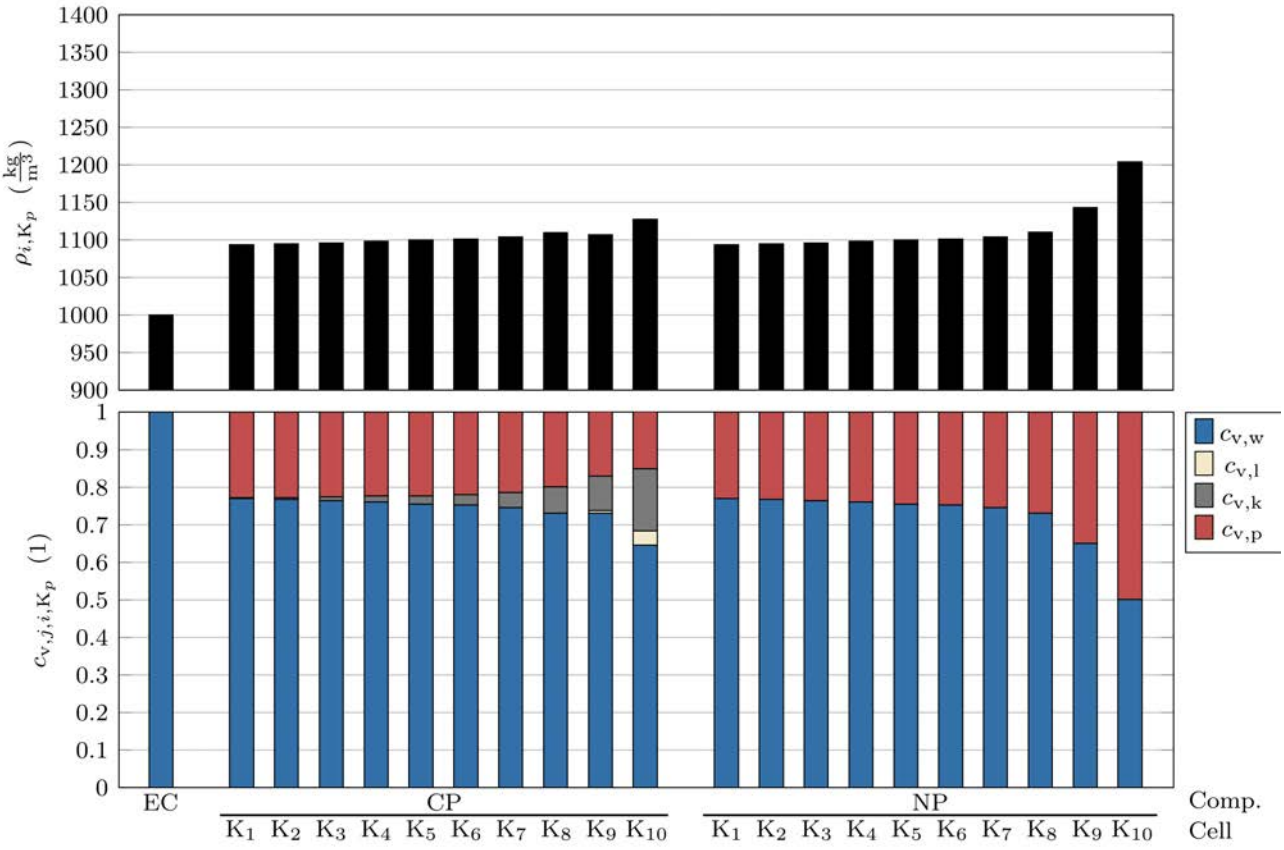


*Fig. 5.6: Histochemical configurations of the keratinocytes under investigation: (top) Volumetric mass densities, $\rho_{i,\mathrm{K}_p}$, illustrated by black bars for each different keratinocyte model, $\mathrm{K}_p$, and categorized according to the cell compartments (i.e. EC, CP, and NP). (bottom) Histochemical composition of the cell compartments expressed as volume fractions, $c_{v,j,i,\mathrm{K}_p}$, relative to the total volume of the individual compartments using the same categories. The index $j \in \{w;\ l;\ k;\ p\}$ denotes the content of water, lipids, keratin and protein, and the index $i \in \{CP;\ NP;\ EC\}$ denotes the individual cell compartments of the keratinocytes.*

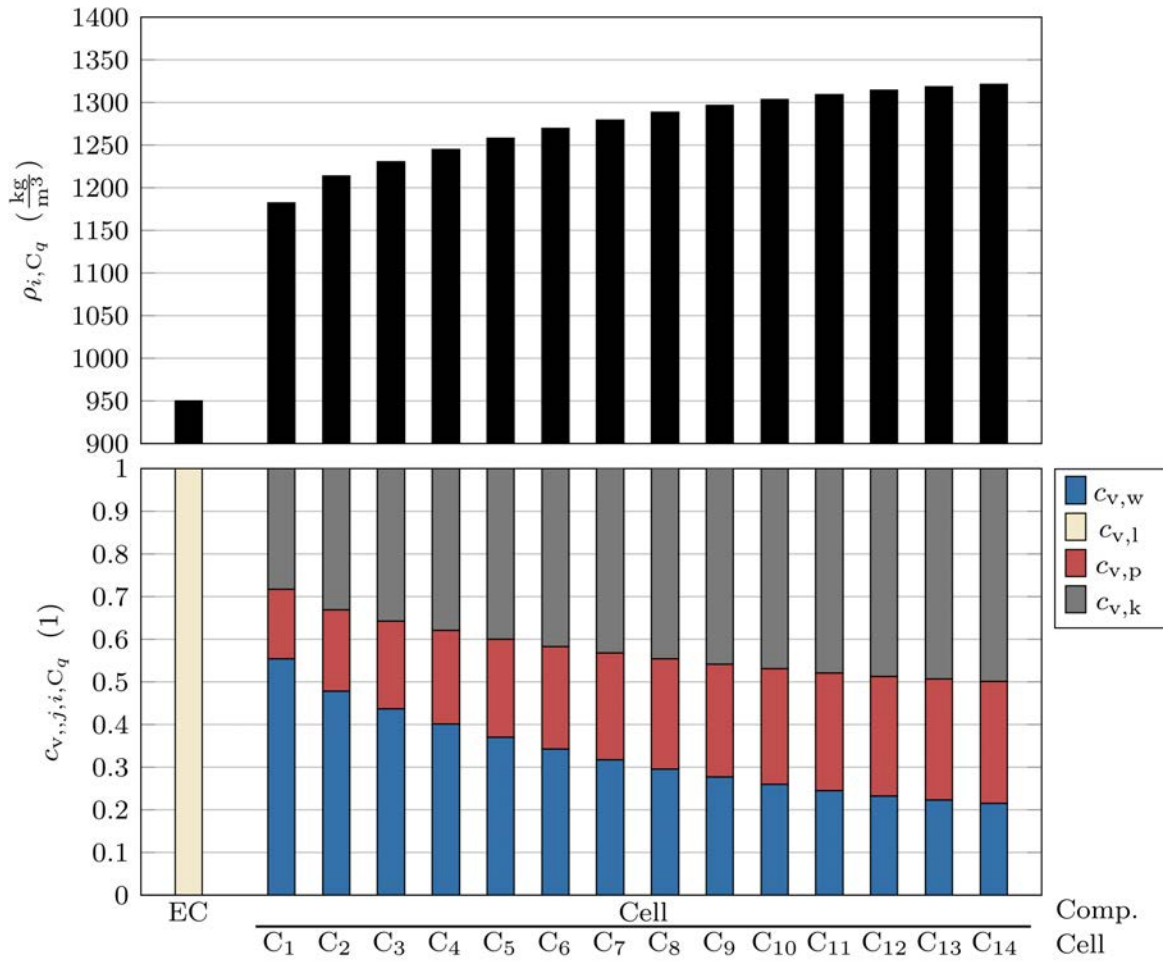


*Fig. 5.7: Histochemical configurations of the corneocytes under investigation: (top) Volumetric mass densities, $\rho_{i,C_q}$, illustrated by black bars for each different corneocyte model, $C_q$, and categorized according to the cell compartments (i.e.* EC, Cell*). (bottom) Histochemical composition of the cell compartments expressed as volume fractions, $c_{v,j,i,C_q}$, relative to the total volume of the individual compartments using the same categories. The index $j \in \{w;\ l;\ k;\ p\}$ denotes the content of water, lipids, keratin and protein, and the index $i \in \{Cell;\ EC\}$ denotes the individual cell compartments of the corneocytes.*

$K_p$, categorized according to the cell compartments (i.e. EC, CP, and NP). The bottom diagram illustrates the volume fractions, $c_{\mathrm{v},j,i,\mathrm{K}_p}$, relative to the total volume of the individual compartments using the same categories. The biochemical composition of the corneocytes within the SC is analogous to the derivation above. With the difference that the distribution of the respective substances is much simpler. Through exocytosis, the EC fills with lipids, so that the water together with the keratin and the other protein compounds in the SC are only inside the cell body. Fig. 5.7 provides an overview of the histochemical configurations of the corneocytes in each cell layer of the SC. The top diagram illustrates the volumetric mass densities, $\rho_{i,\mathrm{C}_q}$, by black bars for each different corneocyte model, $\mathrm{C}_q$, categorized according to the cell compartments (i.e. EC, Cell). The bottom diagram illustrates the volume fractions, $c_{\mathrm{v},j,i,\mathrm{C}_q}$, relative to the total volume of the individual compartments using the same categories.

## 5.3 Effective material properties of the bottom-up model of the epidermis

Based on the material composition of the cells at the microscopic scale outlined in the previous section, the effective material properties of the cell compartments are determined using analytical mixing rules in Section 5.3.1. Subsequently, these material properties will be used in the parametric CAD models of the kratinocytes and corneocytes to determine the effective material properties of the cell layers using quasi-static numerical simulations in Section 5.3.2.

### 5.3.1 Effective material properties of the parametric cell models on a microscopic scale

Considering the compartments of the cell models as multiphase composites consisting of water, proteins, keratin and lipids, the effective dielectric properties of these compartments in each cell layer can be calculated using analytical mixing rules. However, such calculations require knowledge of both the volume fraction and the dielectric properties of each substance present in each compartment. The volume fractions of each material have already been derived in Section 5.2 and can be taken from Figs. 5.6 and 5.7. However, the permittivities of the basic cell substances remain to be derived from the scientific literature, starting with those of the water in the following.

The dispersive properties of the extracellular medium, cytoplasm, and nucleoplasm are approximated by the dielectric functions of physiological salt solutions. This approach is adopted for modeling the cellular water within each compartment so that its lossy dispersive permittivities, $\underline{\varepsilon}_{\mathrm{r,w},i}(\omega)$, are modeled by a Debye-type equation:

$$\underline{\varepsilon}_{\mathrm{r,w},i}(\omega) = \varepsilon_{\mathrm{r,w},i,\infty} + \frac{\varepsilon_{\mathrm{r,w},i,\mathrm{s}} - \varepsilon_{\mathrm{r,w},i,\infty}}{1+\mathrm{j}\frac{\omega}{\omega_0}} - \mathrm{j}\frac{\sigma_{\mathrm{w},i,\mathrm{s}}}{\varepsilon_0 \omega} \tag{5.20}$$

with $i \in \{\mathrm{CP};\ \mathrm{NP};\ \mathrm{EC};\ \mathrm{Cell}\}$. The Debye coefficients corresponding to the individual compartments are summarized in Tab. 5.7.

*Tab. 5.7: Debye coefficients for modeling the dispersive dielectric material properties of the cytoplasm (CP), nucleoplasm (NP) and extracellular medium (EC), representing the dispersive material properties of the water in the corresponding compartment, $\underline{\varepsilon}_{r,w,i}(\omega)$, with $i \in \{CP;\ NP;\ EC;\ Cell\}$.*

| Compartment | $\varepsilon_{\mathrm{r,w},i,\mathrm{s}}$ | $\varepsilon_{\mathrm{r,w},i,\infty}$ | $f_0$ (GHz) | $\sigma_{\mathrm{w},i,\mathrm{s}}$ (S/m) |
|---|---|---|---|---|
| **Cytoplasm (CP)** | 67 | 5 | 17.9 | 0.32 |
| **Nucleoplasm (NP)** | 67 | 5 | 17.9 | 0.32 |
| **Extracellular medium (EC)** | 67 | 5 | 17.9 | 0.55 |
| **Cell body (Cell)** | 67 | 5 | 17.9 | 0.32 |

The dielectric properties of the protein content and those of the keratin are considered to be independent of the frequency with the following values

$$\underline{\varepsilon}_{\mathrm{r,p}} = 2.5 - \mathrm{j}0 \quad \text{and} \quad \underline{\varepsilon}_{\mathrm{r,k}} = 3.548 - \mathrm{j}0.244,$$

where the former value is taken from [26] and the latter from [28].

The material properties of the lipids are modeled by a double Debye equation defined as

$$\underline{\varepsilon}_{\mathrm{r,l}}(\omega) = \varepsilon_{\mathrm{r,l},\infty} + \frac{\Delta\varepsilon_{\mathrm{r,l},1}}{1+\mathrm{j}\frac{\omega}{\omega_{0,1}}} + \frac{\Delta\varepsilon_{\mathrm{r,l},2}}{1+\mathrm{j}\frac{\omega}{\omega_{0,2}}} - \mathrm{j}\frac{\sigma_{\mathrm{l,s}}}{\varepsilon_0 \omega} \tag{5.21}$$

whose coefficients are adopted from [26] and summarized in Tab. 5.8.

*Tab. 5.8: Debye coefficients to model the dispersive permittivity of lipids (adopted from [26]).*

| | $\varepsilon_{\mathrm{r,l},\infty}$ | $\Delta\varepsilon_{\mathrm{r,l},1}$ | $\Delta\varepsilon_{\mathrm{r,l},2}$ | $f_{0,1}$ (THz) | $f_{0,2}$ (THz) | $\sigma_{\mathrm{l,s}}$ (S/m) |
|---|---|---|---|---|---|---|
| **Lipids (l)** | 2.15 | 0.2 | 0.1 | 1 | 10 | 0 |

The initial permittivities of water are incrementally combined with the other basic components (i.e. protein, keratin and lipids) using the Hanai-Bruggeman (HB) mixing formula to account for the influence of different keratinization and hydration stages within the epidermis on the effective material parameters of the individual cell compartments:

$$0 = (1-\Phi^s)\cdot\left(\frac{\underline{\varepsilon}^s_{\mathrm{r},i,\mathrm{K}_p,\mathrm{HB}}-\underline{\varepsilon}^s_{\mathrm{r},i,\mathrm{K}_p,\mathrm{I}}}{\underline{\varepsilon}^s_{\mathrm{r},i,\mathrm{K}_p,\mathrm{H}}-\underline{\varepsilon}^s_{\mathrm{r},i,\mathrm{K}_p,\mathrm{I}}}\right)\cdot\left(\frac{\underline{\varepsilon}^s_{\mathrm{r},i,\mathrm{K}_p,\mathrm{H}}}{\underline{\varepsilon}^s_{\mathrm{r},i,\mathrm{K}_p,\mathrm{HB}}}\right)^{\frac{1}{3}}, \tag{5.22}$$

where $s$ denotes the incremental mixing step. The dielectric material properties of the substance considered to be the inclusion are denoted by $\underline{\varepsilon}^s_{\mathrm{r},i,\mathrm{K}_p,\mathrm{I}}$ and those which are considered to be the host medium by $\underline{\varepsilon}^s_{\mathrm{r},i,\mathrm{K}_p,\mathrm{H}}$. $\Phi^s$ denotes the volume fraction of the inclusions relative to the total volume of the two-phase mixture. $\underline{\varepsilon}^s_{\mathrm{r},i,\mathrm{K}_p,\mathrm{HB}}$ denotes the effective permittivity of each step. In any step where $s \geq 2$, $\underline{\varepsilon}^s_{\mathrm{r},i,\mathrm{K}_p,\mathrm{H}} = \underline{\varepsilon}^{s-1}_{\mathrm{r},i,\mathrm{K}_p,\mathrm{HB}}$. Tab. 5.9 provides an overview of the mixing procedure used to determine the effective permittivities of the individual cell compartments, $i \in \{\mathrm{CP};\ \mathrm{NP};\ \mathrm{Cell}\}$, at any given cell layer of the viable epidermis, $\mathrm{K}_p$, and the SC, $\mathrm{C}_q$.

*Tab. 5.9: Overview of the mixing procedure used to determine the effective permittivities of the individual cell compartments, $i \in \{CP;\ NP;\ Cell\}$, in any given cell layer of the viable epidermis, $K_p$, and the SC, $C_q$. $s$ denotes the incremental mixing step. The dielectric material properties of the substance considered to be the inclusion are denoted by $\underline{\varepsilon}^s_{r,i,K_p,I}$ and those which are considered to be the host medium by $\underline{\varepsilon}^s_{r,i,K_p,H}$. Here, $\underline{\varepsilon}_{r,w}$, $\underline{\varepsilon}_{r,p}$, $\underline{\varepsilon}_{r,k}$ and $\underline{\varepsilon}_{r,l}$ denote the dielectric values of the water (i.e. physiological salt solution), the protein, the keratin and the lipids respectively.*

| | **Keratinocytes** | | | | **Corneocytes** | |
|---|---|---|---|---|---|---|
| $s$ | **CP** | | **NP** | | **Cell** | |
| | $\underline{\varepsilon}^s_{\mathrm{r},i,\mathrm{K}_p,\mathrm{H}}$ | $\underline{\varepsilon}^s_{\mathrm{r},i,\mathrm{K}_p,\mathrm{I}}$ | $\underline{\varepsilon}^s_{\mathrm{r},i,\mathrm{K}_p,\mathrm{H}}$ | $\underline{\varepsilon}^s_{\mathrm{r},i,\mathrm{K}_p,\mathrm{I}}$ | $\underline{\varepsilon}^s_{\mathrm{r},i,\mathrm{C}_q,\mathrm{H}}$ | $\underline{\varepsilon}^s_{\mathrm{r},i,\mathrm{C}_q,\mathrm{I}}$ |
| **1** | $\underline{\varepsilon}_{\mathrm{r,w}}$ | $\underline{\varepsilon}_{\mathrm{r,p}}$ | $\underline{\varepsilon}_{\mathrm{r,w}}$ | $\underline{\varepsilon}_{\mathrm{r,p}}$ | $\underline{\varepsilon}_{\mathrm{r,w}}$ | $\underline{\varepsilon}_{\mathrm{r,p}}$ |
| **2** | $\underline{\varepsilon}_{\mathrm{r,wp}}$ | $\underline{\varepsilon}_{\mathrm{r,k}}$ | | | $\underline{\varepsilon}_{\mathrm{r,wp}}$ | $\underline{\varepsilon}_{\mathrm{r,k}}$ |
| **3** | $\underline{\varepsilon}_{\mathrm{r,wpk}}$ | $\underline{\varepsilon}_{\mathrm{r,l}}$ | | | | |

The resulting effective permittivities of the individual cell compartments in each cell layer of the viable epidermis, $\underline{\varepsilon}_{\mathrm{r},i,\mathrm{K}_p}$, are shown in Fig. 5.8. The real and imaginary parts of the dielectric function of the EC space are shown in Figs. 5.8(a) and (b). These are identical for all cell layers of the viable epidermis, assuming that biochemical changes within each cell layer are expressed only by material accumulation within cell bodies (see Section 5.2). In this way, the graphs illustrate the Debye type characteristic of the EC, as described in Tab. 5.8. Figs. 5.8(c) and (d) show the real and imaginary parts of the effective permittivities calculated using the HB mixing rule according to Tab. 5.9. It can be seen that the permittivities of the top layer of the SG, $\mathrm{K}_{10}$, shown as a blue dotted line, have lower values than those of the basal layer, $K_1$, shown by a red line. The range of values across the cell layers resulting from the different material compositions within the CP is illustrated by a gray area. These differences are caused by increasing keratin and lipid deposition within the CP towards the skin surface. Comparing the permittivities of the CP with those of the NP (see Fig. 5.8(e) and (f)), it can be seen that in both cases, there is also a range of values with lower permittivities for layers closer to the skin surface, and the range of values is significantly broader for the NP than for the CP.

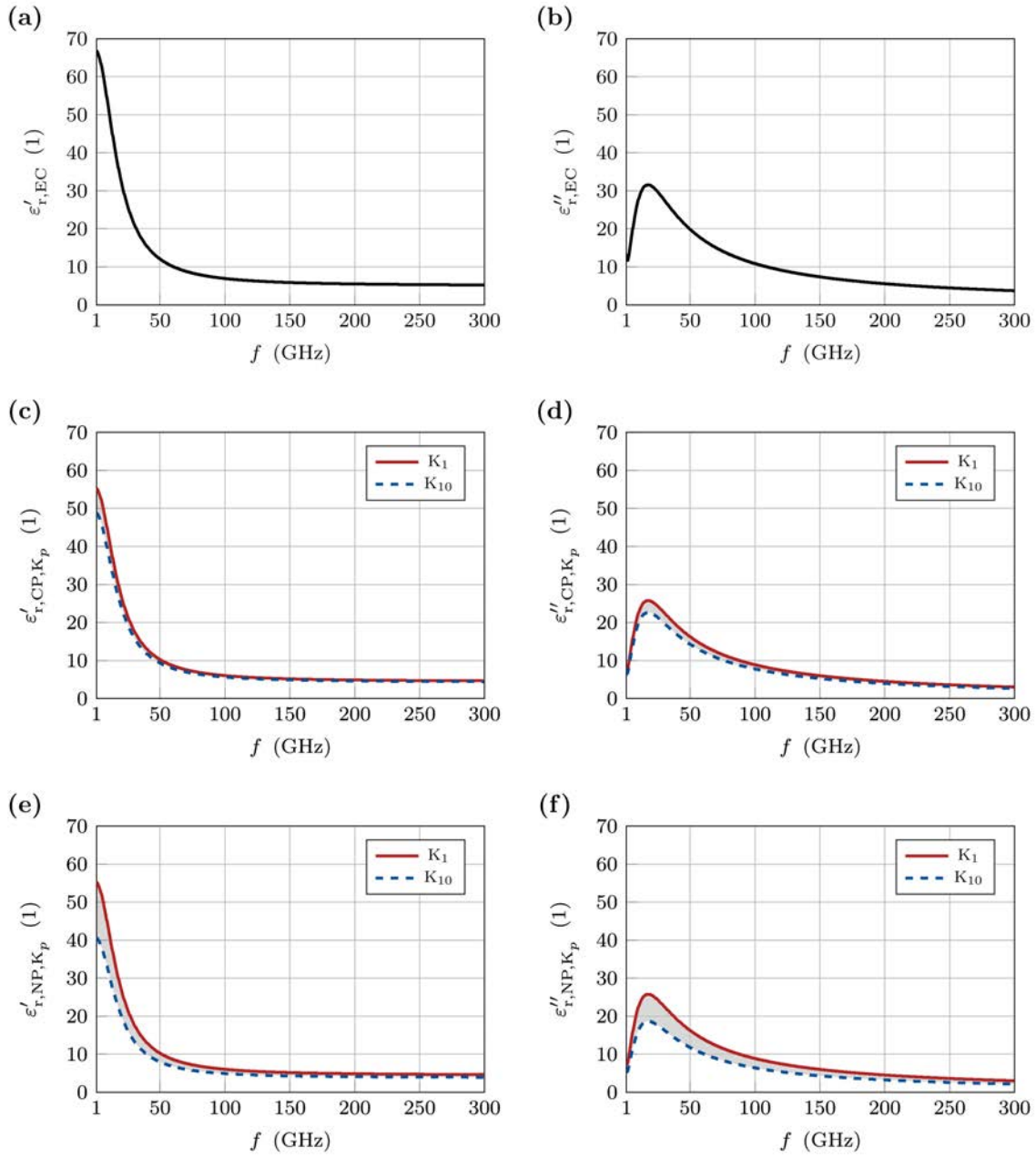


*Fig. 5.8: Overview of the dielectric material properties of the cell compartments in each cell layer of the viable epidermis determined using the mixing procedure summarized in Tab. 5.9. Real and imaginary parts of the dielectric permittivity are shown for the extracellular medium (EC) in (a) and (b), for the cytoplasm (CP) in (c) and (d), and for the nucleoplasm (NP) in (e) and (f). The range of values across the cell layers resulting from different material compositions within the CP and NP is illustrated by a gray-shaded area bound at the top by the dielectric properties of cell layer $K_1$ and at the bottom by cell layer $K_{10}$.*

This is due to the shrinkage of the nucleus and the condensation of the chromatin contained therein into a uniform mass, which was accounted for in Section 5.2 by shifting the water/protein ratio in favor of the protein. The resulting effective permittivities of the individual cell compartments in each cell layer of the SC, $\underline{\varepsilon}_{r,i,C_q}$, are shown in Fig. 5.9. Figs. 5.9(a) and (b) show the real and imaginary parts of the EC space. In contrast to the viable epidermis, saline solution is not used to model its dielectric properties. As described in detail in Section 5.2, the keratinocytes of the SG secrete lipid deposits from the cell interior in a process known as exocytosis. These lipid deposits form an extracellular lipid matrix in which the corneocytes are embedded. Therefore, the graphs of the dielectric functions presented here show the Debye characteristic specified in Tab. 5.8 for lipids, which is assumed to be

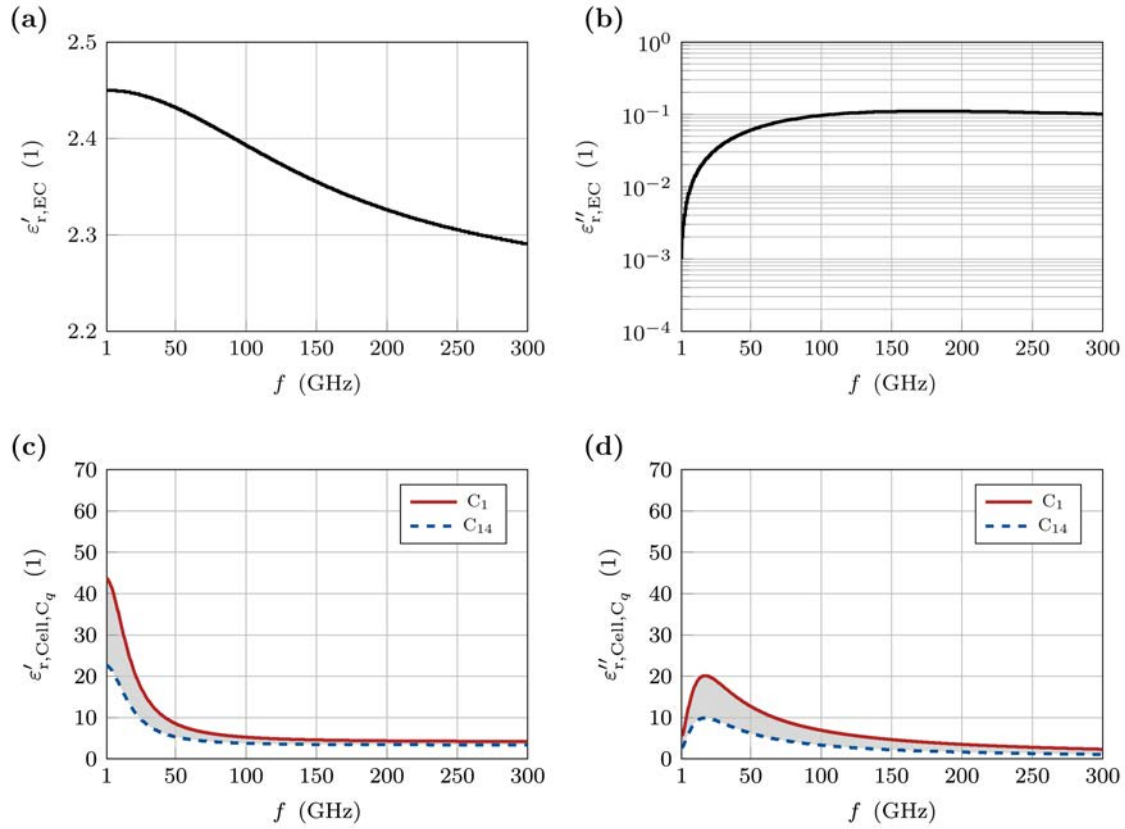


*Fig. 5.9: Overview of the dielectric material properties of the cell compartments in each cell layer of the SC determined using the mixing procedure summarized in Tab. 5.9. Real and imaginary parts of the dielectric permittivity are shown for the extracellular medium (EC) in (a) and (b), for the cell body (Cell) in (c) and (d). The range of values across the cell layers resulting from different material compositions within the cell body is illustrated by a gray-shaded area bound at the top by the dielectric properties of cell layer $C_1$ and at the bottom by cell layer $C_{14}$.*

constant for all layers of the SC. Since lipids have significantly lower values for the real and imaginary parts of their dielectric permittivities compared to physiological salt solutions, it was necessary to deviate from the previously uniformly chosen range of values (0 to 70) for the representation and, in the case of Fig. 5.9(b), to resort to a logarithmic representation. Moving on to the effective permittivities of the cell bodies shown in Figs. 5.9(c) and (d), it can be seen that both the real and imaginary parts of the permittivity show a significant range of values between the lowermost and uppermost cell layers. This is represented by a gray area bounded by a red line corresponding to layer $C_1$ and a blue dashed line corresponding to layer $C_{14}$. The decrease in permittivity towards the skin surface is associated with a decrease in the amount of water bound in the cell body (see Fig. 5.7).

### 5.3.2 Effective material properties of the epidermal sublayers on a macroscopic scale

Having calculated the effective material properties of the cell compartments in the previous section, they can now be implemented into the parametric CAD models of each cell layer. Placing these models in the virtual capacitor setup (see Appendix A), numerical homogenization yields the effective material parameters of each cell layer of the viable epidermis, $\underline{\tilde{\varepsilon}}_{r,K_p}$, and the SC, $\underline{\tilde{\varepsilon}}_{r,C_p}$. The These quantities, respective $\underline{\tilde{\varepsilon}}_{r,K_p}$ and $\underline{\tilde{\varepsilon}}_{r,C_q}$ are illustrated in Figs. 5.10(a) and (b) for the cell layers of the viable epidermis and in Figs. 5.10(c) and (d) for the cell layers of the SC. Comparing Figs. 5.10(a) and (b) with (c) and (d), it can be seen that the loss of water in the SC causes a broader range of values compared to the metabolism of keratin and lipids in the viable epidermis.

The simulation was performed on a PC equipped with two Intel Xeon E5-2697 V4 processors (36 cores) and 512 GB of memory. The frequency range of interest (i.e. 1 GHz to 300 GHz) was examined and sampled with 45 linearly distributed frequency points per cell model. The data points

between these sampled points were interpolated using piecewise cubic Hermite splines in post-processing. The simulation for each frequency point took approximately 33 min using a MUMPS solver. Post-processing of the data was performed within the MATLAB programming environment (version R2020a) [27].

Volumetric mass densities of each cell layer on a macroscopic scale, $\rho_{\mathrm{K}_p/\mathrm{C}_q}$, are determined by:

$$\rho_{\mathrm{K}_p/\mathrm{C}_q} = \sum_i \rho_{i,\mathrm{K}_p/\mathrm{C}_q} \cdot c_{\mathrm{v},i,\mathrm{K}_p/\mathrm{C}_q} \tag{7.23}$$

where, $\rho_{\mathrm{K}_p/\mathrm{C}_q}$ denotes volumetric mass densities of the individual cell compartments in each cell layer and $c_{\mathrm{v},i,\mathrm{K}_p/\mathrm{C}_q}$ its corresponding volume fraction (see Eqs. 5.4 and 5.19). In Fig. 5.11, it can be seen that the reduction of the water content within the cell layers towards the skin surface leads to a significant increase in the volumetric mass density.

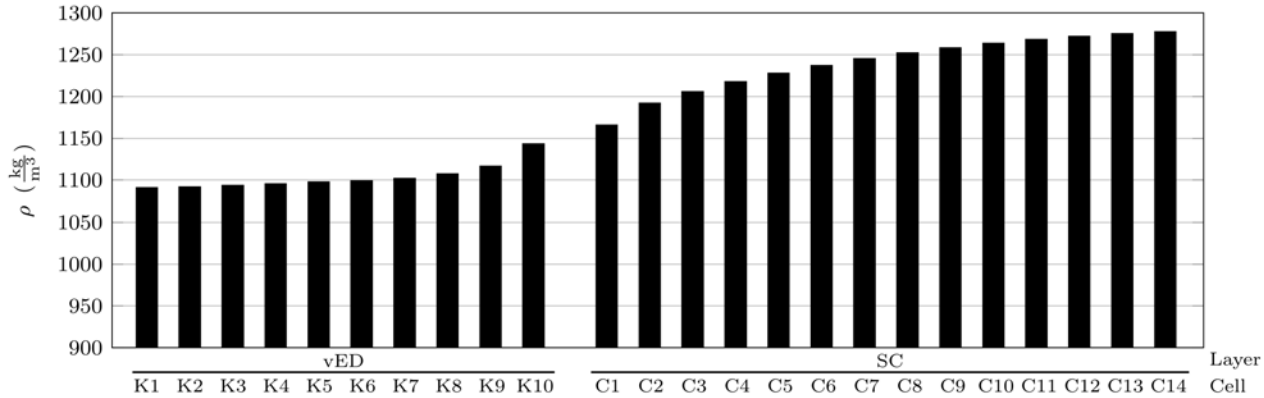


*Fig. 5.11: Volumetric mass densities of each cell layer in viable epidermis and the stratum corneum, $\rho_{K_p/C_q}$, illustrated by black bars and categorized according to the individual layers (i.e. $K_p$ and $C_q$).*

## 5.4 Conclusions

■ In this chapter, a hierarchical, computational bottom-up multiscale model of the epidermis has been developed, which ultimately leads to a coherent description of the EM material properties of the epidermis at both a macroscopic and the microscopic level (including the (sub-)cellular level). In contrast to previous multiscale approaches [27, 28, A6], which considered the epidermis to be homogenized in its entirety and thus neglected any physiological variation within this skin layer, here the epidermis has been considered as a biological system with morphology determined by the life cycle of its predominant cell type, the keratinocytes (or corneocytes). This consideration of the epidermis as an evolving system has resulted in to a stratified cell model that includes 10 cell layers in the viable epidermis and 14 cell layers in the SC. The differentiation of basal keratinocytes towards the skin surface during the keratinization process has been represented in this layer model by gradual changes from one layer to the next, which have been accounted for by two aspects:

(1) Changes in cell geometry and cell structure, and

(2) changes in the histochemical composition of the cell.

Both aspects have been considered at the microscopic level, i.e. for the models of the individual cells, as well as at the macroscopic level, i.e. for the layer model of the entire epidermis. The complex intertwined relationship between both of these aspects and the two levels on which they have been considered has been used to create a holistic representation of the epidermis. The key elements of this developmental process are recapitulated in the following.

■ Initially, parametric CAD models were created for both keratinocytes and corneocytes, representing their microstructure. Then, in order to implement cell differentiation, these were adapted to the physiological conditions of each cell layer using geometric parameters derived from the scientific

literature. The thicknesses of the epidermal sublayers were then determined from the adapted cell models. Data from [18] and [19] were then used to derive a concentration profile for the epidermis at a macroscopic scale, considering the histochemical composition of the epidermis as a multiphase composite of water, lipids, keratin and a general protein component. From the macroscopic concentration profile, the histochemical composition of each cell layer was determined and projected onto the respective cell compartments at the microscopic scale. Based on the concentration profiles of the individual cell compartments in each cell layer, the effective permittivities of the compartments were calculated using an incremental mixing procedure using the HB mixing formula and assigned to the parameterized cell models as material parameters. The effective material properties of the individual cell layers were determined on a macroscopic scale using quasi-static computer-aided EM homogenization.

# 6 The importance of physiological variations across the epidermis for dosimetric investigations of EM exposure of the skin

In the following, extensive dosimetric studies of the skin will be performed to identify physiological variations across the epidermis as an important factor significantly affecting both the transmission of EM energy into the body surface and the distribution of this energy across the epidermis. A particular focus of these investigations will be on the proliferative pool of the epidermis (i.e., the basal and sub-basal rows), which is of particular importance for skin resurfacing. Therefore, accurate prediction of EM exposure in these layers is essential to assess the risk of adverse health effects on miotic activity. The investigations will be carried out as a comparison between two stratified skin models:

(1) A model derived entirely from the scientific literature based on measured material properties of the individual sublayers of the skin, hereafter referred to as the «reference model». This represents the current state of the art in skin modeling used in virtual EM exposure studies;

(2) A modified version of this model in which the epidermis is replaced by the equivalent layer from the bottom-up model introduced in Section 5. This combination of the purely numerical tissue model of the epidermis and the existing measured models of the other skin layers is hereafter referred to as the «hybrid model».

The layered topology and the dielectric properties of the individual skin layers considered in the reference model are based on data reported in [1] and [2]. These studies were chosen as a scientific reference for two reasons: their great influence on the current exposure guidelines [3] (see Section 1), and the fact that they are the only scientific source providing distinct measurements of all skin sublayers in a frequency range from 1 GHz to 1 THz. The comparison between the reference model and the hybrid model thus allows a dosimetric analysis of the skin with a direct relationship to current exposure guidelines, and links numerically obtained exposure data with corresponding exposure measurements published in the references cited above.

A detailed introduction to these skin models and their implementation within a computational simulation environment is provided in Section 6.1. To outline the dosimetric analysis that follows, Section 6.2 presents the methodology and measures employed in the analysis. Subsequently, in Section 6.3, a thorough evaluation of the skin models is conducted, including an assessment of the permittivities of the individual epidermal cell layers incorporated into the hybrid model. Moving on to Section 6.4, the chapter presents the results of the investigations. This section is divided into two subsections: a reflectometric analysis of the skin models is presented first, followed by a dosimetric analysis of the power intake across the epidermis. The subsequent section, Section 6.5, delves into a comprehensive discussion of the obtained results. Finally, the key findings and main points discussed throughout this chapter are summarized in Section 6.6.

## 6.1 Macroscopic exposure setup

In order to study skin exposure in the most general manner, an exposure setup was established to simulate skin irradiation at operating frequencies between 1 GHz and 300 GHz, hereafter referred to as the macroscopic exposure setup. The skin model considered in this setup has a layered topology comprising the epidermis (ED), the dermis (D), the hypodermis (HYP) and underlying muscle tissue (MC) which is illustrated in Fig. 6.1(a). The thickness of the epidermis, $t_{\mathrm{ED}}$, corresponds to that of the bottom-up model derived in Section 5 and thus equals 132,43 µm. The thicknesses of the remaining skin layers have been adopted from [1] and correspond to the mean values at the forearm resulting in thicknesses of $t_{\mathrm{D}} = 1080\ \mu\mathrm{m}$ and $t_{\mathrm{HYD}} = 3890\ \mu\mathrm{m}$. For numerical reasons outlined later in this section, the thickness of the muscle tissue, $t_{\mathrm{MC}}$, is considered to be infinite. For the calculation of the *SAR* in later chapters, it is necessary to assign volumetric mass densities, $\rho_k$, with $k \in \{\mathrm{ED};\ \mathrm{D};\ \mathrm{HYP};\ \mathrm{MC}\}$, to each skin sublayer. These values are taken from [29] resulting in the volumetric mass densities given in Tab. 6.1. All of the thicknesses and volumetric mass densities mentioned above apply to both the reference model and the hybrid model, with only one exception: $\rho_{\mathrm{ED}}$.The hybrid model applies the specific volumetric mass densities for each epidermal

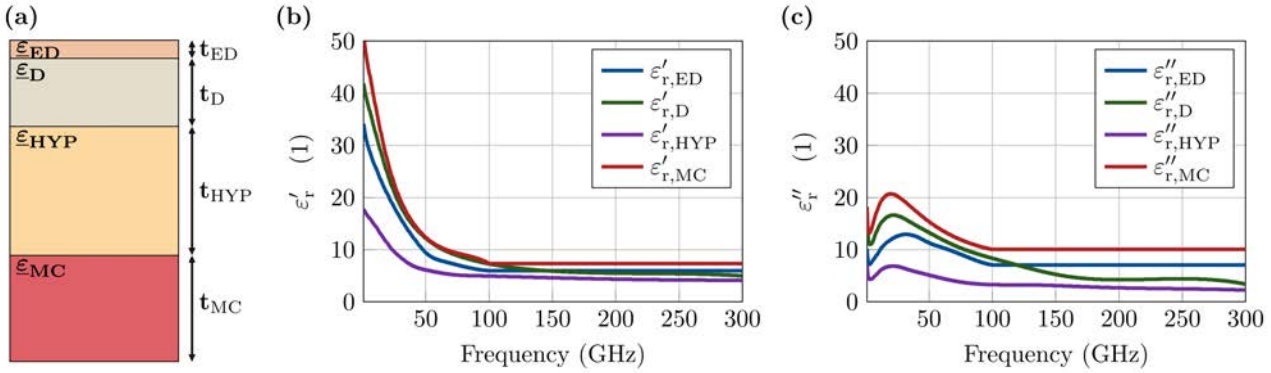


*Fig. 6.1: Overview of the layered topology of the skin model (not to scale) and the complex dielectric material properties, $\underline{\varepsilon}_{r,k}$, assigned to the individual sublayers of the skin: (a) Illustration of the stratified skin model showing the complex permittivities, $\underline{\varepsilon}_{r,k}$ and thicknesses, $t_k$, assigned to the individual tissue layers. (b) Real part of the permittivity, $\underline{\varepsilon}'_{r,k}$. (c) Imaginary part of the permittivity, $\underline{\varepsilon}''_{r,k}$. The index $k \in \{ED;\ D;\ HYP;\ MC\}$ denotes epidermis, dermis, hypodermis and muscle tissue respectively.*

cell layer, $\rho_{\mathrm{ED,K}_p/\mathrm{C}_q}$, shown in Fig. 5.11. The thicknesses of the individual skin layers, $t_k$, and the volumetric mass densities assigned to these layers, $\rho_k$, are summarized in Tab. 6.1. In addition to the values above, complex dispersive permittivities need to be applied to the individual skin layers with the real and imaginary values, $\underline{\varepsilon}_{\mathrm{r,k}}$, displayed in Figs. 6.1(b) and (c) respectively. These material parameters, which were originally published in [1] and [2], are based on measurements on pig skin. However, it should be noted that there is a lack of data contained in this data source. Only the material properties of the dermis and hypodermis, $\underline{\varepsilon}_{\mathrm{r,D}}$ and $\underline{\varepsilon}_{\mathrm{r,HYP}}$, have been reported over the whole frequency range under investigation. The effective material properties of the remaining sublayers of the skin, $\underline{\varepsilon}_{\mathrm{r,ED}}$ and $\underline{\varepsilon}_{\mathrm{r,MC}}$, have only been reported between 1 GHz and 100 GHz. To compensate for the lack of data, the values of $\underline{\varepsilon}_{\mathrm{r,ED}}$ and $\underline{\varepsilon}_{\mathrm{r,MC}}$ for frequencies above 100 GHz are set equal to those at 100 GHz. The dispersive permittivities of the individual epidermal cell layers, $\underline{\tilde{\varepsilon}}_{\mathrm{r,K}_p/\mathrm{C}_q}$, which are considered in the hybrid model, can be taken from Fig. 5.10.

*Tab. 6.1: Overview of the thicknesses of the individual skin layers, $t_k$, and of the volumetric mass densities, $\rho_k$, assigned to these layers.*

| | Epidermis (ED) | Dermis (D) | Hypodermis (HYP) | Muscle (MC) |
|---|---|---|---|---|
| **Thickness $t_i$ (µm)** | 132.43 | 1080 | 3890 | $\infty$ |
| **Density $\rho_i$ (kg/m$^3$)** | 1190 | 1116 | 971 | 1041 |

After defining the skin model, it needs to be embedded in a generic exposure setup, which is numerically implemented using the COMSOL Multiphysics software environment [30], allowing the determination EM fields penetrating in the individual skin layers. This macroscopic exposure setup is illustrated in Fig. 6.2. A plane wave is emitted from a non-reflective port at an angle of incidence, $\alpha$, (here 0 °C) having either s or p-polarization with respect to the reflection plane (i.e. xz plane). The amplitude of the incident plane wave corresponds to a constant input power, $P_{\mathrm{inc}}(\omega)$, which is derived from the incident power density, $S_{\mathrm{inc}}(\omega)$, defined in the basic restrictions (see Tab. 1.1). The reflected power, $P_{\mathrm{R}}$, is detected by the same non-reflective port, and the power transmitted to the skin tissue, $P_{\mathrm{T}}$, is calculated from $P_{\mathrm{T}} = P_{\mathrm{inc}} - P_{\mathrm{R}}$. From these values, the power reflection coefficient, $R$, and the power transmission coefficient, $T$, are given by

$$R = \frac{P_{\mathrm{R}}}{P_{\mathrm{inc}}} \tag{6.1}$$

$$T = \frac{P_{\mathrm{T}}}{P_{\mathrm{inc}}} \tag{6.2}$$

To avoid further reflections of waves from the outer top and bottom boundaries, the computational domain is terminated above and below with perfectly matched layers (PML). In addition, periodic boundary conditions (PBCs) are introduced into the macroscopic exposure setup to prevent fringing fields. Figs. 6.2(a) and (b) illustrate the different material properties assigned to the individual skin layers depending on the choice of either the reference or the hybrid model introduced earlier. Both models have a square-shaped surface under exposure with an area of $1\ \mathrm{mm}^2$.

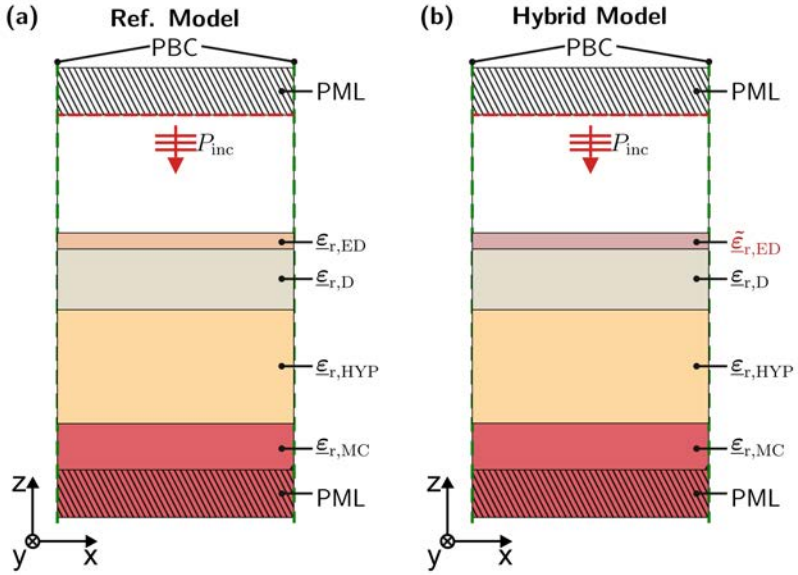


*Fig. 6.2: An overview of the macroscopic exposure setup: The stratified skin model is exposed to a plane EM wave using a non-reflective port. The amplitude of the incident plane wave corresponds to a constant input power, $P_{inc}(\omega)$, which is derived from an incident power density, $S_{inc}(\omega)$, defined in the basic restrictions outlined in Section 1. The top and bottom of the computational domain are terminated with perfectly matched layers (PML). Periodic boundary conditions (PBC) are used to prevent fringing fields. The square-shaped surface area under exposure is $1\ mm^2$. The complex permittivities of the individual skin layers, $\underline{\tilde{\varepsilon}}_{r,k}$, are adopted from [1] and [2]. The index $k \in \{ED;\ D;\ HYP; MC\}$ denotes epidermis, dermis, hypodermis and muscle respectively. The hybrid model deviates from the reference model by assigning material properties calculated using bottom-up multiscale modeling, $\underline{\tilde{\varepsilon}}_{r,ED}$, comprising the effective permittivities of the individual epidermal skin layers, $\underline{\tilde{\varepsilon}}_{r,K_p}$ and $\underline{\tilde{\varepsilon}}_{r,C_q}$, derived in Section 5.*

The simulation was performed on a PC equipped with an Intel i7-6700k processor (4 cores) and 64 GB of memory. In this study, a frequency range between 1 GHz and 300 GHz was investigated and sampled with 227 frequency points distributed linearly. The data points in between these sampled points were interpolated using cubic splines in post-processing. The simulation for each frequency point lasted approximately 10 seconds using a MUMPS solver. The post-processing of the data was performed within the MATLAB programming environment (version R2020a) [27].

## 6.2 Outline of the dosimetric analysis of the epidermis

In order to assess the importance of physical variations across the epidermis, the EM exposure of the skin is investigated in a three-fold analysis. In the first step, the total power transmitted to the skin is analyzed in a reflectometric analysis. Following on from this, the power transfer to deeper sublayers of the skin is investigated. In the last step, the power distribution across the epidermal cell layers, $\mathrm{K}_p$ and $\mathrm{C}_q$, is analyzed. While the reflectometric analysis of the total power transmitted to the skin tissue is performed using the power reflection and transmission coefficient introduced in Section 6.1 (see Eqs. 6.1 and 6.2), the latter two aspects need additional introduction. As shown in Figs. 6.3(a) and (b), the sub-layered structure of the epidermis is illustrated in both the reference model and the bottom-up model. As indicated by the different color schemes, the individual cell layers in the reference model are assigned identical dispersive material properties, $\underline{\varepsilon}_{\mathrm{r,ED}}(\omega)$, while

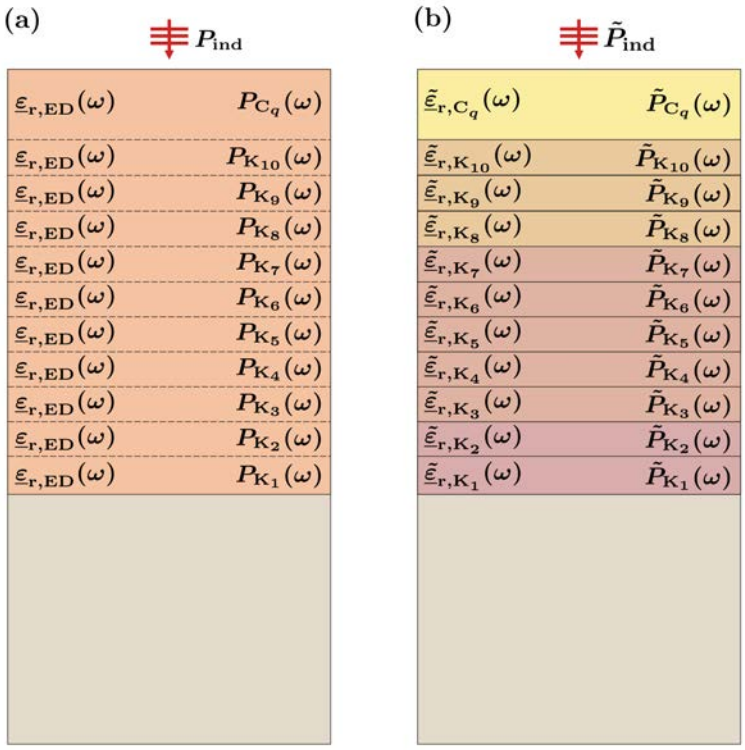


*Fig. 6.3: Conceptual overview of the dosimetric analysis of the epidermis, illustrating its layered structure: All of the individual cell layers in the reference model, $K_p$ and $C_q$, are assigned identical dispersive material properties, $\underline{\varepsilon}_{r,ED}(\omega)$, while those of the hybrid model have individual ones, $\underline{\tilde{\varepsilon}}_{r,K_p/C_q}(\omega)$. This is indicated by the different color schemes given to these layers in Figs. (a) and (b). The implementation of these cell layers in the macroscopic exposure setup as distinct computational domains allows the integration of the volumetric loss density, $p(\vec{r},\omega)$, over each individual layer. This leads to the determination of the power induced within each of these layers, $P_{K_p/C_q}(\omega)$. Considering the power transmitted to the skin tissue, $P_T(\omega)$, which differs between models due to different epidermal permittivities, a comparative analysis of the power transfer to deeper sublayers of the skin and the power distribution across the epidermal cell layers must be expressed relative to $\tilde{P}_T(\omega)$. In all of the above parameters, a tilde will be added to refer to the hybrid model rather than the reference model.*

those of the hybrid model have individual ones, $\underline{\varepsilon}_{\mathrm{r,K}_p/\mathrm{C}_q}(\omega)$. The implementation of these cell layers in the macroscopic exposure setup as distinct computational domains allows the integration of the volumetric loss density, $p(\vec{r},\omega)$, over each individual layer. This leads to the determination of the power induced within each of these layers, $P_{\mathrm{K}_p/\mathrm{C}_q}(\omega)$. To enable an accurate comparison between the transfer of power into deeper sublayers of the skin provided by each of the models, the power absorbed by the epidermis,

$$P_{\mathrm{ED}}(\omega) = \sum_{p=1}^{10} P_{\mathrm{K}_p}(\omega) + \sum_{q=1}^{14} P_{\mathrm{C}_q}(\omega) \tag{6.3}$$

needs to be expressed relative to the total power transmitted to the skin tissue, as this obviously differs between models. This is given by

$$A_{\mathrm{ind,ED}}(\omega) = \frac{P_{\mathrm{ED}}(\omega)}{P_{\mathrm{T}}(\omega)} \tag{6.4}$$

In order to compare the power distribution within the epidermis resulting from the two models, the power absorbed by the viable epidermis (vED) and the SC, $P_{\mathrm{vED}}$ and $P_{\mathrm{SC}}$, are expressed with respect to the total power absorbed by the epidermis, $P_{\mathrm{ED}}$, giving

$$A_{\mathrm{ED,vED/SC}}(\omega) = \frac{P_{\mathrm{vED/SC}}(\omega)}{P_{\mathrm{ED}}(\omega)} \tag{6.5}$$

A more detailed overview of the distribution of the power across the individual cell layers of the epidermis is given by

$$A_{\mathrm{ED,K}_p/\mathrm{C}_q}(\omega) = \frac{P_{\mathrm{K}_p/\mathrm{C}_q}(\omega)}{P_{\mathrm{ED}}(\omega)} \tag{6.6}$$

where $P_{\mathrm{K}_p/\mathrm{C}_q}(\omega)$ denotes the power absorbed by these layers. In all of the above parameters, a tilde will be added to refer to the hybrid model rather than the reference model.

### 6.3 Evaluation of the skin models: Revealing biases and assessing epidermal permittivities

In order to interpret and ultimately draw meaningful conclusions from the simulation results presented in the next section, a detailed comparison of the two skin models is required. This comparison aims to reveal biases in the reference model and assess the permittivities of the individual epidermal cell layers, which are considered only in the hybrid model. To provide such a comprehensive analysis, it is necessary to delve into the measurements conducted by Sasaki, as documented in [1]. According to the study, the measurements of individual skin layers were performed 48 hours after slaughter. During transport, the sample was kept at a temperature of 4 °C to slow down biological decay. The actual measurements were carried out at a temperature ranging from 34 °C to 37 °C. The reported thickness of the epidermis was 1.1 mm, while the dermis measured 1.5 mm in thickness. However, further studies on pig skin from different sites, as outlined in [31], indicate significantly lower average epidermal thicknesses ranging from 51.6 µm to 59.9 µm. Considering these findings and the undulating topology of the epidermis/dermis interface (see Fig. 3.1, it is likely that the sectioning of the epidermis in [1] was performed with insufficient accuracy, potentially including parts of the dermis. Therefore, it must be borne in mind when comparing the hybrid model with the reference model that these measurements may contain a certain bias in the measured epidermal material properties that result from this commonly occurring difficulty. Additionally, it should be noted that the measurements of $\underline{\varepsilon}_{\mathrm{r,ED}}$ are limited to frequencies up to 100 GHz, which prevents the analysis of correlations at higher frequencies. Consequently, the evaluation of the correlation will be primarily based on $\underline{\varepsilon}_{\mathrm{r,D}}$, as it closely corresponds to the epidermis in terms of water concentration.

Given these measurement-related challenges, a comparison is performed between the calculated and adopted epidermal permittivities. Fig. 6.4 presents the dispersive permittivities of the epidermis in the hybrid model ($\underline{\tilde{\varepsilon}}_{\mathrm{r,K}_p/\mathrm{C}_q}$), the reference model ($\underline{\varepsilon}_{\mathrm{r,ED}}$), and the dermis ($\underline{\varepsilon}_{\mathrm{r,D}}$). Comparing the real parts of the dispersive permittivities of the individual epidermal cell layers calculated using the bottom-up model ($\tilde{\varepsilon}'_{\mathrm{r,K}_p/\mathrm{C}_q}$) with the measured permittivities of the epidermis ($\varepsilon'_{\mathrm{r,K}_p/\mathrm{C}_q}$) and dermis ($\varepsilon'_{\mathrm{r,D}}$) from [1, 2], a strong correlation is observed, particularly in the viable epidermis as shown in Fig. 6.4(a). Moving attention to the stratum corneum, Fig. 6.4(c) indicates a prominent correlation between the measured material parameters and those of the bottommost cell layer ($C_1$), with the degree of correspondence decreasing towards the skin surface (cell layer $C_{14}$). This observation can be attributed to the water concentration profile within the epidermis, as depicted previously in Fig. 5.4(a), which demonstrates a substantial decrease in water content within the stratum corneum (SC) and consequently leads to a lower permittivity. Considering the work of Ziskin and Alekseev [32, 33], which emphasizes the significance of water content in determining tissue material properties, the histochemical assumptions made in the derivation of $\underline{\tilde{\varepsilon}}_{\mathrm{r,K}_p/\mathrm{C}_q}$ using the bottom-up model of the epidermis can be deemed reliable.

Examining the imaginary parts shown in Figs. 6.4(b) and (d), it becomes evident that extrapolating $\underline{\varepsilon}_{\mathrm{r,ED}}$ beyond 100 GHz by equating it with $\underline{\varepsilon}_{\mathrm{r,ED}}$ at 100 GHz leads to notable deviations from both the effective permittivities predicted by the bottom-up model ($\underline{\tilde{\varepsilon}}''_{\mathrm{r,K}_p/\mathrm{C}_q}$) and the measured permittivities of the dermis ($\underline{\varepsilon}''_{\mathrm{r,D}}$). In contrast, a generally strong correlation is observed between $\underline{\varepsilon}''_{\mathrm{r,D}}$ and $\underline{\tilde{\varepsilon}}''_{\mathrm{r,K}_p/\mathrm{C}_q}$, with significant deviations from $\underline{\varepsilon}''_{\mathrm{r,D}}$ are only observed for the upper cell layers of the SC, which can be explained by the lower water content in those layers.

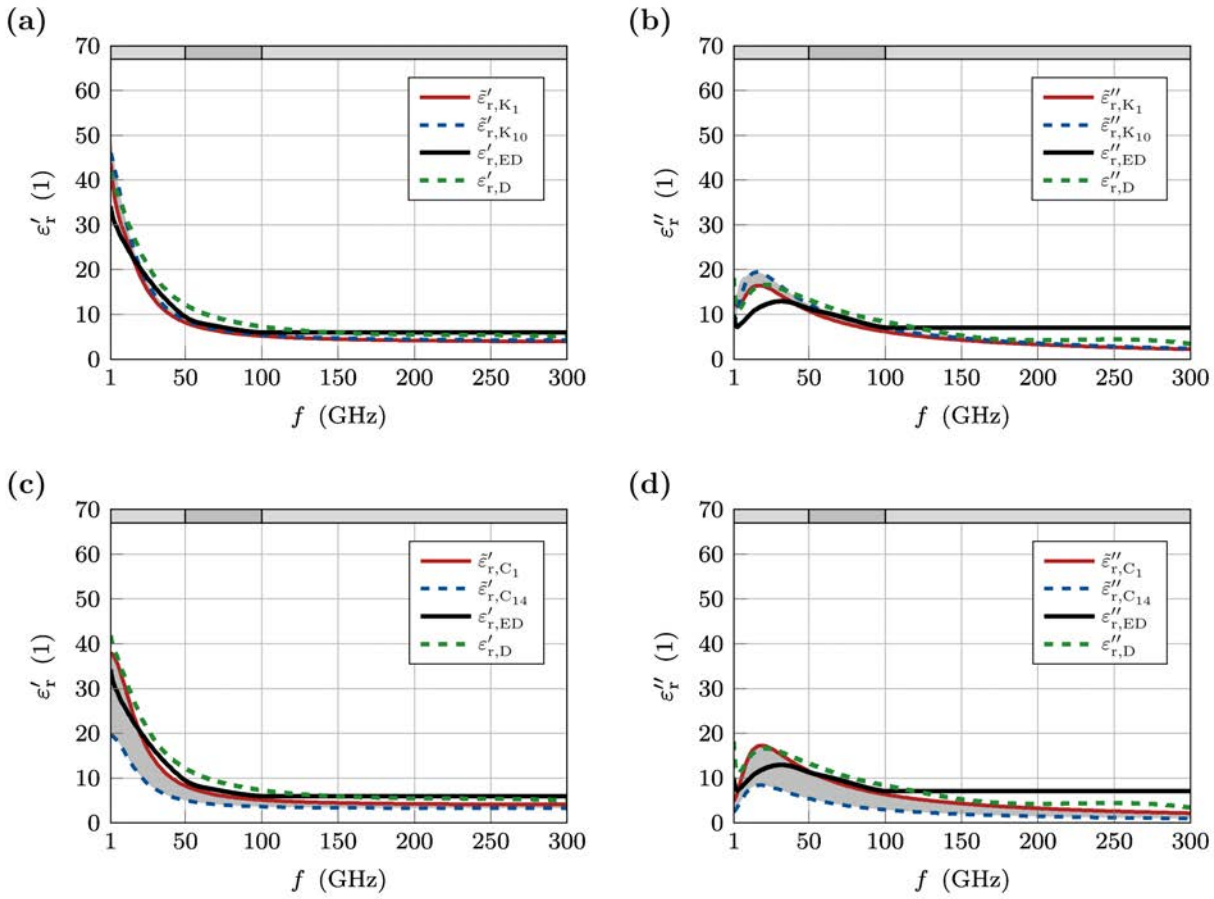


*Fig. 6.4: Comparison of the measured material properties of the epidermis, $\underline{\varepsilon}_{r,ED}$, and the dermis, $\underline{\varepsilon}_{r,D}$, taken from [1, 2] with those of the epidermal cell layers, $\tilde{\underline{\varepsilon}}_{r,ED}$, determined using the bottom-up model. (a) and (b) show the real and imaginary parts of the measured material properties respectively, comparing the data with that for the viable epidermis determined using the bottom-up model (see Section 5). (c) and (d) show the equivalent comparison with the SC.*

In summary, the evaluation of skin models reveals biases in the reference model due to incorrect sectioning of the epidermis and potential inclusion of dermal parts. In addition, the limited availability of measurements for higher frequencies necessitates the use of the dermal permittivity for correlation analysis. As such, deviations arise when extrapolating beyond 100 GHz. However, a strong correlation persists for the dermal permittivity with significant deviations occurring only in the upper layers of the stratum corneum due to varying water concentration. Comparing the calculated epidermal permittivities with those adopted from Sasaki [1, 2], a significant agreement is observed between the real parts of individual epidermal cell layers and measured values, particularly in the viable epidermis. The above assessment demonstrates that the permittivities derived from the bottom-up model can be considered reliable, enabling more precise investigations in the following. The evaluation of the skin models revealed biases in the reference model due to two facts: (1) an incorrect sectioning of the epidermis and likely inclusion of dermal components, and (2) the lack of epidermal measurements, $\underline{\varepsilon}_{r,ED}$, at frequencies higher than 100 GHz.

## 6.4 Results

In the following, the results generated by the macroscopic exposure setup are presented illustrating two aspects: (1) The total power intake of the skin, and (2) the absorption of the individual cell layers of the epidermis.

### 6.4.1 Reflectometric analysis of the skin models

The simulation results of the reflectometric analysis of the reference and hybrid models are displayed in Fig. 6.5. In Fig. 6.5(a), the power of the EM wave to which the skin is exposed, $P_{\mathrm{inc}}$, is shown as a solid black line. In addition, the dashed black and dashed red lines illustrate the power transmitted in the skin tissue of the reference and hybrid model respectively. These are denoted by $P_{\mathrm{T}}$ and $\tilde{P}_{\mathrm{T}}$. Comparing these values, there is a difference between the two skin models starting at about 100 GHz and becoming more significant with increasing frequency. The same result can also be observed in Fig. 6.5(b), where the power reflection and transmission coefficients of the reference model, $R$ and $T$, are plotted alongside those of the hybrid model, $\tilde{R}$ and $\tilde{T}$. Moving on to Fig. 6.5(c), the relative differences in reflection and transmission between the two skin models, defined as $\Delta R = (R - \tilde{R})/R$ and $\Delta R = (T - \tilde{T})/T$, are analyzed in more detail. Regarding the relative deviations between the two models, the frequency interval studied can be divided into three subintervals: ① an interval between 1 GHz and 50 GHz where only moderate deviations are observed, reaching a maximum of about 4.8 % and -4 % at 24 GHz for reflection and transmission respectively; ② an interval between 50 GHz and 100 GHz where negligible deviations can be observed; ③ an interval between 100 GHz and 300 GHz where significant deviations occur with increasing frequency reaching a maximum of about -56.4 % and 24.7 % at 280 GHz for reflection and transmission respectively.

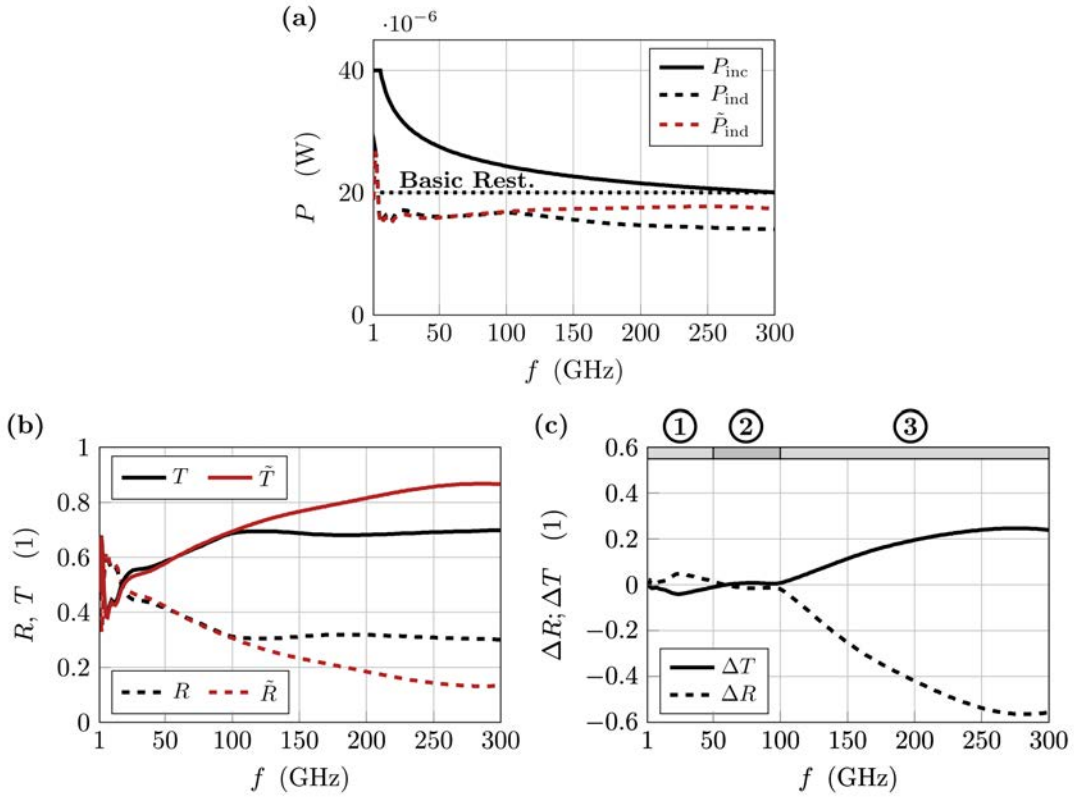


*Fig. 8.5: Overview of the simulation results of the reflectometric analysis of the reference and hybrid models: (a) Incident power, $P_{inc}(\omega)$, derived from $S_{inc}(\omega)$ corresponding to a square skin area of 1 $mm^2$. $P_T(\omega)$ and $\tilde{P}_T(\omega)$ denote the power absorbed by the reference model and the hybrid model respectively. The constant labeled "Basic Rest." corresponds to the absorbed power density, $S_{ab}(\omega)$, defined in [3] as a basic restriction (see Tab. 1.1). (b) Spectral analysis of the power reflection and the power transmission coefficients. $R(\omega)$ and $T(\omega)$ correspond to the reference model and $\tilde{R}(\omega)$ and $\tilde{T}(\omega)$ correspond to the hybrid model. (c) Relative deviation of $R(\omega)$ and $T(\omega)$ between the two skin models.*

Moving on to the dosimetric analysis of the epidermis in the next section, the power transfer to deeper sublayers of the skin and the power distribution across the epidermal cell layers are analyzed in the context of these subintervals.

### 6.4.2 Dosimetric analysis of the epidermis

The results of the power absorbed by the epidermis, $P_{\mathrm{ED}}(\omega)$, relative to the power transmitted in the skin, $P_{\mathrm{T}}(\omega)$, are shown in Fig. 6.6.

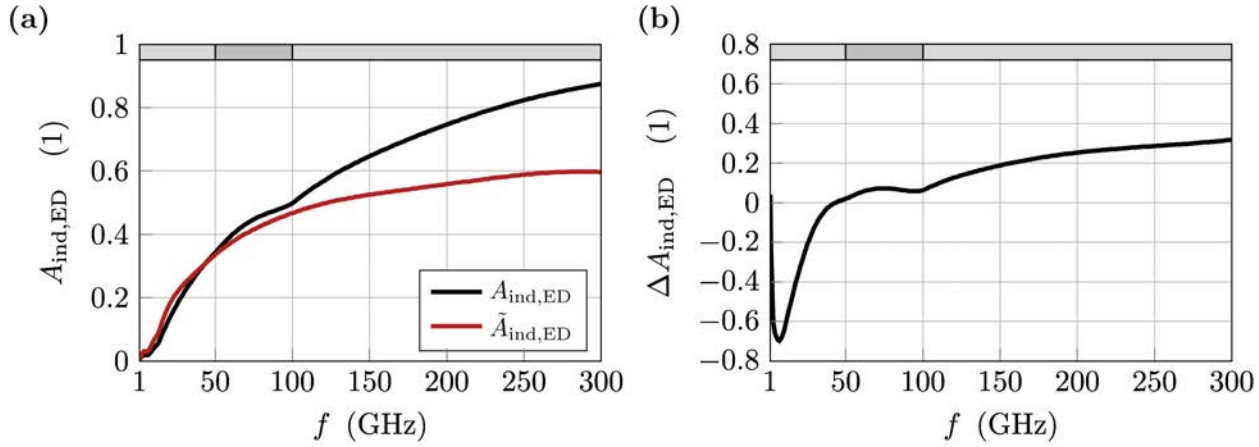


*Fig. 6.6: Overview of the power absorbed by the epidermis (ED), $P_{ED}(\omega)$, relative to the power transmitted to the skin tissue, $P_T$: (a) Spectral analysis of the absorption coefficients according to Eq. 6.4, where that of the reference model, $A_{ind,ED}$, is shown as a solid black line and that of the hybrid model, $\tilde{A}_{ind,ED}$, is shown as a solid red line. (b) Relative deviation between the two skin models.*

In Fig. 6.6(a), solid black and red lines illustrate the absorption coefficients of the epidermis as defined in Eq. 6.4 for the reference and hybrid model respectively. These are denoted by $A_{\mathrm{ind,ED}}$ and $\tilde{A}_{\mathrm{ind,ED}}$. Comparison of the two graphs shows that absorption within the epidermis at 1 GHz is only 0.5 % of the power transmitted to the skin tissue, but increases rapidly with increasing frequency, reaching 35 % at the upper end of interval ①, at 50 GHz. This trend continues at frequencies higher than 50 GHz, although the increase in absorption, especially in the hybrid model, is significantly lower, reaching about 60 % at 300 GHz. The absorption in the reference model increases to 87 % at 300 GHz and shows a discontinuity at 100 GHz, which is due to the decision to keep $\underline{\varepsilon}_{\mathrm{r,ED}}$ fixed at all for frequencies higher than 100 GHz. Moving on to Fig. 6.6(b), the relative differences in epidermal absorption between the two skin models, $\Delta A_{\mathrm{ind,ED}}$, are displayed in more detail. It can be seen that the relative deviation is -65 % in interval ① increasing a moderate 8 % to 32 % in interval ② before increasing gradually after the discontinuity to a final value of 32 % in interval ③.

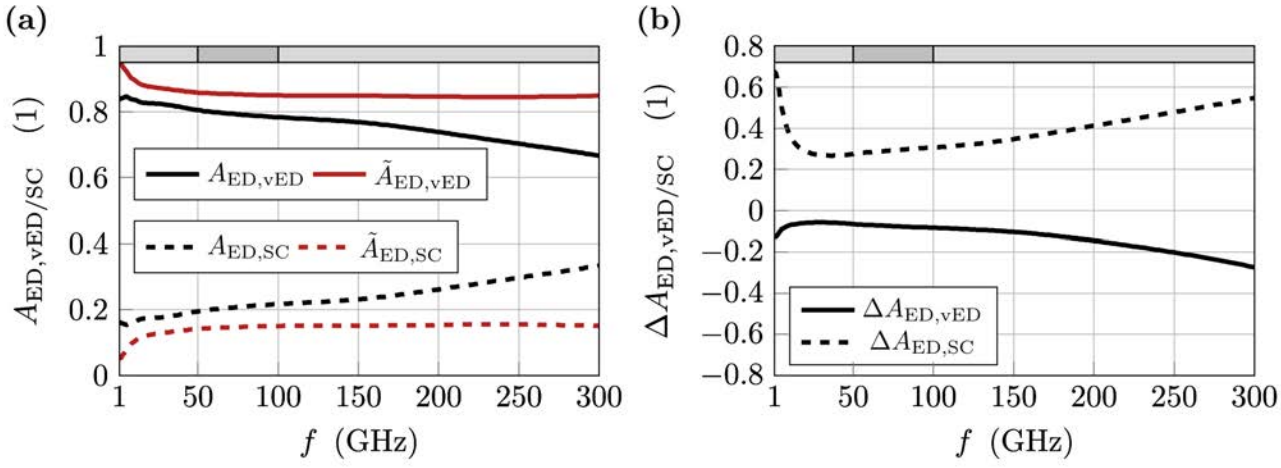


*Fig. 6.7: Analysis of the power distribution across the epidermis in accordance with Eq. 6.5: (a) Power absorbed by the epidermis in the reference and hybrid models, denoted by $A_{ED,vED/SC}$ and $\tilde{A}_{ED,vED/SC}$ respectively. (b) Relative deviation of $\Delta A_{ED,vED/SC}$ between the two skin models.*

Having analyzed the power absorbed by the epidermis, its distribution within this skin layer is now examined. Following Eq. 6.5 above, the results of the power absorbed by the viable epidermis (vED) and the SC, $P_{\mathrm{vED}}$ and $P_{\mathrm{SC}}$, are shown in Fig. 6.7 relative to the total power absorbed by the epidermis, $P_{\mathrm{ED}}$. In Fig. 6.7(a), the solid black and red lines illustrate the fraction of power absorbed by the viable epidermis, $A_{\mathrm{ED,vED}}$ and $\tilde{A}_{\mathrm{ED,vED}}$, and the dashed black and red lines illustrate the fraction of power absorbed by the SC, $A_{\mathrm{ED,SC}}$ and $\tilde{A}_{\mathrm{ED,SC}}$. In addition, the corresponding relative deviations between the two skin models, $\Delta A_{\mathrm{ED,vED}}$ and $\Delta A_{\mathrm{ED},SC}$, are shown in Fig. 6.7(b). It can be seen that the reference model predicts a significantly higher absorption within the SC and thus shows lower absorption within the viable epidermis.

Following these results, which only distinguishes between the larger-scale structures of the epidermis, a detailed analysis of the power distribution within the individual cell layers of the viable epidermis, $\mathrm{K}_p$, is now performed, the results of which are shown in Fig. 6.8. Following Eq. 6.6, the power absorbed by these cell layers, $P_{\mathrm{K}_p}$, relative to the total power absorbed by the epidermis, $P_{\mathrm{ED}}$, is shown in Figs. 6.8(a) and (b) for the reference and hybrid model respectively. The graphs corresponding to each of the examined cell layers are represented by solid, dashed, dotted, and dash-dotted lines. They are colored in magenta ($K_1$ through $K_4$), green ($K_5$ through $K_8$), and blue ($K_9$ and $\mathrm{K}_{10}$), as indicated in the legend. The relative deviation between the two models, $\Delta A_{\mathrm{ED,K}_p}$, are displayed in Fig. 6.8(c). Focusing on the proliferative pool of the epidermis only, it being of particular interest in this report, $\Delta A_{\mathrm{ED,K}_1}$ and $\Delta A_{\mathrm{ED,K}_2}$ show deviations ranging between -29 % at the beginning of interval ① and -49 % at the end of interval ③. In addition, an overview of the power distribution across the SC is provided in Appendix C for completeness.

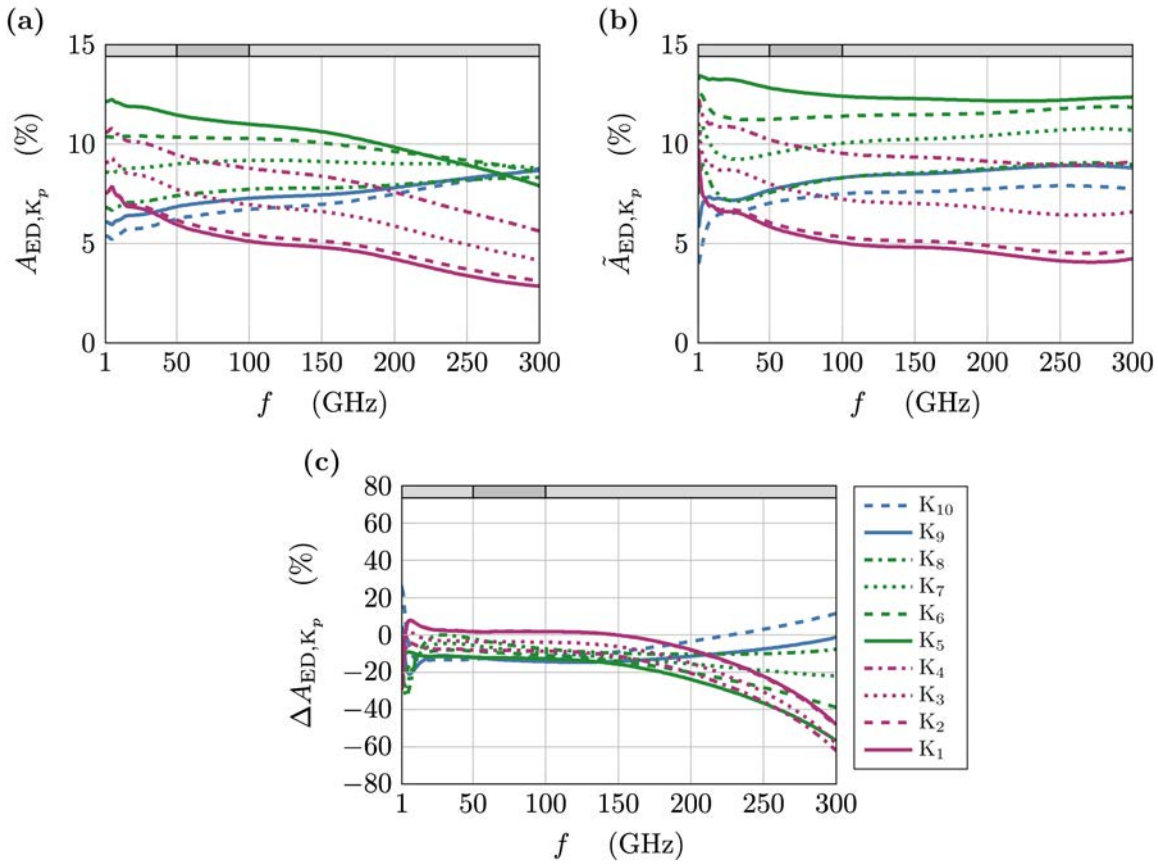


*Fig. 6.8: Analysis of the power distribution over the epidermal cell layers, $K_p$, according to Eq. 6.6: (a)-(b) Power absorbed by the epidermal cell layers, $K_p$, in the reference and hybrid models, denoted by $A_{ED,K_p}$ and $\tilde{A}_{ED,K_p}$, respectively. (c) Relative deviation of $\Delta A_{ED,K_p}$ between the two skin models, $\Delta A_{ED,K_p}$. The plots corresponding to each of the investigated cell layers are represented by solid, dashed, dotted and dash-dotted lines. They are colored in magenta ($K_1$ through $K_4$), green ($K_5$ through $K_8$), and blue ($K_9$ and $K_{10}$) as indicated in the legend.*

## 6.5 Discussion

The comparison of the reflection and transmission properties of the two skin models in Section 6.4 shows significant differences at frequencies above 100 GHz. The power transmission coefficient calculated for the hybrid model is up to 24 % higher than that calculated for the reference model. This indicates a strong underestimation of the energy absorption of skin tissues using the reference model. With reference to the evaluation of the skin models performed in Section 6.3, it can be assumed that the imaginary part of the permittivity of the epidermis is significantly smaller than the extrapolated value used in the reference model. The extrapolation of the measured epidermal permittivity, $\underline{\varepsilon}_{\mathrm{r,ED}}(f > 100\ \mathrm{GHz}) = \underline{\varepsilon}_{\mathrm{r,ED}}(f = 100\ \mathrm{GHz})$, was performed to compensate for the missing data above the delimiting frequency. Consequently, the model based on [1] seems to be require careful consideration in dosimetric studies of the skin above 100 GHz because of this strong underestimation of the power transmitted to the tissue.

Another observation in the investigations performed in this study was the distribution of the power intake throughout the skin tissue. As shown in Fig. 6.6 (see Section 6.4.2), the epidermis initially absorbs only a small fraction of the power transmitted to the tissue between 1 GHz and 50 GHz (about 3 %), but dynamically increases to 38 % in both models. The close agreement continues for frequencies between 50 GHz and 100 GHz, with a more saturated increase in absorption. For frequencies above 100 GHz, however, the larger imaginary part of the epidermal permittivity of the reference model leads to strong deviations and an overestimation of the absorbed power by up to 35 %. This strong overestimation of the power absorbed in the epidermis naturally leads to a strong underestimation of the power absorbed in the dermis. Moving away from the simplified stratified representation of the skin chosen for exposure studies and interpreting this fact in the context of an anatomically correct representation of the skin, a higher induced power in the dermis would be expected to result in a higher temperature rise in this sublayer and thus a direct effect on the thermoreceptors located there. Targeted power induction in the tissue in which these receptors are embedded could, given a sufficient level and duration of exposure, result in a physiological response of the organism to the stress of the exposure and trigger thermoregulatory mechanisms, such as increased blood flow to the skin and activation of sweat glands.

An important objective of these studies is also to provide dosimetric information on the power input to the basal and subbasal cell layers of the epidermis (i.e., $K_1$ and $K_2$) necessary for skin renewal. Information on the power distribution within the epidermis can be obtained from Figs. 6.7 and 6.8. Here, Fig. 6.7 shows that absorption by the dead cells of the SC is significantly overestimated by the reference model and thus, the absorption within the viable epidermis is significantly underestimated. This overestimation of the power input at the body surface greatly biases the predictions of temperature evolution within the skin, as this power is much more easily dissipated to the environment by convection and evaporation due to transpiration. A more detailed analysis of the power distribution within the cell layers $K_1$ through $K_{10}$ in Fig. 6.8 shows that the absorption within the proliferative pool of the epidermis is underestimated by the reference model by up to 50 %. The use of the reference model for frequencies above 100 GHz thus leads to biased interpretations, especially at these cell locations.

## 6.6 Summary and conclusion

■ In this study, extensive dosimetric investigations were conducted to assess the transmission and distribution of EM fields in the skin, taking into account physiological variations across the epidermis. The investigations compared a reference model, based on measured material properties reported in [1] and [2], with a hybrid model that combined the purely numerical tissue model of the epidermis and the existing measured models of the other skin layers. Embedding the two skin models in a FEM-based simulation environment, a macroscopic exposure setup was established to simulate skin irradiation at frequencies between 1 GHz and 300 GHz. The macroscopic exposure setup allowed for the determination of local EM fields induced in the skin layers and thus enabled a comparative assessment of the two skin models considering both reflectometric and dosimetric aspects.

■ The evaluation of these skin models revealed biases in the reference model due to two factors: (1) an incorrect sectioning of the epidermis and likely inclusion of dermal components, and (2) the lack of epidermal measurements, $\underline{\varepsilon}_{\mathrm{r,ED}}$, at frequencies higher than 100 GHz. These biases necessitated the inclusion of the dermal permittivity, $\underline{\varepsilon}_{\mathrm{r,D}}$ which allowed the verification of the numerically determined permittivities of the individual epidermal cell layers, $\underline{\tilde{\varepsilon}}_{\mathrm{r,K}_p/\mathrm{C}_q}$. The verification performed on $\underline{\varepsilon}_{\mathrm{r,ED}}$, $\underline{\varepsilon}_{\mathrm{r,D}}$, and $\underline{\tilde{\varepsilon}}_{\mathrm{r,K}_p/\mathrm{C}_q}$ showed a strong correlation between all of these permittivities for frequencies up to 100 GHz. However, when extrapolating beyond 100 GHz, deviations occurred, especially between $\underline{\varepsilon}''_{\mathrm{r,ED}}$ and the imaginary parts of the other permittivities, indicating a significant overestimation of this value in the reference model, calculated using dispersive complex material properties, $\underline{\tilde{\varepsilon}}_{\mathrm{r,K}_p/\mathrm{C}_q}$, as outlined in Section 5. Nevertheless, the dermal permittivity showed a substantial correlation, except for notable deviations found exclusively in the upper layers of the stratum corneum, which could be attributed to a reduction in water concentration. These results demonstrated the reliability of permittivities derived from the bottom-up model and its histochemical assumptions.

■ The significant overestimation of $\underline{\varepsilon}''_{\mathrm{r,ED}}$ in the reference model had major consequences for both the power tranmitted to the skin and the distribution of that power across its sublayers. One of these consequences was revealed by the reflectometric analysis performed in Section 6.4. There, significant differences in reflection and transmission properties were shown for frequencies above 100 GHz, with the transmitted power being underestimated by the reference model by up to 24 %. Consequently, the reference model must be carefully reevaluated for dosimetric studies above 100 GHz, as subtle changes in the material properties of the epidermis can have a major effect on the total transmission of EM energy to the skin. This has implications for the current ICNIRP restrictions [3] as the dosimetric assessment conducted in [1], leading to the reference model, was used to derive an absorbed power density of 200 $\mathrm{W/m^2}$ which was set as an operational adverse health effect threshold (see Section 1). However, based on the reduction factor of 2 to 10 established for occupational and general exposure, respectively, no direct risks or potential adverse health effects can be inferred from the underestimated results given above.

■ In addition, the evaluation of the power absorbed by the epidermis in Section 6.4.2 showed that the larger imaginary part of the epidermal permittivity in the reference model yields an overestimation of the absorbed power by up to 35 % at frequencies above 100 GHz, resulting in a strong underestimation of the power absorption in deeper skin layers. When considering a more anatomically accurate representation of the skin, the induced power in the dermis would be expected to cause a more pronounced temperature increase within this layer. This, in turn, would have a direct effect on the thermoreceptors located there. Consequently, if the tissue surrounding these receptors were exposed to a targeted power induction of sufficient intensity and duration, it would have the potential to trigger physiological responses in the organism. These responses might include increased blood flow to the skin and activation of sweat glands as a direct result of the exposure-induced stress.

■ In addition to the results recapitulated in the previous paragraph, the analysis of energy distribution in the epidermis underlines the importance of accurately representing physiological variations within this skin layer by using individual permittivities for each cell layer. The analysis, which divided the epidermis into the stratum corneum (SC) and the viable epidermis (see Fig. 6.7), revealed that the reference model significantly overestimated absorption by the dead cells of the stratum corneum, leading to a substantial underestimation of absorption within the living cells of the viable epidermis. This overestimation of power at the surface of the skin could introduce a significant bias in predicting the temperature evolution within the skin, as this power easily dissipates to the environment through convection and evaporation. Furthermore, the comprehensive analysis of power distribution across the individual cell layers, from $K_1$ to $K_{10}$ (as depicted in Fig. 6.8), revealed discrepancies in the estimation of absorption within the viable epidermis using the reference model. These discrepancies ranged from an overestimation of 20 % to an underestimation of 60 % depending on the specific location within the viable epidermis and the frequency. Notably, regarding the basal and sub-basal cell layers of the epidermis (i.e., $K_1$ and $K_2$), which are crucial for skin renewal, the reference model underestimates the absorption in this layer by up to 50 % at 300 GHz. Importantly, this observation applies not only to frequencies above 100 GHz but also to frequencies below this threshold.

Consequently, using the reference model leads to biased interpretations, particularly at these specific cell locations at frequencies above 100 GHz.

■ In conclusion, the reference model is clearly suitable for frequencies up to 100 GHz, but the extrapolation of the measured material parameters for frequencies above 100 GHz leads to a significant overestimation of the reflection of EM waves at the skin surface. This leads to an underestimation of the power transmitted to the skin tissue compared to the hybrid model. Comparing the results of the current study with those presented in [34], in which the SC was identified as an impedance matching layer, it appears that not only the thickness of the individual cell layers, but also the water concentration profile across the epidermis can lead to such an effect. Furthermore, the layer-by-layer representation of the epidermis in the hybrid model allows a detailed assessment of the power distribution within the epidermis. This shows the strong influence of the different permittivities within the individual cell layers corresponding to the water concentration profile profile and the metabolization of keratin. Thus, the hybrid model demonstrates that numerically derived material representations of tissue layers, which inhibit strong physiological variations, complement purely measurement-based skin models and allow for the targeted investigation of physiological structures that have been identified as important (such as the proliferative pool).

# 7 Scale-back projection

In the previous chapter, a comparison between the hybrid skin model and the reference model based on the work of Sasaki et al. [1] showed that physiological variations in the epidermis significantly affect the absorption properties of the skin. In this chapter, the consistent representation of the epidermis by the bottom-up model, encompassing both the macroscopic and microscopic scales, is used to develop a top-down multiscale approach, referred to as scale-back projection. This approach allows the projection of the macroscopically determined EM field distribution within the epidermis onto the microstructure of the underlying epidermal cell models.

It is shown that scale-back projection provides a solid foundation for the determination of a measure that will be referred to as the statistical *micro-SAR*. This measure is derived from a statistical analysis of field variations due to the microstructure of epidermal cells, and represents a means to quantify EM absorption and its location in a realistic manner. This allows the investigation of three key aspects:

(1) The quantification of field variations resulting from the morphology and histological composition of the fully resolved epidermal cell structures using statistical analysis (arithmetical mean, standard deviation).

(2) The investigation of differences between the conventional *SAR*, as specified by ICNIRP, and the statistical *micro-SAR* proposed here at the microscopic scale.

(3) The introduction of parameters to quantify methodological consistency in the projection of field values at both the macroscopic and microscopic scales.

By considering currently accepted reference levels for exposure at the macroscopic scale, this study allows the assessment of the above aspects within the context of the ICNIRP guidelines, in two frequency intervals: $F_1$ (ranging from 1 GHz to 6 GHz) and $F_2$ (ranging from 24 GHz to 52 GHz) which are either currently in use or being considered for use in 5G telecommunication standards. Based on this, it is discussed whether and how scale-back projection can be integrated as a microdosimetric investigation tool into the repertoire of conventional multiphysics simulations.

Section 7.1 provides a comprehensive introduction to the implementation of the scale-back projection within the computational simulation environment, detailing the methods and measures used in the analysis. This is followed by Section 7.2, which provides a detailed examination of the key aspects outlined above. This includes a comparison of the statistical micro-*SAR* with the currently accepted *SAR* limits for local limb exposure as defined by ICNIRP. Finally, the main findings are summarized and discussed in Section 7.3.

## 7.1 Methodology

The methodology section of this chapter is structured into three parts. The first part provides a detailed explanation of the implementation of the scale-back projection, emphasizing the connection between the macroscopic and microscopic scales. In the second part, a thorough outline of the microdosimetric assessment conducted using the scale-back projection is presented, introducing the relevant measures involved. Lastly, an analytical approach is introduced to investigate the methodological consistency of the scale-back projection and propose measures to evaluate the quality of the linkage between the two hierarchical scales.

### 7.1.1 Implementation of the scale-back projection

The methodology of the scale-back projection is illustrated in Fig. 7.1, and can be described as a two-fold procedure linking the representation of epidermal tissues at two hierarchical levels: (1) on a macroscopic scale, and (2) on a microscopic scale. On a macroscopic scale, the spatial distribution of EM fields across the individual sublayers of the skin is determined using the macroscopic exposure setup introduced in Section 6 as illustrated in Fig. 7.1(a). Efficient numerical calculation is facilitated by the homogenized tissue representation of these layers using the hybrid skin model. The input power, $P_{\mathrm{ind,K}_p/\mathrm{C}_q}(\omega)$, corresponds to the incident power density, $S_{\mathrm{inc}}(\omega)$, defined in the reference levels (see Tab. 1.2). The EM wave is propagating along the z-direction, perpendicular to

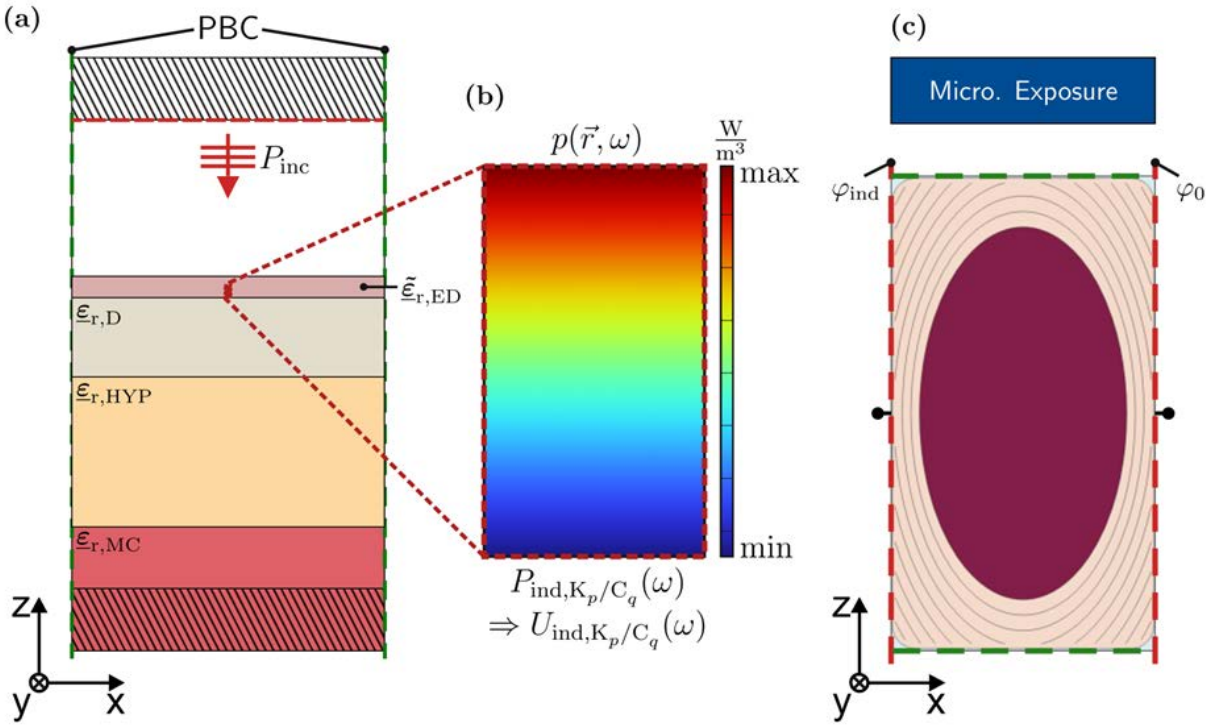


*Fig. 7.1: Conceptual overview of the scale-back projection: (a) Macroscopic exposure setup to determine EM fields induced in the hybrid skin model as introduced in Section 6. This setup allows the determination of the levels of exposure in each cell layer of the epidermis ($K_p$ and $C_q$). Considering only a single microvolume within each individual cell layer that corresponds to the specific size of the computational domain of its underlying parametric cell model, it is possible to determine the power induced in any of these microvolumes, $P_{ind,K_p/C_q}(\omega)$, as illustrated in (b). The induced power is then used to derive a voltage, $U_{ind,K_p/C_q}(\omega)$, which leads to an equivalent level of exposure on the microscopic scale (as outlined in Eq. 7.3). The corresponding potential difference, $\varphi_{ind,K_p/C_q}(\omega)$, is then applied across the microscopic exposure setup shown in (c).*

the skin surface, and polarized in the x-direction. By subdividing the epidermis into separate computational subdomains, it is possible to determine the induced volumetric loss densities, $p(\vec{r},\omega)$, within microvolumes corresponding to the specific size and location of individual epidermal cells (i.e., $K_p$ and $C_q$), as described in Chap. 5. The integration of $p(\vec{r},\omega)$ over these microvolumes yields the power induced in a single cell, denoted as $P_{\mathrm{ind,K_p/C_q}}(\omega)$, as illustrated in Fig. 7.1(b).

At the microscopic scale, the epidermal cells are represented using the parametric cell models introduced in Section 5. These models are then incorporated into the virtual capacitor setup, outlined in Appendix A for quasi-static EM analysis of eukaryotic cells. This setup is referred to as the microscopic exposure setup in the following. The linkage between the macroscopic and microscopic exposure setups is achieved by converting $P_{\mathrm{ind,K_p/C_q}}(\omega)$ into a voltage, $U_{\mathrm{ind,K_p/C_q}}(\omega)$, representing an equivalent level of expousure on the microscopic scale. The voltage $U_{\mathrm{ind,K_p/C_q}}(\omega)$ is derived using the equivalent circuit representation of the virtual capacitor experiment, originally used to determine macroscopic material properties of individual epidermal cell layers (see Appendix B, Fig. B.1) and is calculated as follows:

$$P_{\mathrm{ind,K_pC_q}}(\omega) = \tilde{G}_{\mathrm{K_p/C_q}}(\omega) \cdot U_{\mathrm{ind,K_p/C_q}}(\omega) \tag{7.1}$$

where $\tilde{G}_{\mathrm{K_p/C_q}}(\omega)$ represents the effective macroscopic conductance of the parametric cell models corresponding to the individual epidermal cell layers. By replacing $\tilde{G}_{\mathrm{K_p/C_q}}(\omega)$ in Eq. 9.1 with the expression

$$\tilde{G}_{\mathrm{K}_p/\mathrm{C}_q}(\omega) = \frac{\tilde{\sigma}_{\mathrm{K}_p\mathrm{C}_q}(\omega)\cdot A_{\mathrm{YZ},\mathrm{K}_p/\mathrm{C}_q}}{l_{\mathrm{x},\mathrm{K}_p/\mathrm{C}_q}} \tag{7.2}$$

the voltage $\mathrm{U}_{\mathrm{ind},\mathrm{K}_p/\mathrm{C}_q}(\omega)$ can be determined as follows:

$$U_{\mathrm{ind},\mathrm{K}_p/\mathrm{C}_q}(\omega) = \sqrt{\frac{P_{\mathrm{ind},\mathrm{K}_p/\mathrm{C}_q}(\omega)\cdot l_{\mathrm{UC,x},\mathrm{K}_p/\mathrm{C}_q}}{\tilde{\sigma}_{\mathrm{K}_p/\mathrm{C}_q}(\omega)\cdot A_{\mathrm{YZ},\mathrm{K}_p/\mathrm{C}_q}}} \tag{7.3}$$

where $A_{\mathrm{YZ},\mathrm{K}_p/\mathrm{C}_q} = l_{\mathrm{UC,y},\mathrm{K}_p/\mathrm{C}_q} \cdot l_{\mathrm{UC,z},\mathrm{K}_p/\mathrm{C}_q}$ denotes the cross-sectional area of the microvolume in the YZ plane and $\tilde{\sigma}_{\mathrm{K}_p/\mathrm{C}_q}(\omega) = \omega\varepsilon_0\varepsilon''_{\mathrm{r},\mathrm{K}_p/\mathrm{C}_q}(\omega)$ denotes the conductivity of any given homogenized epidermal cell layer. $U_{\mathrm{ind},\mathrm{K}_p/\mathrm{C}_q}(\omega)$ is now applicable to a microscopic exposure setup by applying the corresponding potential difference, $\varphi_{\mathrm{ind},\mathrm{K}_p/\mathrm{C}_q}(\omega)$, to the Dirichlet boundary conditions considered in the quasi-static unit cell approach presented in Appendix A. The application of $U_{\mathrm{ind},\mathrm{K}_p/\mathrm{C}_q}(\omega)$ in the x-direction is consistent with the polarization of the EM wave exposure at the macroscopic scale, as shown in Fig. 7.1(c).

### 7.1.2 Microdosimetric assessment

The scale-back projection allows microdosimetric *SAR* assessments at both microscopic and macroscopic scales. At the macroscopic scale, it considers the homogeneous material representation of individual epidermal cell layers, while at the microscopic scale, it considers the fully resolved cell structure of individual epidermal cell models. *SAR* values at both scales can be determined using either the ICNIRP calculation rule (see Eq. 4.2), which relates the induced power within a microvolume to the mass contained in that volume, or by statistical analysis of field changes. At the macroscopic scale, the specific absorption rate, denoted as $SAR_{\mathrm{ma},\mathrm{K}_p/\mathrm{C}_q}$, is calculated using the conventional definition (see Section 1):

$$SAR_{\mathrm{ma},\mathrm{K}_p/\mathrm{C}_q} = \frac{\iiint_{V_{\mathrm{UC}}} p(\vec{r},\omega)\mathrm{d}V}{\iiint_{V_{\mathrm{UC}}} \rho_{\mathrm{K}_p/\mathrm{C}_q}\mathrm{d}V} = \frac{P_{\mathrm{ind},\mathrm{K}_p/\mathrm{C}_q}(\omega)}{m_{\mathrm{K}_p/\mathrm{C}_q}} \tag{7.4}$$

where $p(\vec{r},\omega)$ and $\rho_{\mathrm{K}_p/\mathrm{C}_q}$ represent the volumetric loss densities induced in the individual microvolumes across the epidermal cell layers (see Fig. 7.1) and the volumetric mass densities of the homogeneous cell layers (see Fig. 5.11) respectively. The independent layer-wise values, $P_{\mathrm{ind},\mathrm{K}_p/\mathrm{C}_q}(\omega)$ and $m_{\mathrm{K}_p/\mathrm{C}_q}$, denote the corresponding induced losses and masses determined via integration over each microvolume, $V_{\mathrm{UC},\mathrm{K}_p/\mathrm{C}_q}$, for each cell layer. In contrast to this conventional assessment of the *SAR*, it is possible to perform a statistical analysis over these microvolumes that allows the quantification of field variations within the microvolume due to the attenuation of the penetrating wave. The results of this analysis are represented by the arithmetic mean value, denoted as $\mu_{\mathrm{SAR,ma},\mathrm{K}_p/\mathrm{C}_q}$, which is calculated as:

$$\mu_{\mathrm{SAR,ma},\mathrm{K}_p/\mathrm{C}_q} = \frac{1}{V_{\mathrm{UC},\mathrm{K}_p/\mathrm{C}_q}} \iiint_{V_{\mathrm{UC}}} \frac{p(\vec{r},\omega)}{\rho_{\mathrm{K}_p/\mathrm{C}_q}}\,\mathrm{d}\,V, \tag{7.5}$$

and the standard variation, denoted as $s_{\mathrm{SAR,ma},\mathrm{K}_p/\mathrm{C}_q}$, calculated by

$$s_{\mathrm{SAR,ma},\mathrm{K}_p/\mathrm{C}_q} = \sqrt{\frac{1}{V_{\mathrm{UC},\mathrm{K}_p/\mathrm{C}_q}} \iiint_{V_{\mathrm{UC}}} \left(\frac{p(\vec{r},\omega)}{\rho_{\mathrm{K}_p/\mathrm{C}_q}} - \mu_{\mathrm{SAR,ma},\mathrm{K}_p/\mathrm{C}_q}\right)\mathrm{d}\,V} \tag{7.6}$$

In this equation, the symbol $s$ has been chosen to represent the standard deviation instead of the commonly used $\sigma$ to avoid potential ambiguities with conductivity. Note that $\mu_{\mathrm{SAR,ma},\mathrm{K}_p/\mathrm{C}_q} = SAR_{\mathrm{ma},\mathrm{K}_p/\mathrm{C}_q}$.

At the microscopic scale, at which the individual epidermal cell layers are represented using their corresponding parametric cell models, it is also possible to determine a *SAR* that is calculated using the conventional definition:

$$SAR_{\mathrm{mi,K}_p/\mathrm{C}_q} = \frac{\iiint_{V_{\mathrm{UC}}} p(\vec{r},\omega)\mathrm{d}V}{\iiint_{V_{\mathrm{UC}}} \rho_{\mathrm{K}_p/\mathrm{C}_q}(\vec{r})\mathrm{d}V} = \frac{P_{\mathrm{ind,K}_p/\mathrm{C}_q}(\omega)}{m_{\mathrm{K}_p/\mathrm{C}_q}} \tag{7.7}$$

Here, it is important to note that even though $p(\vec{r},\omega)$ and $\rho_{\mathrm{K}_p/\mathrm{C}_q}(\vec{r})$ differ significantly from their corresponding values on the macroscopic scale, $P_{\mathrm{ind,K}_p/\mathrm{C}_q}(\omega)$ and $m_{\mathrm{K}_p/\mathrm{C}_q}$ remain equal to their corresponding values, resulting in the fact that $SAR_{\mathrm{mi,K}_p/\mathrm{C}_q} = SAR_{\mathrm{ma,K}_p/\mathrm{C}_q}$. Consequently, the conventional representation of *SAR* at the microscopic scale does not offer any additional insights. However, it is now possible to use the results of a similar statistical analysis to define a new measure which demonstrates differences between the two scales, and thus the influences of cell morphology (size, shape, internal organization) and histochemical composition on field variations within the microstructure. This measure quantifies both the absorption and its location within the cell, leading to the redefinition of $SAR_{\mathrm{mi,K}_p/\mathrm{C}_q}$ (from Eq. 9.7) as a statistical *micro-SAR*:

$$SAR_{\mathrm{mi,K}_p/\mathrm{C}_q} = \mu_{\mathrm{SAR,mi,K}_p/\mathrm{C}_q} \pm s_{\mathrm{SAR,mi,K}_p/\mathrm{C}_q} \tag{7.8}$$

where the determination of the microscopic arithmetic mean value, $\mu_{\mathrm{SAR,mi,K}_p/\mathrm{C}_q}$, can be determined by

$$\mu_{\mathrm{SAR,mi,K}_p/\mathrm{C}_q} = \iiint_{V_{\mathrm{UC}}} \frac{p(\vec{r},\omega)}{\rho_{\mathrm{K}_p/\mathrm{C}_q}(\vec{r})}\mathrm{d}V \tag{7.9}$$

Due to the implementation of membranes as boundary conditions in the parametric models of individual epidermal cells, as defined in Eq. A.3 and A.8 in Appendix A, the volumetric loss density, $p(\vec{r},\omega)$, is not defined within these cell structures and is thus not directly accessible for volume integration in the COMSOL software environment. To overcome this limitation, Eq. 7.9 needs to be rearranged to account for the individual cell structures:

$$\mu_{\mathrm{SAR,mi,K}_p/\mathrm{C}_q} = \frac{1}{V_{\mathrm{UC,K}_p/\mathrm{C}_q}} \sum_i \iiint_{V_{\mathrm{UC}}} \frac{p(\vec{r},\omega)}{\rho_{\mathrm{K}_p/\mathrm{C}_q}(\vec{r})}\mathrm{d}V \tag{7.10}$$

$$= \frac{1}{V_{\mathrm{UC,K}_p/\mathrm{C}_q}} \sum_i \frac{1}{\rho_i} \iiint_{V_{UC}} p(\vec{r},\omega)\,dV \tag{7.11}$$

$$\mu_{\mathrm{SAR,mi,K}_p/\mathrm{C}_q} = \frac{1}{V_{\mathrm{UC,K}_p/\mathrm{C}_q}} \sum_i \frac{P_i}{\rho_i} \tag{7.12}$$

In the above equations, the index $i$ represents the different cell structures, namely the extracellular medium (EC), the cytoplasm (CP), the nucleoplasm (NP), and the membranes (M). The variables $P_i$ and $\rho_i$ correspond to the power induced and the volumetric mass density assigned to each respective cell structure. By employing the concept of spatial segmentation as described in [A6], it becomes possible to determine the power contributions $P_{\mathrm{EC}}$, $P_{\mathrm{CP}}$, and $P_{\mathrm{NP}}$ through volume integration within the epidermal cell models. The associated membrane power contribution, denoted by $P_{\mathrm{M}}$, can also be obtained by subtracting the sum of $P_{\mathrm{EC}}$, $P_{\mathrm{CP}}$, and $P_{\mathrm{NP}}$ from $P_{\mathrm{tot}}$, where $P_{\mathrm{tot}}$ is the total induced power determined between the terminals (i.e. the electrodes) of the computational domain. In addition, the determination of $P_{\mathrm{tot}}$ in the microscopic exposure setup serves as a means to assess the consistency between the macroscopic and microscopic scales. This is evaluated by comparing the induced power $P_{\mathrm{Cell}}$ (macroscopic) and $P_{\mathrm{tot}}$ (microscopic), where the required condition $P_{\mathrm{Cell}} = P_{\mathrm{tot}}$ is checked and found to be satisfied.

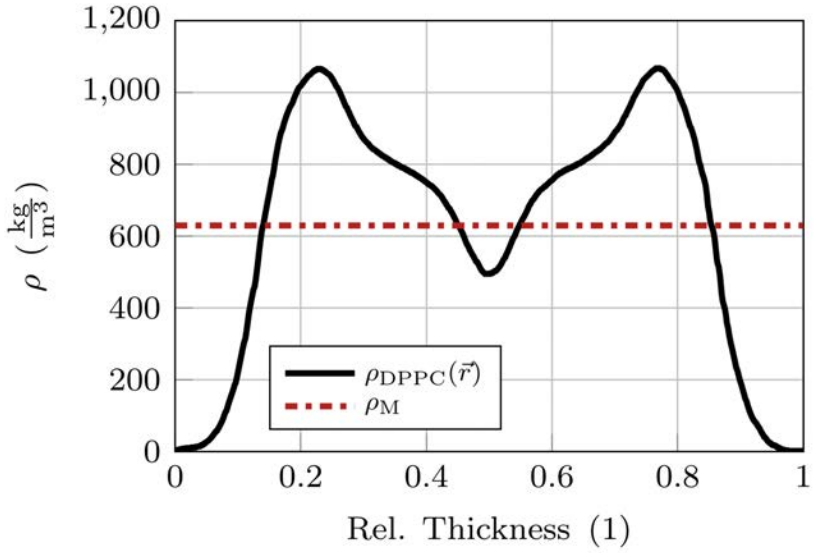


*Fig. 7.2: Profile of the volumetric mass density across membranes represented by an uncharged dipalmitoylphosphatidylcholine (DPPC) phospholipid bilayer, $\rho_{DPPC}(\vec{r})$, adopted from [35], plotted against the relative thickness with respect to that of the membranes, which typically measures 6 µm to 10 µm. The average value, $\langle\rho_{DPPC}(\vec{r})\rangle$, serves as $\rho_M$ in Eq. 7.12 and represents the volumetric mass density of the membranes in the epidermal cell models.*

To solve Eq. 7.12, it is necessary to specify the volumetric mass density of the membranes, $\rho_M$. This is done by considering the volumetric mass density profile $\rho_{\mathrm{DPPC}}(\vec{r})$ across an uncharged dipalmitoylphosphatidylcholine (DPPC) phospholipid bilayer, as shown in Fig. 7.2. This density profile, which has been adopted from [35], provides an estimate of the average density of DPPC molecules in the bilayer, denoted as $\langle\rho_{\mathrm{DPPC}}(\vec{r})\rangle$. Thus, $\langle\rho_{\mathrm{DPPC}}(\vec{r})\rangle$ is used to approximate $\rho_{\mathrm{M}}$. After obtaining $\mu_{\mathrm{SAR,mi,K}_p/\mathrm{C}_q}$ by solving Eq. 7.12, it becomes possible to determine the variability of the *SAR* values across the computational domain using the following equation for the standard deviation:

$$s_{\mathrm{SAR,ma,K}_p/\mathrm{C}_q} = \sqrt{\frac{1}{V_{\mathrm{UC,K}_p/\mathrm{C}_q}} \iiint_{V_{\mathrm{UC}}} \left(\frac{p(\vec{r},\omega)}{\rho(\vec{r})} - \mu_{\mathrm{SAR,mi,K}_p/\mathrm{C}_q}\right)^2 \mathrm{d}V} \qquad (7.13)$$

However, it should be noted that due to the decision to implement membranes as boundary conditions, the integral in this equation does not consider field values within the membranes themselves. While this limitation does not render the analysis invalid, it needs to be considered in the results section, as only an incomplete picture of the field and loss distribution is provided for the macroscopic exposure setup.

In order to provide a comprehensive statistical assessment of the distribution of $SAR_{\mathrm{mi}}(\vec{r},\omega)$, it is important to determine the minimum and maximum values occurring within the epidermal cell models. This can be achieved using the following equations:

$$SAR_{\mathrm{min,mi,K}_p/\mathrm{C}_q} = \min\left(\frac{p(\vec{r},\omega)}{\rho(\vec{r})}\right) \qquad (7.14)$$

$$SAR_{\mathrm{max,mi,K}_p/\mathrm{C}_q} = \max\left(\frac{p(\vec{r},\omega)}{\rho(\vec{r})}\right) \qquad (7.15)$$

By calculating these minimum and maximum values, a more comprehensive understanding of the range of *SAR* values within the cell models can be obtained. This evaluation is performed in two frequency intervals: $F_1 \in [1\ \mathrm{GHz}, 6\ \mathrm{GHz}]$ and $F_1 \in [24\ \mathrm{GHz}, 52\ \mathrm{GHz}]$.

### 7.1.3 Methodological consistency of the scale-back projection

In addition to the statistical analysis outlined above, the methodological consistency between the macroscopic and microscopic scales in the scale-back projection must be evaluated. The macroscopic exposure setup determines the distribution of EM fields within the skin using full-wave simulation. This even takes into account field variations within the investigated microvolumes themselves, which occur due to the damping of the penetrating wave within the tissues (see Fig. 7.1(b)). In contrast, the microscopic exposure setup uses a quasi-static capacitor approach, where the outer boundaries of the computational domain are assigned two numerical features: (1) periodic boundary conditions implemented to avoid fringing fields, and (2) Dirichlet boundary conditions used for the application of the voltage $U_{\mathrm{ind,K}_p/\mathrm{C}_q}$. The Dirichlet boundary conditions enforce a constant potential, $\varphi_{\mathrm{ind,K}_p/\mathrm{C}_q}$, resulting from the application of this voltage in the x-direction. This constant potential, however, is not consistent with the decay of EM waves penetrating the corresponding microvolume in the macroscopic exposure setup, leading to an inherent discrepancy between the macroscopic and microscopic scales in the scale-back projection. Nevertheless, considering both of these scales, this inherent methodological discrepancy becomes negligible when the variability of the EM field values observed in the microdosimetric exposure setup becomes significant in comparison to that in the microvolumes at the macroscopic scale. To quantify this, the agreement between the exposure setups at the two scales can be evaluated by considering the coefficient of variation, defined as:

$$CV_{\mathrm{SAR,ma/mi,K}_p/\mathrm{C}_q} = \frac{s_{\mathrm{SAR,ma/mi,K}_p/\mathrm{C}_q}}{\mu_{\mathrm{SAR,ma/mi,K}_p/\mathrm{C}_q}} \tag{7.16}$$

Here, «ma» and «mi» in the indices refers to statistical measures of microvolumes on the macroscopic and microscopic scales respectively. A low coefficient of variation in the macroscopic setup and a high coefficient of variation in the microscopic setup indicate suitable methodological consistency between the two scales. To assess the coupling quality, the ratio of $CV_{\mathrm{SAR,mi,K}_p/\mathrm{C}_q}$ to $CV_{\mathrm{SAR,ma,K}_p/\mathrm{C}_q}$ is utilized, represented as:

$$\gamma_{\mathrm{SAR,K}_p/\mathrm{C}_q} = \frac{CV_{\mathrm{SAR,mi,K}_p/\mathrm{C}_q}}{CV_{\mathrm{SAR,ma,K}_p/\mathrm{C}_q}} \tag{7.17}$$

This ratio allows the assessment of the quality of coupling between the macroscopic and microscopic scales with a high value for $\gamma_{\mathrm{SAR,K}_p/\mathrm{C}_q}$ indicating strong coupling.

## 7.2 Results

The results derived from the application of the scale-back projection are presented in the following sections. First, the EM exposure in the epidermis is investigated by means of the statistical *micro-SAR*, which is used to quantify the variability of *SAR* values observed within the cellular microstructure of epidermal cells. In addition, the distribution of these values across the cell models is evaluated using histograms and field plots. Following this analysis, a comparison is made between the statistical *micro-SAR* and the conventional representation of the *SAR* on a macroscopic scale. The methodological consistency between the microscopic and macroscopic scales is then evaluated. Finally, the study examines how well the statistical *micro-SAR* conforms to current safety guidelines, particularly those defined in the basic restrictions for limiting local exposure in the extremities.

### 7.2.1 Microdosimetric assessment of the epidermis using scale-back projection

The microdosimetric analysis of $SAR(\vec{r}, \omega)$ using the statistical measures defined in Eqs. 7.14 to 7.15 is shown in Fig. 7.3 for basal keratinocytes (i.e. parametric cell model $K_1$) as an illustrative example[1] because these cells are particularly important for skin resurfacing. The figure presents diagrams

[1] Appendix D complements the presented findings by including detailed statistical analysis of all epidermal cell models, $K_p$to $C_q$, in Figs. D.1 to D.24.

corresponding to frequency interval $F_1$ in Figs. 7.3(a), (c), and (e), and frequency interval $F_2$ in Figs. 7.3(b), (d), and (f). In Figs. 7.3(a) and (b), the $SAR_{\mathrm{mi,K_1}}(\omega)$ is plotted on a semi-logarithmic scale for frequency intervals $F_1$ and $F_2$ respectively. The statistical mean, $\mu_{\mathrm{SAR,mi,K_1}}$, is represented by a solid black line. The dark-gray-shaded area surrounding $\mu_{\mathrm{SAR,mi,K_1}}$ corresponds to a range of values within one standard deviation of the mean, $\mu_{\mathrm{SAR,mi,K_1}} \pm s_{\mathrm{SAR,mi,K_1}}$. The upper and lower bounds of this range are indicated by dashed-dotted lines positioned above and below the mean. To complete this statistical analysis, the light-gray-shaded area surrounding $\mu_{\mathrm{SAR,mi,K_1}} \pm s_{\mathrm{SAR,mi,K_1}}$ illustrates the entire range of values monitored within the computational domain of the microscopic exposure setup. This range is bounded at the top by the maximum value, $SAR_{\mathrm{max,mi,K_1}}$, and at the bottom by the minimum value, $SAR_{\mathrm{min,mi,K_1}}$. The *SAR* values shown here cover a large range, with the central frequencies of intervals $F_1$ and $F_2$ (3.5 GHz and 38 GHz respectively) being used as an illustrative example in Tab. 7.1.

*Tab. 7.1: Illustrative overview of the variation of SAR values in basal keratinocytes for the central frequencies within intervals $F_1$ and $F_2$ at 3.5 GHz and 38 GHz.*

| $f$ | $\mu_{\mathrm{SAR,mi,K_1}}$ | $s_{\mathrm{SAR,mi,K_1}}$ | $SAR_{\mathrm{max,mi,K_1}}$ | $SAR_{\mathrm{min,mi,K_1}}$ |
|---|---|---|---|---|
| 3.5 GHz | $6.4683\,\mathrm{W kg^{-1}}$ | $4.1594\,\mathrm{W kg^{-1}}$ | $27.0293\,\mathrm{W kg^{-1}}$ | $0.0063\,\mathrm{W kg^{-1}}$ |
| 38 GHz | $26.3634\,\mathrm{W kg^{-1}}$ | $18.5791\,\mathrm{W kg^{-1}}$ | $137.1015\,\mathrm{W kg^{-1}}$ | $0.8956\,\mathrm{W kg^{-1}}$ |

However, before moving on to a comprehensive analysis of the variability of *SAR* values across all of the cell models using $CV_{\mathrm{SAR,mi,K}_p/\mathrm{C}_q}$, which will be presented at the end of this subsection, it is important to first analyze the frequency of occurrence of *SAR* values across basal keratinocytes. This is illustrated using histograms in Figs. 7.3(c) and (d) for the two aforementioned sample frequencies. The histograms visually represent the distribution of $SAR(\vec{r}, \omega)$ relative to the volume of the computational domain. Both histograms show that the majority of *SAR* values across this domain exhibit a unimodal distribution which is slightly skewed to the right. However, this general trend is disrupted by a significant accumulation of low values, which account for approximately 30 % of the cell volume forming a second peak in the data. This accumulation can be attributed to the nucleus, which occupies roughly 30 % of the cell volume, as shown in Fig. 5.3. This reasoning is supported by the field plots in Fig. 7.3(e) and (f), which show the *SAR* distribution in the XZ and YZ planes of the computational model of the basal keratinocytes for 3.5 GHz and 38 GHz respectively. These field plots illustrate low field values within the nucleus. This observation aligns with previous findings discussed in [A6], which describe the electrical shielding provided by the nuclear envelope to the nucleoplasm. In summary, the significant accumulation of low values in the distribution of the specific absorption rate can be attributed to the *SAR* values within the nucleus, while the unimodal distribution of values corresponds to the *SAR* occurring in the cytoplasm and extracellular space. Upon closer analysis of the histograms shown in Figs. 7.3(c) and (d), it becomes evident that the calculated mean value, $\mu_{\mathrm{SAR,mi,K_1}}$, does not accurately represent the central tendency of the distribution resulting from the microscopic exposure setup at 3.5 GHz. This discrepancy can be attributed to the implementation of membranes as boundary conditions, as explained in the methodology section of this chapter. The histograms are determined using mathematical operations based on volume integration within the COMSOL Multiphysics software environment and values corresponding to the membranes, modeled as boundary conditions, are thus not captured. The large discrepancy between the expected mean value from the distribution of *SAR* values shown in the histogram and $\mu_{\mathrm{SAR,mi,K_1}}$ suggests a significant contribution to the *SAR* within the membranes. To investigate this missing contribution, the power levels induced in the membranes, cytoplasm, nucleoplasm and extracellular medium are shown in Fig. 7.4 represented by $P_{\mathrm{M}}$, $P_{\mathrm{CP}}$, $P_{\mathrm{NP}}$ and $P_{\mathrm{EC}}$ respectively. In addition, the power levels for the cell as a whole are given by $P_{\mathrm{tot}}$. This is performed separately for each of the frequency intervals, $F_1$ and $F_2$, as shown in Figs. 7.4(a) and (b) respectively. Comparing Fig. 7.4(a) with Fig. 7.4(b), it can be seen that the membranes contribute significantly to absorption

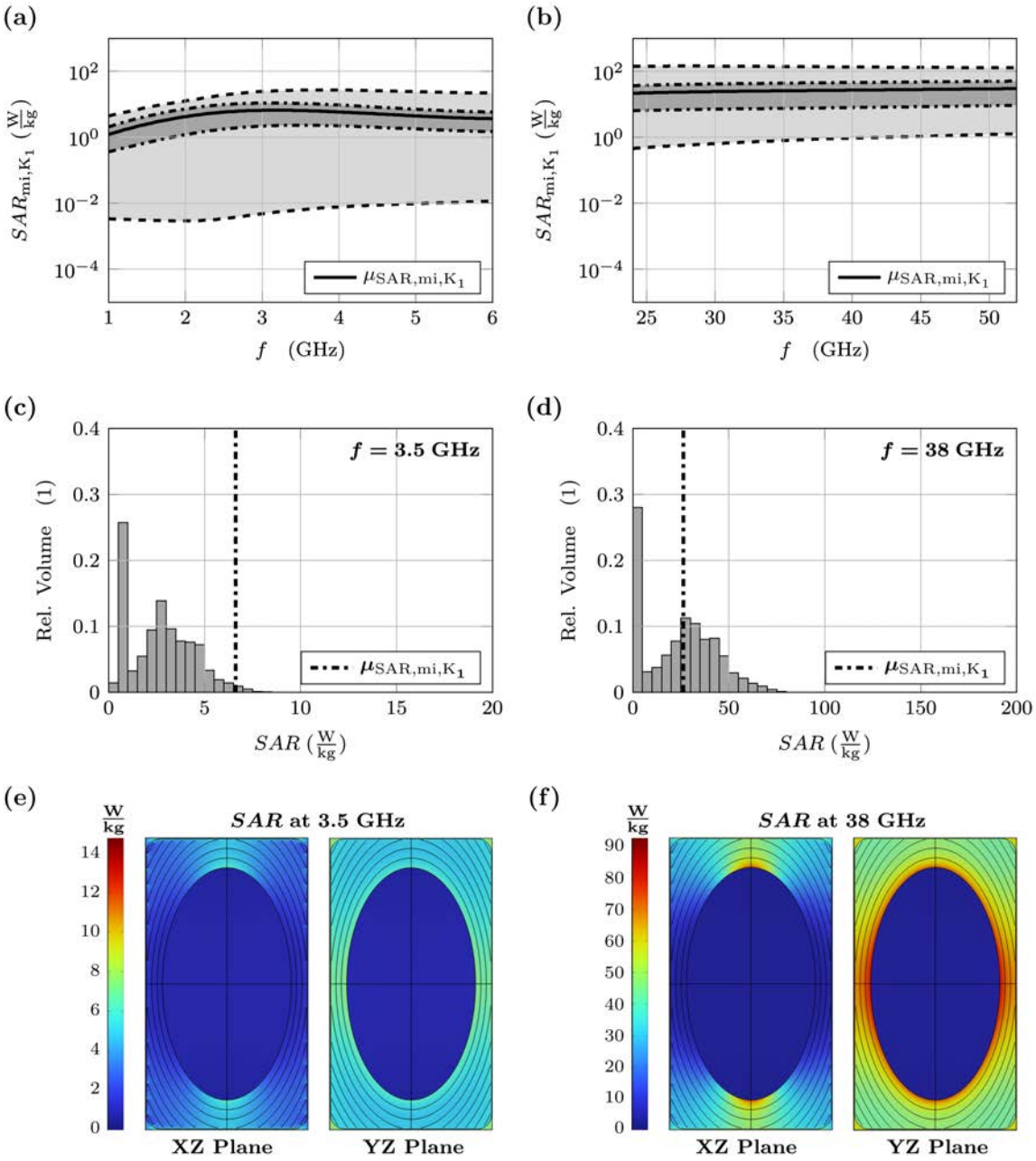


*Fig. 7.3: Microdosimetric analysis of $SAR(\vec{r},\omega)$ in basal keratinocytes. (a) Semi-logarithmic plot of $SAR_{mi,K_1}(\omega)$ for frequency interval $F_1$, illustrating the statistical measures. The solid black line represents the statistical mean ($\mu_{SAR,mi,K_1}$), while the dark-gray-shaded area corresponds to values within one standard deviation of the mean, denoted as $\mu_{SAR,mi,K_1} \pm s_{SAR,mi,K_1}$. The dashed-dotted lines above and below the mean indicate the upper and lower bounds of this range. The light-gray-shaded area represents the entire range of values observed within the computational domain, bounded by the maximum value ($SAR_{max,mi,K_1}$) at the top and the minimum value ($SAR_{min,mi,K_1}$) at the bottom. (b) Similar plot as in (a), but for the frequency interval $F_2$. (c) & (d) Histograms representing the distribution of $SAR(\vec{r},\omega)$ values at 3.5 GHz and 38 GHz. Note the discrepancy between $\mu_{SAR,mi,K_1}$ and the central tendency of the histogram shown in (c), which is due to the implementation of membranes as boundary conditions, as explained in the methodology section of this chapter. (e) & (f) Field plots of $SAR(\vec{r},\omega)$ in basal keratinocytes illustrating the XZ and YZ planes for 3.5 GHz and 38 GHz, respectively.*

in frequency interval $F_1$, while their contribution in frequency interval $\mathrm{F}_2$ is almost negligible. This observation is even more evident when considering the relative induced power, $P_i/P_{\mathrm{tot}}$, shown in Figs. 7.4(c) and (d). There, it can be seen that the membrane losses account for approximately 30-60 % of the total cell losses in $F_1$, while accounting for less than 10 % in $F_2$. As this comprehensive

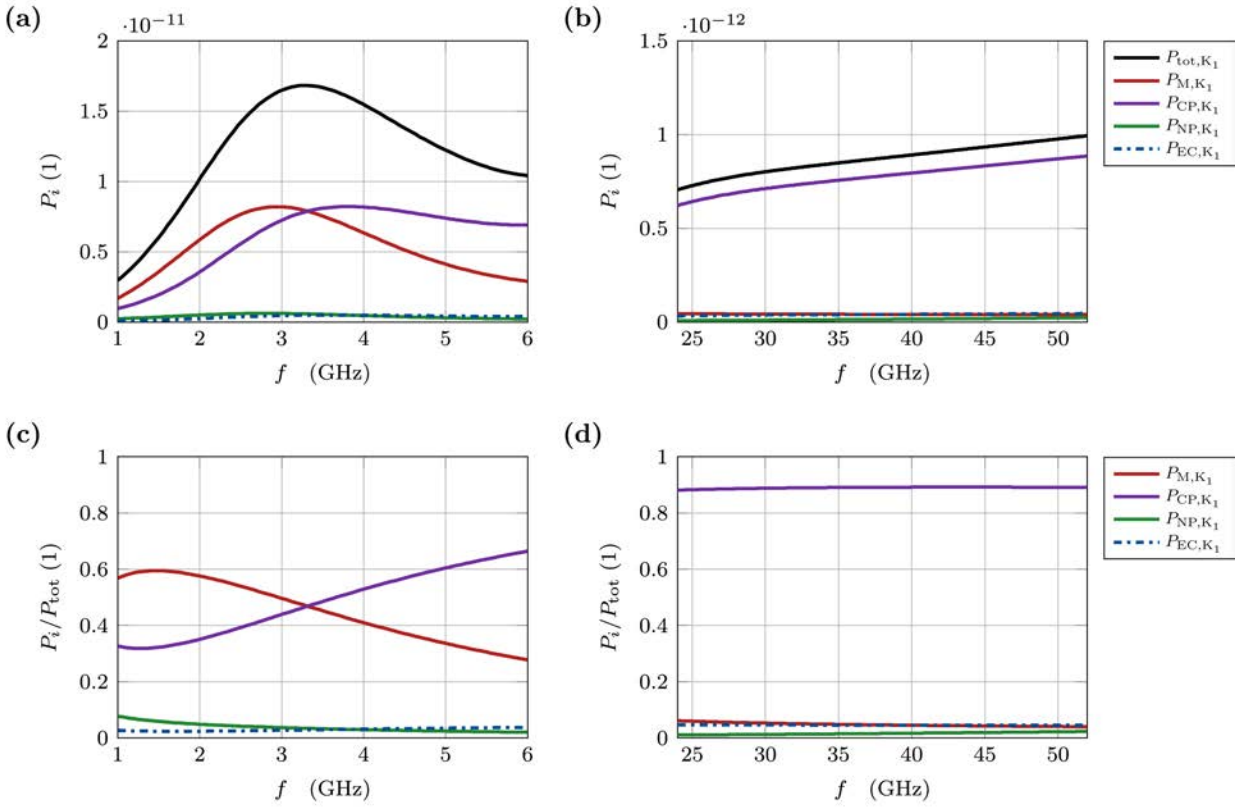


*Fig. 7.4: Power levels induced within each structure of the cell, represented by $P_{tot}$, $P_M$, $P_{CP}$, $P_{NP}$ and $P_{EC}$, depicted by black, red, purple, green, and blue lines, respectively. The analysis is performed separately for frequency intervals $F_1$ and $F_2$, as shown in (a) and (b). (c) and (d) show the relative cell losses expressed as $P_i/P_{tot}$.*

analysis demonstrates the variability of *SAR* values in basal keratinocytes, and acknowledges the computational constraints imposed by the built-in operations of the COMSOL Multiphysics software environment for capturing their distribution, the focus now shifts to quantifying the variability of *SAR* values across all epidermal cell models with these issues in mind. This analysis is illustrated in Fig. 7.5 for the viable epidermis and in Fig. 7.6 for the SC.

In Fig. 7.5, $\mu_{\text{SAR,mi,K}_p}$ and $s_{\text{SAR,mi,K}_p}$ are shown in (a) and (b), while (c) shows $CV_{\text{SAR,mi,K}_p}$ to quantify the variability of *SAR* values over interval $F_1$. Similarly, Figs. 9.5(d)-(f) illustrate these values for interval $F_2$. The plots illustrate the range of values across all cell models, $K_1$ through $K_{10}$, represented by gray-shaded areas bounded by dashed black lines, while solid black lines represent their averages. To maintain a connection with the detailed analysis of basal keratinocytes performed above, the values for $K_1$ are additionally represented by magenta lines. In Figs. 7.5(c) and (f), it can be observed that the coefficient of variation ranges between 0.3 and 0.71 in both intervals. This wide range underlines the significant influence of cell morphology on the variability of *SAR* values within each cell model, and emphasizes the necessity to study each cell layer individually. However, by determining the arithmetic mean of $CV_{\text{SAR,mi,K}_p}$, an average value for the variability within the viable epidermis can be given as a rough estimate, ranging from 0.53 to 0.62 in $\text{F}_1$ and from 0.52 to 0.59 in $F_2$. To quantify the variability of *SAR* values across the cell models of the SC, $\mu_{\text{SAR,mi,C}_q}$, $s_{\text{SAR,mi,C}_q}$ and $CV_{\text{SAR,mi,C}_q}$ are shown in Figs. 7.6(a)-(c) in interval $\text{F}_1$ and in (d)-(f) in interval $\text{F}_2$. The plots illustrate the range of values across all cell models, $C_1$ through $C_{14}$, in a manner corresponding to Fig. 7.5. In Figs. 7.6(c) and (f), a distinct observation arises: The coefficient of variation in the SC is almost frequency independent, displaying a much narrower range of values, spanning from 0.27 to 0.37, in both intervals. As a result, an almost constant average value of 0.33 emerges. The negligible frequency dependence and the much narrower range of values can be attributed to the much lower water content in the histochemical composition of the corneocytes and their much simpler geometric arrangement, lacking any intracellular compartmentalization and organelle membranes.

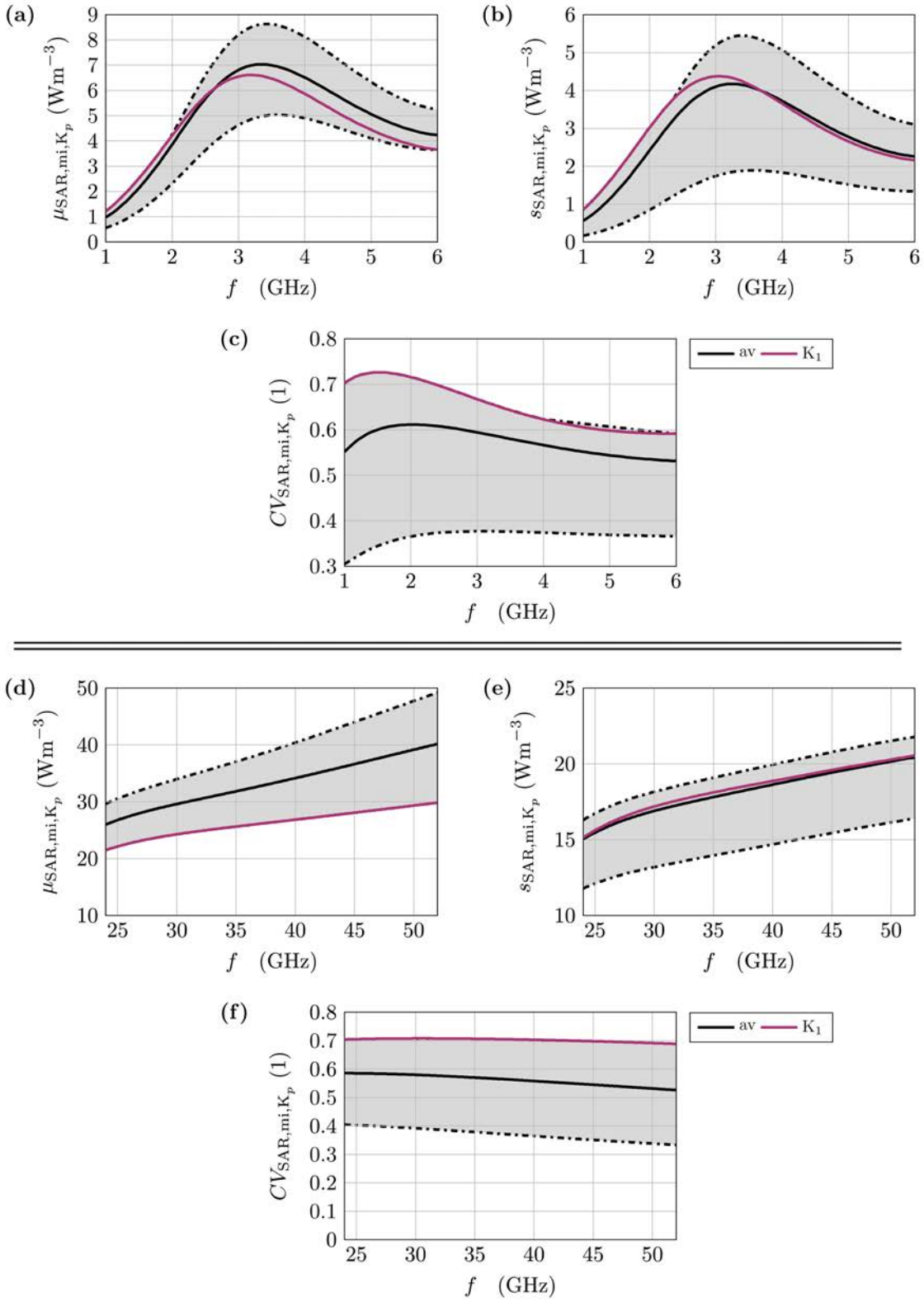


*Fig. 7.5: Viable Epidermis – Analysis of the variability of SAR values in the cell models of the viable epidermis ($K_1$ through $K_{10}$): Plots of the statistical parameters $\mu_{SAR,mi,K_p}$ and $s_{SAR,mi,K_p}$ are shown in (a) and (b), respectively, while (c) illustrates $CV_{SAR,mi,K_p}$ for quantification of SAR values within the frequency interval $F_1$. Correspondingly, Figs. 7.5(d)-(f) present these values for interval $F_2$. The plots visualize the range of values across all cell models by gray-shaded areas bordered by dashed black lines, with solid black lines representing their averages. Following the previous analysis of basal keratinocytes, the values for $K_1$ are additionally shown by magenta lines.*

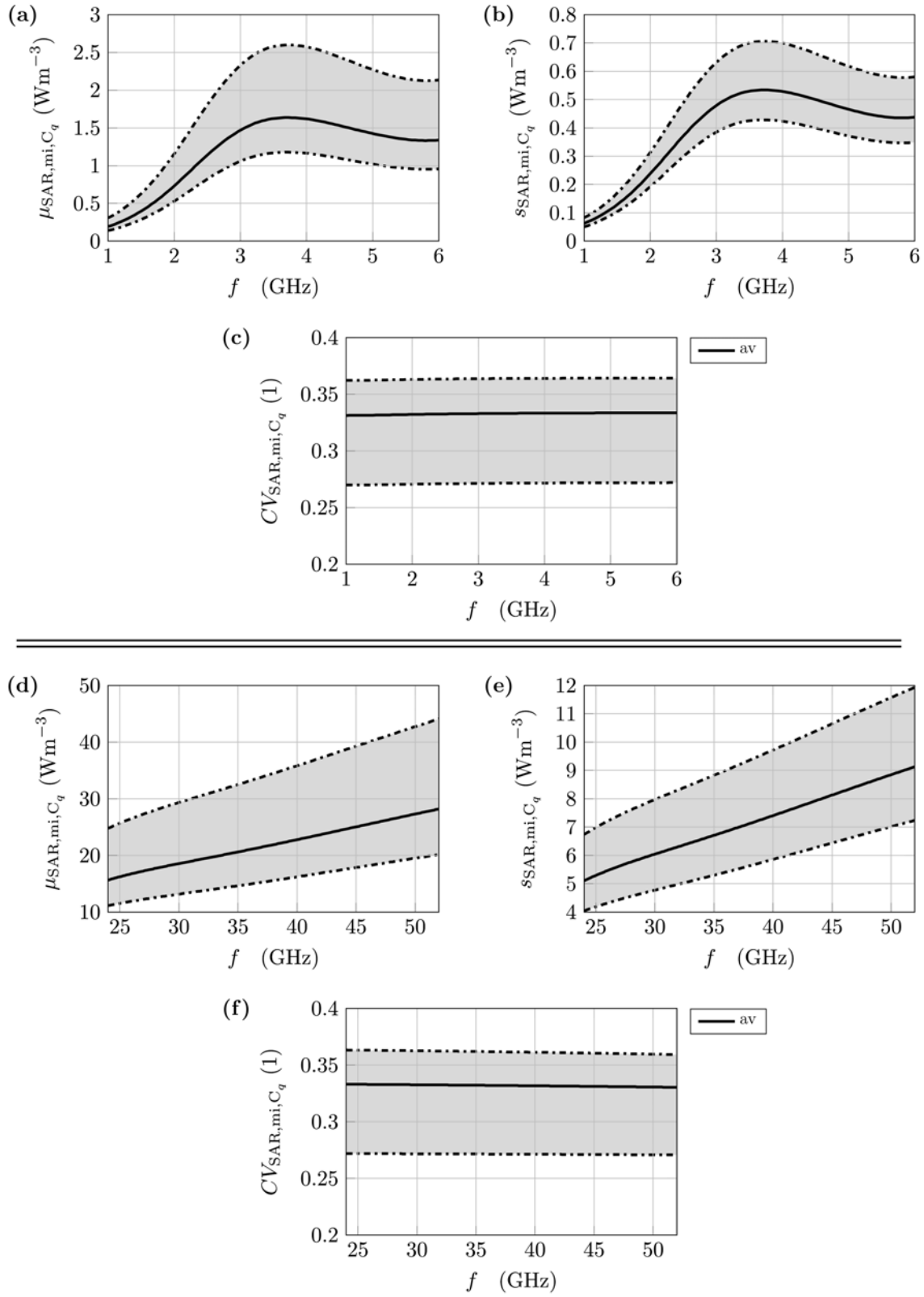


*Fig 7.6: Stratum Corneum – Analysis of the variability of SAR values in the cell models of the SC ($C_1$ through $C_{14}$): Plots of the statistical parameters $\mu_{SAR,mi,C_q}$ and $s_{SAR,mi,C_q}$ are shown in (a) and (b), respectively, while (c) illustrates $CV_{SAR,mi,C_q}$ for quantification of SAR values within the frequency interval $F_1$. Correspondingly, Figs. 7.6(d)-(f) present these values for interval $F_2$. The plots visualize the range of values across all cell models by gray-shaded areas bordered by dashed black lines, with solid black lines representing their averages.*

### 7.2.2 Comparison of the statistical *micro-SAR* and the conventional representation of the *SAR* at the macroscopic scale

After investigating the field variability of the *SAR* in the microstructure of a basal keratinocyte, it is now necessary to compare $\mu_{\mathrm{SAR,mi,K}_p/\mathrm{C}_q}$ with $SAR_{\mathrm{ma,K}_p/\mathrm{C}_q}$, conventionally determined by the homogeneous bulk representation of individual cell layers. This evaluation focuses on epidermal cells within the viable epidermis and the SC in Figs. 7.7 and 7.8, respectively. In Fig. 7.7, $SAR_{\mathrm{ma,K}_p}$ and $\mu_{\mathrm{SAR,mi,K}_p}$ are shown in (a) and (b), while (c) shows the relative deviation between these values, denoted as $\Delta SAR_{\mathrm{K}_p}$, for frequency range $F_1$. Similarly, Figs. 7.7(d)-(f) illustrate these values for the frequency range $F_2$. The curves in each plot correspond to specific epidermal cell models, represented by solid, dashed, dotted, and dashed-dotted lines, and colored in magenta ($K_1$ through $K_4$), green ($K_5$ through $K_8$), and blue ($K_9$ and $K_{10}$) as indicated in the legend. Comparing $SAR_{\mathrm{ma,K}_p}$ and $\mu_{\mathrm{SAR,mi,K}_p}$ in Figs. 7.7(a) and (b), it can be seen that the curves for all cell models show the same basic trend with a maximum between 3 GHz and 4 GHz. However, the magnitude of this maximum is much smaller for $SAR_{\mathrm{ma,K}_p}$ than for $\mu_{\mathrm{SAR,mi,K}_p}$.

This can be explained by the loss distribution within the epidermal cell models. As shown in the sectional images of the cell model of basal keratinocytes in Fig. 7.3(e) and indicated by the histogram in Fig. 7.3(d), the nucleus is largely shielded from EM radiation by the organelle membranes in the surrounding cytoplasm. In addition, the distribution of the power input within the cell shown in Fig. 7.4 demonstrates that the total power of the cell forms a maximum at about 3.2 GHz, which is mainly split into equal parts of 45 % in the cytoplasm and the membranes. This underlines the usefulness of the piecewise determination of the *SAR* contributions of the individual cell structures in Eq. 7.12 for the calculation of $\mu_{\mathrm{SAR,mi,K}_p}$ as a means to quantify cell losses and their location within individual cells. Regarding $\Delta SAR_{\mathrm{K}_p}$ in Fig. 7.7(c), it can be seen that the *SAR* estimated from the graph, $SAR_{\mathrm{ma,K}_p}$, is up to 45 % lower than the microscopically measured $\mu_{\mathrm{SAR,mi,K}_p}$. These statements can also be applied to frequency range $F_2$ shown in Figs. 7.7(d)-(f). Both $SAR_{\mathrm{ma,K}_p}$ and $\mu_{\mathrm{SAR,mi,K}_p}$ show the same monotonous slope in the plotted graphs, which essentially reflects the lower attenuation of the penetrating wave. The deviation of the two values, $\Delta SAR_{\mathrm{K}_p}$, is much smaller here than in $F_1$ due to the smaller loss contribution of the membranes. However, it is still significant with a value of up to 13 %.

Moving on to the analysis of the individual cell layers of the SC, $SAR_{\mathrm{ma,C}_q}$, $\mu_{\mathrm{SAR,mi,C}_q}$ and $\Delta SAR_{\mathrm{C}_q}$ are illustrated in Figs. 7.8(a)-(c) for frequency interval $F_1$ and in (d)-(f) for frequency interval $F_2$. The curves in each plot correspond to specific corneocyte models, represented by solid, dashed, dotted, and dashed-dotted lines, and colored in magenta ($C_1$ through $C_4$), green ($C_5$ through $C_8$), blue ($C_9$ through $C_{12}$) and gray ($C_{13}$ and $C_{14}$) as indicated in the legend. It can be seen that $SAR_{\mathrm{ma,C}_q}$ and $\mu_{\mathrm{SAR,mi,C}_q}$ are almost identical with deviations, $\Delta SAR_{\mathrm{C}_q}$, ranging between 1 % and 3 % depending on the cell layer. The small deviations within the SC compared to the significant deviations within the viable epidermis are due to differences in the modeling of keratinocytes and corneocytes, or more specifically, the inclusion of organelle membranes. At the transition between the stratum granulosum and the stratum corneum, keratinocytes are metabolically deactivated, and their organelles and the nucleus dismantled. The lamellar bodies, which contain keratin and lipids in addition to organelles, fuse with the plasma membrane and shed their contents into the cell body [36]. Thus, the corneocytes, as described in detail in Section 5, are regarded as protein sacs that no longer contain organelles, and thus organelle membranes no longer need to be modeled. This leads to lower differences between the *SAR* on a macroscopic and microscopic scale.

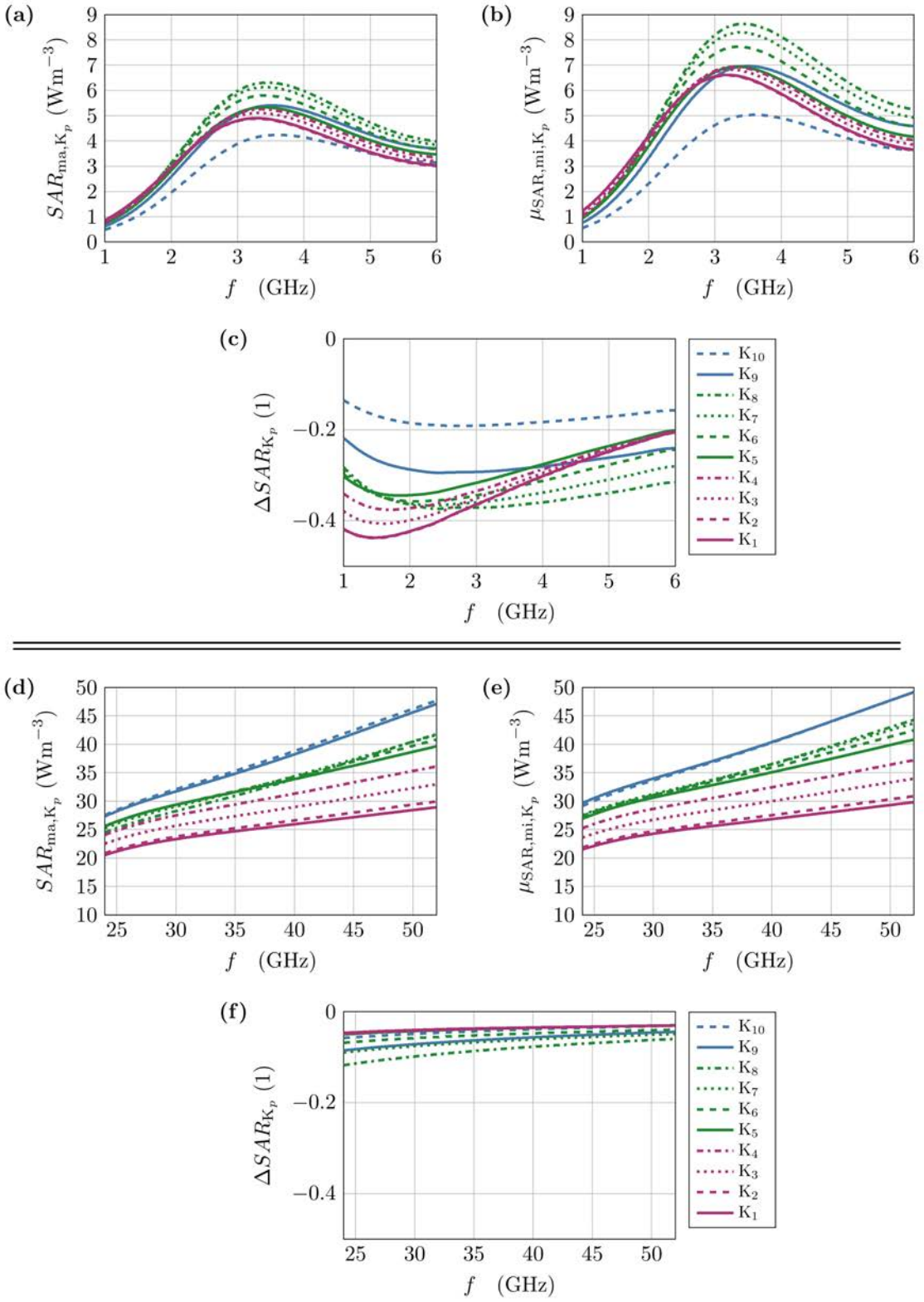


*Fig. 7.7: Viable Epidermis - Comparison between the SAR derived from the conventional representation of the microvolumes at a macroscopic scale, denoted as $SAR_{ma,K_p}$ in (a) & (d), and the statistical micro-SAR, denoted as $\mu_{SAR,mi,K_p}$ in (b) & (e), in the frequency interval $F_1$ in (a)-(c), and $F_2$ in (d)-(f): (a) & (d) show $SAR_{ma,K_p}$ while (b) & (e) show $\mu_{SAR,mi,K_p}$ for each frequency range; (c) & (f) depict the relative deviation between these values, denoted as $\Delta SAR_{K_p}$. The plots corresponding to each of the investigated epidermal cell models are represented by solid, dashed, dotted, and dash-dotted lines. They are colored in magenta ($K_1$ through $K_4$), green ($K_5$ through $K_8$), and blue ($K_9$ and $K_{10}$) as indicated in the legend.*

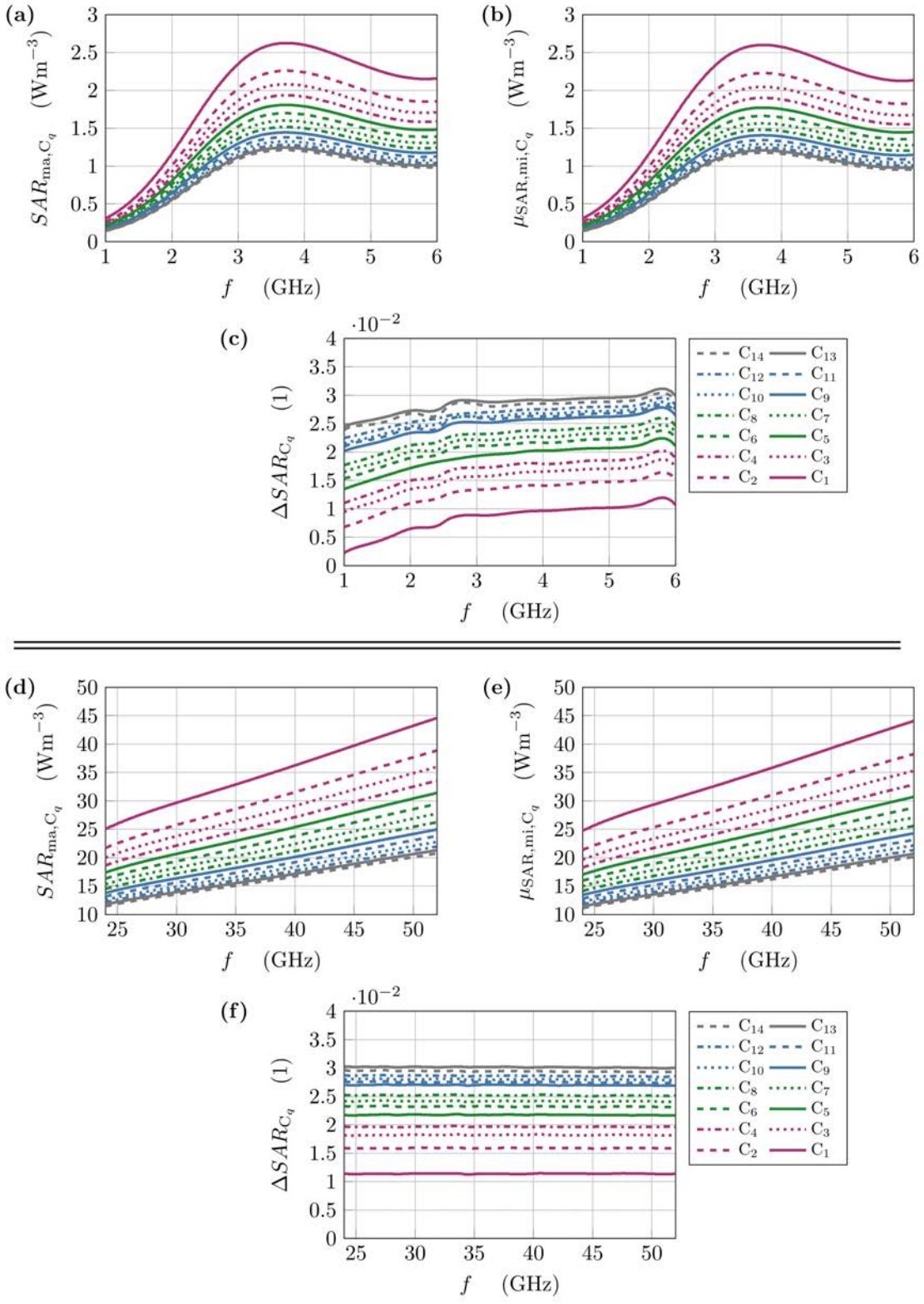


*Fig. 7.8: Stratum corneum – Comparison between the SAR derived from the conventional representation of the microvolumes at a macroscopic scale, denoted as $SAR_{ma,C_q}$ in (a) & (d), and the statistical micro-SAR, denoted as $\mu_{SAR,mi,C_q}$ in (b) & (e), in the frequency interval $F_1$ in (a)-(c), and $F_2$ in (d)-(f): (a) & (d) show $SAR_{ma,C_q}$ while (b) & (e) show $\mu_{SAR,mi,C_q}$ for each frequency range; (c) & (f) depict the relative deviation between these values, denoted as $\Delta SAR_{C_q}$. The plots corresponding to each of the investigated cell layers are represented by solid, dashed, dotted and dashed-dotted lines. They are colored in magenta ($C_1$ through $C_4$), green ($C_5$ through $C_8$), blue ($C_9$ through $C_{12}$) and gray ($C_{13}$ and $C_{14}$) as indicated in the legend.*

### 7.2.3 Methodological consistency between the microscopic and macroscopic scales

The methodological consistency, evaluated by the coefficient $\gamma_{\mathrm{SAR,K}_p/\mathrm{C}_q}$, is examined in this subsection. The consistency analysis is presented for the cell models of the viable epidermis in Fig. 7.9(a) and (b) for the frequency ranges $F_1$ and $\mathrm{F}_2$ respectively. Similarly, Figs. 7.9(c) and (d) display the consistency analysis for the cell layers of the SC covering the same frequency ranges. The plots depict the lowermost and uppermost cell models of the viable epidermis ($K_1$ and $K_{10}$) and SC ($C_1$ and $C_{14}$) as solid red and solid blue lines, respectively. The entire range of values is represented as a gray-shaded area bounded by dashed black lines. It can be seen that $\gamma_{\mathrm{SAR,K}_p}$ is greater than 200 in $\mathrm{F}_1$ and greater than 20 in $F_2$ in the viable epidermis, which means that the field variation in the cell models on a microscopic scale is at least 20 to 200 times greater than the field variations caused by the attenuation of the penetrating wave across the microvolumes in each cell layer on a macroscopic scale. In the SC, $\gamma_{\mathrm{SAR,C}_q}$ is greater that 10 in $F_1$ and greater than 200 in $F_2$. The methodological consistency of the scale-back projection is assured based on this factor, as the field variations within the microstructure of the cell are significantly larger than those within the microvolumes of the cell layers. This justifies the use of the scale-back projection for microdosimetric investigations. In addition to this observation, some noticeable features in the presented curves need to be clarified. Particularly noticeable in frequency range $\mathrm{F}_1$, a maximum is evident throughout the range of values in $\gamma_{\mathrm{SAR,K}_p}$, peaking at approximately 2.8 GHz. Additionally, there is a wide bandwidth of values in $\gamma_{\mathrm{SAR,C}_q}$, which also reaches a maximum around 2.8 GHz in the upper range of values.

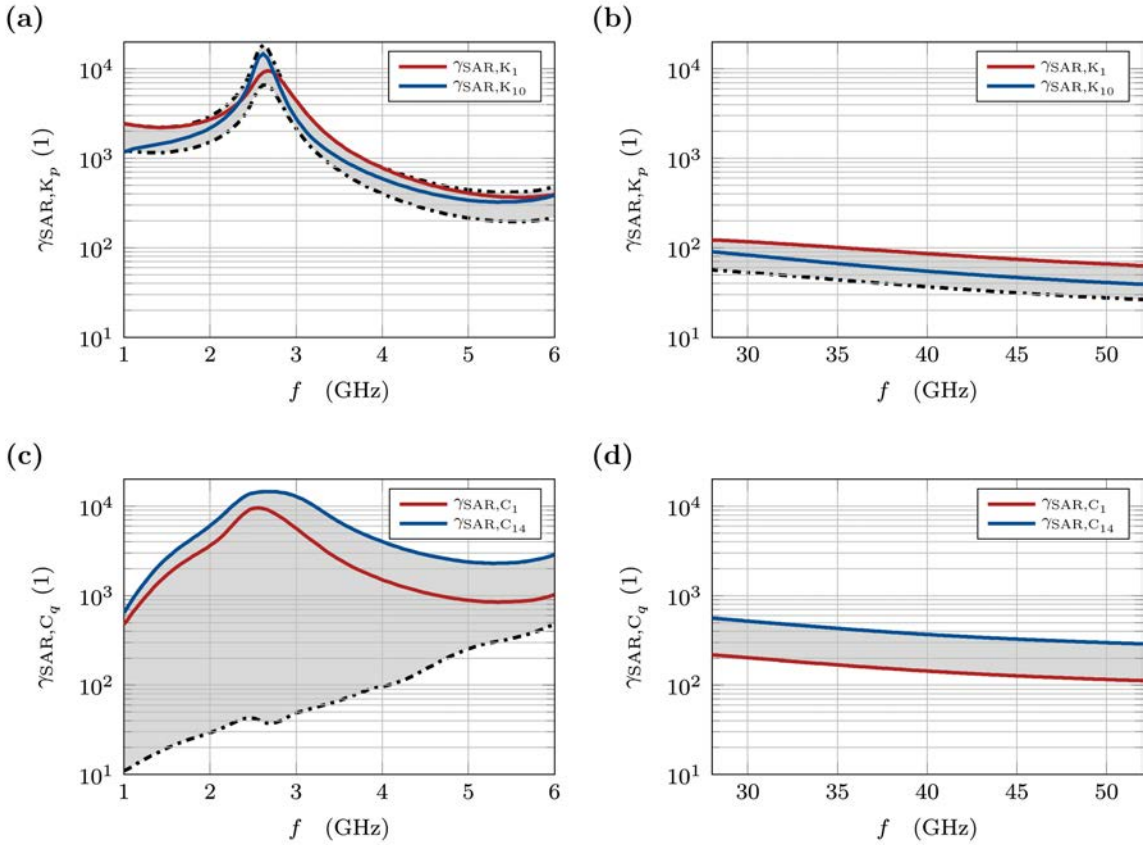


*Fig. 7.9: Consistency analysis of the methodological consistency, evaluated by the coefficient $\gamma_{SAR,K_p/C_q}$, for cell models of the viable epidermis and SC in different frequency ranges. Figures (a) and (b) present the consistency analysis for the viable epidermis in frequency ranges $F_1$ and $F_2$ respectively, while Figures (c) and (d) display the analysis for the SC covering the same frequency ranges. The plots show the lowermost and uppermost cell models of the viable epidermis ($K_1$ and $K_{10}$) and the SC ($C_1$ and $C_{14}$) as solid red and solid blue lines, respectively, with the entire range of values represented as a gray-shaded area bounded by dashed black lines.*

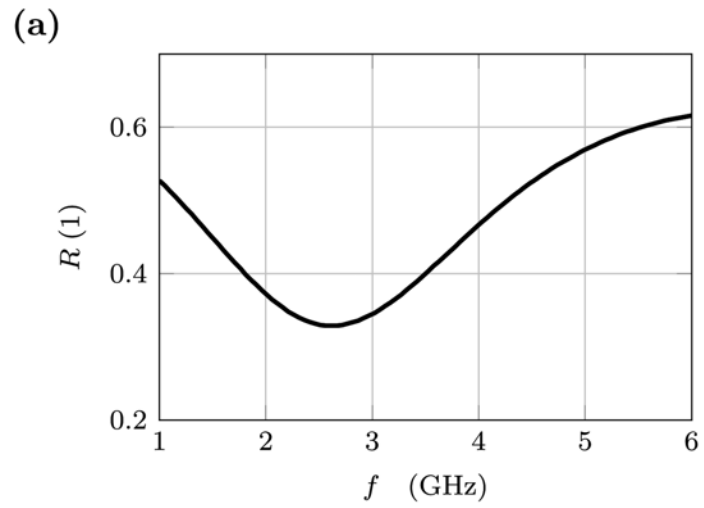


*Fig. 7.10: Power reflection coefficient, $R$, of the macroscopic exposure setup in the frequency interval $F_1$.*

From the definition of $\gamma_{\mathrm{SAR,K}_p/\mathrm{C}_q}$ given in Eq. 7.17, it is inferred that the observed maximum and spread of data could be attributed to effects on either a microscopic scale (i.e., $CV_{\mathrm{SAR,mi,K}_p/\mathrm{C}_q}$) or a macroscopic scale (i.e., $CV_{\mathrm{SAR,ma,K}_p/\mathrm{C}_q}$). A decomposition of $CV_{\mathrm{SAR,mi,K}_p/\mathrm{C}_q}$ and $CV_{\mathrm{SAR,ma,K}_p/\mathrm{C}_q}$ into their respective arithmetic means, $\mu_{\mathrm{SAR,ma/mi,K}_p/\mathrm{C}_q}$, and standard deviations, $s_{\mathrm{SAR,ma/mi,K}_p/\mathrm{C}_q}$, on both the macroscopic and microscopic scales (while not explicitly shown here due to its irrelevance to the current investigation) shows that neither the observed maximum nor the spread of the data are due to phenomena in the microscopic exposure model, but can instead be attributed to $s_{\mathrm{SAR,ma/mi,K}_p/\mathrm{C}_q}$. An explanation for this can be provided by considering the layered structure of the skin in which partial reflections and transmissions at the interfaces between these layers lead to superpositions that can yield two effects: (1) standing waves within the individual layers decreasing the variability of EM fields, and (2) dispersions in the reflectance and transmission of the overall skin structure. An indication of this hypothesis can be found in the spectral response of the power reflection coefficient of the macroscopic exposure setup, as shown in Fig. 7.10, which shows that a minimum in the total reflectance coincides with the maximum, as well as the spread of data, in $\gamma_{\mathrm{SAR,K}_p}$ and $\gamma_{\mathrm{SAR,C}_q}$. This observation, alongside the impedance-matching properties of the epidermis mentioned in Section 6, could be further explored in a detailed analysis using the transfer matrix method. However, such an exploration is beyond the scope of the present investigations and is introduced here merely as an ancillary suggestion to consider the effects of multiple reflections within the skin as a layered medium.

### 7.2.4 The statistical *micro-SAR* compared to the basic restrictions for the limitation of local exposure in the limbs

Moving away from the analysis of the methodological consistency of the scale-back projection, Figs. 7.11(a) and (b) provide an overview of $\mu_{\mathrm{SAR,mi,K}_p}$ for all modeled keratinocytes of the viable epidermis for frequency intervals $F_1$ and $F_2$ respectively. The diagrams use the same labeling scheme for the cell models as used in Fig. 7.7. The bars displayed in red and green highlight values above and below $SAR_{10\mathrm{g}}$ as currently defined in the basic restrictions. In Fig. 7.11(a), it is observed that $\mu_{\mathrm{SAR,mi,K}_p}$ starts to exceed the threshold of 4 W/kg from about 2 GHz and remains above this value throughout the entire interval $\mathrm{F}_1$. It can also be seen that $\mu_{\mathrm{SAR,mi,K}_p}$ forms a maximum at about 3.4 GHz across all cell models, varying between 5 W/kg and 9 W/kg depending on the cell model. However, in interval $F_2$, $\mu_{\mathrm{SAR,mi,K}_p}$ increases monotonically with increasing frequency, and all values significantly exceed the threshold provided by the basic restrictions as illustrated in Fig. 7.11(b).

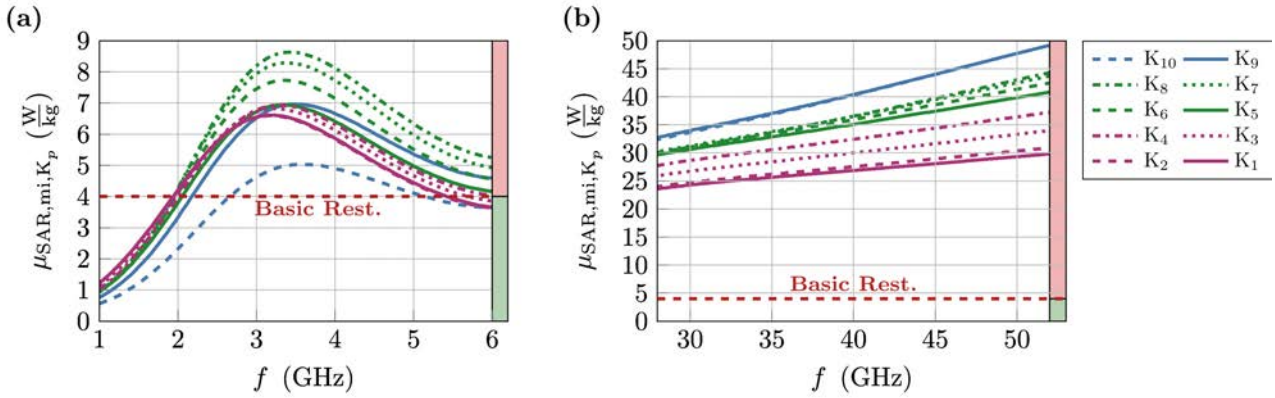


*Fig. 7.11: Viable Epidermis – Overview of $\mu_{SAR,mi,K_p}$ within individual keratinocytes of the viable epidermis: (a) & (b) Distribution of $\mu_{SAR,mi,K_p}$ in the viable epidermis for intervals $F_1$ and $F_2$ respectively. The plots corresponding to each of the investigated cell models are represented by solid, dashed, dotted and dashed-dotted lines. They are colored in magenta ($K_1$ through $K_4$), green ($K_5$ through $K_8$), and blue ($K_9$ and $K_{10}$) as indicated in the legend.*

Similarly, Fig. 7.12 presents an overview of the mean exposure levels induced in the corneocytes, $\mathrm{C}_q$, for the same frequency intervals. The distribution of $\mu_{\mathrm{SAR,mi,C}_q}$ in the stratum corneum (SC) is shown in Figs. 7.12(a) and (b). Again, the same labeling scheme is used for the cell models as found in Fig. 7.8. Comparing Fig. 7.12 with Fig. 7.11, it can be observed that $\mu_{\mathrm{SAR,mi,C}_q}$ follows a similar general trend, with maxima developed at 3.4 GHz in interval $\mathrm{F}_1$ and a monotonic increase in interval $F_2$. However, the average *SAR* values in the corneocytes are significantly lower, resulting in maximum values below 3 W/kg in interval $\mathrm{F}_1$ and maximum values below 45 W/kg in interval $F_2$. In Fig. 7.12(b), it is evident that the threshold of 4 W/kg is significantly exceeded in all of the cell models.

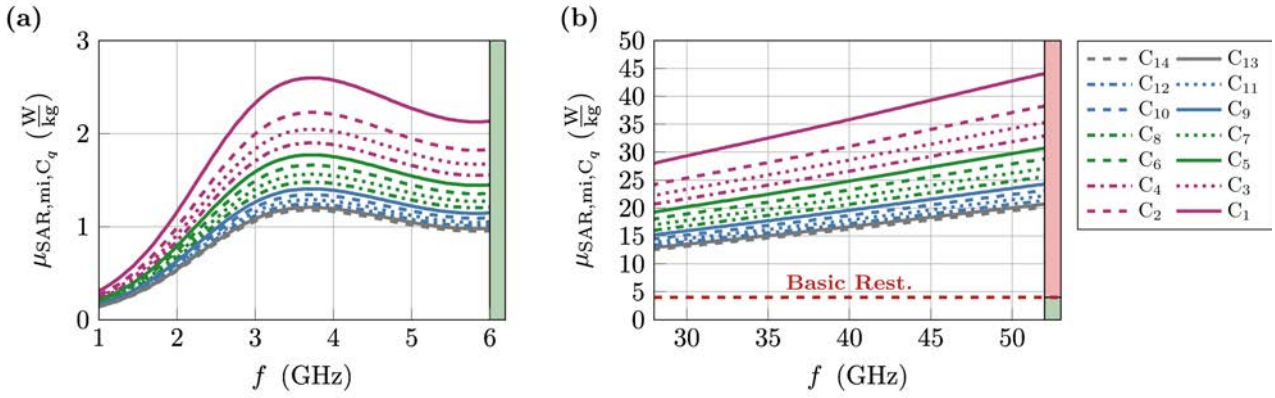


*Fig. 7.12: Stratum corneum – Overview of $\mu_{SAR,mi,C_q}$ within individual corneocyte models of the SC: (a) & (b) Distribution of $\mu_{SAR,mi,C_q}$ in the SC for intervals $F_1$ and $F_2$ respectively. The plots corresponding to each of the investigated cell layers are represented by solid, dashed, dotted and dashed-dotted lines. They are colored in magenta ($C_1$ through $C_4$), green ($C_5$ through $C_8$), blue ($C_9$ through $C_{12}$) and gray ($C_{13}$ through $C_{14}$) as indicated in the legend.*

## 7.3 Interpretation and final remarks

■ The application of scale-back projection to the bottom-up model of the epidermis has introduced a top-down multiscale approach, enabling a thorough investigation of the complex relationship between morphology, histochemical composition, and absorption behavior within epidermal cells. Conducted at two interrelated hierarchical scales, namely, the macroscopic and microscopic scales, this investigation examined the level of EM exposure using the *SAR* within microvolumes that represent the smallest living units within the tissue (i.e., a cell) in each individual cell layer. At the macroscopic scale, these microvolumes constitute a homogeneous medium, representing individual

epidermal cells through their effective material properties. This homogenization approach focuses on the broader aspects of cell behavior in relation to the overall skin structure. The *SAR* at this scale can be expressed in terms of $SAR_{\mathrm{ma,K}_p/\mathrm{C}_q}(\omega)$, following the conventional method of integrating the power density over the microvolume of interest and dividing by the integral of the volumetric mass density over the same volume (see Eq. 9.4). At the microscopic scale, the microvolumes encompass fully resolved cell models, wherein the morphology and histochemical composition of the cells are considered in great detail. This representation facilitates a comprehensive understanding of the influence of cellular structures on EM field absorption. For this, however, the *SAR* must be expressed in statistical terms, defining $SAR_{\mathrm{mi,K}_p/\mathrm{C}_q}(\omega) = \mu_{\mathrm{SAR,mi,K}_p/\mathrm{C}_q}(\omega) \pm s_{\mathrm{SAR,mi,K}_p/\mathrm{C}_q}(\omega)$, referred to as the *micro*-SAR. It is called this because its arithmetic mean, $\mu_{\mathrm{SAR,mi,K}_p/\mathrm{C}_q}(\omega)$, averages the *SAR* over the individual cell structures under consideration (see Eq. 9.12), allowing realistic consideration of EM absorption and its spatial distribution on the microscopic scale in a single representative scalar expression.

■ By using the *micro-SAR* to assess the variability of $SAR(\vec{r},\omega)$ in epidermal cells, Sec. 7.2.1 illustrated how the morphology and histochemical composition of these cells significantly shape the field distribution within the microstructure of the tissue. Using basal keratinocytes as an illustrative example, the detailed analysis of the field distribution based on sectional images and histograms showed that the membranes make a surprisingly large contribution to the absorption, especially in frequency interval $F_1$, with a value of up to 60 %, while the nucleus, which is largely field-free due to the surrounding organelle membranes, contributed little to the absorption with a value of less than 10 %. This uneven distribution of loss contributions is all the more significant when one considers that the volumetric fraction of the computational domain comprising membranes is only 3 %, while that representing the nucleus is a much larger 30 %. In addition, these structures are assigned very different volumetric mass densities $\rho_{\mathrm{M}} = 629\ \mathrm{kg/m^3}$ and $\rho_{\mathrm{NP}} = 1049\ \mathrm{kg/m^3}$. These differences in loss contributions, volumetric proportions, and mass densities further highlight the intricate relationship between morphology, composition, and absorption behavior within the epidermal cells and amplify the importance of considering these aspects combined in $\mu_{\mathrm{SAR,mi,K}_p/\mathrm{C}_q}(\omega)$.

■ In addition, the analysis of $CV_{\mathrm{SAR,mi,K}_p}$ showed that the variability of *SAR* values within the viable epidermis ranged in average between 30 % and 71 % within one standard deviation, $s_{\mathrm{SAR,mi,K}_p}$, around the respective mean value, $\mu_{\mathrm{SAR,mi,K}_p}$, in both frequency intervals $F_1$ and $F_2$. The corresponding analysis of $CV_{\mathrm{SAR,mi,C}_q}$ demonstrated an almost frequency-independent average variability of *SAR* values of 33 %. The significant impact of neglecting the intricate structure of epidermal cells during SAR calculations was illustrated in Sec. 7.2.2, where it was shown to lead to a substantial underestimation of epidermal exposure. This was demonstrated by comparing $SAR_{\mathrm{ma,K}_p/\mathrm{C}_q}$ with $\mu_{\mathrm{SAR,mi,K}_p/\mathrm{C}_q}$. The comparison revealed that the macroscopic measure $SAR_{\mathrm{ma,K}_p/\mathrm{C}_q}$ underestimates the exposure of skin tissue by up to 45 %. In Sec. 7.2.3, the methodological consistency of scale-back projection, as evaluated by the coefficient $\gamma_{\mathrm{SAR,K}_p/\mathrm{C}_q}$, revealed that the microscopic field variations in cell models are much greater than the macroscopic field variations within cell layers, thereby justifying the application of scale-back projection in microdosimetric investigations. Sec. 7.2.4 demonstrated that $\mu_{\mathrm{SAR,mi,K}_p/\mathrm{C}_q}$ significantly exceeds the $SAR_{10\mathrm{g}}$ threshold of 4 W/kg across both frequency ranges. However, a straightforward numerical comparison at this stage might lead to an oversimplified assumption that $SAR_{10\mathrm{g}}$ significantly underestimates the EM exposure of the skin. A nuanced interpretation of this result calls for a reassessment of the initial purpose behind the establishment of $SAR_{10\mathrm{g}}$ as a metric in the context of conventional dosimetric multiphysics simulations. Moreover, it requires a conceptual comparison of this intent with that of the scale-back projection approach.

■ Conventionally, the SAR is defined in terms of a generic cubic volume equivalent to a specific mass of water, in contact with the skin surface, encompassing all constituent tissue types. Within this paradigm, the spatially averaged *SAR* is related to the maximum temperature increase within this defined volume, serving as a mass-based EM exposure metric, and prescribes local exposure limits across a broad frequency spectrum from 100 kHz to 6 GHz. At the lower end of this spectrum,

EM field attenuation within tissue can be considered negligible due to the extended wavelengths involved. At higher frequencies, however, the field attenuation becomes significant, resulting in a significant decrease in penetration depth with increasing frequency. This necessitates consideration of an optimal volume that provides a meaningful measure of EM exposure.

■ To reconcile the significant shift in field attenuation and penetration depth over the frequency range from 1 GHz to 6 GHz, Hirata et al. [37] examined the correlation between temperature distribution and mass-averaged *SAR* over a range of volumes. These volumes corresponded to water masses ranging from 0.1 g to 100 g. In the search for an optimal volume size, the challenge was to adequately capture a significant amount of data without including less significant trailing values, while at the same time avoiding smaller volumes that might capture only a fraction of the necessary data, thus providing an incomplete picture. To achieve this balance, they used the coefficient of determination, a statistical tool that assesses the quality of a best-fit line to data, which in this case was the predicted temperature increase derived from the multiphysics simulations. Their analyses identified a peak correlation at a 10 g water-equivalent volume, which represents a reliable relationship between the average *SAR* and the temperature distribution over the frequency range of 1 GHz to 6 GHz, as described in [37]. It is important to note, however, that this 10 g volume, encapsulates what appears to be the entire 'relevant' depth of the temperature profile, thereby providing the best balance within the 1 GHz to 6 GHz frequency range. As illustrated by the example of EM exposure of the human head by a dipole antenna in [37, 38], $SAR_{10\mathrm{g}}$ proves to be an appropriate metric in scenarios where the temperature profile is dominated by spatially variable irradiation patterns (such as an antenna aperture) and complex organ-scale geometries with heterogeneous tissue compositions, including the highly temperature-sensitive cerebral matter. Despite its suitability within these constraints, $SAR_{10\mathrm{g}}$ serves as a statistical compromise, not an optimal solution, and may not provide the highest fidelity solution universally.

■ In contrast, scale-back projection examines EM exposure in distinct microvolumes, each of which represents the smallest living unit within the tissue, namely a cell. This approach allows a more precise quantification of EM absorption at individual depth levels, each corresponding to an individual cell layer. Thus, scale-back projection not only provides a high-resolution exposure profile across the skin, but also represents a potential tool for augmenting the methodological repertoire of conventional multiphysics simulations. When applying the absorption profile obtained by scale-back projection to subsequent thermal simulations, this approach allows for a much more accurate representation of the effects of EM irradiation on specific skin structures identified as thermally sensitive, in this case the proliferative pool of the epidermis. Thus, scale-back projection potentially provides more detailed access to thermal effects at the microstructural level and provides valuable insight into the complex interplay of EM exposure, absorption, and thermal response within the skin.

# 8 Conclusion and outlook

## 8.1 Conclusion

■ In the context of this work, scale-back projection was introduced as an innovative top-down multiscale approach. This method allows the consideration of the complex interplay between morphology, histochemical composition and EM absorption at the cellular level, while taking into account the specific position of individual cells within the layered structure of the skin for accurate microdosimetric analyses. For its application, however, scale-back projection requires a comprehensive material description that must be tailored to the specific anatomical characteristics of the tissue under study.

■ Considering this requirement, a hierarchical bottom-up model of the epidermis was developed that offers a coherent description of the material properties both macroscopically and microscopically. Unlike earlier bottom-up models [A34, 29], the epithelial tissue of the epidermis was regarded as a symbiotic biological system shaped by the life cycle of its predominant cell type, the keratinocytes (or corneocytes). By subdividing the epidermis into 24 cell layers, the differentiation of basal keratinocytes towards the skin surface is represented through gradual changes across these layers. This took into account two primary aspects: (1) alterations in cell geometry and internal structure, and (2) changes in the histochemical composition of the cells. The microstructure of the epidermal cells was represented using parametric CAD models. These models were adapted to the physiological conditions specific to each individual cell layer using geometric parameters derived from the literature, as outlined in detail in Section 5. Thanks to the adapted cell models, the thicknesses of individual epidermal layers were determined on a macroscopic scale, ensuring anatomical accuracy. As these thicknesses sum to the total thickness of the epidermis, the histochemical composition could be conceptually represented using concentration profiles, treating the tissue as a composite of water, lipids, keratin, and a general protein component. These concentration profiles were then used to derive the histochemical composition for each cell layer and project it onto individual cell compartments of the corresponding parametric cell models, treating their biochemical composition at a «molecular scale». By employing mixing formulas in an incremental mixing procedure, the effective permittivities were determined and then set as material parameters for the compartments of the parameterized cell models. With the parametric cell models now fully realized, capturing detailed cytoanatomical features and ensuring accurate histochemical data when describing the permittivities of the cell compartments, it was possible to determine the effective material properties of each cell layer using numerical homogenization. With this innovative approach, the bottom-up model enables the reconstruction of the formation, maturation, and eventual death of epidermal cells, and seamlessly translates this life cycle into effective material properties, consistently describing the epidermis at both the macroscopic and microscopic scale in a single integrated model.

■ The integration of the bottom-up model of the epidermis into a complete skin model is achieved by the simplified assumption that the individual sublayers of the skin are modular, i.e. that their exact modifications with respect to thickness and the choice of the underlying material parameters can be considered independently. Based on this assumption, two skin models could be implemented, the topological properties of which correspond to those of the skin of the forearm. The first model was denoted as the reference model and was based on metrologically derived tissue models published by Sasaki et al. in [1, 2]. These studies formed the basis for exposure regulations as established by ICNIRP, thus allowing direct comparisons to be drawn between those guidelines and this study. In addition, having real measurements at the heart of its simulation models, Sasaki et al. provides the closest reference information available to a real case. The second model, referred to as the hybrid model, combined the bottom-up model of the epidermis with the metrologically derived tissue models of the other skin layers mentioned above. The material properties of the individual cell layers of the bottom-up model were validated by comparing them with the epidermal and dermal values found therein.

■ Embedding the two skin models in FEM-based simulations, a macroscopic exposure set was established to simulate skin irradiation at frequencies between 1 GHz and 300 GHz. By analyzing the transmittance of EM waves to the skin models and assessing the EM absorption across the

individual cell layers of the epidermis, the study revealed the following findings and associated conclusions:

- The assessment of the skin models highlighted biases in the metrological representation of the epidermis in the reference model. These biases can be attributed to: (1) missectioning of the epidermis, potentially incorporating dermal components, and (2) the absence of epidermal measurements for frequencies greater than 100 GHz.
- To address the aforementioned absence of data in the reference model, the extrapolation $\underline{\varepsilon}_{\mathrm{r,ED}}(f > 100\ \mathrm{GHz}) = \underline{\varepsilon}_{\mathrm{r,ED}}(f = 100\ \mathrm{GHz})$ was considered. As a result, deviations from the hybrid model were noted at frequencies above 100 GHz. Specifically: (1) The reference model underestimated the EM energy transmitted into the skin by as much as 24 %, and (2) overestimated the absorbed EM energy within the epidermis by up to 35 %.
- Regardless of these biases, the analysis of the energy distribution across the epidermis for the entire frequency range revealed: (1) overestimation of absorption by the dead cells of the stratum corneum by up to 70 %, and (2) underestimation of absorption by the living cells of the viable epidermis by up to 60 %, depending on the cell layer examined (i.e., $K_1$ through $K_{10}$ or $C_1$ through $C_{14}$). This demonstrated the importance of accurately representing physiological changes across the epidermis in dosimetric investigations, even at a macroscopic scale.

■ After investigating the macrosopic effects of physiological changes across the epidermis, scale-back projection was applied to the hybrid model. In a twofold procedure, power was first determined for cellular microvolumes on a macroscopic scale, with these microvolumes precisely corresponding to the size and specific location of individual epidermal cells. This data was then projected onto corresponding cell models on a microscopic scale, which capture the cellular structure and histochemical composition with high detail. Applying statistical analysis to the spatial *SAR* distribution in these parametric cell models, it was possible to define a statistical *micro-SAR*, $SAR_{\mathrm{mi,K}_p/\mathrm{C}_q} = \mu_{\mathrm{SAR,mi,K}_p/\mathrm{C}_q} \pm s_{\mathrm{SAR,mi,K}_p/\mathrm{C}_q}$. This enabled the precise determination of EM absorption using the statistical average, $\mu_{\mathrm{SAR,mi,K}_p/\mathrm{C}_q}$, and the estimation of the variability of this absorption across the cellular microstructure using the standard variation, $s_{\mathrm{SAR,mi,K}_p/\mathrm{C}_q}$. Based on the extensive microdosimetric investigations conducted using scale-back projection within the 5G frequency ranges of 1-6 GHz and 24-52 GHz, the following conclusions can be drawn:

- The comprehensive comparison between $\mu_{\mathrm{SAR,mi,K}_p/\mathrm{C}_q}$ and $SAR_{\mathrm{ma,K}_p/\mathrm{C}_q}$ revealed an underestimation of epidermal absorption using conventional methods by up to 45 %, especially between 1-6 GHz where the membranes significantly contribute to the total absorption.
- In addition, the analysis of the coefficients of variation showed a surprisingly high level of variability in the microstructure. For the viable epidermis, $CV_{\mathrm{SAR,mi,K}_p}$ showed that the variability of *SAR* values ranged between 30 % and 71 % of one standard deviation, $s_{\mathrm{SAR,mi,K}_p}$, around the respective mean value, $\mu_{\mathrm{SAR,mi,K}_p}$. The corresponding analysis of $CV_{\mathrm{SAR,mi,K}_p}$ for the stratum corneum demonstrated an almost frequency-independent average variability of *SAR* values of 33 %, with an overall range from 27 % to 36 %.

Based on these findings, it has been demonstrated that scale-back projection allows the determination of more accurate exposure profiles of irradiated tissues by considering its underlying microstructure. The use of these profiles in conventional multiphysics simulations therefore has the potential to enhance the accuracy of EM dosimetry.

## 8.2 Outlook

In the subsequent section, potential directions for future research and further refinements of the approaches presented are discussed along with any associated challenges.

■ The next logical step in research is to develop hierarchical bottom-up models for the other skin sublayers: the dermis and the hypodermis. However, there are two challenges, one minor and one major, in developing such models. The minor one is the design and implementation of a dedicated

tissue scale in parametric tissue models that captures the amorphous histological organization of tissues such as the dermis. This is a process which requires detailed histoanatomical knowledge, especially if physiological changes across these layers are to be captured. How the implementation of such a tissue scale in computational models could be achieved was discussed in [A6] using the illustrative example of generic hypodermis models. In these, the amorphous histological organization, i.e. the arrangement of cells relative to each other, was modeled using computational domains that confined a large number of randomly arranged cells. The major challenge is to develop methodological approaches that bridge the organ, tissue, and cellular scales. The strategy used for the epidermis, which exploited its regular, dense histological organization to approximate the tissue as a general cell arrangement based on a primitive orthorhombic unit cell, is not applicable to other skin tissues. Consequently, the approach that allowed efficient numerical treatment using a detailed single cell model with boundary conditions that account for periodicity is no longer valid.

■ Another important endeavor is to extend the simulation environment to have multiphysics capabilities which can perform thermal simulations. A first step towards implementation would be to determine the temperature profile of the epidermis based on the micro-SAR, using $\mu_{\mathrm{SAR,mi,K}_p/\mathrm{C}_q}$ to quantify the absorption of the tissue microstructure along with the subsequent temperature increase. In the long term, the implementation of a multiscale approach to thermal simulation may also be a desirable goal to determine heat hotspots within single cells, especially in close proximity to organelle membranes.

■ A further aspect worthy of investigation would be to determine to what extent and in which frequency intervals physiological changes in the epidermis lead to impedance-matching effects that significantly influence the transmission behavior of the skin. The fact that impedance-matching properties can be attributed to the SC, depending on its thickness, has been extensively demonstrated in a recent study by Christ et al. in [34]. However, with the bottom-up model of the epidermis developed here, it would be possible to identify not only the thickness of the SC as the cause of such an effect, but also the gradual transition of the material properties from one cell layer to the next. One possible approach to investigate the impedance matching properties of the epidermis would be to quantify partial reflectance and transmittance occurring at the interfaces defined by the layered topology of the epidermis using the transfer-matrix method. This method would allow the capture of the superposition of multiple reflections and transmissions at these interfaces considering the layered structure of the epidermis. Such an approach would elucidate whether impedance matching effects arise predominantly from the pronounced material contrast at the SG/SC interface - where water concentration drops most rapidly - or from combined interactions across all epidermal cell layer interfaces. From these insights, the necessary level of detail for modeling the epidermis to accurately simulate the transmission behavior of the skin on a macroscopic scale could be determined.

■ Finally, there are potential avenues for further developing the bottom-up model of the epidermis. One significant modification would be to account for glucose levels in the extracellular medium. Such an adaptation could facilitate non-invasive monitoring of pathologies manifested by changes in the chemical composition of the extracellular medium, such as diabetes. Specifically, this would permit investigations into the sensitivity of metabolic changes to the effective macroscopic material properties within individual cell layers, paving the way for monitoring a range of pathologies non-invasively, such as novel glucose monitoring within the fingernail bed [A5].

# Part II: Experimental studies

## 9 Transmission and reflection measurements of skin samples

The outcomes from the present FSM project together with the scientific preparatory work [A29] carried out in the *MARIE TRR 196* project [N5], but also our longstanding research expertise in the field of multiscale EM skin modeling [A31, A32, A33] has enabled us acquire several complementary research projects with a distinct affinity to mm-wave/THz dosimetry: *terahertz.NRW* [N1], *6GEM* [N2], and *TRICorder* [N3], where the latter encompasses the preparatory research for the DFG excellence cluster proposal *insighTHz* [N4], which is currently under review. Within the framework of *6GEM* and *TRICorder* we have purchase relevant high-end microwave measurement equipment for the dosimetric assessment of biological tissue layers, which lies way beyond the budget of the FSM project.

### 9.1 Analysis of the high-precision transmission and reflection measurement systems

The two purchased MCK setups from *SWISSto12 SA* [P2] consist both of a circular corrugated horn antenna-based transmission measurement setup, where one of the antennas is mounted on a linear translation stage as shown in Fig.9.1 and thus allows for a form-fit insertion of the measurement sample in its central gap. A nice overview of the overall MCK measurement system is shown in the following animation: https://youtu.be/OZLNENg1Q-U. The operating frequencies of the purchased MCK setups covers the frequency range from 26.5 GHz to 40 GHz (WR28, $K_a$ band) and from 110 GHz to 170 GHz (WR6, D band). Additional MCK systems for complementary frequency bands up 1100 GHz are accessible from project partners within the mentioned project collaborations [N1, N3, N5].


*Fig.9.1: The material characterization kit (MCK) from SWISSto12 [P2] is a dielectric material characterization solution based on high-precision transmission/reflection mm-wave measurements under controlled and thus highly reproducible conditions. The acquired setups operate in the ranges from 26 GHz to 40 GHz (WR28, Ka band) and 110 GHz to 170 GHz (WR6, D band), whereas the first setup addresses the 5G frequencies under investigation. The material probe is fitted into the gap between the two horn antennas.*

The determination of the material parameter, specifically the complex permittivity, relies on the utilization of the *Baker-Jarvis (BJ)* algorithm [43], which is embedded in the firmware of the MCK system. Notably, the firmware exhibits shortcomings in accurately addressing the *systematic power leakage* introduced by the Device Under Test (DUT) in the small antenna gap. This deficiency may lead to potential overestimation of the loss tangents or imaginary parts of the dielectric function. To rectify this issue, a custom implementation of the BJ algorithm, designed to be more precise and controllable, was incorporated. The BJ algorithm [43] operates on the transmission/reflection method, comprehensively considering the entire behavior of scattering quantities resulting from the interaction with the DUT within the antenna gap across the frequency spectrum of interest. In contrast, the well-known *Nicholson-Ross-Weir (NRW)* algorithm [40, 41] and its modified version [42] typically rely on a shortened transmission line approach. However, the NRW algorithm's stability in frequency behavior is compromised, especially for low-loss materials, making it potentially inaccurate [44]. As a result, the BJ algorithm is deemed superior in such cases. In the following comprehensive investigations have

been carried out in order to (i) inquire for the proper algorithmic assessment of the complex dielectric function based on the comprehensive NIST reports elucidating different aspects/versions of the BJ algorithm [45, 46, 47], and (ii) in conjunction with an experimental study on the power leakage from the small antenna gap where the test sample is usually form-fitted into [A3].

## 9.2 Parasitic radiation leakage in the MCK characterization setup

This study [A3] marks the first quantitative investigation into the phenomenon of parasitic radiation traversing through the sample into free space within the sandwiched antenna-sample-antenna configuration of the material characterization kit MCK from SWISSto12 [P2]. The analysis of the time-averaged Poynting vector, derived from conducted nearfield (NF) measurements, provides evidence supporting the existence of the hypothesized parasitic radiation. Furthermore, this conclusion is confirmed through independent far-field (FF) measurements (not shown in this section).

The cylindrical measurement setup (CMS), employed to demonstrate the presence of parasitic radiation emanating through the gap [Fig. 9.2 (b)] occupied by the sample into free space, is presented in Fig. 9.2 (a). In this configuration, the MCK setup designed for operation in the WR28 waveguide band has been disassembled and streamlined to its fundamental components. These components include two corrugated circular horn antennas, complete with the transition to a coaxial port, all attached to an optical rail. The so reduced MCK is then affixed to the CMS, which facilitates independent movement through five stages corresponding to a cylindrical coordinate system. These stages consist of two concentric rotational stages for azimuthal adjustments, two linear stages aligned with different radial axes – one of which is mounted on the inner rotational stage and can thus be rotated – and a linear stage in the axial direction. As depicted in Figure 9.2 (b), the two antennas have been positioned with a separation gap distance $d$, facilitating the measurement of the electric $[E_\rho, E_\alpha, E_z]^T$ or magnetic $[H_\rho, H_\alpha, H_z]^T$ near-field (NF) in cylindrical coordinates. This measurement is conducted within distinct regions: Region ① (above the waveguiding region), region ② (above the plane metal plates at the antennas faces), and region ③ (outside the MCK). The specific positions for measuring the near-field in each region are illustrated in Figure 9.2 (c), where NF-probes are moved accordingly. The coordinate system is illustrated in Figure 9.2 (c).

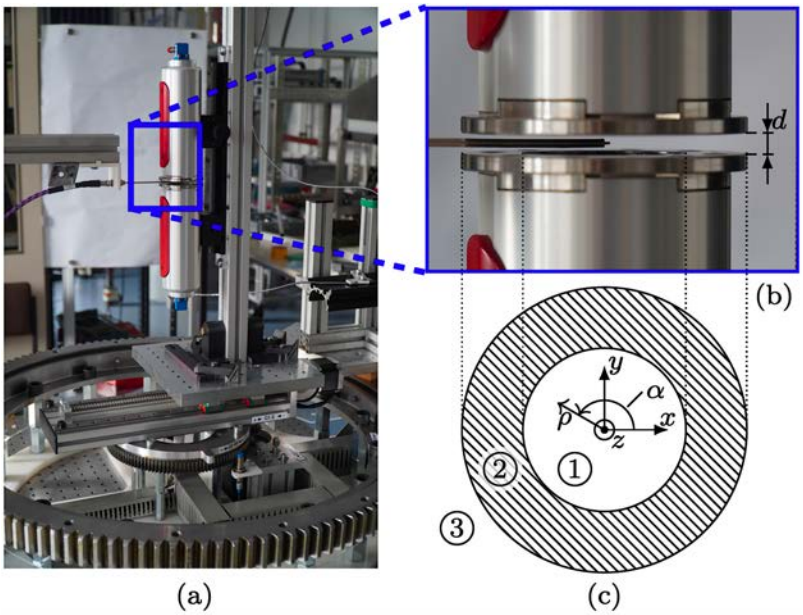


*Fig.9.2: (a) Introduction to the compact MCK in a mounted and aligned state on the cylindrical measurement system (CMS). (b) Close-up view of the near-field (NF) probe positioned precisely at the center of the gap (z = 0) with a width of d between the two corrugated horn antennas. (c) Sketch of the top view of one antenna in the z = 0 plane, featuring the coordinate system utilized throughout this document. Regions ①, ②, and ③ correspond to areas above the antenna, above the metal sheet at the antenna's front face, and external to the MCK, respectively [A3].*

For the experimental measurements, we utilized two home-made near-field (NF) probes, as illustrated in Figure 9.3 (a). These probes were constructed using a commercially available coaxial cable (HUBER+SUHNER SUCOFORM 86) with polytetrafluoroethylene as the dielectric material. The inner and outer conductor radii were specified as 0.53 mm and 2.1 mm, respectively, ensuring single-mode operation within the desired WR28 waveguide band. The first probe, referred to as the *E*-probe and magnified in Figure 9.3 (b), is designed to be sensitive to a z'-directed electric field [according to the coordinate system in Figure 9.3 (d)]. This sensitivity is achieved by allowing the inner conductor to protrude open-ended by approximately 1.6 mm. Conversely, the second probe, known as the *H*-probe and magnified in Figure 9.3 (c), is engineered to be sensitive to a y'-directed magnetic field [as shown in Figure 9.3 (d)]. This sensitivity is achieved by bending the protruding inner conductor into an approximately semicircular loop with an inner radius of 0.5 mm, effectively short-circuiting the inner and outer conductor.

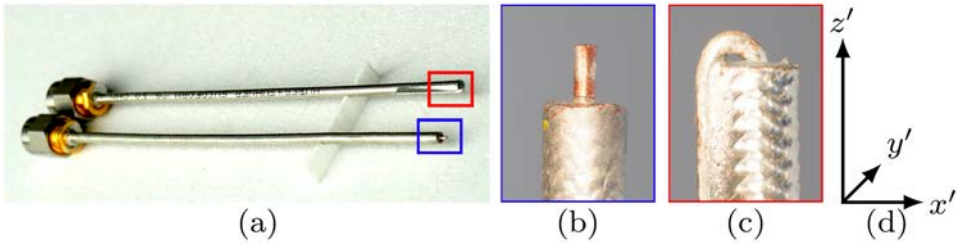


*Fig.9.3: (a) Image of the electric and magnetic near-field (NF) probes created in-house; (b) presents a micrograph of the lower probe, designed to detect an electric field directed along the z' axis; while (c) showcases a micrograph of the upper probe, sensitive to a magnetic field directed along the y' axis; (d) introduces the orientation of the coordinate system [A3].*

Despite the *E*-probe's superior performance, we chose the *H*-probe for measuring the field in region ② due to the presence of the antenna's metal faces in the $z = \pm d/2$ plane. In this plane, a predominant *z*-polarized electric field exists preventing the *E*-probe from effectively capturing and measuring this field. Hence, the *H*-probe was considered more suitable for this scenario. In Fig. 9.4, the radial electric field component ($E_\rho$) magnitude in region ① and the azimuthal magnetic field component ($H_\alpha$) magnitude in region ② are illustrated at the $z = 0$ plane (center of the gap between antennas). These measurements were conducted for a gap width of $d = 5$ mm [refer to Fig. 9.2 (b)] across the WR28 frequency band. In region ①, where the *E*-probe outperforms the *H*-probe (as seen in Fig. 9.4), the results reveal a *y*-polarized electric field of the circular horn antennas predominant $HE_{11}$ mode, notably indicated by the vanishing magnitude at $\alpha = 0°$.

However, in region ②, the presence of the antenna's metal faces in the $z = \pm d/2$ plane suggests a prevailing *z*-polarized electric field, which cannot be measured with the *E*-probe. Consequently, a vanishing *z* component of the magnetic field is anticipated in this region. Hence, the *H*-probe is employed to measure the azimuthal magnetic field $H_\alpha$ in region ②. The results reveal a significant coupling from the electromagnetic field in the MCK characterization setup's guiding region to a radial parallel-plate waveguide represented by the gap region and, subsequently, to free space yielding the undesired power leakage. It's evident that this coupling is heavily influenced by the sample clamped between the antennas, thereby impacting the obtained results.

To showcase parasitic radiation from the gap into free space, we simulated the time-averaged Poynting vector– a representation of active power flow – outside the MCK. The electric field components $[E_\rho, E_\alpha, E_z]^T$ were measured at $\rho \in \{40\text{mm}, 41\text{mm}\}$, $z \in \{-0.5\text{ mm}, 0.5\text{ mm}\}$, and $\alpha \in [-80°, 120°]$ using the *E*-probe. The time-averaged Poynting vector $\mathrm{Re}\{\boldsymbol{S}\}$ was then calculated from these measured values according to

$$\mathrm{Re}\{\boldsymbol{S}\} = \mathrm{Re}\left\{-\frac{j}{2\omega\mu_0}[\boldsymbol{E} \times (\nabla \times \boldsymbol{E})^*]\right\} \tag{9.1}$$

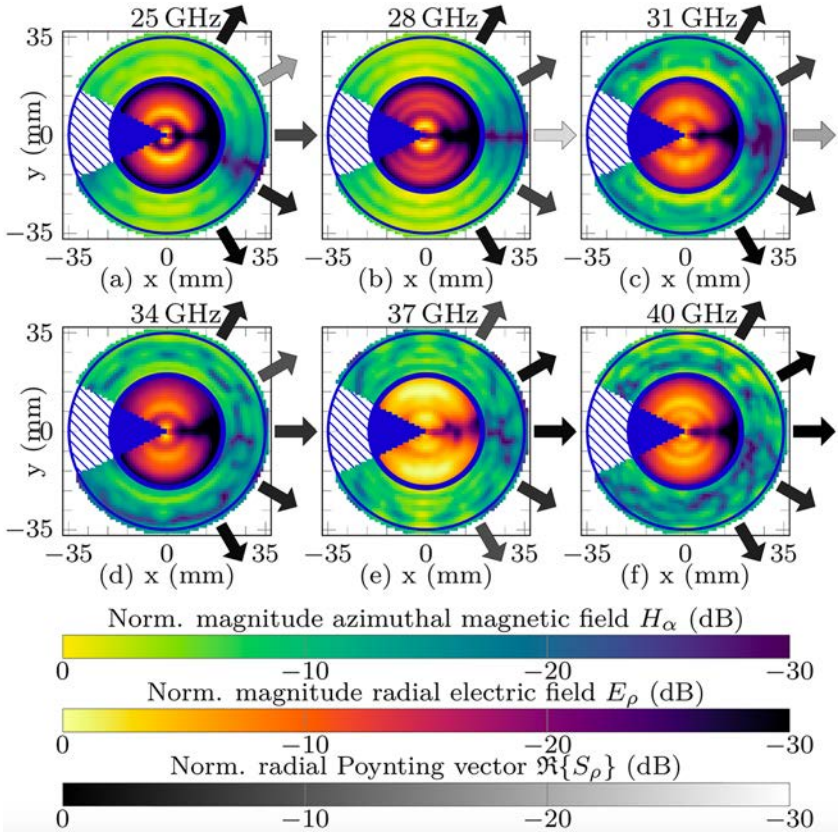


*Fig.9.4: Measured near-fields: The normalized radial component of the electric field, $E_\rho$ (dB), is depicted in the gap at a distance of d = 5 mm. This representation encompasses region ① (within the inner blue circle). Additionally, the normalized azimuthal component of the magnetic field, $H_\alpha$ (dB), is shown for region ② (between the two blue circles). The color intensity in the figure indicates the magnitude (in dB), and the gray arrows indicate the direction of the predominant radial component of the time-averaged Poynting vector $S_\rho$ [refer to Fig. 9.5]. It's noteworthy that the field in the blue-filled area (region ①) and the hatched area (region ②) could not be measured due to the specific mechanical fixture in place [A3].*

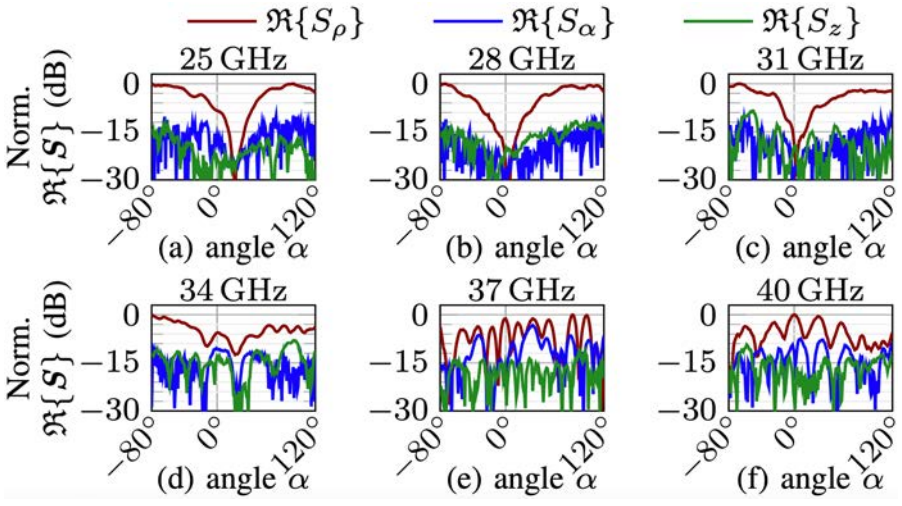


*Fig.9.5: Radiation pattern of the power leakage from measured near-fields (NFs): direction components of the time-averaged Poynting vector Re{**S**} = R{[$S_\rho$, $S_\alpha$, $S_z$]$^T$} at ρ ≈ 40 mm and z = 0 calculated from the measured electric near-field at ρ ∈ {40 mm, 41 mm}, z ∈ {−0.5 mm, 0.5 mm}, and polar angles α ∈ [−80°, 120°] [A3].*

The resulting directional components of the time-averaged Poynting vector are presented in Fig. 9.5, highlighting the predominant radial component. This corresponds to radiation emanating from the gap between the two corrugated circular horn antennas into free space, as indicated by the gray intensity of the arrows in Fig. 9.4. Lastly, the far-field radiation pattern (not shown here) retrieved from the measured nearfield components with a subsequent near-to-far-field transform yielded an $E_z$-polarized radiation, further confirming the occurrence of parasitic radiation into free space through the gap of the MCK setup.

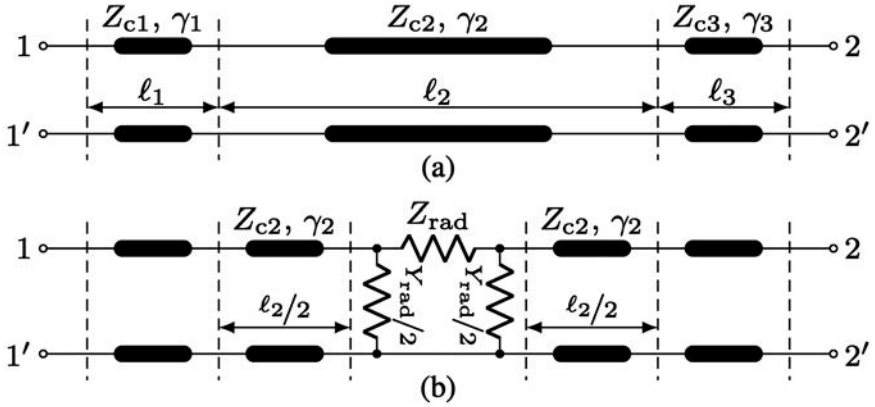


*Fig.9.7: (a) Electrical equivalent circuit (EC) of the MCK setup for material characterization typically comprising three waveguide sections. The sections of length $\ell_1$ and $\ell_3$ are the accessing waveguides filled with a known dielectric, while the section of length $\ell_2$ represents the material under test (MUT). $Z_{c1}$, $Z_{c2}$, and $Z_{c3}$, along with $\gamma_1$, $\gamma_2$, and $\gamma_3$, stand for the characteristic impedances and propagation constants of the respective regions. (b) EC model of a comparable setup where the sample is form-fitted into a gap between the two corrugated circular horn antennas. The lumped elements $Z_{rad}$ and $Y_{rad}$ offer a simplified model to account for the E-coupling and H-coupling to the emerging radial parallel-plate waveguide (gap between the antennas), which ultimately radiates into free space. [A3].*

To avoid mistakenly attributing radiation as dielectric loss within the material under test (MUT), it is crucial to consider the junction to the radial parallel-plate waveguide in the *algorithmic framework* of the numerical material retrieval procedure. A simplified equivalent circuit (EC) model is depicted in Fig. 9.7, where Fig. 9.7 (a) represents the typical, namely idealized waveguide-based transmission and reflection measurement setup and Fig. 9.7 (b) models the used antenna-based setup comprising the radiating gap region. The latter is modelled by incorporating lumped elements $Z_{rad}$ and $Y_{rad}$, which address *E*-coupling and *H*-coupling to the radial parallel-plate waveguide, accounting for the resulting radiation losses. Using the described setup, the losses and their EC representations are in principle experimentally accessible. However, this basic model adds complexity to the calculation of material parameters since $Z_{rad}$ and $Y_{rad}$ may vary with frequency, with the material properties, and with both, the shape and placement of the MUT. Particularly for low-loss (and high permittivity) materials, neglecting radiation can introduce a significant systematic error. The goal of our current research is to incorporate the model shown in Fig. 9.7 (b) into the BJ material retrieval algorithm described in [45, 46, 47], which is neither straight-forward nor easy to implement.

### 9.3 A look through artificial human tissues at the Ka- and D-band

Human skin with its surface of around 1.5-2.0 $m^2$ and a weight of approximately 3.3-4.0 kg is the largest organ of the human body. Human tissue is difficult to access for experimental purposes such as e.g. exposition measurements in the 5G and 6G frequency range (Ka band: 26.4-40 GHz; D band: 110-170 GHz). In our study [A13] we therefore employ two tissue phantom samples from *SynDaver Labs* (https://syndaver.com), as illustrated in Fig. 9.8. The samples, labeled «2 N» and «4 N» versions of skin, have thicknesses of 1 mm and 1.3 mm, respectively, with/without subcutaneous fat layers measuring either 3 mm or 5 mm. Designed to mimic different body regions, these samples replicate living human tissue properties, including mechanical stiffness, thickness, and penetration forces. Composed of salt, water, and fiber, they simulate human tissue conditions. The 2 N and 4 N penetration force values represent typical pain thresholds and imitate soft skin areas like the face, groin, or forearm. The 4 N sample simulates higher skin toughness, resembling regions like the abdomen or back. Thicker samples generally correspond to areas with greater skin toughness. It's crucial to note that these artificial tissues lack certain details, such as nerves, blood vessels, or hair follicles.

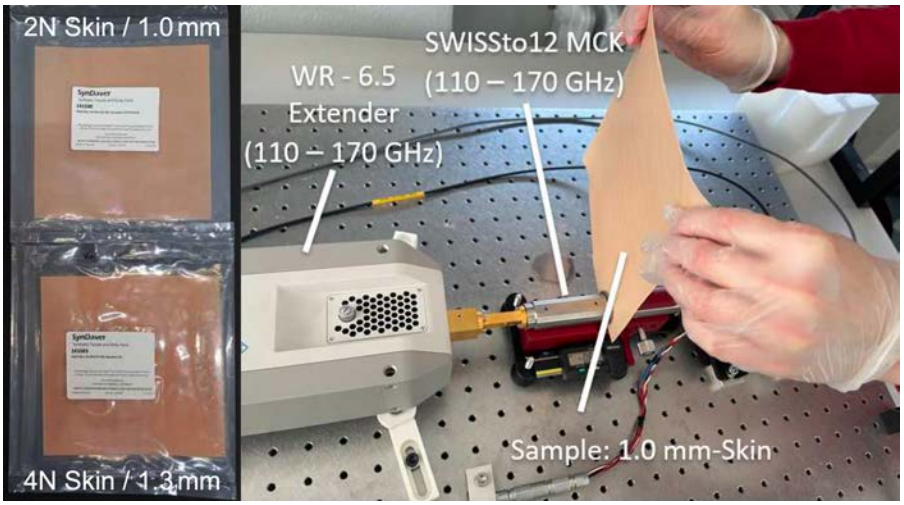


*Fig.9.8: Characterization of artificial human tissue: (left) artificial skin samples from Syndaver Labs delivered as 20 × 20 cm patches; (right) the SWISSto12 characterization setup with a test sample using the particular MCK kit specified for the D band together with a VNA and two corresponding frequency extenders [A13].*

The VNA integration in the MCK system involves a two-stage calibration process. Initially, the two-port short calibration method establishes error-correcting reference planes at the ends of the waveguides respective corrugated horn antennas by using a metallic shim as a short circuit to normalize the reflection coefficient $S_{11}$ of the S-parameters. Following that, the «thru» calibration connects the two waveguides of the VNA with the SWISSto12 MCK to record the normalized transmission coefficient $S_{21}$. It's crucial to acknowledge that, akin to any measurement device, uncertainties may be present in the measurement of S-parameters for this MCK setup. These uncertainties are contingent on factors such as sample contouring, thickness, roughness, and the incident direction of the electro-magnetic wave with respect to the tissue's layer structure.

In contrast to the direct standard of the MCK kit, the calibration involves two measurement steps involving the spectral response $S_{21}$ of the empty gap, which is then complemented by the measurement of the artificial tissue sample that is form-fitted into the same gap (the order of measurements is usually the other way round to retrieve the real sample thickness). The penetration loss $T_p$ (i.e. the net power loss factor of the proper tissue sample) is achieved according to

$$T_p^{[dB]}(\omega) = S_{21}^{[dB]}(\omega)\Big|_{air\ gap} - S_{21}^{[dB]}(\omega)\Big|_{tissue\ sample} \qquad (9.2).$$

The variations in the transmission coefficients is influenced by factors such as wavelength, time delay from reflections, sample thickness, and mechanical uncertainties when holding the samples accordingly in the MCK setup. In the D-band frequency range, the typical dynamic range for measurements is 85 dB, while it is 80 dB for Ka-band measurements. A linear regression curve is thus introduced [blue line in Fig. 9.9 (left)] in order to contribute to a reliable representation of the peneration loss, which demonstrates a monotonically increasing and frequency-dependent trend for all samples in the Ka- as well as in the D-band. Despite the increasing trend, differences in losses for the same tissue sample remain relatively constant when comparing start, center, and stop frequencies, as indicated in Fig. 9.9 (right).

| Sample | Frequency (GHz) | *Tp* (dB) |
|---|---|---|
| Skin 2N (1.0 mm) | 25 | 17.42 |
| | 32.5 | 18.09 |
| | 40 | 19.21 |
| | 110 | 16.85 |
| | 140 | 13.13 |
| | 170 | 13.78 |
| Skin 4N (1.3 mm) | 25 | 19.41 |
| | 32.5 | 20.37 |
| | 40 | 20.98 |
| | 110 | 18.74 |
| | 140 | 19.32 |
| | 170 | 21.87 |

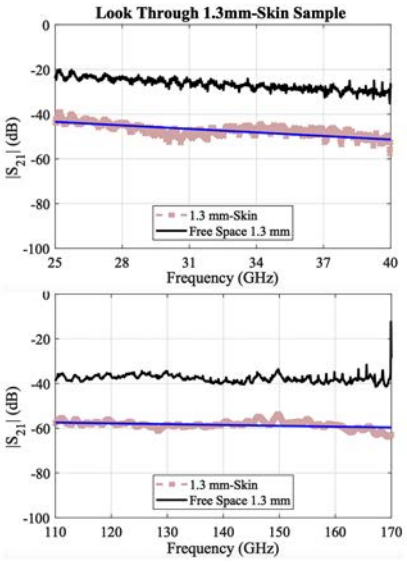


*Fig.9.9: Results of the transmission measurements through the artificial skin samples: (right) a (representative) spectral response of the transmission factor $S_{21}$ for the empty gap (air) in the MCK kit depicted as black curve together with the $S_{21}$ spectrum for the corresponding tissue layer (4N: 1.3 mm) represented by the purple curve for both, the Ka- (top) and the D-band (bottom). The latter includes a fit to a linear penetration loss model indicated by the blue line; (left) extracted penetration loss $T_p$ for the two artificial tissue layers at start, center, and stop frequencies of the Ka- respective the D-band [A13].*

As mentioned, penetration losses increase with higher frequencies and thicknesses. Specifically, the 1.0 mm thick skin phantom exhibits a decreasing trend in the D-band. This underscores the challenge of detecting penetration losses in thin tissue phantoms, as they demonstrate nearly constant losses, especially in the case of artificial skin. Following the interpretation also stated in [A8] the penetration loss in the D-band displays lower values compared to the Ka-band, which seemingly contradicts the fact that penetration depths tends to get considerably smaller for higher frequencies especially towards mm-waves (cf. Part I and in particular [A6], and Part III with [A1, A2, A8]). This may be attributed to the following issues when aiming beyond the Ka-band: (i) the skin sample as a whole shows a potential decrease in the reflection behavior, (ii) the tissue microstructure of the artificial tissue itself absorbs less power. Both are speculative claims that have to be further investigated. Nevertheless, it's worth emphasizing, that the artificial tissue phantom involved here, is still far from a natural human skin, when higher frequencies come into play. This is valid regarding both, the skin's macrostructure with its distinct layers and the underlying cellular microstructure. The artificial skin phantom involved here is based on a multi-layer 3D printing or a micro-weaving fabrication process using natural plant fibers to mimic mechanical consistency, thermal conductivity, skin color, different ethnicities, and – as claimed in the corresponding product description – to reproduce the electrical properties of the corresponding skin. As *SynDaver Labs* discloses any further details concerning the proper manufacturing and in particular of their sample's microstructure, artificial skin is therefore not well suited for the EM microdosimetry respective its experimental validation. Hence, exposure studies on real tissue samples from e.g. pig skin are thus heavily investigated.

## 9.4 Material characterization of pig tissue samples

### 9.4.1 Characterization of sausage slices as test scenario

In order to get e grip to the material characterization of the pig skin samples in the light of the power leakage issues mentioned in Section 9.2 with respect to the proper handling of these soft tissue samples a first measurement was carried out with two different meat samples, namely Lyonnais sausage slices and salami slices. The samples are measured as layer stacks with increasing slice number (i.e. with increasing sample thickness) in order to deduce the associated attenuation factors in the framework of a well-known cutback measurement scenario. These measurements were carried out virtually at the edge frequencies of the $K_a$ band and they involve appropriate time gating to manage residual reflections in the waveguide- respective horn antenna-based measurement setup. The results are depicted in Fig.9.10.

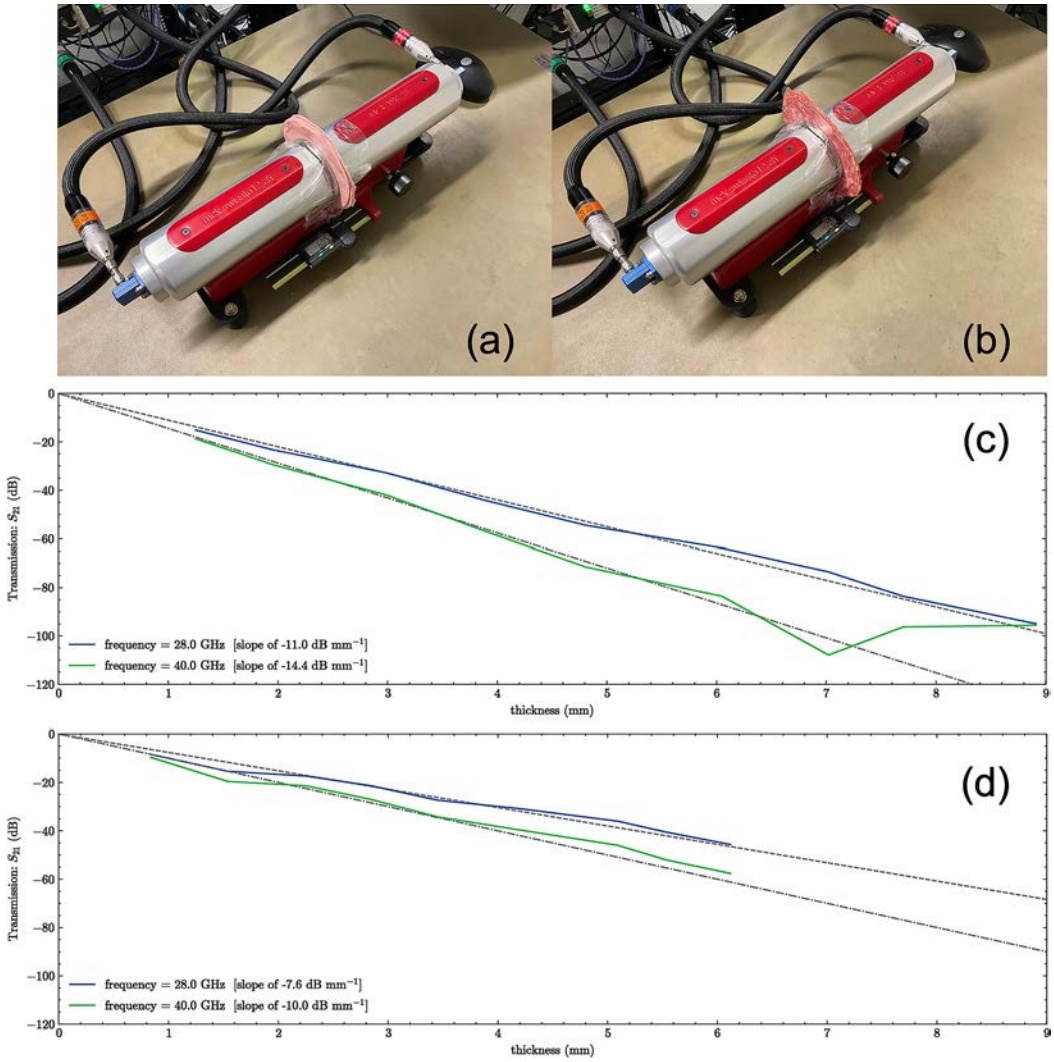


*Fig.9.10: Cutback measurements with stacked sausage slices: (a) 6-fold stacked Lyonnaise meat sausage sample (6.05 mm) in the SWISSto12 MCK setup; (b) 6-fold stacked salami sample (4.20 mm); (c) transmission factor $S_{21}$ at 28 GHz (blue) and 40 GHz (green) as a function of the Lyonnais sausage sample thickness (cutback measurement); transmission factor $S_{21}$ at 28 GHz (blue) and 40 GHz (green) as a function of the salami sample thickness (cutback measurement).*

For the Lyonnais sausage we got attenuation factors of 11 dB/mm @ 28 GHz and 14.4 dB/mm @ 40GHz, whereas the salami sample reveals attenuation factors of 7.6 dB/mm @ 28 GHz and 10 dB/mm at 40 GHz. With these figures it is possible to determine the electromagnetic energy uptake in any of the samples with a given thickness when using a corresponding propagation model associated to the Beer-

Lambert law. The results correspond well to the expectations that higher operation frequencies yield higher attenuation factors and that the coarsly structured salami with its large fat inclusions seems more «transparent» than the fine-structures Lyonnais meat sample.

### 9.4.2 Data processing and calibration procedure in conjunction with the MCK system

In view of the pig skin samples to be measured, we provide a short outline of the calibration and measurement process for the MCK transmission/reflection setup, along with postprocessing of scattering parameters. This is a refined reiteration of procedure already described in the 2nd project report [A18]. Our system's firmware is built upon our customized extension to the BJ algorithm [43]. Initially, the calibration involves two reference measurements for S-parameters $S_{11}$ and $S_{21}$. A short-circuit measurement employs a metal plate inserted into the MCK waveguide system gap, while a through-connection measurement directly connects open-ended waveguides respective corrugated horns without any gap. During measurement, the material under test (MUT) is gently inserted into the MCK-system gap (cf. Fig. 9.1). Due to the absence of a torque screw, maintaining low pressure is crucial for reproducibility, especially with our soft tissue samples. Excessive pressure may cause inaccurate MUT thickness readings and a distorted probe surface. The MUT thickness ($t_{MUT}$) is determined using the system's built-in precision caliper, seen in Figs. 9.1 and Fig. 9.10. Spreading thicknesses and non-flat surfaces are excluded from subsequent calculations due to their potential impact on measurement accuracy, representing systematic errors.

The reflection coefficient is normalized by dividing it by the reflection coefficient of the initial short-circuit measurement. Similarly, the transmission coefficient of the material under test (MUT) is normalized to the transmission coefficient of the through-connection. These normalizations set the reference plane at the open-ended waveguide respective horn antennas' position. The time domain representation shows main reflection and transmission events at $t$ = 0, corresponding to the proper MUT's reflection and transmission factors. A Kaiser-Bessel windowing function with a shape factor $\alpha$ = 5 (similar to the Hamming window) and a width of 400 ps centered at $t$ = 0 is applied as a time gate filter. This ensures that only strong relevant reflections are retained. The resulting normalized and time-gated scattering parameters are presented in Fig. 9.10 and Fig. 9.11. The firmware in the SWISSto12 MCK system allows for adjusting the spectral margin to manage this influence.

The measured, now normalized and time-gated reflection and transmission coefficients $S_{11}$ and $S_{21}$ of the MUT are finally applied to the following complex valued equation, given by Baker-Jarvis et. al. [43], which is based on an intrinsic transmission line model of the MUT, where one section of length $t_{MUT}$ stands for the gap section filled with the MUT:

The normalized and time-gated reflection ($S_{11}$) and transmission ($S_{21}$) coefficients of the material under test (MUT) are then used in subsequent complex-valued equation (9.3) following Baker-Jarvis et al. [43]. This equation is derived from an intrinsic transmission line model of the MUT, where a section of length $t_{MUT}$ represents the gap filled with the MUT.

$$S_{21} + \beta\, S_{11} = \frac{T\cdot\left(1-\Gamma^2\right) + \beta\ \Gamma\cdot\left(1-T^2\right)}{1-T^2\Gamma^2} \tag{9.3}$$

where $\beta$ is a weighting factor that defines the contribution of the transmission and reflection coefficients in the analysis for both parameter sets, namely for the measurement and for the transmission line model. $T$ stands for the transmission coefficient and $\Gamma$ is the reflection coefficient of the modelled intrinsic MUT section, which are defined as following

$$T = \mathrm{e}^{-\gamma\cdot t_{MUT}} \tag{9.4}$$

$$\Gamma = \frac{\gamma_0-\gamma}{\gamma_0+\gamma} \tag{9.5}$$

where the following quantities

$$\gamma_0 = \frac{j\omega}{c_0} \tag{9.6}$$

$$\gamma = \frac{j\omega}{c_0 \cdot \sqrt{\varepsilon_r' - j\varepsilon_r''}} \tag{9.7}$$

are the propagation constants of vacuum and of the MUT, respectively. The complex relative permittivity, encompassing real part $\varepsilon_r$' and imaginary part $\varepsilon_r$", is determined from equation (9.3). This equation generates a set of non-linear equations that necessitates numerical solving through a fixed-point iteration for each frequency point. An initial guess for the complex permittivity is estimated from literature data at the center frequency of the spectral range. For stability, each subsequent iteration at a given frequency point starts with the solution from the previous point. The algorithm initiates at the center frequency and iterates in both directions, towards lower and higher frequencies. The starting position is chosen at the center frequency to minimize side-lobe levels, given the spectral window of the time gate filter and the confined spectral dataset. The initialization of the fixpoint iteration using a reasonable guess of the weighting factor $\beta$ is the most crucial issues of this retrieval algorithm. A pragmatic but knowledge-based approach in this regard is currently under intense investigation.

### 9.4.3 Characterization of pig skin samples

Based on the elucidations made in Section 9.4.2 different sample of pork rind have been analyzed. In the following two exemplary samples of pig skin are documented, namely sample A with a thickness of 3.90 mm and sample B having a thickness of 3.89 mm as shown in Fig. 9.11. At these thicknesses both skin samples cover all the characteristic skin layers (such as SC, E, D, and HYP) representing a correspondingly asymmetric inhomogeneity with respect to the propagation direction. This leads to a further problem, since (i) the dielectric functions determined are to be understood as effective quantities and (ii) the respective reflection coefficients on both sides of the sample are therefore unequal.

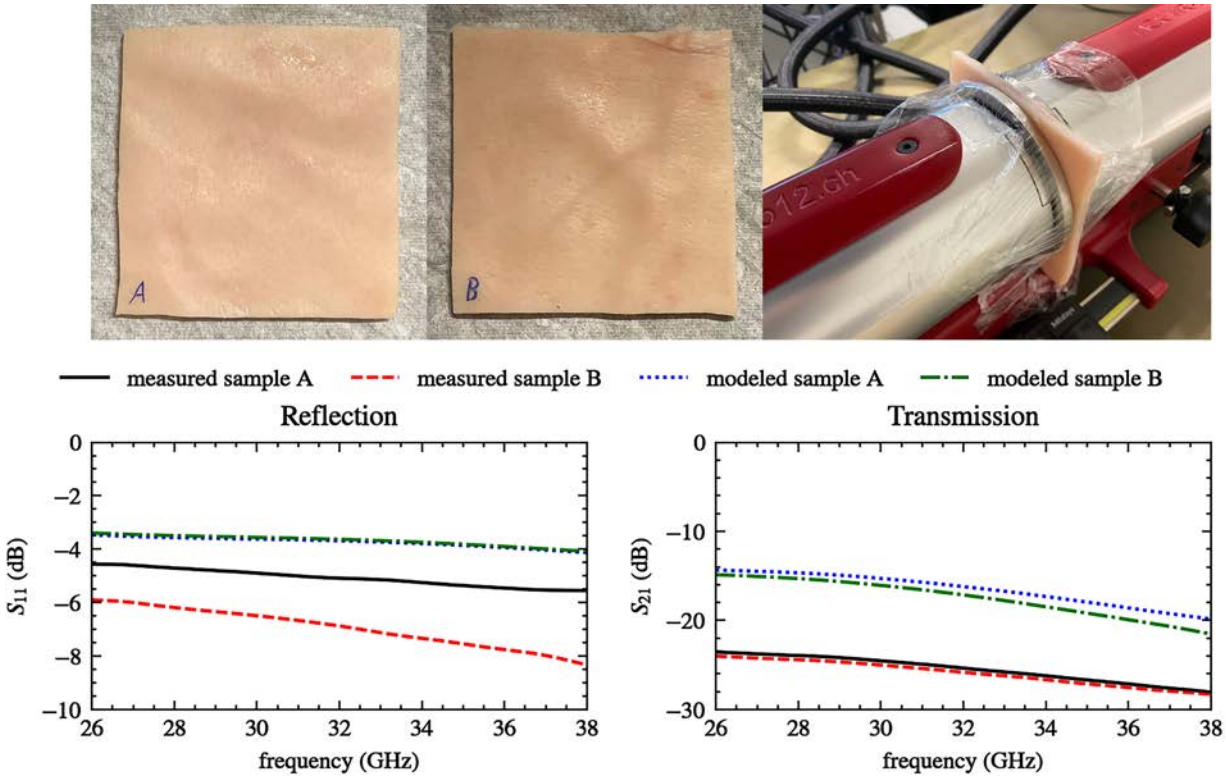


*Fig.9.11: Transmission and reflection measurements at two different pig skin samples: (top row) top views on sample A (thickness 3.90 mm) and sample B (thickness 3.89 mm), and close up of the MCK setup with sample A; (bottom row) spectral responses of the reflection and transmission factor showing measured (black, red) and modeled (blue, green) curves.*

The latter is not foreseen in the standard BJ algorithm [45, 46, 47] used here, as the algorithm is conceptualized for homogenous material probes. Hence reliable compromises are needed, which puts a pragmatic stance on the formal material parameter retrieval procedure. In our setup the skin surface facing the SC is accessed by waveguide port 1 (shown at the front in Fig. 9.11, top right) whereas the backside of the skin encompassing D or more likely HYP is in contact to waveguide port 2, yielding a considerable difference between the $S_{11}$ and $S_{22}$ parameter. For the retrieval of the dielectric function, namely its real part $\varepsilon_r'$ and imaginary part $\varepsilon_r''$, the choice of $S_{11} \coloneqq S_{22}$ has been made, while also modeling the spectral responses of the reflection and transmission factors (in a corresponding transmission line model of the sample) for a resulting homogenous skin probe. These quantities, namely the measured and modeled S-parameters are used for observation in the framework of the above-mentioned pragmatism together with the one mentioned in Section 9.4.2 in conjunction to the weighting factor $\beta$ that quantifies the contribution of the reflection spectra in comparison to the transmission spectra [cf. eq. (9.3)] for the retrieval of the dielectric function. With the found best value of $\beta$ = –20 dB, the influence of the stated choice of the reflection factors gets virtually negligible. The resulting dielectric functions of the two pig skin samples A and B are displayed in Fig. 9.12.

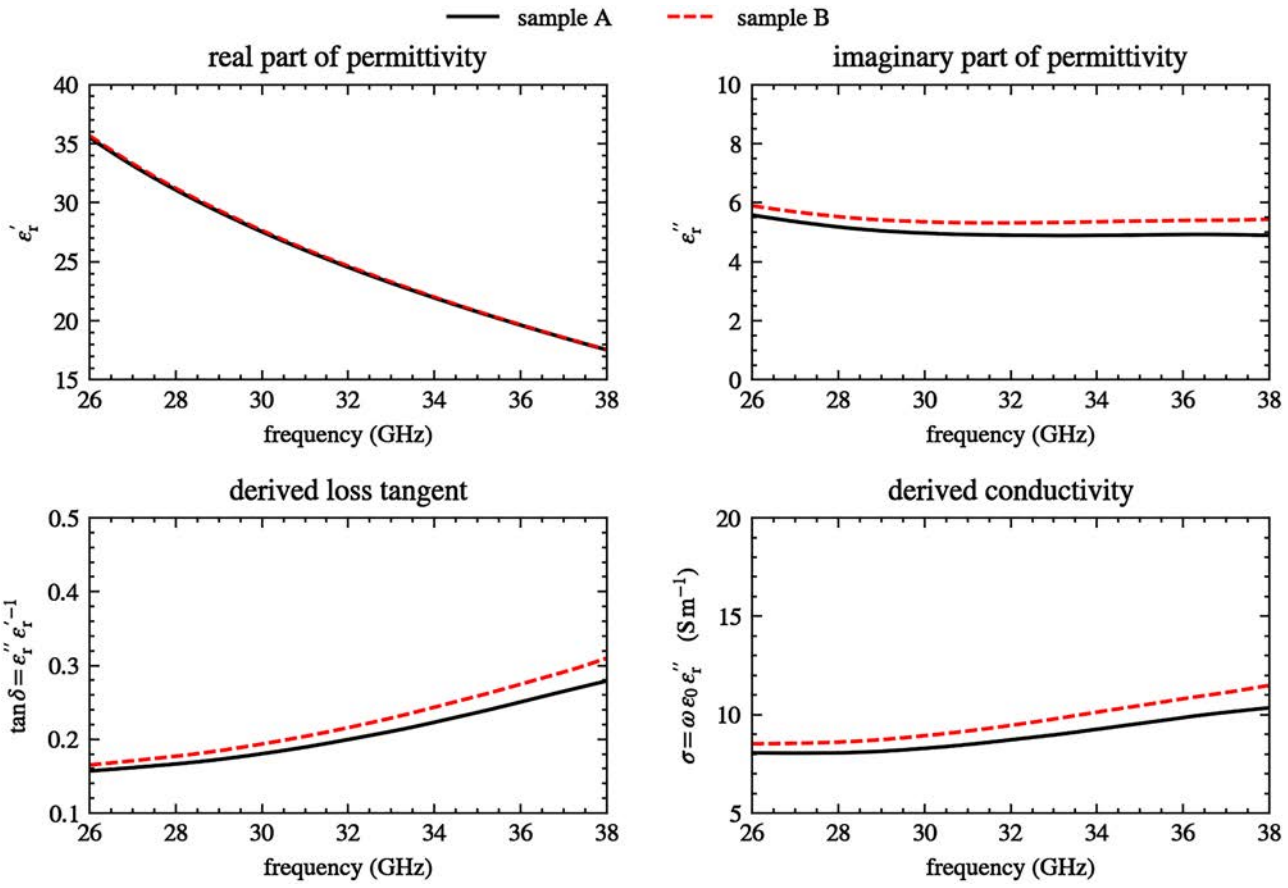


*Fig.9.12: Experimentally retrieved dielectric function of the pig skin samples A and B within the $K_a$-band: (top row) real part $\varepsilon_r'$ and imaginary part $\varepsilon_r''$ of the permittivity together with the loss quantities, namely tan$\delta$ and the associated conductivity $\sigma$.*

Please note that the earlier spectral responses of the transmission factors $S_{21}$ in Fig. 9.9 of Section 9.3 do not directly correspond to the $S_{21}$ spectra shown here in Fig. 9.11 due to distinctly differences in the normalization respective calibration philosophies. On a conceptional level, the current spectra of Fig. 9.11 agree better to what has been termed as penetration loss $T_P$ in Section 9.3, which translates to levels of the transmission factor of around –20 dB (for a thickness of the artificial skin layer of 1.3 mm). The material characterization of human tissue respective the estimate of electromagnetic energy uptake in the corresponding tissue probe given a predefined exposure power density remains also a central part of our ongoing and future bioelectromagnetics research activities.

## 9.5 Conclusion and outlook

### 9.5.1 Characterization of skin samples

As elucidated in the prior Section 9.3 with respect to artificial skin samples and in Section 9.4 on the analysis of pig skin tissue, our studies define an important leap towards the characterization and the dosimetric analysis of human skin. Hence, we are still one small step too short in in terms of a conclusive verification of the proposed virtual model-based microdosimetry. Nevertheless, thanks in part to the FSM project, we have been able to carry out various externally funded research projects [N1, N2] that will enable us to continue this research. In the framework of the collaborative project 6GEM [N2] we could purchase the automatized mm-wave near-field scanner setup consisting of the vectorial *EUmmWVx* probe from *SPEAG* (cf. Section 9.5.2. and [P3]) which has been recently installed in our lab. In addition we also got funding to install our *ATE BioEM Center* (https://www.uni-due.de/ate-bioemcenter/) [A19] that allows us to pool research project activities and experimental resources under this umbrella. We have also applied for a DFG Cluster of Excellence in the DFG Excellence Strategy with our large collaborative project *«insighTHz»* [N3, N4], which will be partly dedicated to biomedical sensors [A12, A32] and monitoring of plants and insects [A10, A11, A14, A15, A19, A20], where the interaction of EM waves at mm-wave/THz frequencies with a variety of biological tissue types will play a key role in these future research efforts.

### 9.5.2 Robotized near-field scanner setup with accurate vectorial E-field probe

The *6GEM* [N2] project facilitated the acquisition of an automated millimeter-wave near-field scanner setup, comprising the vectorial *EUmmWVx* field probe from SPEAG in conjunction with a robot arm (i.e. the advanced *DASY8 MP8B TX2-60L* system) [P3]. This configuration enables spatially-resolved electric field scans, leading to the derivation of power density scans at respective sample surfaces. The scanner system operates at frequencies from 750 MHz to 110 GHz and maintains a positional accuracy of 0.1 mm. The mm-wave probe scans the *E*-field with 2 mm distance from test sample (free space) and deduces power density, *H*-field and far-field analysis using total field reconstruction. The system was installed in the last week of November 2023 (see Fig. 9.13) and, with its spatially resolved scanning capabilities, represents an important experimental measure for verifying our virtual microdosimetry of skin tissue.

*Fig.9.13: The DASY8 MP8B TX2-60L system [P3]: (left) front view of the robotized scanner setup; (right) typical scene during installation and corresponding instructions by the SPEAG personnel also showing the controller unit in the background.*

### 9.5.3 Scanning coaxial mm-wave near-field probes

As discussed in the previous research report [A18] we had also started constructing our own near-field probes. To achieve a high spatial resolution, compact home-made coaxial probes, approximately 500 µm in footprint has been developed within the framework of the CRC/TRR 196 MARIE project [N5]. Operating as a transmission line, the coaxial line lacks a lower cutoff frequency but has an upper cutoff around 500 GHz. The coaxial line terminates in a short respective an open circuit at its far end, functioning as a miniature *H*-field respective *E*-field probe [A9]. The system employs two WR3 waveguides (220-330 GHz), with the coaxial probes mounted on a movable precision *xyz*-stage. This setup is an integral part of our in-house (hemi-) spherical millimeter-wave/THz antenna/reflectometry measurement system [A28]. We have successfully fabricated reliable waveguide transitions for rectangular waveguide-to-coaxial line connections in WR3 waveguides and have upgraded them for the WR28 (26.5-40 GHz) waveguide system in order to address the lower 5G frequency range together with suitable *H*- and *E*-field probes, where the latter have been already depicted in Fig. 9.3.

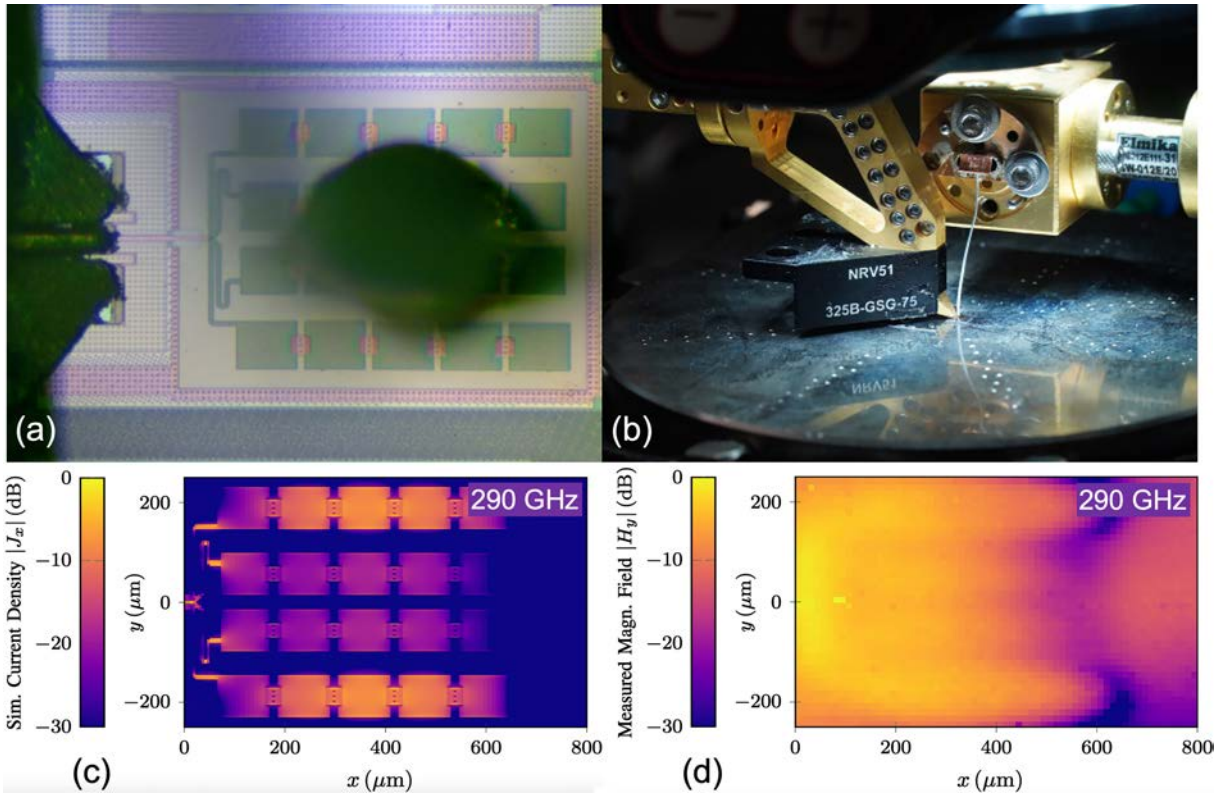


*Fig.9.14: On the resolution of the home-made near-field probes: (a) Example of a traveling-wave chip antenna array; (b) scanner setup with H-probe on antenna chip; 3D-FDTD simulations of the current density distribution in the antenna structure; (d) 2D-scanned $H_y$-field component just few µm above the surface [A9].*

An exemplary near-field measurement of a traveling-wave antenna array realized onto a SiGe chip has been carried out at 290 GHz [A9]. Fig. 9.14 documents the overall measurement scenario with the resulting 2D-near-field scan of the emergent *H*-field in Fig. 9.14 (d).

The presented experiment is exemplary for an inherent resolution issue, where the latter is also effective in the corresponding 5G frequency range (e.g. into the $K_a$-band): The «footprint» of the coaxial near-field probe is still too large to get a correspondingly resolved near-field scan, given the lateral extent of the underlying coaxial cable. Currently we are working on deconvolution procedures applied to the 2D image data looking for suitable point spread functions given associated to the coaxial probe's fields. This is mandatory in order to achieve a sufficient spatial resolution in the near-field scans of correspondingly illuminated tissue probes, which is now part of our current activities.

# Part III: A numerical 5G/6G exposition study

## 10 Gender-specific electromagnetic power absorption in human skin tissue

This investigation involved the uniform modeling of human skin across six distinct body regions (abdomen, back, breast, dorsum of foot, dorsum of hand, and scalp) for both male and female subjects within a homogeneous ethnic population. The work relies on a turkish dermatological study, where the thicknesses of the epidermis, dermis, and total skin from the assigned body regions have been measured (cf. Fig. 10.1) with a new ethical histometric technique [48]. Hence, the skin models were structured into the following 4 layers: stratum corneum (SC), epidermis/dermis (E+D), hypodermis (HYP), and muscle (MUSC) tissue involving in total 180 human skin tissue probes from 15 male and 15 female body donors. Subsequently, the twelve deduced skin models underwent exposure to electromagnetic (EM) waves within the 5G respective 6G frequency ranges. The study focused on the simulation of gender-specific power absorption and penetration depths in the skin tissue layers for each assigned body region [A1, A2, A8]. The operating frequency in our study include the standard 5G bands, namely the ranges 5G NR/FR1 (≤ 7.125 GHz) and 5G NR/FR2 (24.25-71 GHz), as well as the range up to 100 GHz.

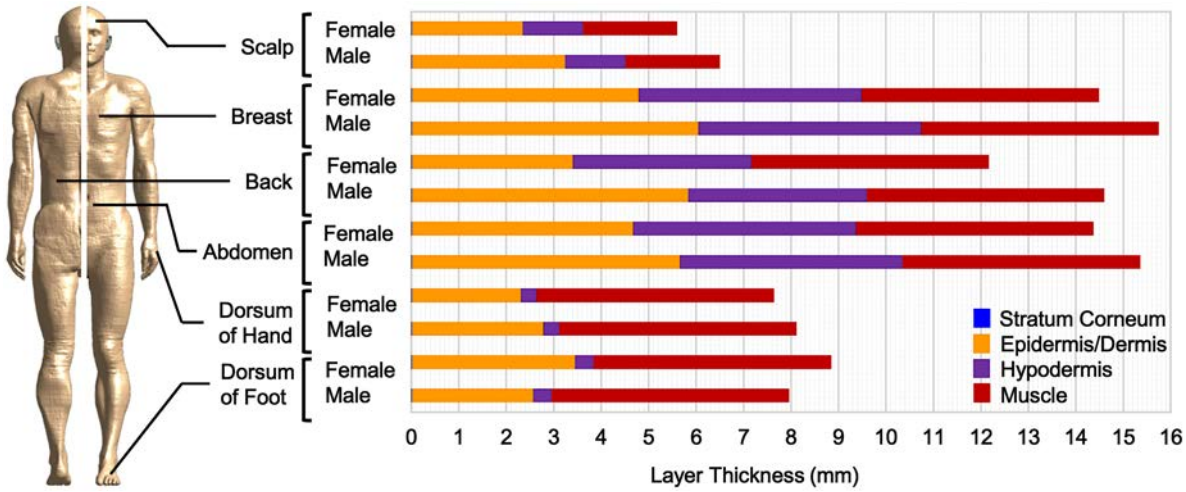


*Fig.10.1: Layer thicknesses from skin samples according to a Turkish dermatological study [48], which are retrieved from the 6 different indicated body parts of 15 female and 15 male body donors [A2, A8].*

The resulting 4-layer skin model is numerically analyzed as a 2D computational electromagnetics problem using the COMSOL Multiphysics simulation software [3], which is based on the Finite Element Method (FEM). The skin model is exposed to a plane wave with a power flux equivalent to 1 W/m$^2$ within the frequency range of 1-100 GHz. The subsequent analysis focuses on examining the integrated absorbed power within each layer and evaluating the penetration depths. The corresponding results for the penetration depths are given in Figs. 10.2 and 10.3, where Fig. 10.2 displays the electric field profiles from which the penetration depths were retrieved. The corresponding values at the given frequencies amount to: ≫ 8 mm @ 1 GHz; 7.61 mm @ 6GHz; 1.10 mm @ 24 GHz; 0.42 mm @ 71 GHz; 0.35 mm @ 100 GHz. The comprehensive results are shown in Fig. 10.3 for all female and male skin probes at the same distinct frequencies. This figure clearly indicates that in the 5G NR/FR2 range irrespective type of skin probe (≥ 24 GHz) the power is absorbed within the epidermis/dermis layer. As stated in Part I on the microdosimetric investigation of the human skin, the most vital layer is the *stratum basale* (SB) in the epidermis (E) where the keratinozytes are generated and proliferate towards the skin surface within roughly 30 days. This is the reason why future research should focus on the epidermis (E) and in particular to its sub-structure comprising the stratum spinosum (SS), stratum granulosum (SG) and the outmost stratum corneum (SC). The absorbed power integrated across the respective skin layers is depicted in Fig. 10.4, revealing a noticeable gender-specific distinction.

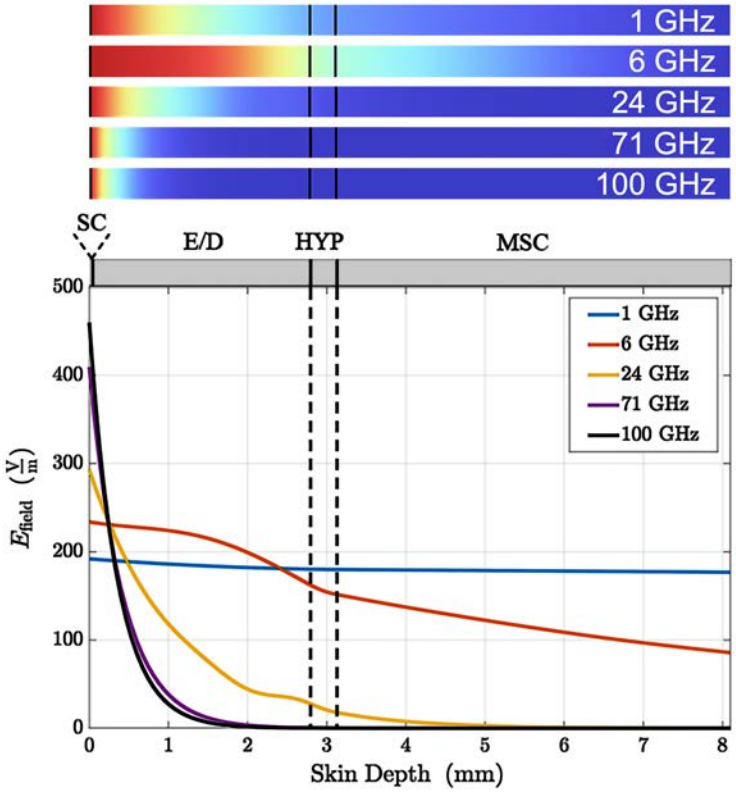


*Fig.10.2: Simulated skin penetration at a male dorsum of hand; (top) the color scale uses a relative calibration for each of the electrical field data at its corresponding frequency; (bottom) the electrical field profiles of the penetration scenario where the skin surface is at the outmost left. The associated retrieved penetration depths are given in the text [A1, A8].*

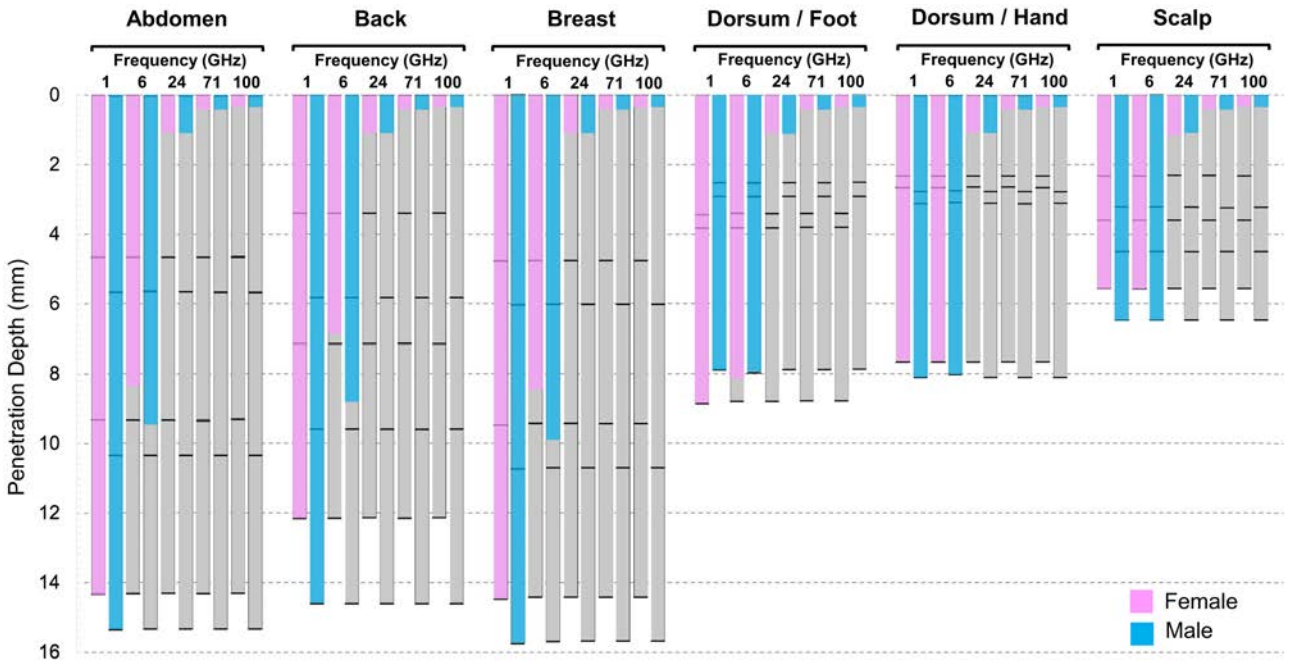


*Fig.10.3: Simulated skin penetration depths at 5 distinct frequencies in the 5G/6G range according to the skin models of the 6 different body regions [A2, A8]. For operating frequencies of 24 GHz and above, only the SC and E+D skin layers are permeated.*

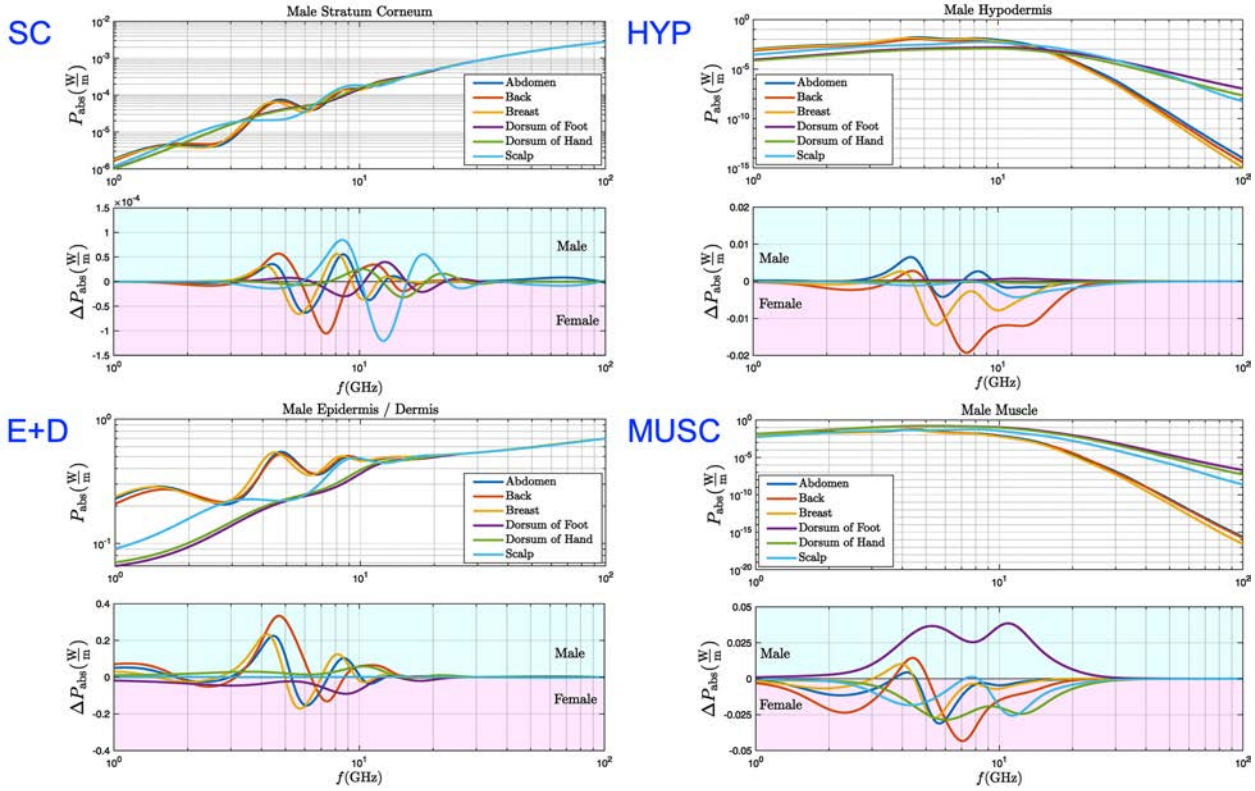


*Fig.10.4: Simulated power absorption in the 4 specific skin layers, namely stratum corneum (SC), Epidermis and Dermis (E+D), Hypodermis (HYP), and muscle tissue (MUSC) for the male/female skin tissue samples at the 6 different body locations (i.e. abdomen, back, dorsum of foot, dorsum of hand, and scalp). The power absorption is explicitly displayed only for the male tissue probes but together with the differences of the power absorption to the one in the corresponding female tissue probes. The spectral responses of the differences in power absorption may be interpreted as the following: Negative curve sections (ranging into the purple region) indicate a dominant absorption in the corresponding layer of the female tissue probe, whereas a positive curve sections (ranging into the light blue region) stands for a dominant absorption in the corresponding layer of the male tissue probe. [A1, A2, A8].*

The differences in the power absorption are defined as the female data subtracted from the male data yielding positive values for a dominant absorption in the corresponding layer of the male tissue, whereas vice versa negative values stand for a dominant absorption in the corresponding layer of the female tissue. This is conceptualized in Fig. 10.4 using light blue (male) respective purple (female) color shading to visualize the dominant gender specific power absorption. While inspecting Fig. 10.4 on the simulated power absorption within the 4 specific skin layers in the different skin probes the following becomes evident. The most significant gender-specific differences occur in a distinct frequency band between 3-25 GHz. Hence, only the 5G NR/FR1 range is therefore affected. The stratum corneum (SC) shows on average an indifferent gender specificity, which seems comprehensible as the electromagnetic field has to transfer through the SC first before interacting with any subsequent gender-specific layer structure. Looking now at the E+D layers reveals that the male samples absorb more radiation power on average, which is due to the larger thicknesses of the E+D layers in the male tissue probes (an exception is the dorsum of foot, where the situation is reversed, namely the female tissue probes undergo a larger power absorption in the E+D layer). It is therefore not surprising, that there is a dominance of power absorption in the subsequent layers HYP and MUSC of the female tissue probes, as their E+D layer seems more «transparent» with respect to EM power transfer.

Our future studies are currently scrutinizing the gender-specific analysis with a loser look to the detailed skin layer structure. This includes the distinction between the epidermis (E) and the dermis (D) layer as well as their distinct sub-layers in the epidermis (E) and the stratum corneum (SC). We shall also carry out comparative gender- and ethno-specific exposure studies based on our tissue model including the comprehensive data sets on the skin thicknesses of Korean [49] and Chinese [50] adults.

## 11. Conclusions and outlook

With reference to the envisaged tasks (cf. Fig.11.1) as described in the project proposal [A30] the following conclusions can be drawn:

**■ Task 1 – Setup of simulation workbench with hierarchical multi-scale EM skin model**

- T1.1 – Setup of the comprehensive hierarchical multi-scale EM model of the skin: The simulation workbench is operational with respect to the bottom up multiscale EM skin modeling. This includes also the *microscopic* model of idealized keratinocytes with their subcellular structure as well as their differentiation in sub-layers with regard to the stratum basale (SB), stratum spinosum (SS), stratum granulosum (SG) and stratum corneum (SC) [A17]. The associated *macroscopic* material model for the specific skin tissue layers are available from (i) bottom-up multiscale modeling, and (ii) from corresponding literature. The model now allows also the differentiation of field exposure and power absorption including *micro-SAR* with respect to the modeled cell compartments.

- T1.2 – Setup of the overall simulation workbench of the exposure scenario: The simulation workbench regarding its link to the exposure scenarios is operational including for the relevant skin layers and their inner differentiation (i.e. epidermis with sub-layers).

- T1.3 – Definition of volumetric boundary conditions (based on mean field quantities): This essential task within the scale-back projection from the exposure scenario into the skin's microstructure is operational using (i) stochastic measures such as the *expectation value* of the E-field (mean field) within the cell under different polarizations as quantity to be rescaled/fitted to the E-field of the corresponding EM simulation of the macroscopic multilayer skin model. As an alternative (ii) the *potential difference/voltage* across the unit cell in the quasi-static microscopic model is retrieved from the power that is absorbed within a corresponding unit cell volume of a keratinocyte (i.e. in the vital basal layer), where this power absorption is determined from the corresponding exposure simulation of the macroscopic multi-layered skin model. These averaged values are thus used as calibration quantity between the microscopic cell model and the macroscopic multi-layer skin model.

- T1.4 – Model validation: A reliable validation of the simulation workbench based on corresponding experiments such as e.g. transmission measurements in the 5G frequency range using corresponding skin samples have been carried out. Reference simulations with *sim4life* were carried out supported by the bachelor thesis [T11] and are be complemented by the research activities envisaged in the *6GEM* project [N2]. Nevertheless, we are still one step too short in in terms of a conclusive verification of the proposed virtual model-based microdosimetry. This will be in the focus of our further experimental investigations, where our near-field scanners may play a crucial role.

**■ Task 2 – Setup of numerical microdosimetry in the microstructure/at the cell level**

- T2.1 – Parametrized cell model: The cornerstone to this task lies in the (sub-) cellular model of the keratinocyte as described in T1.1. The histochemical parametrization allows of different derivatives of this cell's shape and structure according to the layer-wise differentiation of the epidermis according to the stratum basale (SB), stratum spinosum (SS), stratum granulosum (SG) and stratum corneum (SC). This includes in particular keratinocytes in the epidermis (E) with its division in 10 sub-layers and corneocytes in the stratum corneum (SC) with its 14 sub-layers. The corresponding compartmentalization of the cell allows for the separation of the various contributions to the energy intake in the (sub-) cellular structure and facilitates to study the influence of relevant cellular domains on the macroscopic material properties of the corresponding tissue layer [A17].

- T2.2 – Scale-back projection: The scale-back projection, namely the linkage of the data from the macroscopic exposure scenarios to the modelled quantities in the microstructure (respective vice versa) has been carried out in the framework the virtual microdosimetry (i.e. numerical microscopic exposure analysis of keratinocytes in the epidermis). This model scenario is now apt to be linked to experimental exposure settings as foreseen in Task 3. This has not yet been carried out, but is foreseen in our further research activities.

**■ Task 3 – Microdosimetric assessment of mm-wave/5G exposure levels**

- T3.1 – Critical assessment of homogeneous multilayer skin models: Various reference simulations of EM exposure in multilayer skin models have been carried out in order to provide reference data to be compared to those from the virtual microdosimetry as well as to insect exposure, which is investigated in the framework of our joint project *terahertz.NRW* [N1]. A critical assessment of homogeneous multilayer skin models [32, 33] which are widespread in current EM skin dosimetry at 5G/mm-wave frequencies with respect of the inherent tissue inhomogeneities has been started using precise transmission and reflection measurements at various tissue samples. The used MCK kit was be further analyzed and calibrated in order to get reliable material parameters (i,e, dielectric functions) due to an inherent systematic power leakage out of the sample volume. The assessment of the macroscopic skin model is now going on is planned to be part of a further research collaboration with activities carried out by the group of Dr. Jürg Fröhlich.

- T3.2 – Exposure overview study of the tissue's microstructure: A first stochastic analysis of EM exposure within the parametrized cellular structure of keratinocytes has been performed using the model as described in Task 2. This model was linked to illumination scenarios with measures such as the power density. The systematic variations in the exposure limits based on the inhomogeneities given by the tissue's and corresponding cellular microstructure have been estimated within a stochastic analysis of the first two skin layers (E) and (SC). This has been carried out in the framework of a systematic numerical exposure study for the frequency range 1-300 GHz with a detailed look into the ranges of 1-6 GHz and 24-54 GHz. Subsequently, quantified the variations of the *micro-SAR* originating from the cellular microstructure of the skin and assessed how they potentially influence the *SAR* exposure limits set by ICNIRP [3] for 5G frequencies. As an example, the CV of the *micro-SAR* within the basal layer turned out to amount to 58 % at 3.5 GHz, which is in the 5G NR/FR1 band.

**■ Task 4 – Experimental validation**

- T4.1: Setup of the transmission and reflection measurement system with tailored sample holders: Measurements on various meat tissue samples (chicken, beef) have been carried out in the D band in order to accurately assess the inherent problem of power leakage in the gap of the *SWISSto12* MCK transmission/reflection measurement setup. This has been scrutinized within further, more realistic experimental studies, which encompassed precise transmission/reflection measurements with the MCK test kit in both, the $K_a$- and D-band, using tissue samples like Lyonnais sausage slices, salami slices, artificial skin and pig skin. A rotary azimuthal near-field scan of the MCK kits gap region (where the material sample is usually form-fitted into) in the $K_a$-band confirmed a significant power leakage out of the characterization setup, which will give rise to a systematic overestimation of the dissipative part of the retrieved dielectric function [A3]. A model-based implementation of this dissipative contribution into the BJ algorithm for a correspondingly corrected retrieval of the dielectric function is currently being investigated. It's worth mentioning that this is far from trivial as the correction has always to cope with very large bandwidths.

- T4.2: Experimental validation of the multiscale tissue simulation workbench (in transmission): A first step on the experimental validation of the simulation workbench in the framework of a frequency-scaled, tailored randomized water-air composite layer made of water-filled straws was already reported in the 1. Status Report [A25]. This activity is complemented by further research

on the full-wave analysis of large sets of randomized scatterers. Here we developed one of the currently fastest full-wave electromagnetic (EM) simulators based on the *Recursive Aggregated Centered T-Matrix Algorithm (RACTMA)* for the ultra-efficient analysis of large random aggregates of arbitrary cylindrical scatterers (more than 3000) at speeds of 250 (up to several thousand) different excitations per second [A7, A10]. This allows to tackle realistic surface systems consisting of large aggregates of randomized scatterers/unit cells. As mentioned in T3.1 the critical assessment of the homogeneous multilayer skin models at 5G/mm-wave frequencies implemented in the simulation workbench based on corresponding experiments is currently under investigation.

- T4.3: Exposure experiment series on tissue samples at 5G/mm-wave frequencies: Preparatory work for spatially resolved exposure experiments have earlier been carried out by designing 3 different near-field probes for 2D surface scans of the skin tissue surface, which will be illuminated from the back side. These approaches included a dielectric near-field probe based on 3D-printed rectangular dielectric waveguides, coaxial H-respective E-field probes for the 220-330 GHz frequency band (upper cutoff at 500 GHz) and the $K_a$-band (26.5-40 GHz), together with a microstrip line-based two-wire mm-wave H-field probe. All home-made near-field probes have resolution issues (in particular the dielectric ones). The footprints of the coaxial probe's near fields are considerably large and compromises the resolution of the near-field scans. Further investigations on a refined spatial resolution using deconvolution schemes with associated corresponding point-spread functions are currently under investigation. An promising solution to this problem is given by our new near-field scanner from SPEAG with its corresponding firmware, which will improve our near-field capabilities considerably. The recently installed robotized near-field scanner system *DASY8 MP8B TX2-60L* carries the vectorial field probe *EUmmWVx* operating in the D-band (110-170 GHz). Prospective measurement campaigns with spatially-resolved exposure experiment at 5G and higher frequencies will be carried out in the framework of *6GEM* [N2].

  Numerical study on 5G exposure: A comprehensive numerical exposure study based on a Turkish dermatological data set of skin layer structures from 15 male and 15 female body donors unveiled a gender-specific electromagnetic power absorption in human skin tissue in particular in the distinct frequency band between 3-25 GHz [A1, A2].

- T4.4: Prospective dosimetric THz measurements: These experimental campaigns at THz frequencies have not yet been carried out but are officially foreseen in two of our large joint research projects, namely *6GEM* [N2] and *terahertz.NRW* [N1].

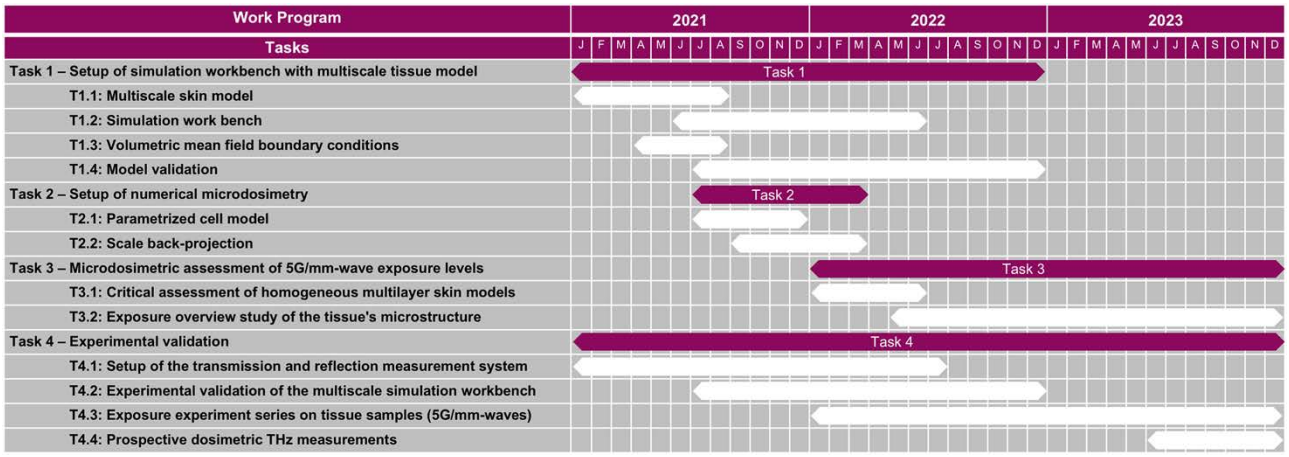


*Fig.11.1: Time table of the project [A30] indicating the corresponding project tasks and their timeline.*

# 12. Bibliography and lists

## 12.1 List of references

[1] K. Sasaki, M. Mizuno, K. Wake, and S. Watanabe, “Monte Carlo simulations of skin exposure to electromagnetic field from 10 GHz to 1 THz,” *Phys. Med. Biol.,* vol. 62, no. 17, p. 6993–7010, 2017, doi: 10.1088/1361-6560/aa81fc.

[2] K. Sasaki, K. Wake, and S. Watanabe, “Measurement of the dielectric properties of the epidermis and dermis at frequencies from 0.5 GHz to 110 GHz,” *Phys. Med. Biol.*, vol. 59, no. 16, p. 4739–4747, 2014, doi: 10.1088/0031-9155/59/16/4739.

[3] "Guidelines for limiting exposure to electromagnetic fields (100 kHz to 300 GHz)," Int. Comm. on Non-Ionizing Radiation Protection, ICNIRP Publication, *Health. Phys.*, vol. 118, no. 5, pp. 483-524, 2020, doi: 10.1097/HP.0000000000001210.

[4] "Guidelines for limiting exposure to time-varying electric and magnetic fields (1 Hz to 100 kHz)," Int. Comm. on Non-Ionizing Radiation Protection, ICNIRP Publication, *Health Phys*., vol. 99, no. 6, pp. 818-836, 2010, doi: 10.1097/HP.0b013e3181f06c86.

[5] Dr. H. Jastrow, "Workshop Anatomy for the Internet," http://www.drjastrow.de.

[6] K. A. Holbrook and G. F. Odland, “Regional differences in the thickness (cell layers) of the human stratum corneum: an ultrastructural analysis,” *J. Inv. Derm.*, vol. 62, no. 4, pp. 415–422, 1974, doi: 10.1111/1523-1747.ep12701670.

[7] A. J. Klein-Szanto, “Clear and dark basal keratinocytes in human epidermis: A stereologic study,” *J. Cut. Path*., vol. 4, no. 5, pp. 275-280, 1977, doi: 10.1111/j.1600-0560.1977.tb00916.x.

[8] H. Pinkus, “Examination of the epidermis by the strip method of removing horny layers. I. Observations on thickness of the horny layer, and on mitotic activity after stripping,” *J. Invest. Dermat*., vol. 16, no. 6, pp. 383-386, 1951, doi: 10.1038/jid.1951.45.

[9] N. S. Penneys, “Location of proliferating cells in human epidermis,” *Arch. Dermat*., vol. 101, no. 3, pp. 323-327, 1970, doi: 10.1001/archderm.101.3.323.

[10] G. D. Weinstein, J. L. McCullough, and P. Ross, “Cell proliferation in normal epidermis”, *J. Invest. Dermat.*, vol. 82, no. 6, pp. 623-628, 1984, doi: 10.1111/1523-1747.ep12261462.

[11] M. R. Gdula, K. Poterlowicz, A. N. Mardaryev, A. A. Sharov, Y. Peng, M. Y. Fessing, and V. A. Botchkarev, “Remodeling of three-dimensional organization of the nucleus during terminal keratinocyte differentiation in the epidermis,” *J. Invest. Dermat*., vol. 133, no. 9, pp. 2191-2201, 2013, doi: 10.1038/jid.2013.66.

[12] P. Corcuff, C. Bertrand, and J. L. Leveque, "Morphometry of human epidermis in vivo by real-time confocal microscopy," *Arch. Dermat. Res.*, vol. 285, no. 8, pp. 475-481, 1993, doi: 10.1007/BF00376820.

[13] G. Kroemer, L. Galluzzi, P. Vandenabeele, J. Abrams, E. S. Alnemri, E. H. Baehrecke, M. V. Blagosklonny, W. S. El-Deiry, P. Golstein, D. R. Green, M. Hengartner, R. A. Knight, S. Kumar, S. A. Lipton, W. Malorni, G. Nuñez, M. E. Peter, J. Tschopp, J. Yuan, M. Piacentini, B. Zhivotovsky, and G. Melino, “Classification of cell death: recommendations of the Nomenclature Committee on Cell Death 2009,” *Cell Death & Differentiation*, vol. 16, no. 1, pp. 3-11, 2009, doi: 10.1038/cdd.2008.150.

[14] L. Chrit, P. Bastien, G. D. Sockalingum, D. Batisse, F. Leroy, M. Manfait, and C. Hadjur, “An in vivo randomized study of human skin moisturization by a new confocal Raman fiber-optic microprobe: assessment of a glycerol-based hydration cream,” *Skin Pharm. Phys.*, vol. 19, no. 4, pp. 207-215, 2006, doi: 10.1159/000093116.

[15] P. W. Wertz, “Stratum corneum Lipids and Water,” *Exog. Dermat*., vol. 3, no. 2, pp. 53-56, 2004, doi: 10.1159/000086155.

[16] L. Chen, G. Lian, and L. Han, “Use of bricks and mortar model to predict transdermal permeation: Model development and initial validation,” *Ind. Eng. Chem. Res.*, vol. 47, no. 17, pp. 6465–6472, 2008, doi: 10.1021/ie701711v.

[17] Sonja Huclova, *Modeling of cell suspensions and biological tissue for computational electromagnetics*. *Diss. ETH Zürich*, No. 19863, Zürich, July 18, 2011, doi: 10.3929/ETHZ-A-006711951.

[18] R. R. Warner, M. C.Myers, and D. A. Taylor, “Electron probe analysis of human skin: determination of the water concentration profile,” *J. Inv. Derm.*, vol. 90, no. 2, pp. 218–224, 1988, doi: 10.1111/1523-1747.ep12462252.

[19] S. Grayson and P. M. Elias, “Isolation and lipid biochemical characterization of stratum corneum membrane complexes: implications for the cutaneous permeability barrier,” *J. Inv. Derm.*, vol. 78, no. 2, pp. 128–135, 1982, doi: 10.1111/1523-1747.ep12505953.

[20] H. Fischer, I. Polikarpov, and A. F. Craievich, “Average protein density is a molecular-weight-dependent function,” *Histoch. and Cell Bio.*, vol. 13, no. 10, pp. 2825–2828, 2004, doi: 10.1110/ps.04688204.

[21] R. Moll, M. Divo, and L. Langbein, “The human keratins: biology and pathology,” *Protein Sci.*, vol. 129, no. 6, pp. 705–733, 2008, doi: 10.1007/s00418-008-0435-6.

[22] T. Gouw and J. C. Vlugter, “Physical Properties of Triglycerides. I. Density and Refractive Index,” *Europ. J. Lipid Sci. Tech.*, vol. 68, no. 7, pp. 544–549, 1966, doi: 10.1002/lipi.19660680705.

[23] N. Betzalel, P. Ben Ishai, Y. Feldman, “The human skin as a sub-THz receiver – Does 5G pose a danger to it or not?” *Environ. Res*., vol. 163, May 2018, doi: 10.1016/j.envres.2018.01.032.

[24] O. Spathmann, M. Zang, J. Streckert, V. Hansen, M. Saviz, K. Statnikov, U. Pfeiffer, and M. Clemens, "Numerical computation of temperature elevation in human skin due to electromagnetic exposure in the THz frequency range," *IEEE Trans. Terahertz Sci. Technol*., vol. 5, no. 6, pp. 978-989, Nov. 2015, doi: 10.1109/TTHZ.2015.2476962.

[25] T. Z. Rizvi and M. A. Khan, “Temperature-dependent dielectric properties of slightly hydrated horn keratin,” *Int. J. Biol. Macromol.*, vol. 42, no. 3, pp. 292–297, 2008, doi: 10.1016/j.ijbiomac.2008.01.001.

[26] C. Reid, *Spectroscopic methods for medical diagnosis at terahertz wavelengths*, Ph.D. Dissertation, University College London, London, UK, 2006.

[27] MATLAB® (v. 2020b), The MathWorks Inc., Available: http://www.mathworks.com/.

[28] M. Saviz, L. Mogouon Toko,O. Spathmann, J. Streckert, V.Hansen, M. Clemens, and R. Faraji-Dana, “A new open-source toolbox for estimating the electrical properties of biological tissues in the terahertz frequency band,” *J. Infrared Millim. Terahertz Waves*, vol. 34, no. 9, pp. 529–538, 2013, doi: 10.1007/s10762-013-9997-z.

[29] O. Spathmann, M. Zang, J. Streckert, V. Hansen, M. Saviz, T. M. Fiedler, K. Statnikov, U. R. Pfeiffer, and M. Clemens, “Numerical Computation of Temperature Elevation in Human Skin Due to Electromagnetic Exposure in the THz Frequency Range,” *IEEE Trans. THz Sci. Technol.*, vol. 5, no. 6, pp. 978–989, 2015, doi: 10.1109/TTHZ.2015.2476962.

[30] COMSOLMultiphysics® (v. 5.6), COMSOLAB, [online] Available: http://www.comsol.com.

[31] M. Khiao-In, *From porcine skin samples in situ to three-dimensional human skin constructs in vitro. Studying skin with a focus on the 3R principles*, Ph.D. Dissertation, Freie Universität Berlin, Berlin, Germany, 2022.

[32] M. C. Ziskin, S. I. Alekseev, K. R. Foster, and Q. Balzano, “Tissue models for RF exposure evaluation at frequencies above 6 GHz,” *Bioelectromagnetics*, vol. 41, no. 1, pp. 173–189, 2018, doi: 10.1002/bem.22110.

[33] S. I. Alekseev and M. C. Ziskin, “Human skin permittivity determined by millimeter wave reflection measurements,” *Bioelectromagnetics*, vol. 28, no. 5, pp. 331–339, 2007, doi: 10.1002/bem.20308.

[34] A. Christ, T. Samaras, E. Neufeld, and N. Kuster, “RF-induced temperature increase in a stratified model of the skin for plane-wave exposure at 6-100 GHz,” *Rad. Prot. Dos.*, vol. 188, no. 3, p. 350–360, 2020, doi: 10.1093/rpd/ncz293.

[35] R. R. Gullapalli, M. C. Demirel, and P. J. Butler, “Molecular dynamics simulations of dii-c18(3) in a DPPC lipid bilayer,” Phys. *Chem. Chem. Phys.*, vol. 10, no. 24, pp. 3548–3560, 2008, doi: 10.1039/b716979e.

[36] S. Lippens, G. Denecker, P. Ovaere, P. Vandenabeele, and W. Declercq, “Death penalty for keratinocytes: apoptosis versus cornification,” *Cell Death Differ.*, vol. 12, no. 2, pp. 1497–1508, 2005, doi: 10.1038/sj.cdd.4401722.

[37] A. Hirata and O. Fujiwara, “The correlation between mass-averaged SAR and temperature elevation in the human head model exposed to RF near-fields from 1 to 6 GHz,” *Phys. Med. Biol.*, vol. 54, no. 23, pp. 7227–7238, 2009, doi: 10.1088/0031-9155/54/23/013.

[38] A. Hirata, M. Fujimoto, T. Asano, J. Wang, O. Fujiwara, and T. Shiozawa, “Correlation Between Maximum Temperature Increase and Peak SAR with Different Average Schemes and Masses,” *IEEE Trans. Electromagn. Compat,* vol. 48, no. 3, pp. 569–578, 2006, doi: 10.1109/TEMC.2006.877784.

[39] I. Krakovský and V. Myroshnychenko, “Modeling dielectric properties of composites by finite-element method,” *J. Appl. Phys*., vol. 92, no. 11, pp. 6743–6748, 2002, doi: 10.1063/1.1516837.

[40] A. M. Nicolson and G. F. Ross, “Measurement of the intrinsic properties of materials by time domain techniques,” *IEEE Trans. Instrum. Meas*., vol. 19, no. 4, pp. 377-382, Nov. 1970, doi: 10.1109/TIM.1970.4313932.

[41] W. B Weir, "Automatic measurement of complex dielectric constant and permeability at microwave frequencies," *Proc. IEEE*, vol. 62, no. 1, pp. 33-36, Jan. 1974, doi: 10.1109/PROC.1974.9382.

[42] O. Luukkonen, S. I. Maslovski, and S. A. Tretyakov, "A stepwise Nicolson-Ross-Weir-based material parameter extraction method," *IEEE Antennas Wireless Propag. Lett*., vol. 10, pp. 1295-1298, Nov. 2011, doi: 10.1109/LAWP.2011.2175897.

[43] J. Baker-Jarvis, E. J. Vanzura, and W. A. Kissick, "Improved technique for determining complex permittivity with the transmission/reflection method," *IEEE Trans. Microwave Theory Techn*., vol. 38, no. 8, pp. 1096-1103, Aug. 1990, doi: 10.1109/22.57336.

[44] C. Baer, B. Hattenhorst, C. Schulz, B. Will, I. Rolfes, and T. Musch, "Effective permittivity determination of randomized mixed materials using 3D electromagnetic simulations," *2015 IEEE MTT-S International Microwave Symposium (IMS 2015)*, May 17-22, Phoenix, Arizona, USA, pp.1-4, 2015, doi: 10.1109/MWSYM.2015.7166797.

[45] J. Baker-Jarvis, *Transmission/Reflection and Short-Circuit Line Permittivity Measurements*. NIST Technical Note 1341, Gaithersburg, MD, USA: National Institute of Standards and Technology (NIST), 1990.

[46] J. Baker-Jarvis, M. D. Janezic, J. H. J. Grosvenor, and R. G. Geyer, *Transmission/Reflection and Short-Circuit Line Methods for Measuring Permittivity and Permeability*. NIST Technical Note 1355-R, Gaithersburg, MD, USA: National Institute of Standards and Technology (NIST), 1993.

[47] J. Baker-Jarvis, M. D. Janezic, B. F. Riddle, R. T. Johnk, P. Kabos, C. L. Holloway, R. G. Geyer, C. A. Grosvenor, *Measuring the Permittivity and Permeability of Lossy Materials: Solids, Liquids, Metals, Building Materials, and Negative-Index Materials*, NIST Technical Note 1536, Gaithersburg, MD, USA: National Institute of Standards and Technology (NIST), 2005.

[48] P. Oltulu, B. Ince, N. Kokbudak, S. Findik, and F. Kilinc, "Measurement of epidermis, dermis, and total skin thicknesses from six different body regions with a new ethical histometric technique," *Turkish Journal of Plastic Surgery*, vol. 26, no. 2, pp. 56-61, 2018, doi: 10.4103/tjps.tjps_2_17.

[49] Y. Lee, K. Hwang, "Skin thickness of Korean adults," *Surg. Radiol. Anat.*, vol. 24, no. 3-4, pp. 183-189, Jan. 2002, doi: 10.1007/s00276-002-0034-5.

[50] S. Wang, R.-X. Yu, W. Fan, C.-X. Li, W.-M. Fei, S. Li, J. Zhou, R. Hu, M. Liu, F. Xu, J. Xu, and Yong Cui, "Detection of skin thickness and density in healthy Chinese people by using high-frequency ultrasound," *Surg. Radiol. Anat.*, vol. 29, no. 1, article no. e13219, pp. 1-9, Jan. 2002, doi: 10.1111/srt.13219.

## 12.2 List of own publications

[A1] S. Doğusan, M. Jalali, J. T. Svejda, and D. Erni, "Gender differences with respect to electromagnetic power absorption in human skin tissue at 5G/6G frequencies," *4th YRA MedTech Symposium (YRA-MedTech 2024*), Young Researchers Academy – MedTech in NRW, Feb. 1, FH Aachen, Campus Jülich, Germany, 2024, (accepted)

[A2] S. Doğusan, M. Jalali, J. T. Svejda, and D. Erni, "Gender-specific electromagnetic power absorption in human skin tissue at 5G/6G frequencies," *15h German Microwave Conference (GeMiC 2024)*, March 11-13, University of Duisburg-Essen, Mercator Conference Center (Mercatorhalle) Duisburg, Duisburg, Germany, 2024 (accepted).

[A3] M. Degen, J. T. Svejda, M. Jalali, A. Rennings, and D. Erni, "The occurrence of parasitic radiation in the transmission–reflection material characterization using a sandwiched antenna–sample–antenna setup," *15h German Microwave Conference (GeMiC 2024)*, March 11-13, University of Duisburg-Essen, Mercator Conference Center (Mercatorhalle) Duisburg, Duisburg, Germany, 2024 (accepted).

[A4] M. Jalali, J. T. Svejda, B. Sievert, and D. Erni, "Investigating a possible shielding behavior of the European honey bee's cuticle at THz frequencies," *15h German Microwave Conference (GeMiC 2024)*, March 11-13, University of Duisburg-Essen, Mercator Conference Center (Mercatorhalle) Duisburg, Duisburg, Germany, 2024 (accepted).

[A5] M. Jalali, A. Prokscha, Y. Yun, T. Kubiczek, J. T. Svejda, S. Preu, J. Balzer, T. Kaiser, and D. Erni, "Non-invasive glucose sensing via the fingernail bed using THz radiation," *Current Directions in Biomedical Engineering (CDBME)*, vol. 9, no. 1, pp. 507-510, Sept. 2023, doi: 10.1515/cdbme-2023-1127.

[A6] Karsten Leonard Kevin Jerbic, *Computational multiscale models for microdosimetric investigations of skin tissues under electromagnetic exposure*. Ph.D. Dissertation University of Duisburg-Essen, Duisburg, 2024.

[A7] M. Degen, V. Jandieri, B. Sievert, J. T. Svejda, A. Rennings, and D. Erni, "An efficient analysis of scattering from randomly distributed obstacles using an accurate recursive aggregated centered T-matrix algorithm," *IEEE Trans. Antennas Propagat.*, vol. 71, no. 12, pp. 9849-9862, Dec. 2023, doi: 10.1109/TAP.2023.3316792.

[A8] D. Erni, K. Jerbic, M. Jalali, J. T. Svejda, and J. Froehlich, "Wo werden mm-Wellen im Gewebe absorbiert? Forschungsansätze für eine virtuelle Mikrodosimetrie der Haut," *Science Brunch No. 36 – Die Mobilkommunikation erschliesst immer höhere Frequenzen. Was sind die Herausforderungen und Trends?* Forschungsstiftung Strom und Mobilkommunikation (FSM) / Swiss Research Foundation for Electricity and Mobile Communication (FSM), Nov. 23, Haus zum Rüden, Constaffel Saal, Zürich, Switzerland, 2023, (invited presentation).

[A9] B. Sievert, J. Wittemeier, J. T. Svejda, N. Pohl, D. Erni, and A. Rennings, "Coaxial cable-based magnetic and electric near-field probes to measure on-chip components up to 330 GHz," *IEEE Antennas Wireless Propag. Lett.*, vol. 22, no. 10, pp. 2472-2476, Oct. 2023, doi: 10.1109/LAWP.2023.3291571.

[A10] B. Sievert, M. Degen, F. Brix, U. Krämer, D. Erni, and A. Rennings, 'Plant stem imaging by combining RCS-measurements and semi-analytical T-matrix-based field calculation," *6th Int. Workshop on Mobile THz Systems (IWMTS 2023),* July 3-5, Kameha Grand, Bonn, Germany, Tutorial Session 6 'Insect and Plant Monitoring', 2023.

[A11] F. Sheikh, A. Prokscha, A. Batra, M. Jalali, A. Rennings, U. Krämer, M. Vossiek, N. Weimann, J. Balzer, T. Kaiser, and D. Erni, "Environmental sensing: Wireless continuous real-time plant and insect monitoring,"*BMT 2023 – 57th DGBMT Annual Conference on Biomedical Engineering/VDE-DGBMT,* Deutsche Gesellschaft für Biomedizinische Technik, Sept. 26-28, Mercator Conference Center (Mercatorhalle) Duisburg, Duisburg, Germany, poster at the UDE booth in the conference exhibition, 2023.

[A12] M. Jalali, A. Prokscha, T. Kubiczek, J. T. Svejda, S. Preu, T. Kaiser, J. Balzer, D. Erni, «nailSense – Nichtinvasives THz-Glukosesensing durch den Nagel hindurch», Erfindungsmeldung, Anmelder: Universität Duisburg-Essen, Universität Duisburg-Essen, Aug. 3, 2023, (German patent application no. DE 10 2023 207 437.0).

[A13] A. Prokscha, F. Sheikh, M. Jalali, Y. Zantah, B. Sievert, M. Al-Hasan, D. Erni, and T. Kaiser, "A look through artificial human tissues at Ka-band and D-band," *6th Int. Workshop on Mobile THz Systems (IWMTS 2023),* July 3-5, Kameha Grand, Bonn, Germany, Session 5: 'Terahertz Systems and Applications (2)', pp. 1-5, 2023, doi 10.1109/IWMTS58186.2023.10207780.

[A14] M. Jalali, J. T. Svejda, S. Doğusan, and D. Erni, "A bioelectromagnetics center for exposure analyses of biological organisms at 6G frequencies," *4th 6GEM General Assembly*, June 14-15, LogistikCampus, TU Dortmund, Dortmund, Germany, Poster Session: 'WP4.8: 6G.Bioelectromagnetics Interactions', 2023.

[A15] M. Jalali, J. T. Svejda, and D. Erni, "THz Interaction with western honey bees," *6th Int. Workshop on Mobile THz Systems (IWMTS 2023),* July 3-5, Kameha Grand, Bonn, Germany, Tutorial Session 6 'Insect and Plant Monitoring', 2023.

[A16] S. Doğusan, M. Jalali, and D. Erni, "Analysis of the electromagnetic behavior of human skin from 5 GHz to 30 GHz," *4th 6GEM General Assembly*, June 14-15, LogistikCampus, TU Dortmund, Dortmund, Germany, Poster Session: 'WP4.8: 6G.Bioelectromagnetics Interactions', 2023.

[A17] K. Jerbic, J. T. Svejda, B. Sievert, A. Rennings, J. Fröhlich, and D. Erni, "The importance of subcellular structures to the modeling of biological cells in the context of computational bioelectromagnetics simulations," *Bioelectromagnetics*, vol. 44, no. 1-2, pp. 26-46, Jan.-Feb., 2023, doi: 10.1002/bem.22436.

[A18] K. Jerbic and D. Erni, *2. Project Report – Multiscale Computational electromagnetic Modeling and Validation of Current and Energy Flows in the Skin Tissue Microstructure at mm-Wave Frequencies (MicroBioEM)*, 2nd project report for the FSM-Project No. A2019-01, University of Duisburg-Essen, Duisburg, Germany, Dec. 31, 2022.

[A19] M. Jalali, J. T. Svejda, and D. Erni, "A bioelectromagnetics center for exposure analyses of biological organisms at 6G frequencies," *3rd 6GEM General Assembly*, Nov. 23-24, Forschungszentrum für das Engineering Smarter Produkt-Service Systeme (ZESS), Bochum, Germany, Poster Session: 'WP4.8: 6G.Bioelectromagnetics Interactions', 2022.

[A20] D. Erni, "Environmental, plant, and insect monitoring," *terahertz.NRW Kickoff Meeting*, Oct. 27, Technologiezentrum Ruhr (TZR), Ruhr-University of Bochum, Bochum, Germany, 2022.

[A21] K. Jerbic, J. T. Svejda, B. Sievert, X. Liu, K. Kolpatzeck, M. Degen, A. Rennings, J. Balzer and D. Erni, "The identification of spectral signatures in randomized (sub-)surface material systems," *5th Int. Workshop on Mobile THz Systems (IWMTS 2022)*, July 4-6, University of Duisburg-Essen, Fraunhofer-inHaus-Center, Duisburg, Germany, Session 4: 'Terahertz Identification and Classification', 2022, (hybrid workshop as both, on-site and online event), doi: 10.1109/IWMTS54901.2022.9832449.

[A22] M. Jalali, K. Jerbic, A. Rennings, J. T. Svejda, and D. Erni, "Towards a virtual microdosimetry of biological tissue at 6G frequencies," *1st 6GEM Annual Meeting/2nd General Assembly*, June 29-30, Fraunhofer-InHaus-Center, Duisburg, Germany, Session WP4: 'WP4.8: 6G.Bioelectromagnetics Interactions', 2022.

[A23] K. Jerbic, J. T. Svejda, B. Sievert, A. Rennings, J. Froehlich, and D. Erni, "The role of organelles in electromagnetic microdosimetry based on broadband multiscale skin models of eukaryotic cells," *BioEM 2022*, June 19-24, Aichi Industry and Labor Center (WINC AICHI), Nagoya, Japan, Session 14: 'S14: Computational Dosimetry', pp. 337-340, 2022.

[A24] K. Jerbic, J. T. Svejda, B. Sievert, A. Rennings, J. Froehlich, and D. Erni, "The importance of subcellular structures to the modeling of biological cells in the context of computational bioelectromagnetics simulations," *arXiv:2206.09757* [physics.app-ph], Bibcode: 2022arXiv220609757J, (https://arxiv.org/abs/2206.09757v1), June 20, 2022, doi: 10.48550/arXiv.2206.09757.

[A25] K. Jerbic and D. Erni, *1. Project Report – Multiscale Computational electromagnetic Modeling and Validation of Current and Energy Flows in the Skin Tissue Microstructure at mm-Wave Frequencies (MicroBioEM)*, 1st project report for the FSM-Project No. A2019-01, University of Duisburg-Essen, Duisburg, Germany, Dec. 23, 2021.

[A26] K. Jerbic and D. Erni, *Initial Report – Multiscale Computational electromagnetic Modeling and Validation of Current and Energy Flows in the Skin Tissue Microstructure at mm-Wave Frequencies (MicroBioEM)*, initial project report for the FSM-Project No. A2019-01, University of Duisburg-Essen, Duisburg, Germany, March 23, 2021.

[A27] G. Solomakha, J. T. Svejda, C. van Leeuwen, A. Rennings, A. J. Raaijmakers, S. Glybovski, D. Erni, "A self-matched leaky-wave antenna for ultrahigh-field MRI with low specific absorption rate," *Nat. Commun.*, vol. 9, article no. 455, pp. 1-11, Jan. 19, 2021, doi: 10.1038/s41467-020-20708-w.

[A28] B. Sievert, J. T. Svejda, D. Erni, and A. Rennings, "Spherical mm-wave/THz antenna measurement system," *IEEE Access*, vol. 8, no. 1, pp. 89680-89691, Dec. 2020, doi: 10.1109/ACCESS.2020.2993698.

[A29] K. Jerbic, K. Neumann, J. T. Svejda, B. Sievert, A. Rennings, and D. Erni, "Limits of effective material properties in the context of an electromagnetic tissue model," *IEEE Access*, vol. 8, pp. 223806-223826, Dec. 28, 2020, doi: 10.1109/ACCESS.2020.3045327.

[A30] D. Erni, *Multiscale Computational Electromagnetics Modeling and Validation of Current and Energy Flows in the Skin Tissue Microstructure*, project proposal to this FSM-Project No. A2019-01, Univ. Duisburg-Essen, Duisburg, Germany, May, 2020.

[A31] D. Erni, K. Jerbic, A. Rennings, S. Huclova, and J. Froehlich, "Mehrskalige elektromagnetische Gewebemodelle für den mm-Wellen-Bereich," *FSM-Workshop: Millimeterwellen – Stand der Forschung*, Forschungsstiftung Strom und Mobilkommunikation, June 18-19, ETH Zurich, Zürich, Switzerland, 2019, (invited presentation). [cf. https://www.ate.uni-due.de/data/dokumente_2019_public/FSM_Workshop_2019_Erni.pdf].

[A32] J. Froehlich, S. Huclova, C. Beyer, and D. Erni, book chapter 12 "Accurate multi-scale skin model suitable for determining sensitivity and specificity of changes of skin components," pp. 353-394, in *Computational Biophysics of the Skin*, Bernard Querleux (Ed.), Singapore: Pan Stanford Publishing Pte. Ltd., (ISBN-978-981-4463-84-3), 2014.

[A33] S. Huclova, D. Erni and J. Fröhlich, "Modelling and validation of dielectric properties of human skin in the MHz region focusing on skin layer morphology and material composition," *J. Appl. Phys. D*, vol. 45, no. 2, Jan. 18, 2012, doi: 10.1088/0022-3727/45/2/025301.

[A34] Sonja Huclova, *Modeling of cell suspensions and biological tissue for computational electromagnetics*. Diss. ETH Zürich, No. 19863, Zürich, July 18, 2011, doi: 10.3929/ethz-a-006711951.

## 12.3 List of tools and products

[P1] FEM solver *COMSOL Multiphysics* (V. 5.6), COMSOL AB, Stockholm, Sweden, [accessed: Dec. 2021]: http://www.comsol.com.

[P2] MCK mm-wave/THz material characterization system from *SWISSto12 SA*, Renens, Switzerland, [accessed Dec. 2021]: https://mck.swissto12.ch, (a portray of the MCK setup is given here: https://youtu.be/OZLNENq1Q-U).

[P3] Robotized SPEAG mm-wave nearfield scanner (*EUmmWVx* with *DASY8* system), SPEAG Zürich, Switzerland, [accessed Dec. 2021]: https://speag.swiss/products/icey/icey-mmw/new-eummwvx-vector-e-probe-3.

[P4] *Ultimaker 5S*, 3D printer, Ultimaker BV, Utrecht, the Netherlands, [accessed Dec. 2021]: https://ultimaker.com/de/3d-printers/ultimaker-s5.

[P5] FDTD solver *EMPIRE XPU*, IMST GmbH, [accessed Dec. 2021]: http://www.empire.de

[P6] *MATLAB* (R 2020b), The MathWorks Inc. [accessed: Sep. 22, 2021]: http://wwwmathworks.com

## 12.4 List of project-related theses and project works

[T1] Nele König, Larissa-Sophie Bonk, *Literaturrecherche zur Ertüchtigung computergestützter elektromagnetischer Hautmodelle*. Project thesis (Bachelor MedTech), Fachgebiet Allgemeine und Theoretische Elektrotechnik (ATE), Universität Duisburg-Essen, Dec. 9, 2021.

[T2] Nele König, *Development of a multiphysics prediction engine for the assessment of exposure limits for electromagnetic fields*, Bachelor thesis (Bachelor MedTech), Allgemeine und Theoretische Elektrotechnik (ATE), Universität Duisburg-Essen, (discontinued due to another study), 2022.

[T3] Jannis Assmann, *Material property library for the hierarchical bottom-up synthesis of tissue properties*, Master thesis, (Master EIT), Fachgebiet Allgemeine und Theoretische Elektrotechnik (ATE), Universität Duisburg- Essen, July 29, 2022.

[T4] Liuxin Qing, *Quasi-electrostatic simulations of predominant skin cells for evaluation of microdosimetric measures*, Bachelor thesis, (Bachelor MedTech), Fachgebiet Allgemeine und Theoretische Elektrotechnik (ATE), Universität Duisburg-Essen, Feb. 17, 2022.

[T5] Rui Sun, *Multiscale simulation of multilayer skin models for the calculation of exposure depth and field distribution of electromagnetic fields*, Master thesis, (Master MedTech), Fachgebiet Allgemeine und Theoretische Elektrotechnik (ATE), Universität Duisburg-Essen, July 1, 2022.

[T6] Kübra Kaya, Tom Neerfeld, *3D-Druck basierte Prototypenentwicklung von Nahfeldproben zur Sondierung von biomedizini-schen Proben bei mm-Wellen-Anregung*. Project thesis (Master EIT), Fachgebiet Allgemeine und Theoretische Elektrotechnik (ATE), Universität Duisburg-Essen, Oct. 5, 2022.

[T7] Elie Kharouf, *Permittivitäts- und Leitfähigkeitsbestimmung mittels Verstimmung eines gekoppelten Resonators von Phantomflüssigkeiten zur Emulierung des menschlichen Körpers bei der 7T-MRT*, Bachelor thesis, (Bachelor MedTech), Fachgebiet Allgemeine und Theoretische Elektrotechnik (ATE), Universität Duisburg-Essen, May 12, 2022.

[T8] Assem Elgazar, *Determining the effect of sample's temperature on the DAK measurement system in gel samples mimicking human tissues*, Master thesis, (Master ISE EEE), Fachgebiet Allgemeine und Theoretische Elektrotechnik (ATE), Universität Duisburg-Essen, Aug. 30, 2022.

[T9] Qingyu Wang, *Measuring the European honey bee's permittivity and conductivity in the mm-wave and THz range*, Bachelor thesis, (Bachelor ISE EEE), Fachgebiet Allgemeine und Theoretische Elektrotechnik (ATE), Universität Duisburg-Essen, 2022, (ongoing).

[T10] Yijun Yan, *Modelling nails in order to determine the glucose level within the nail bed, using THz radiation*, Bachelor thesis, (Bachelor MedTech), Fachgebiet Allgemeine und Theoretische Elektrotechnik (ATE), Universität Duisburg-Essen, 2022, (ongoing).

[T11] Fatema Khalil, *Determining the fraction of absorbed power in each skin layer, using the SIM4LIFE software*, Bachelor thesis, (Bachelor MedTech), Fachgebiet Allgemeine und Theoretische Elektrotechnik (ATE), Universität Duisburg-Essen, 2022, (ongoing).

[T12] Suzan Naasou, *Untersuchung von breitbandigen Magnetfeldproben zur Bestimmung von Nahfeldern im Mikrowellenbereich*, Bachelor thesis (Bachelor EIT), Allgemeine und Theoretische Elektrotechnik (ATE), Universität Duisburg-Essen, March 22, 2023.

[T13] Yijun Yan, *Untersuchung der THz-Ausbreitung in Nagelschichten mit dem Ziel, den Glukosegehalt im Nagelbett zu bestimmen*. Bachelor thesis (Bachelor ISE EEE), Allgemeine und Theoretische Elektrotechnik (ATE), Universität Duisburg-Essen, April 24, 2023.

[T14] Zhengyan Chai, *Study the generated heat within various body tissues due to the magnetic field of MRI devices*, Bachelor thesis (Bachelor ISE EEE), Allgemeine und Theoretische Elektrotechnik (ATE), Universität Duisburg-Essen, May 12, 2023.

[T15] Qingyu Wang, *Measuring European honey bee's permittivity and conductivity in the THz range*. Bachelor thesis (Bachelor ISE EEE), Allgemeine und Theoretische Elektrotechnik (ATE), Universität Duisburg-Essen, May 12, 2023.

[T16] Fatema Khalil, *Bestimmung des absorbierten Leistungsanteils in den einzelnen Hautschichten basierend auf der SIM4LIFE Software.* Bachelor thesis (Bachelor MedTech), Allgemeine und Theoretische Elektrotechnik (ATE), Universität Duisburg-Essen, July 19, 2023.

[T17] Yijia Qian, *Exploring otential hazards of THz radiation on western honey bees.* Bachelor thesis (Bachelor ISE EEE), Fachgebiet Allgemeine und Theoretische Elektrotechnik (ATE), Universität Duisburg-Essen, Sept. 7, 2023.

[T18] Muzzamil Baig Mohammed, *Investigation of the near- and far-field effects of body components on the array-performance of automotive radar systems.* Master thesis (Master MBVT Techn. Logistics), Fachgebiet Allgemeine und Theoretische Elektrotechnik (ATE), Universität Duisburg-Essen, 2023, (ongoing).

[T19] Obada Chamsy Basha, *Integration of a spectral sensor in milking Ssystems for a dynamic in-iine milk analysis.* Master thesis (Master MBVT Mechatronics), Fachgebiet Allgemeine und Theoretische Elektrotechnik (ATE), Universität Duisburg-Essen, 2023, (ongoing).

[T20] Jan Kopper, *Realisierung eines offenen Resonators zur Materialcharakterisierung von Festkörpern, Flüssigkeiten und biologischen Gewebeproben im mm-Wellen-Bereich*. Master thesis (Master EIT), Fachgebiet Allgemeine und Theoretische Elektrotechnik (ATE), Universität Duisburg-Essen, 2023, (ongoing).

## 12.5 List of associated projects / proposals with BioEM-related topics at 5G and beyond

[N1] *«terahertz.NRW – NRW-Netzwerk zur exzellenten Terahertzforschung für Kommunikation, Lokalisierung, Materialcharakterisierung, Medizintechnik & Umweltmonitoring (terahertz.NRW)»,* joint research program funded by the initiative *Netzwerke 2021 (NW 2021)* of the Ministry of Culture and Science of the State of North Rhine-Westphalia (MKW NRW), project duration 01.08.2022–31.07.2026, involved partners University of Duisburg-Essen, Ruhr-University Bochum, University of Wuppertal, and Fraunhofer Institutes IMS and FHR, budget: 5M€, 2022, (accepted pre-proposal).

[N2] «*6GEM: open – efficient – secure – safe (6G-Forschungs-Hub für offene, effiziente und sichere Mobilfunksysteme*», joint research project in the BMBF program '6G-Forschungs-Hubs; Plattform für zukünftige Kommunikationstechnologien und 6G', project duration: 01.08.2021–31.07.2025, involved partners; University of Duisburg-Essen, Ruhr-University Bochum, TU Dortmund, and RWTH Aachen, budget: 6M€, 2021, (running project).

[N3] «*TRICorder – Terahertz Research & Innovation Center»,* research program aiming at 'Terahertz for Humans and Environment' start-up funded by the University of Duisburg-Essen to enable a joint DFG excellence cluster proposal (ExStra), project duration: 01.09.2021–31.12.2023, budget: 1M€, 2021, (running project).

[N4] «*insighTHz»,* proposal for a DFG excellence cluster research program aiming at 'Terahertz for Humans and Environment' by the University of Duisburg-Essen to enable a joint DFG excellence cluster (ExStra) together with University of Wuppertal, TU Dortmund University, Technical University of Darmstadt, and the Fraunhofer IMS, project duration: 7 years, 2023, (submitted in April 2023).

[N5] Deutsche Forschungsgemeinschaft (DFG) Collaborative Research Centre / Transregio "Mobile Material Characterization and Localization by Electromagnetic Sensing," *CRC/TRR 196 MARIE* (Project No. 287022738), [accessed Dec. 2021]: http://www.trrmarie.de/sfbtrr196marie.

# A. Appendix – Quasi-static electromagnetic cell models

The parametric cell models of the keratinocytes (or corneocytes) displayed in Fig. A.1(a)-(f) were placed in a virtual parallel plate capacitor setup to conduct a quasi-static EM analysis between 1 GHz and 100 GHz. This capacitor setup was implemented in the FEM-based software package COMSOL Multiphysics [30].

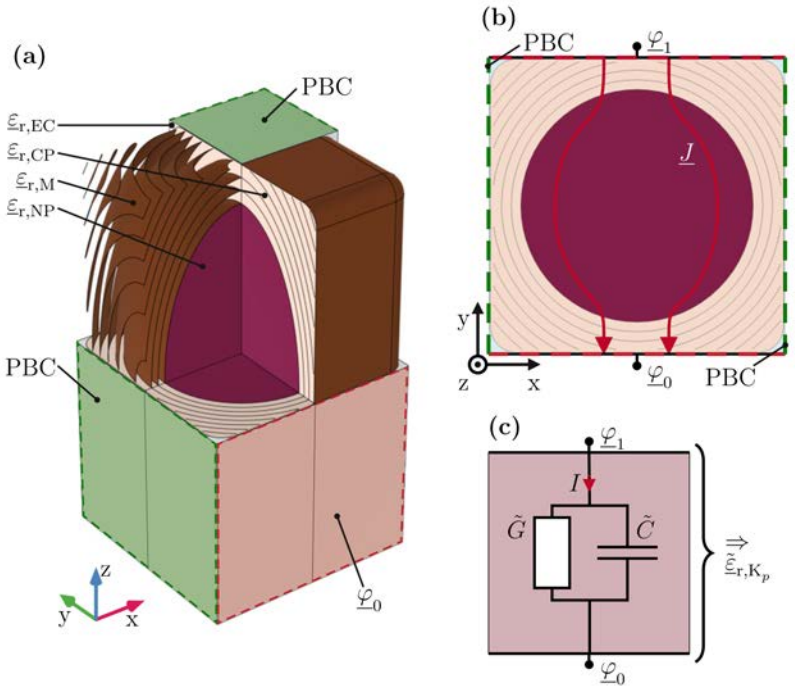


*Fig. A.1: Overview of the virtual capacitor experiment used for the quasi-static EM analysis of the computational domain: (a) Computational domain containing the cell model of a basal keratinocyte as an illustrative example showing the assignment of the dispersive material properties introduced in Sec. 5.3.1 to the individual cell compartments. (b) Cross-section through the computational domain. The voltage, $\underline{U}_0 = \underline{\varphi}_1 - \underline{\varphi}_0$, was applied to two opposing sides of the virtual capacitor set up which were designed to function as electrodes. Periodic boundary conditions (PBC) were applied to the remaining sides of the computational domain. This set up can be interpreted as a spatially periodic (computational) unit cell. (c) Numerical homogenization summarizing the computational domain as an overall shunt impedance allowing the calculation of its effective macroscopic material parameters as outlined in Sec. 5.3.1.*

The computational domain containing the cells is shown as an illustrative example in Fig. A.1(a). This figure also shows the assignment of the dispersive material properties to the individual cell compartments. In the cross-section through the computational domain as shown in Fig. A.1(b), a time-harmonic voltage with constant amplitude, $\underline{U}_0 = \underline{\varphi}_1 - \underline{\varphi}_0$, was applied between two opposing outer boundaries of the domain that were designed to function as electrodes (i.e Dirichlet boundary conditions). $\underline{U}_0$ was arbitrarily set to 1 V. The four remaining boundaries were defined with periodic boundary conditions (PBC) in order to suppress fringing fields and to reduce the memory resources of the subsequent quasi-static EM simulation. Due to this setup, the (computational) unit cell is effectively periodically extended in each direction indicated by the PBC. This approach was used in the past to investigate the effective material parameters of randomized (bio-)composites [A32, A33, A34, 39], and single cells [A6, 28]. In order to cope with the anisotropy of the (ellipsoidal) cells under investigation, the voltage $\underline{U}_0$ is then applied in the other (orthogonal) directions by swapping the electrodes with the PBCs (and vice versa). In order to avoid high aspect ratios in the modeling mesh, the plasma membrane and the membranes of the cell organelles are modeled by a set of equations taking into account the conduction and the displacement current

$$\vec{n} \cdot \underline{\vec{J}}_{\mathrm{up}} = \frac{1}{t_{\mathrm{M}}} (\sigma_{\mathrm{M}} + \mathrm{j}\omega\varepsilon_0\varepsilon_{\mathrm{r,M}})(\underline{\varphi}_{\mathrm{up}} - \underline{\varphi}_{\mathrm{down}}) \tag{A.1}$$

$$\vec{n} \cdot \underline{\vec{J}}_{\mathrm{down}} = \frac{1}{t_{\mathrm{M}}} (\sigma_{\mathrm{M}} + \mathrm{j}\omega\varepsilon_0\varepsilon_{\mathrm{r,M}})(\underline{\varphi}_{\mathrm{down}} - \underline{\varphi}_{\mathrm{up}}) \tag{A.2}$$

where $\underline{\varphi}_{\mathrm{up/down}}$ and $\vec{n} \cdot \underline{\vec{J}}_{\mathrm{up/down}}$ denote the membrane potentials and current densities normal to the upper and lower surfaces of the membrane. $t_{\mathrm{M}}$ represents the thickness of the membrane while $\sigma_{\mathrm{M}}$ and $\varepsilon_{\mathrm{r,M}}$ represent the conductivity and the relative permittivity of the membrane respectively. $\varepsilon_0$ denotes the vacuum permittivity. Referring to Eqs. A.1 and A.2, thin membranes can now be represented by these tailored boundary conditions yielding a highly economic treatment as already proposed in [A34].

The effective material parameters of the cell layers were determined using the virtual capacitor experiment as depicted in Fig. A.1(c). The time-harmonic quasi-static EM analysis in the form of the capacitor setup leads to an effective admittance that is represented by an equivalent electrical parallel circuit consisting of the elements $\tilde{G}(\omega)$ and $\tilde{C}(\omega)$. This is given by

$$\underline{\tilde{Y}}(\omega) = \frac{\underline{I}(\omega)}{\underline{U}_0} = \tilde{G}(\omega) + \mathrm{j}\omega\tilde{C}(\omega) \tag{A.3}$$

where the applied voltage, $\underline{U}_0$, and the resulting current, $\underline{I}(\omega)$, are directly accessible via COMSOL Multiphysics for an angular frequency $\omega = 2\pi f$. The dispersive effective material properties, $\tilde{\varepsilon}_{\mathrm{r}}(\omega)$ and $\sigma(\omega)$, are thus easily deduced according to

$$\underline{\tilde{Y}}(\omega) \cdot \frac{d}{A} = \frac{\underline{I}(\omega)}{\underline{U}_0} \cdot \frac{d}{A} = \tilde{\sigma}(\omega) + \mathrm{j}\omega\varepsilon_0\varepsilon_{\mathrm{r}}(\omega) = \underline{\tilde{\sigma}}(\omega) \tag{A.4}$$

where $d$ is the parallel plate distance and $A$ is the area of the electrode. In Eq. A.4, the right-hand term can be interpreted as the complex effective conductivity of the homogenized effective material, $\underline{\tilde{\sigma}}(\omega)$, from which the required material parameters directly follow:

$$\tilde{\sigma}(\omega) = \mathrm{Re}\{\underline{\tilde{\sigma}}(\omega)\} \tag{A.5}$$

$$\tilde{\sigma}(\omega) = \frac{\mathrm{Im}\{\underline{\tilde{\sigma}}(\omega)\}}{\omega\,\varepsilon_0} \tag{A.6}$$

In order to consider anisotropies in the effective material, the quasi-static capacitor analysis is performed with excitation in the x, y and z directions yielding corresponding frequency-dependent second-rank tensors for the effective conductivity,

$$\overleftrightarrow{\tilde{\sigma}}_{\mathrm{K}_q/\mathrm{C}_q}(\omega) = \begin{pmatrix} \tilde{\sigma}_{\mathrm{x,K}_q/\mathrm{C}_q}(\omega) & 0 & 0 \\ 0 & \tilde{\sigma}_{\mathrm{y,K}_q/\mathrm{C}_q}(\omega) & 0 \\ 0 & 0 & \tilde{\sigma}_{\mathrm{z,K}_q/\mathrm{C}_q}(\omega) \end{pmatrix} \tag{A.7}$$

and

$$\overleftrightarrow{\tilde{\varepsilon}}_{\mathrm{r,K}_q/\mathrm{C}_q}(\omega) = \begin{pmatrix} \tilde{\varepsilon}_{\mathrm{r,x,K}_q/\mathrm{C}_q}(\omega) & 0 & 0 \\ 0 & \tilde{\varepsilon}_{\mathrm{r,y,K}_q/\mathrm{C}_q}(\omega) & 0 \\ 0 & 0 & \tilde{\varepsilon}_{\mathrm{r,z,K}_q/\mathrm{C}_q}(\omega) \end{pmatrix} \tag{A.8}$$

To emphasize an important aspect of macroscopic exposure studies, it should be noted that they focus exclusively on the perpendicular direction of propagation of incident electromagnetic waves. This reduces the simulation effort required to determine the effective material properties of each cell layer, as

$\varepsilon_{\mathrm{r,z,K}_p/\mathrm{C}_q}$ becomes irrelevant. By exploiting the x and y axis symmetry of the parametric cell models, an important observation appears in the equations $\tilde{\varepsilon}_{\mathrm{r,x,K}_q/\mathrm{C}_q}(\omega) = \tilde{\varepsilon}_{\mathrm{r,y,K}_q/\mathrm{C}_q}(\omega) = \tilde{\varepsilon}_{\mathrm{r,K}_q/\mathrm{C}_q}(\omega)$ and $\tilde{\sigma}_{\mathrm{x,K}_q/\mathrm{C}_q}(\omega) = \tilde{\sigma}_{\mathrm{y,K}_q/\mathrm{C}_q}(\omega) = \tilde{\sigma}_{\mathrm{K}_q/\mathrm{C}_q}(\omega)$. Thus, $\tilde{\varepsilon}_{\mathrm{r,K}_q/\mathrm{C}_q}(\omega)$ and $\tilde{\sigma}_{\mathrm{K}_q/\mathrm{C}_q}(\omega)$ terms serve as representations for the effective macroscopic material properties of the individual epidermal cell layers.

## B. Appendix – Modeling shapes of keratinozytes during their life cycle

Cross-sections through the YZ plane of the cell models $K_{1\&2}$, $K_5$, $K_8$, $C_1$ and $C_{14}$ are illustrated in Fig. B.1. The cross-sections of the keratinocytes are each shown in the correct proportions to one another, and those of the corneocytes are also correct with respect to each other. Due to the large aspect ratio of the corneocyte model, it is not possible to show the two types of model in the correct size ratio to each other.

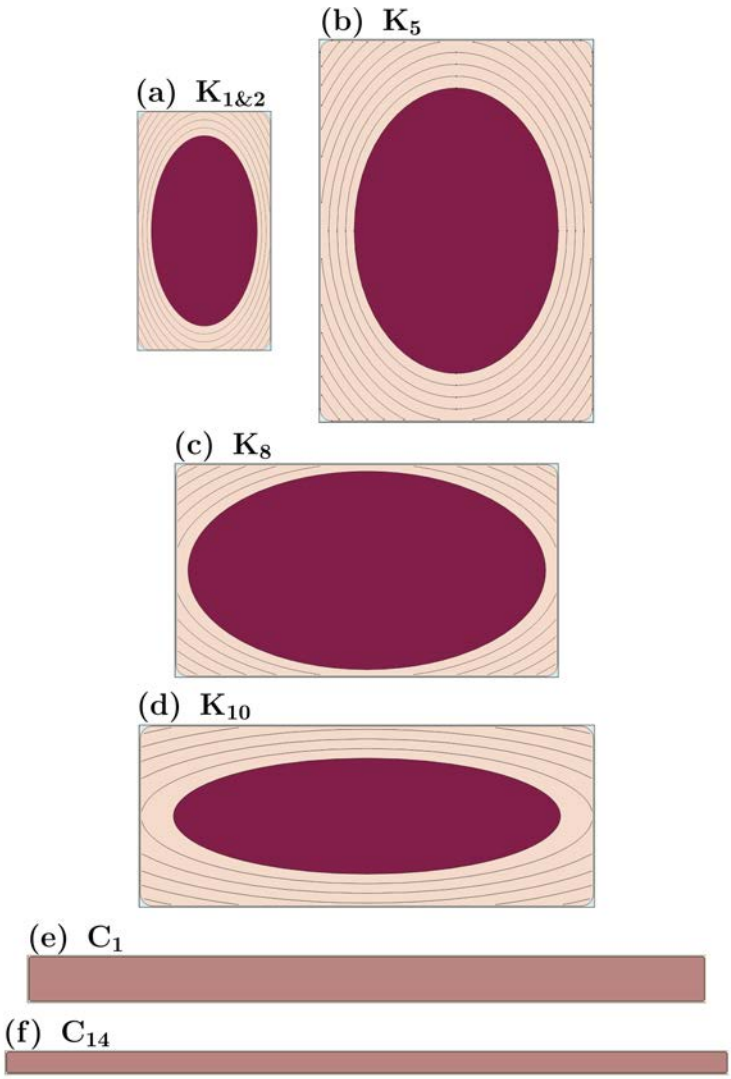


*Fig. B.1: Overview of the cross-sections through the YZ plane of the cell models $K_{1\&2}$, $K_5$, $K_8$, $C_1$ and $C_{14}$. The cross-sections of the keratinocytes and those of the corneocytes are each shown in the correct proportions to one another.*

## C. Appendix – Power distribution in the stratum corneum

Analysis of the power distribution over the epidermal cell layers, $C_q$, according to Eq. 6.6.

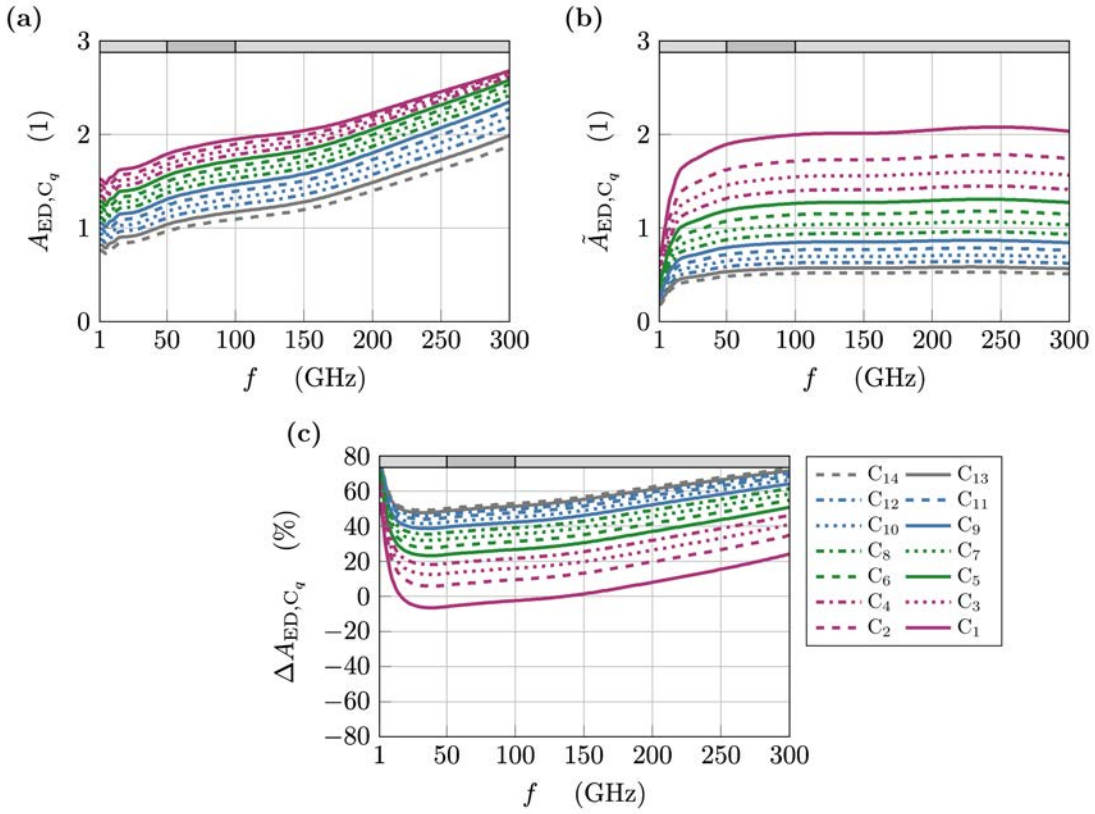


*Fig. C.1: Analysis of the power distribution over the epidermal cell layers, $C_q$, according to Eq. 6.6: (a)-(b) Power absorbed by the epidermal cell layers, $C_q$, in the reference and hybrid models, denoted by $A_{ED,C_q}$ and $\tilde{A}_{ED,C_q}$, respectively. (c) Relative deviation of $\Delta A_{ED,C_q}$ between the two skin models. The plots corresponding to each of the investigated cell layers are represented by solid, dashed, dotted and dashed-dotted lines. They are colored in magenta ($C_1$ through $C_4$), green ($C_5$ through $C_8$), blue ($C_9$ through $C_{12}$) and gray ($C_{13}$ through $C_{14}$) as indicated in the legend.*

Fig. C.1(a) shows that in the reference model, the power distribution within the SC is primarily determined by the distance of the individual cell layers from the skin surface. The power distribution within the hybird model in Fig. C.1(b) shows that the level of hydration has a strong influence on the power distribution within the epidermis, as evidenced by the significantly higher difference between the absorption in cell layer $C_1$ and $C_{14}$. The relative deviation depicted in Fig. C.1(c) shows that the absorption of the SC is overestimated by up to 70 % across the entire spectrum in all cell layers (with the exception of $C_1$).

# D. Appendix – Modeling of *micro-SAR* levels in the epidermis' cellular scale

In this appendix, illustrations are provided to showcase the variability of *SAR* values. These are captured across the cell models of keratinocytes, as depicted in Fig. D.1 through Fig. D.10 (i.e., $K_1$ through $K_{10}$), and also across the cell models of corneocytes, as shown in Fig. D.11 through Fig. D.24 (i.e., $C_1$ through $C_{14}$). Within these figures, $SAR_{\mathrm{mi,K}_p/\mathrm{C}_q}(\omega)$ is illustrated on semi-logarithmic scales in subplots (a) and (b) for frequency intervals $F_1$ and $F_2$, respectively. The mean, $\mu_{\mathrm{SAR,mi,K}_p/\mathrm{C}_q}$, is marked by a solid black line. A dark-gray area around this mean encompasses values within one standard deviation, specifically $\mu_{\mathrm{SAR,mi,K}_p/\mathrm{C}_q} \pm s_{\mathrm{SAR,mi,K}_p/\mathrm{C}_q}$, with dashed-dotted lines signify the bounds of this range. A light-gray area around $\mu_{\mathrm{SAR,mi,K}_p/\mathrm{C}_q} \pm s_{\mathrm{SAR,mi,K}_p/\mathrm{C}_q}$ reveals the full value range within the computational domains, bounded by $SAR_{\mathrm{max,mi,K}_p/\mathrm{C}_q}(\omega)$ and $SAR_{\mathrm{min,mi,K}_p/\mathrm{C}_q}(\omega)$. Additionally, a red dotted line denotes the local SAR exposure threshold, $SAR_{10\mathrm{g}}$, limiting induced power in limbs to below 4 W/kg according to the basic restrictions (see Tab. 4.1).

## D.1 Parametrized cell models of the keratinocytes $K_1$ through $K_{10}$

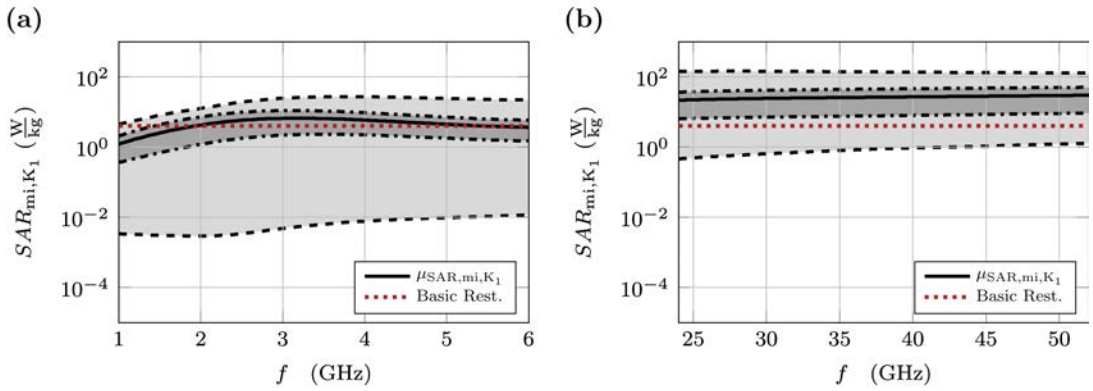


*Fig D.1: $SAR_{mi,K_1}(\omega)$ for cell model $K_1$: (a) Semi-logarithmic representation of SAR values for frequency interval $F_1$. The solid black line indicates the mean, $\mu_{SAR,mi,K_1}$. A dark-gray area surrounds this mean, encompassing values within one standard deviation, $\mu_{SAR,mi,K_1} \pm s_{SAR,mi,K_1}$, demarcated by dashed-dotted lines. The light-gray area illustrates the full range of observed values within the computational domain, bounded by $SAR_{max,mi,K_1}(\omega)$ and $SAR_{min,mi,K_1}(\omega)$. A red dotted line marks the SAR exposure threshold for the public, $SAR_{10g}$, set below 4 W/kg. (b) Plot analogous to (a) for frequency $F_2$.*

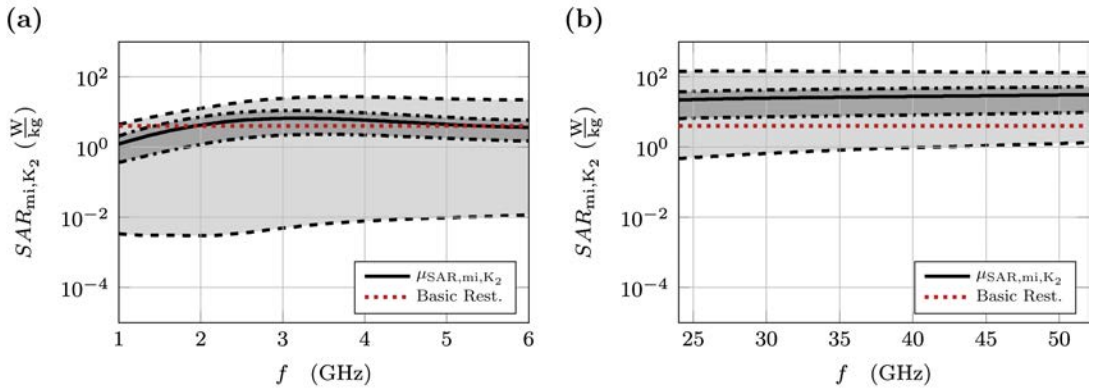


*Fig D.2: $SAR_{mi,K_2}(\omega)$ for cell model $K_2$: (a) Semi-logarithmic representation of SAR values for frequency interval $F_1$. The solid black line indicates the mean, $\mu_{SAR,mi,K_2}$. A dark-gray area surrounds this mean, encompassing values within one standard deviation, $\mu_{SAR,mi,K_2} \pm s_{SAR,mi,K_2}$, demarcated by dashed-dotted lines. The light-gray area illustrates the full range of observed values within the computational domain, bounded by $SAR_{max,mi,K_2}(\omega)$ and $SAR_{min,mi,K_2}(\omega)$. A red dotted line marks the SAR exposure threshold for the public, $SAR_{10g}$, set below 4 W/kg. (b) Plot analogous to (a) for frequency $F_2$.*

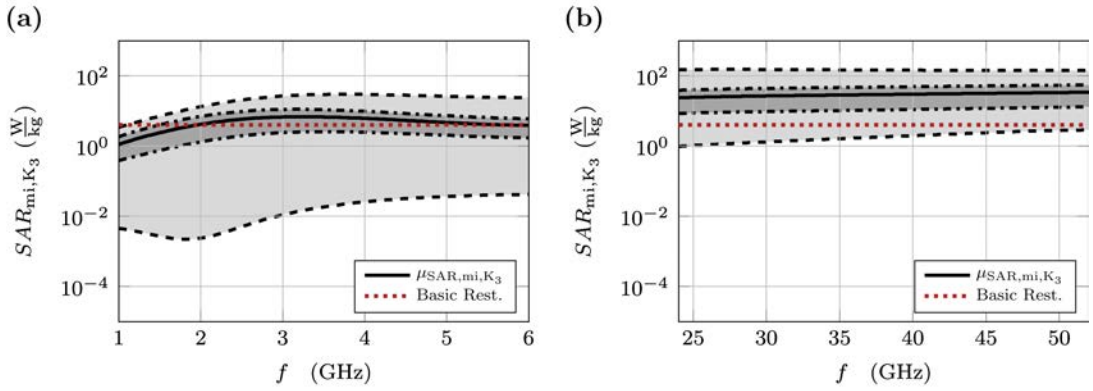


*Fig D.3: $SAR_{mi,K_3}(\omega)$ for cell model $K_3$: (a) Semi-logarithmic representation of SAR values for frequency interval $F_1$. The solid black line indicates the mean, $\mu_{SAR,mi,K_3}$. A dark-gray area surrounds this mean, encompassing values within one standard deviation, $\mu_{SAR,mi,K_3} \pm s_{SAR,mi,K_3}$, demarcated by dashed-dotted lines. The light-gray area illustrates the full range of observed values within the computational domain, bounded by $SAR_{max,mi,K_3}(\omega)$ and $SAR_{min,mi,K_3}(\omega)$. A red dotted line marks the SAR exposure threshold for the public, $SAR_{10g}$, set below 4 W/kg. (b) Plot analogous to (a) for frequency $F_2$.*

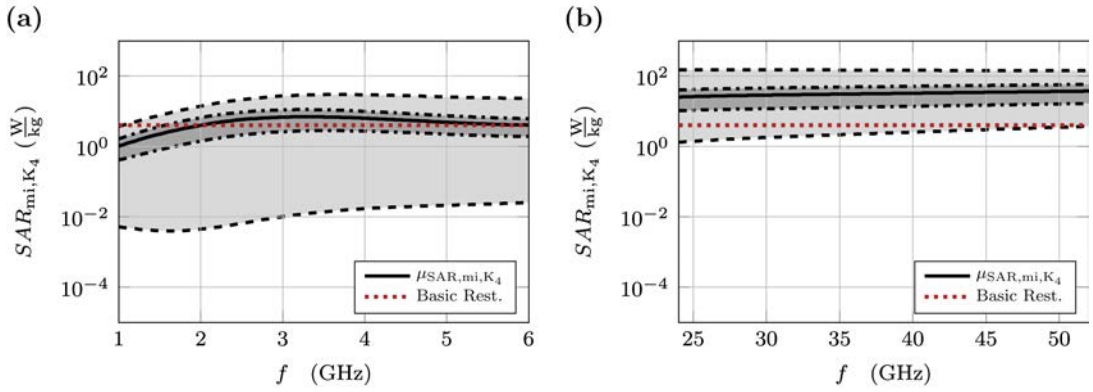


*Fig D.4: $SAR_{mi,K_4}(\omega)$ for cell model $K_4$: (a) Semi-logarithmic representation of SAR values for frequency interval $F_1$. The solid black line indicates the mean, $\mu_{SAR,mi,K_4}$. A dark-gray area surrounds this mean, encompassing values within one standard deviation, $\mu_{SAR,mi,K_4} \pm s_{SAR,mi,K_4}$, demarcated by dashed-dotted lines. The light-gray area illustrates the full range of observed values within the computational domain, bounded by $SAR_{max,mi,K_4}(\omega)$ and $SAR_{min,mi,K_4}(\omega)$. A red dotted line marks the SAR exposure threshold for the public, $SAR_{10g}$, set below 4 W/kg. (b) Plot analogous to (a) for frequency $F_2$.*

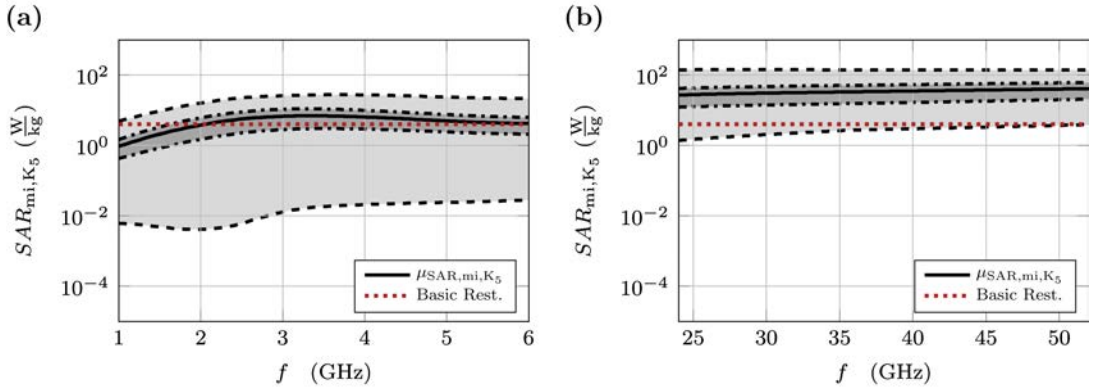


*Fig D.5: $SAR_{mi,K_5}(\omega)$ for cell model $K_5$: (a) Semi-logarithmic representation of SAR values for frequency interval $F_1$. The solid black line indicates the mean, $\mu_{SAR,mi,K_5}$. A dark-gray area surrounds this mean, encompassing values within one standard deviation, $\mu_{SAR,mi,K_5} \pm s_{SAR,mi,K_5}$, demarcated by dashed-dotted lines. The light-gray area illustrates the full range of observed values within the computational domain, bounded by $SAR_{max,mi,K_5}(\omega)$ and $SAR_{min,mi,K_5}(\omega)$. A red dotted line marks the SAR exposure threshold for the public, $SAR_{10g}$, set below 4 W/kg. (b) Plot analogous to (a) for frequency $F_2$.*

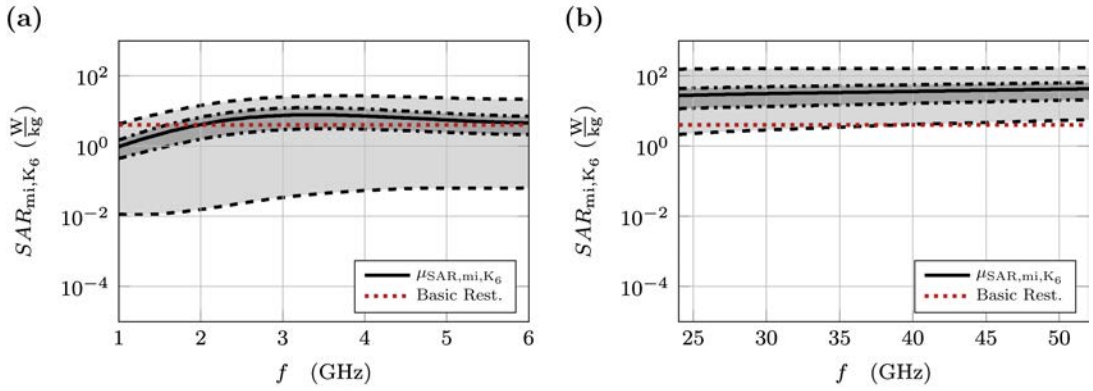


*Fig D.6: $SAR_{mi,K_6}(\omega)$ for cell model $K_6$: (a) Semi-logarithmic representation of SAR values for frequency interval $F_1$. The solid black line indicates the mean, $\mu_{SAR,mi,K_6}$. A dark-gray area surrounds this mean, encompassing values within one standard deviation, $\mu_{SAR,mi,K_6} \pm s_{SAR,mi,K_6}$, demarcated by dashed-dotted lines. The light-gray area illustrates the full range of observed values within the computational domain, bounded by $SAR_{max,mi,K_6}(\omega)$ and $SAR_{min,mi,K_6}(\omega)$. A red dotted line marks the SAR exposure threshold for the public, $SAR_{10g}$, set below 4 W/kg. (b) Plot analogous to (a) for frequency $F_2$.*

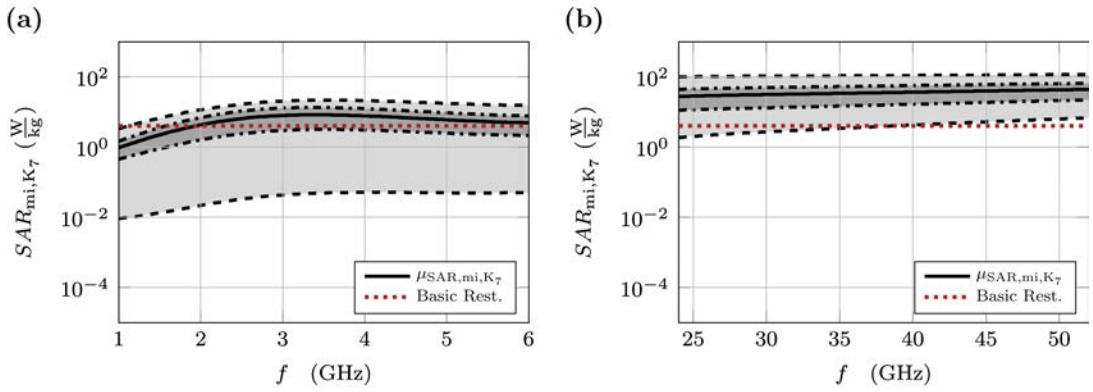


*Fig D.7: $SAR_{mi,K_7}(\omega)$ for cell model $K_7$: (a) Semi-logarithmic representation of SAR values for frequency interval $F_1$. The solid black line indicates the mean, $\mu_{SAR,mi,K_7}$. A dark-gray area surrounds this mean, encompassing values within one standard deviation, $\mu_{SAR,mi,K_7} \pm s_{SAR,mi,K_7}$, demarcated by dashed-dotted lines. The light-gray area illustrates the full range of observed values within the computational domain, bounded by $SAR_{max,mi,K_7}(\omega)$ and $SAR_{min,mi,K_7}(\omega)$. A red dotted line marks the SAR exposure threshold for the public, $SAR_{10g}$, set below 4 W/kg. (b) Plot analogous to (a) for frequency $F_2$.*

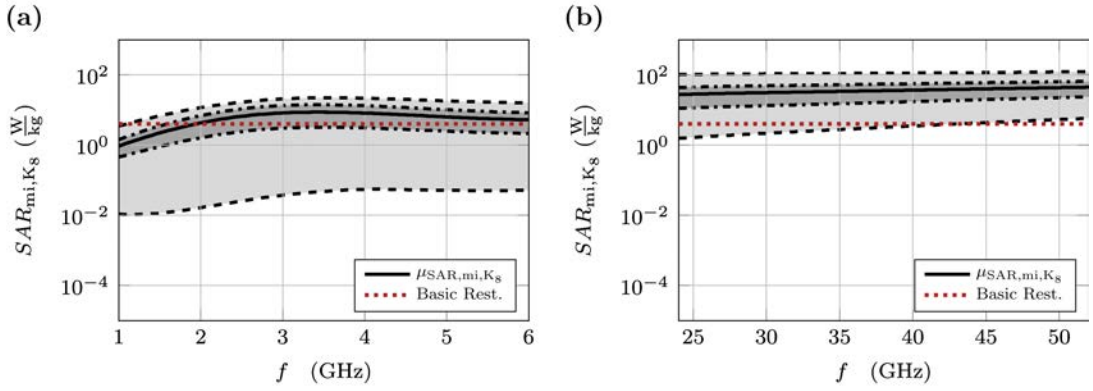


*Fig D.8: $SAR_{mi,K_8}(\omega)$ for cell model $K_8$: (a) Semi-logarithmic representation of SAR values for frequency interval $F_1$. The solid black line indicates the mean, $\mu_{SAR,mi,K_8}$. A dark-gray area surrounds this mean, encompassing values within one standard deviation, $\mu_{SAR,mi,K_8} \pm s_{SAR,mi,K_8}$, demarcated by dashed-dotted lines. The light-gray area illustrates the full range of observed values within the computational domain, bounded by $SAR_{max,mi,K_8}(\omega)$ and $SAR_{min,mi,K_8}(\omega)$. A red dotted line marks the SAR exposure threshold for the public, $SAR_{10g}$, set below 4 W/kg. (b) Plot analogous to (a) for frequency $F_2$.*

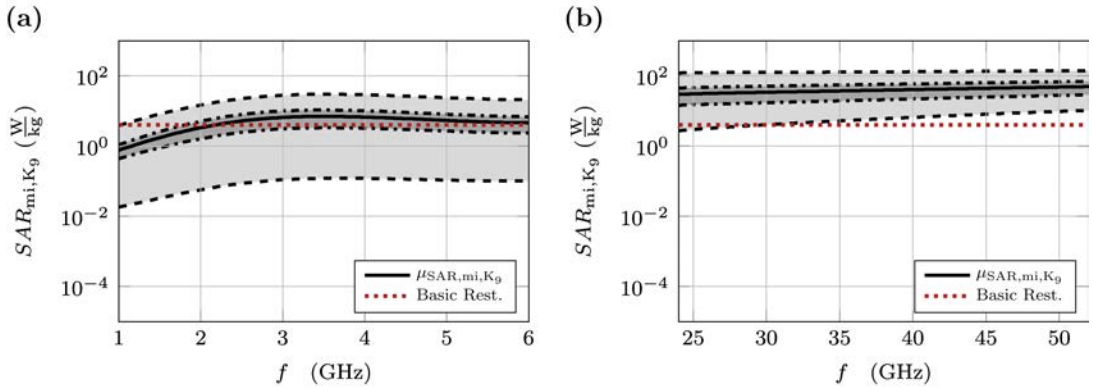


*Fig D.9: $SAR_{mi,K_9}(\omega)$ for cell model $K_9$: (a) Semi-logarithmic representation of SAR values for frequency interval $F_1$. The solid black line indicates the mean, $\mu_{SAR,mi,K_9}$. A dark-gray area surrounds this mean, encompassing values within one standard deviation, $\mu_{SAR,mi,K_9} \pm s_{SAR,mi,K_9}$, demarcated by dashed-dotted lines. The light-gray area illustrates the full range of observed values within the computational domain, bounded by $SAR_{max,mi,K_9}(\omega)$ and $SAR_{min,mi,K_9}(\omega)$. A red dotted line marks the SAR exposure threshold for the public, $SAR_{10g}$, set below 4 W/kg. (b) Plot analogous to (a) for frequency $F_2$.*

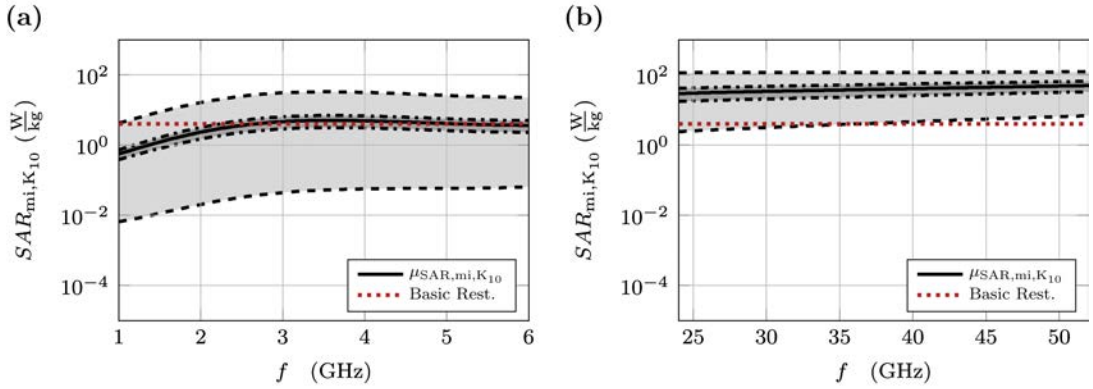


*Fig D.10: $SAR_{mi,K_{10}}(\omega)$ for cell model $K_{10}$: (a) Semi-logarithmic representation of SAR values for frequency interval $F_1$. The solid black line indicates the mean, $\mu_{SAR,mi,K_{10}}$. A dark-gray area surrounds this mean, encompassing values within one standard deviation, $\mu_{SAR,mi,K_{10}} \pm s_{SAR,mi,K_{10}}$, demarcated by dashed-dotted lines. The light-gray area illustrates the full range of observed values within the computational domain, bounded by $SAR_{max,mi,K_{10}}(\omega)$ and $SAR_{min,mi,K_{10}}(\omega)$. A red dotted line marks the SAR exposure threshold for the public, $SAR_{10g}$, set below 4 W/kg. (b) Plot analogous to (a) for frequency $F_2$.*

## D.2 Parametrized cell models of the corneocytes $C_1$ through $C_{14}$

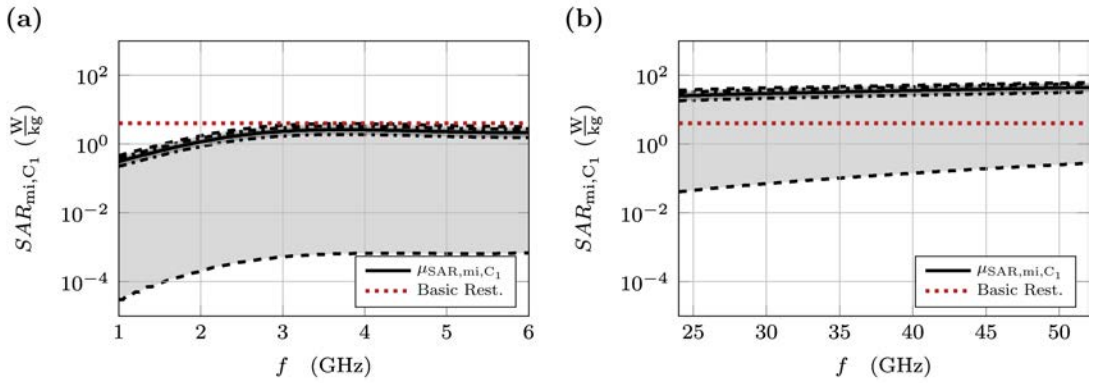


*Fig. D.11: $SAR_{mi,C_1}(\omega)$ for cell model $C_1$: (a) Semi-logarithmic representation of SAR values for frequency interval $F_1$. The solid black line indicates the mean, $\mu_{SAR,mi,C_1}$. A dark-gray area surrounds this mean, encompassing values within one standard deviation, $\mu_{SAR,mi,C_1} \pm s_{SAR,mi,C_1}$, demarcated by dashed-dotted lines. The light-gray area illustrates the full range of observed values within the computational domain, bounded by $SAR_{max,mi,C_1}(\omega)$ and $SAR_{min,mi,C_1}(\omega)$. A red dotted line marks the SAR exposure threshold for the public, $SAR_{10g}$, set below 4 W/kg. (b) Plot analogous to (a) for frequency $F_2$.*

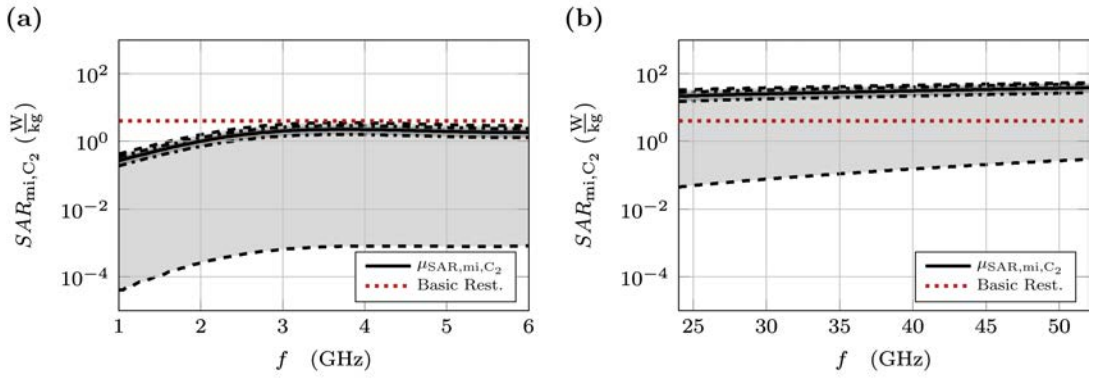


*Fig. D.12: $SAR_{mi,C_2}(\omega)$ for cell model $C_2$: (a) Semi-logarithmic representation of SAR values for frequency interval $F_1$. The solid black line indicates the mean, $\mu_{SAR,mi,C_2}$. A dark-gray area surrounds this mean, encompassing values within one standard deviation, $\mu_{SAR,mi,C_2} \pm s_{SAR,mi,C_2}$, demarcated by dashed-dotted lines. The light-gray area illustrates the full range of observed values within the computational domain, bounded by $SAR_{max,mi,C_2}(\omega)$ and $SAR_{min,mi,C_2}(\omega)$. A red dotted line marks the SAR exposure threshold for the public, $SAR_{10g}$, set below 4 W/kg. (b) Plot analogous to (a) for frequency $F_2$.*

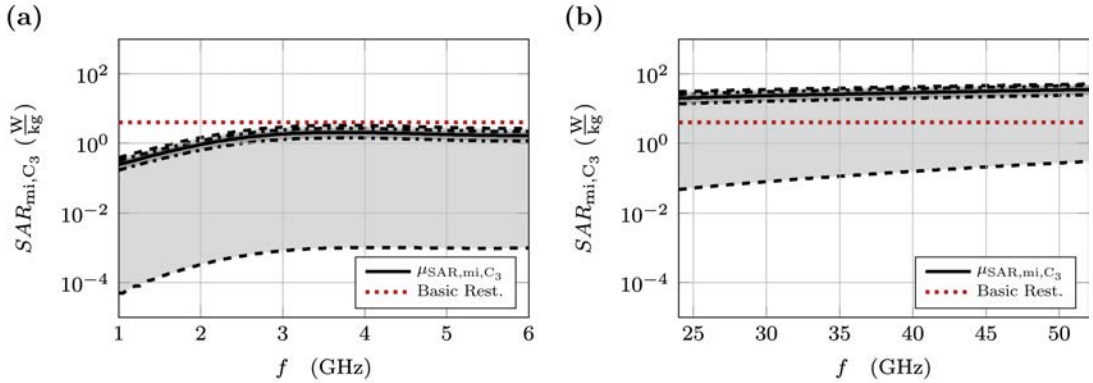


*Fig. D.13: $SAR_{mi,C_3}(\omega)$ for cell model $C_3$: (a) Semi-logarithmic representation of SAR values for frequency interval $F_1$. The solid black line indicates the mean, $\mu_{SAR,mi,C_3}$. A dark-gray area surrounds this mean, encompassing values within one standard deviation, $\mu_{SAR,mi,C_3} \pm s_{SAR,mi,C_3}$, demarcated by dashed-dotted lines. The light-gray area illustrates the full range of observed values within the computational domain, bounded by $SAR_{max,mi,C_3}(\omega)$ and $SAR_{min,mi,C_3}(\omega)$. A red dotted line marks the SAR exposure threshold for the public, $SAR_{10g}$, set below 4 W/kg. (b) Plot analogous to (a) for frequency $F_2$.*

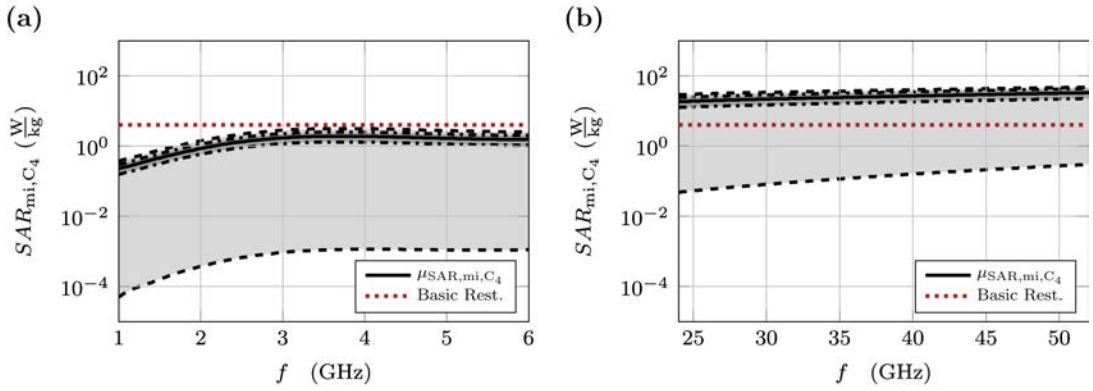


*Fig. D.14: $SAR_{mi,C_4}(\omega)$ for cell model $C_4$: (a) Semi-logarithmic representation of SAR values for frequency interval $F_1$. The solid black line indicates the mean, $\mu_{SAR,mi,C_4}$. A dark-gray area surrounds this mean, encompassing values within one standard deviation, $\mu_{SAR,mi,C_4} \pm s_{SAR,mi,C_4}$, demarcated by dashed-dotted lines. The light-gray area illustrates the full range of observed values within the computational domain, bounded by $SAR_{max,mi,C_4}(\omega)$ and $SAR_{min,mi,C_4}(\omega)$. A red dotted line marks the SAR exposure threshold for the public, $SAR_{10g}$, set below 4 W/kg. (b) Plot analogous to (a) for frequency $F_2$.*

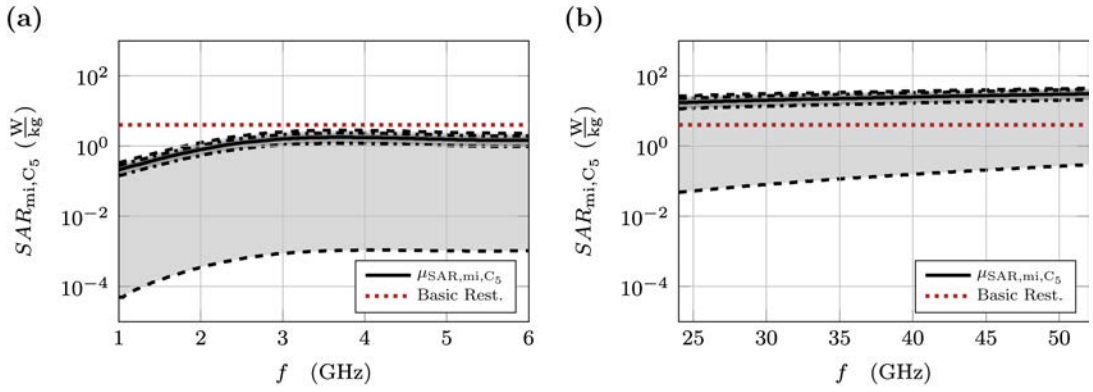


*Fig. D.15: $SAR_{mi,C_5}(\omega)$ for cell model $C_5$: (a) Semi-logarithmic representation of SAR values for frequency interval $F_1$. The solid black line indicates the mean, $\mu_{SAR,mi,C_5}$. A dark-gray area surrounds this mean, encompassing values within one standard deviation, $\mu_{SAR,mi,C_5} \pm s_{SAR,mi,C_5}$, demarcated by dashed-dotted lines. The light-gray area illustrates the full range of observed values within the computational domain, bounded by $SAR_{max,mi,C_5}(\omega)$ and $SAR_{min,mi,C_5}(\omega)$. A red dotted line marks the SAR exposure threshold for the public, $SAR_{10g}$, set below 4 W/kg. (b) Plot analogous to (a) for frequency $F_2$.*

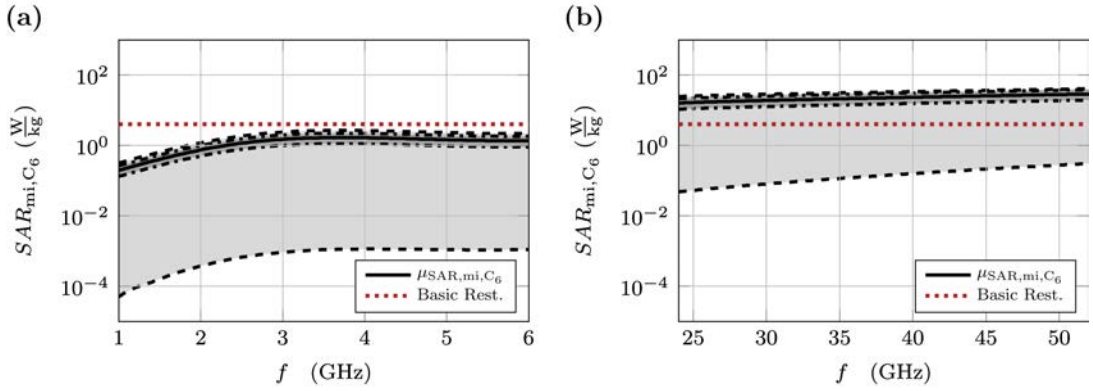


*Fig. D.16: $SAR_{mi,C_6}(\omega)$ for cell model $C_6$: (a) Semi-logarithmic representation of SAR values for frequency interval $F_1$. The solid black line indicates the mean, $\mu_{SAR,mi,C_6}$. A dark-gray area surrounds this mean, encompassing values within one standard deviation, $\mu_{SAR,mi,C_6} \pm s_{SAR,mi,C_6}$, demarcated by dashed-dotted lines. The light-gray area illustrates the full range of observed values within the computational domain, bounded by $SAR_{max,mi,C_6}(\omega)$ and $SAR_{min,mi,C_6}(\omega)$. A red dotted line marks the SAR exposure threshold for the public, $SAR_{10g}$, set below 4 W/kg. (b) Plot analogous to (a) for frequency $F_2$.*

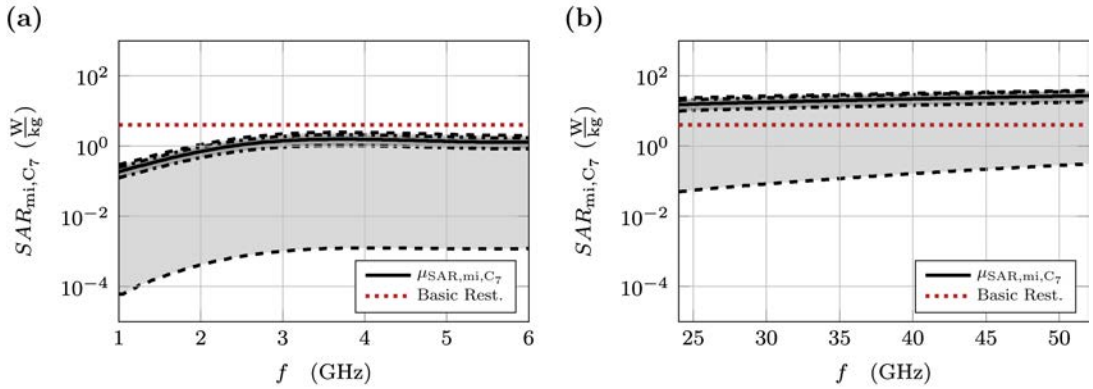


*Fig. D.17: $SAR_{mi,C_7}(\omega)$ for cell model $C_7$: (a) Semi-logarithmic representation of SAR values for frequency interval $F_1$. The solid black line indicates the mean, $\mu_{SAR,mi,C_7}$. A dark-gray area surrounds this mean, encompassing values within one standard deviation, $\mu_{SAR,mi,C_7} \pm s_{SAR,mi,C_7}$, demarcated by dashed-dotted lines. The light-gray area illustrates the full range of observed values within the computational domain, bounded by $SAR_{max,mi,C_7}(\omega)$ and $SAR_{min,mi,C_7}(\omega)$. A red dotted line marks the SAR exposure threshold for the public, $SAR_{10g}$, set below 4 W/kg. (b) Plot analogous to (a) for frequency $F_2$.*

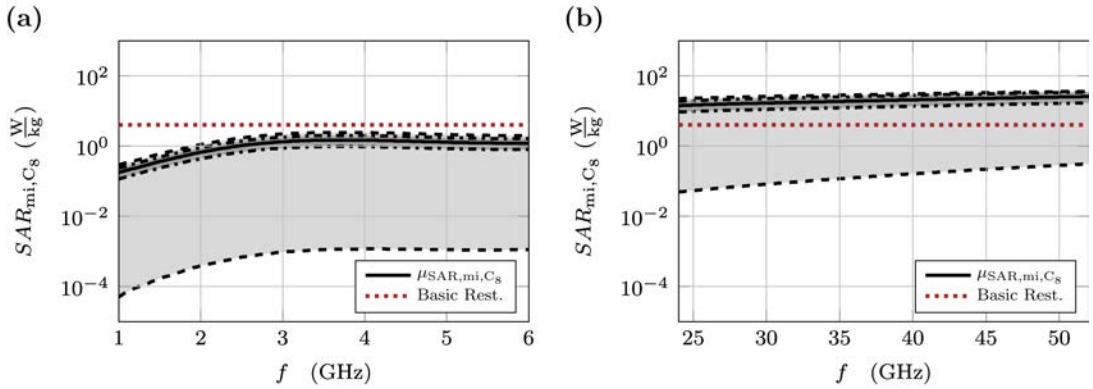


*Fig. D.18: $SAR_{mi,C_8}(\omega)$ for cell model $C_8$: (a) Semi-logarithmic representation of SAR values for frequency interval $F_1$. The solid black line indicates the mean, $\mu_{SAR,mi,C_8}$. A dark-gray area surrounds this mean, encompassing values within one standard deviation, $\mu_{SAR,mi,C_8} \pm s_{SAR,mi,C_8}$, demarcated by dashed-dotted lines. The light-gray area illustrates the full range of observed values within the computational domain, bounded by $SAR_{max,mi,C_8}(\omega)$ and $SAR_{min,mi,C_8}(\omega)$. A red dotted line marks the SAR exposure threshold for the public, $SAR_{10g}$, set below 4 W/kg. (b) Plot analogous to (a) for frequency $F_2$.*

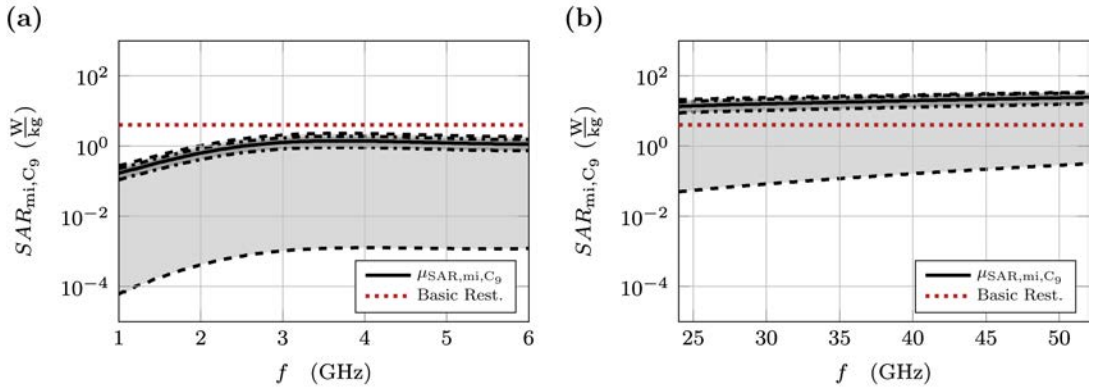


*Fig. D.19: $SAR_{mi,C_9}(\omega)$ for cell model $C_9$: (a) Semi-logarithmic representation of SAR values for frequency interval $F_1$. The solid black line indicates the mean, $\mu_{SAR,mi,C_9}$. A dark-gray area surrounds this mean, encompassing values within one standard deviation, $\mu_{SAR,mi,C_9} \pm s_{SAR,mi,C_9}$, demarcated by dashed-dotted lines. The light-gray area illustrates the full range of observed values within the computational domain, bounded by $SAR_{max,mi,C_9}(\omega)$ and $SAR_{min,mi,C_9}(\omega)$. A red dotted line marks the SAR exposure threshold for the public, $SAR_{10g}$, set below 4 W/kg. (b) Plot analogous to (a) for frequency $F_2$.*

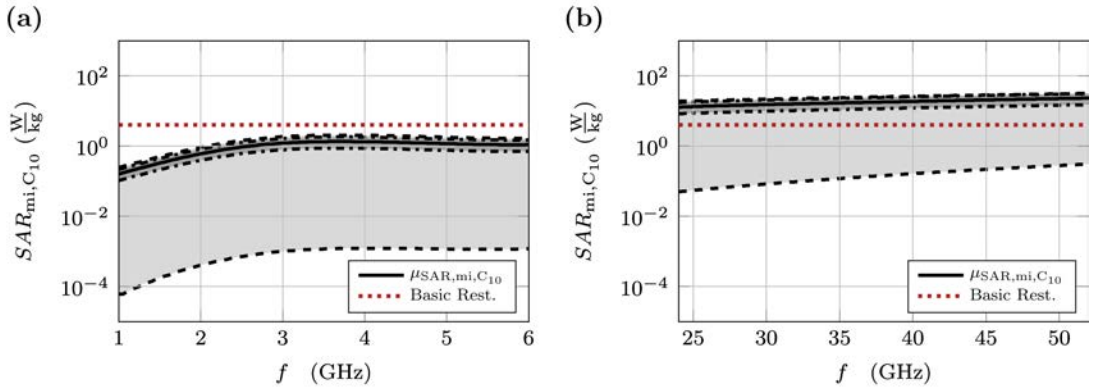


*Fig. D.20: $SAR_{mi,C_{10}}(\omega)$ for cell model $C_{10}$: (a) Semi-logarithmic representation of SAR values for frequency interval $F_1$. The solid black line indicates the mean, $\mu_{SAR,mi,C_{10}}$. A dark-gray area surrounds this mean, encompassing values within one standard deviation, $\mu_{SAR,mi,C_{10}} \pm s_{SAR,mi,C_{10}}$, demarcated by dashed-dotted lines. The light-gray area illustrates the full range of observed values within the computational domain, bounded by $SAR_{max,mi,C_{10}}(\omega)$ and $SAR_{min,mi,C_{10}}(\omega)$. A red dotted line marks the SAR exposure threshold for the public, $SAR_{10g}$, set below 4 W/kg. (b) Plot analogous to (a) for frequency $F_2$.*

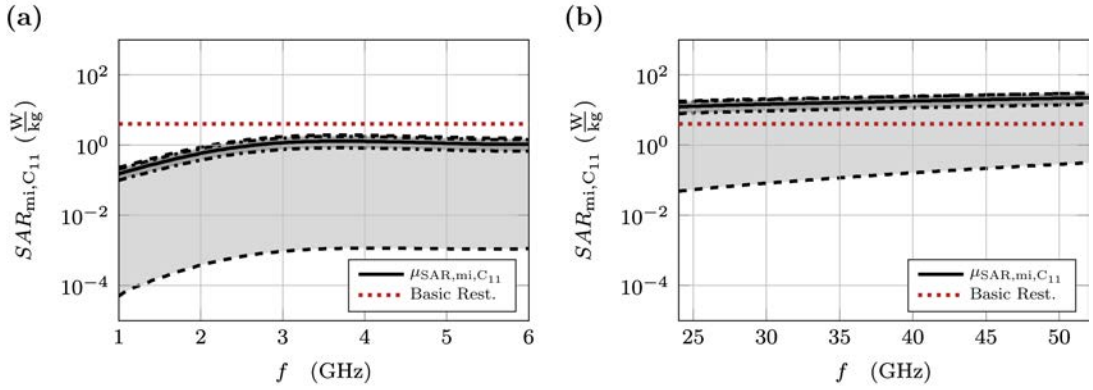


*Fig. D.21: $SAR_{mi,C_{11}}(\omega)$ for cell model $C_{11}$: (a) Semi-logarithmic representation of SAR values for frequency interval $F_1$. The solid black line indicates the mean, $\mu_{SAR,mi,C_{11}}$. A dark-gray area surrounds this mean, encompassing values within one standard deviation, $\mu_{SAR,mi,C_{11}} \pm s_{SAR,mi,C_{11}}$, demarcated by dashed-dotted lines. The light-gray area illustrates the full range of observed values within the computational domain, bounded by $SAR_{max,mi,C_{11}}(\omega)$ and $SAR_{min,mi,C_{11}}(\omega)$. A red dotted line marks the SAR exposure threshold for the public, $SAR_{10g}$, set below 4 W/kg. (b) Plot analogous to (a) for frequency $F_2$.*

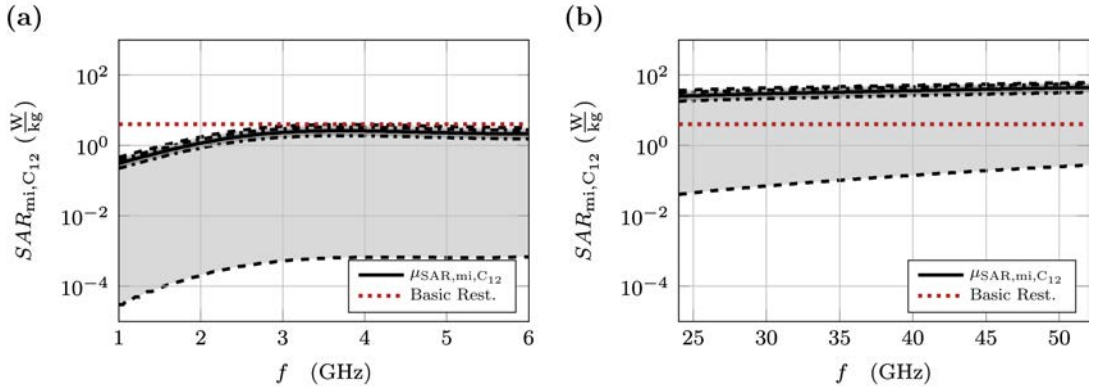


*Fig. D.22: $SAR_{mi,C_{12}}(\omega)$ for cell model $C_{12}$: (a) Semi-logarithmic representation of SAR values for frequency interval $F_1$. The solid black line indicates the mean, $\mu_{SAR,mi,C_{12}}$. A dark-gray area surrounds this mean, encompassing values within one standard deviation, $\mu_{SAR,mi,C_{12}} \pm s_{SAR,mi,C_{12}}$, demarcated by dashed-dotted lines. The light-gray area illustrates the full range of observed values within the computational domain, bounded by $SAR_{max,mi,C_{12}}(\omega)$ and $SAR_{min,mi,C_{12}}(\omega)$. A red dotted line marks the SAR exposure threshold for the public, $SAR_{10g}$, set below 4 W/kg. (b) Plot analogous to (a) for frequency $F_2$.*

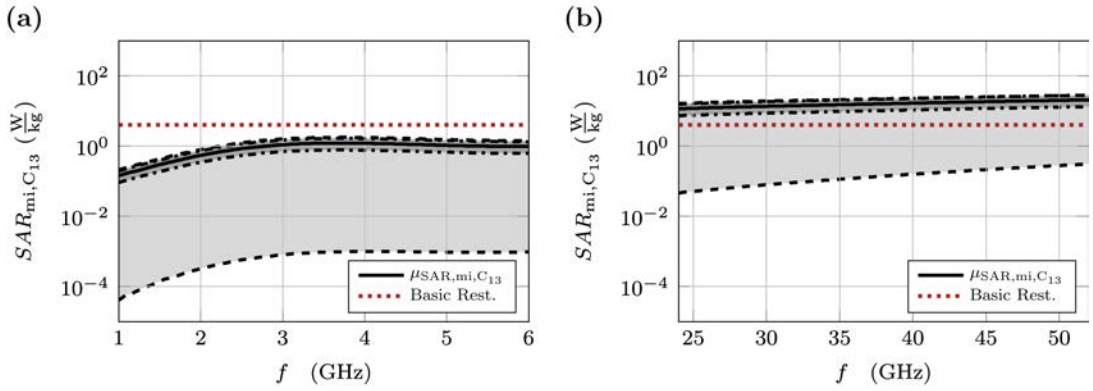


*Fig. D.23: $SAR_{mi,C_{13}}(\omega)$ for cell model $C_{13}$: (a) Semi-logarithmic representation of SAR values for frequency interval $F_1$. The solid black line indicates the mean, $\mu_{SAR,mi,C_{13}}$. A dark-gray area surrounds this mean, encompassing values within one standard deviation, $\mu_{SAR,mi,C_{13}} \pm s_{SAR,mi,C_{13}}$, demarcated by dashed-dotted lines. The light-gray area illustrates the full range of observed values within the computational domain, bounded by $SAR_{max,mi,C_{13}}(\omega)$ and $SAR_{min,mi,C_{13}}(\omega)$. A red dotted line marks the SAR exposure threshold for the public, $SAR_{10g}$, set below 4 W/kg. (b) Plot analogous to (a) for frequency $F_2$.*

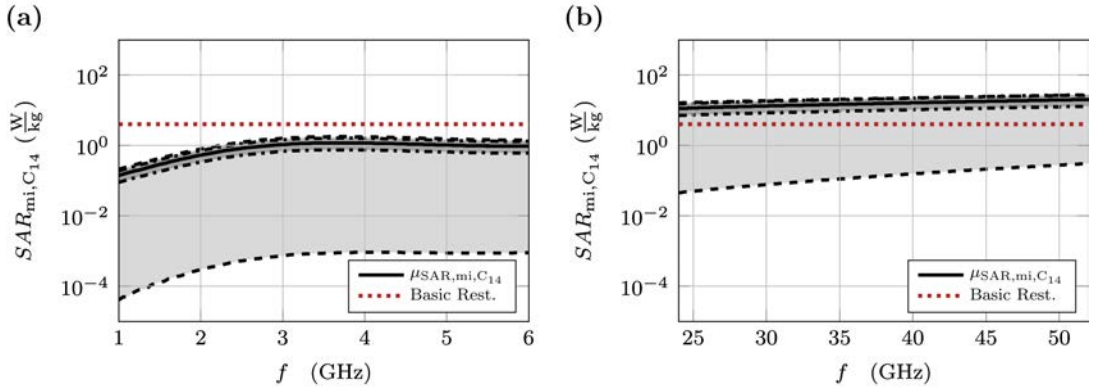


*Fig. D.24: $SAR_{mi,C_{14}}(\omega)$ for cell model $C_{14}$: (a) Semi-logarithmic representation of SAR values for frequency interval $F_1$. The solid black line indicates the mean, $\mu_{SAR,mi,C_{14}}$. A dark-gray area surrounds this mean, encompassing values within one standard deviation, $\mu_{SAR,mi,C_{14}} \pm s_{SAR,mi,C_{14}}$, demarcated by dashed-dotted lines. The light-gray area illustrates the full range of observed values within the computational domain, bounded by $SAR_{max,mi,C_{14}}(\omega)$ and $SAR_{min,mi,C_{14}}(\omega)$. A red dotted line marks the SAR exposure threshold for the public, $SAR_{10g}$, set below 4 W/kg. (b) Plot analogous to (a) for frequency $F_2$.*